Homogenisation of the Electrothermal Behaviour of Granular Material



Caoimhe Mary Rooney

St Anne's College

University of Oxford

A thesis submitted for the degree of

Doctor of Philosophy

Trinity 2019

Maidir le mo thuismitheoirí, go raibh maith agaibh as gach rud.

Acknowledgements

I would like to express my deepest thanks to the following people for making this thesis possible:

Chris Breward and Colin Please for their dedication to the InFoMM CDT and for creating a stimulating and collaborative environment.

My academic supervisors, Colin, whose enthusiasm and excitement for mathematics is inspiring, and Sam Howison, for challenging me to think independently and deeply about a vast range of mathematical curiosities. Thank you for your time, patience and support.

My Norwegian collaborators, Svenn Anton Halvorsen, Manuel Sparta, Aasgeir Valderhaug and Jesse White for hosting me in Kristiansand and their interest in my work.

Ian Griffiths, for his continuous encouragement and guidance from the very beginning and for sharing his refreshing and fun approach to research.

Mo Dalwadi, for taking the time to understand my research and helping me conquer some particularly tricky aspects.

The members of InFoMM Cohort 2, who from the depths of C6 to the tops of Romanian mountains made PhD life an unforgettable experience. I would like to especially thank Jess, whose friendship from the very first day has been invaluable.

Florian, for always making time to tackle my problems, mathematical or otherwise, and for believing in me from start to finish.

My brothers, Conleth and Dáire, for keeping me laughing and reminding me of what's important in life.

Most importantly, my parents, Nichola and Kevin, for their unwavering and insurmountable support and love throughout every aspect of my life. You are my inspiration.

Industrial Acknowledgements

This work is supported by the EPSRC Centre for Doctoral Training in Industrially Focused Mathematical Modelling (EP/L015803/1) and is part of the research project Electrical Conditions and their Process Interactions in High Temperature Metallurgical Reactors (ElMet/247791). ElMet is a cooperation between NORCE (Project Owner), The Norwegian University of Science and Technology (NTNU), and the industrial companies Elkem and Eramet. The University of Santiago de Compostela and University of Oxford are research partners. The project is financially supported by The Research Council of Norway and the two companies.

Abstract

Granular material is a critical component of many industrial applications and is particularly important for metallurgical processes. In particular, granular carbon experiences electrical heating in a metallurgical furnace known as a calciner. As the temperature of the carbon increases, its chemical and physical properties transform, namely to resemble those of graphite. However, the high temperatures within the calciner make experimental measurements very difficult to obtain. Consequently, a fundamental understanding of the inner mechanisms of the process has proved to be most challenging.

Mathematical models can be used to assimilate the behaviour of the furnace by studying the tight coupling between electric and thermal conduction. However, for the multitude of particles present within the calciner, direct or discrete models that consider every particle individually are computationally intractable. It has been shown that the electrothermal behaviour on the scale of a particle is crucial to explain the behaviour on the scale of the furnace, yet the former scale is several orders of magnitude smaller than the latter.

In this thesis, we propose mathematical models to approximate the physical phenomena that govern the operation of the calciner furnace, validate their accuracy and demonstrate their numerical feasibility. The models that we study are founded upon the homogenisation technique known as the method of multiple scales. This is a systematic, effective-medium approach that exploits the vast discrepancy between the scale of the furnace and the scale of the particles to extract homogeneous effective parameters from the heterogeneous media. In particular, we discuss how to extend the standard multiple scales technique to include a nonlinear, nonlocal, integral boundary condition for radiative transfer. Furthermore and significantly, we demonstrate the influence of contact resistance by considering jumps in the electric potential at contact interfaces and conducting an asymptotic analysis to study the effect of microscopic contacts.

Contents

1 Introduction **1**

2 Background and problem outline **4**

2.1 Industrial motivation 4

2.2 Literature review 7

2.3 Modelling techniques 11

2.4 Discussion 13

3 Homogenisation of electric current and heat flow **14**

3.1 Conductivity functions 16

3.2 Method of multiple scales 17

3.3 Steady current conduction 18

3.3.1 Homogenisation via the method of multiple scales 20

3.3.2 Numerical results 25

3.4 Coupled electrothermal conduction 31

3.4.1 Homogenisation of Ohmic heating term 32

3.4.2 Numerical results 39

3.5 Temperature as a function of electric potential 41

3.5.1 Numerical results 47

3.6 Discussion 48

4 Radiative transfer **52**

4.1 Modelling thermal radiation 54

4.2 Homogenisation of integral constraints 55

4.2.1 Variation of the slow scale 56

4.3 Extended multiple scales analysis 61

4.4 Numerical results 69

4.5 Coupling with the electrical problem 74

4.6 Discussion 75

5 Steady current conduction through small contact points **77**
5.1 CT scan of anthracite particles 78
5.2 Explicit solution in two dimensions 80
5.2.1 Electric potential close to small contacts 88
5.3 Solution by matched asymptotics 90
5.3.1 Two dimensional problem 90
5.3.2 Extension to three dimensions 98
5.4 Comparing matched asymptotics with the numerical solution to the 2D cell problem 104
5.5 Discussion 107

6 Contact resistance due to imperfect surfaces **110**
6.1 Modelling imperfect surfaces 111
6.2 Resistance between contacting cylinders 112
6.2.1 Comparing Hertzian theory with experimental data 115
6.2.2 Discussion 120
6.3 Homogenisation of jump condition 120
6.3.1 Problem adaptation 122
6.3.2 Homogenisation of jump condition 124
6.3.3 Deriving the variational form 129
6.3.4 Numerical results 134
6.4 Discussion 140

7 Conclusion **142**
7.1 Summary of key results 142
7.2 Guidelines for the industrial partner 147
7.3 Possible extensions 149

A Defining the electrical and thermal conductivity functions **152**

B Homogenisation of the coupled problem with contact resistance **158**
B.1 Derivation of the boundary condition 158
B.2 Homogenisation 159
B.2.1 Homogenisation of jump condition 161

Bibliography **165**

Chapter 1

Introduction

Granular matter is ubiquitous in industrial processes, second only to water as the most prevalent material. From fine powders to chunky coal, the necessity to understand granular matter is evident, however the irregularity, size and number of individual particles within the bulk makes studying their behaviour extremely difficult.

The metallurgy industry relies on granular material. Processes such as extracting metals from their ores to make refined alloys or the development and production of metallic materials usually involve the manipulation of material in granular form. In particular, many of these industrial processes involve the heating of granular material via large electric currents, thereby requiring extremely high temperatures obtained through huge amounts of electrical energy. There is a great need for a better understanding of the interdependent mechanisms contributing to these processes, in particular, between the electric currents and the temperature distribution. Due to the high temperatures accurate internal measurements are almost impossible to achieve, therefore mathematical models are required to ascertain the behaviour. This insight is vital in understanding how to optimise the process and minimise the energy needed to obtain a satisfactory product. This is exactly the focus of the ElMet Programme (Electrical Conditions and their Process Interactions in High Temperature Metallurgical Reactors), led by research institute NORCE with collaborating companies Elkem and Eramet. The ElMet programme is involved in the investigation of the electrical behaviour in various types of furnaces, including the calciner, which is used for the thermal manipulation of granular carbon to produce a graphite-like material for industrial use.

The work in this thesis is focused on obtaining efficient, accurate and insightful mathematical models for the electrothermal conduction through granular material in a calciner furnace. We begin by explaining the industrial motivation in more detail in Chapter 2 with a discussion into the most important aspects of metallurgical

furnaces. We motivate the need for mathematical models and explore previous modelling techniques applied to similar processes. From this review, we emphasise the role of particle contacts in ascertaining the flow of electric current and heat through a granular material and thus justify the value in studying the effect of small, imperfect contacts.

In Chapter 3, we introduce the physical problem in terms of the relevant mathematical equations and outline the homogenisation technique known as the method of multiple scales which we will use to study various aspects of the electrothermal model. We focus first on electrical conduction in isolation, neglecting Ohmic heating, to demonstrate the method of multiple scales and its suitability for approximating electric conduction in granular material. We extend this model by introducing a coupling with thermal conduction, thus demonstrating our ability to tackle a system of nonlinear, interdependent partial differential equations with ease in comparison to a direct simulation.

We further extend this model in Chapter 4 by including thermal transfer via radiation. Radiative effects are notoriously difficult to include in mathematical models due to their definition as a nonlinear, nonlocal and geometrically-dependent boundary condition. In particular, the nonlocality of the condition poses complications when applying the method of multiple scales to the system of equations. We demonstrate how to adapt the method of multiple scales to allow for this condition and verify our model by comparison to a direct simulation, noting the computational benefit of homogenisation. We draw conclusions into the influence of gas-filled voids between conducting solid on thermal transfer.

Following the conclusion from the literature that particle contacts are crucial to understand current conduction through granular material, we observe CT scan images of a collection of anthracite particles to gain a better understanding of the size of these contacts in Chapter 5. We notice that the contacts are several orders of magnitude smaller than the particle size which motivates us to conduct an asymptotic analysis into the effect of small contacts. By considering simplified two- and three-dimensional geometries, we obtain analytical solutions to the steady current conduction equation through extremely small contacts, in particular, deducing a relationship between the total current through the contact and its size. These relationships allow us to quantify the influence of contact size on the flow of current, which we verify by comparing the result to the numerical solution to the homogenisation cell problem.

Although the size of the contact is extremely significant, the nature of the contacts also contributes to the efficiency of current conduction through a particle contact. We

study such effects in Chapter 6. Following an experimental analysis into the effect of applied force on contact area and hence contact resistance we introduce the effect of oxide layers, or thin insulating films, at contact interfaces to our model and study the influence of such layers on current conduction through the granular material.

Finally, we conclude our results in Chapter 7 and suggest how our models can best be used to benefit our industrial partner, NORCE. We then outline some possible extensions that could be incorporated into the model to increase its relevance to the physical problem and improve model predictions.

Chapter 2

Background and problem outline

Anthracite, a coal of high carbon content, is an extremely valuable material within the metallurgy industry, particularly for use within furnaces as a vital component of electrodes and lining materials. In preparation for such uses the anthracite is subject to heat treatment to ensure that the resulting material exhibits certain properties and characteristics, primarily that its electrical resistivity is minimised. Further to this the material should comprise an insignificant proportion of volatiles whilst being sufficiently dense. A furnace known as a calciner [14] is used for such treatment within which the material is subject to large alternating currents and hence is heated via Ohmic heating. Thus, both the flow of electric current and heat through the anthracite are vital processes that determine the precise transformation of the material to render it suitable for industrial use. Modelling such processes requires a sound understanding of the electrical and thermal conductivity. However, this is complicated by the granular nature of the anthracite, for example due to the contacts between particles and radiation within gas-filled voids.

In this chapter we discuss the industrial motivation for this work, namely the calciner and the processes contributing to the operation of the furnace. This is followed by a discussion of some modelling techniques presented in the literature, with particular focus on models that determine the electrical and thermal conductivity of granular materials. Finally, we will introduce the primary modelling technique that we will implement throughout our analysis, namely the method of multiple scales.

2.1 Industrial motivation

Many metallurgical furnaces involve granular material being heated to high temperatures by the conduction of electric current between submerged electrodes, for example the production of silicon [90], ferromanganese [72] and other ferroalloys [37].

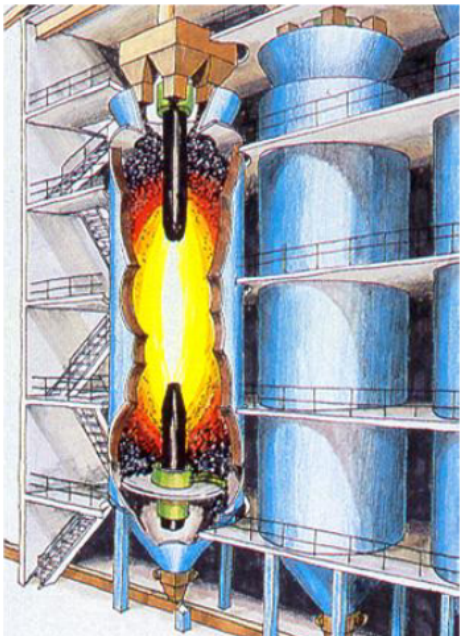


Figure 2.1: Artist's impression of a calciner [43].

Thus modelling such furnaces involves accounting for many similar physical processes exhibiting comparable mathematical complexities and using the same modelling techniques. We concentrate on the calciner furnace as a case study due to its apparent simplicity, namely it only involves one raw material and two electrodes, compared to more complex mixtures of materials and electrode structures in other types of furnaces. The methods and results discussed in this thesis provide a framework that can be extended to other furnaces and even outside of the metallurgical field to other applications involving electrical and thermal conduction through granular materials.

The calciner is a large cylindrical furnace, or what is described as a "shaft furnace", approximately 8 m in height and 2 m in diameter; an artist's impression is depicted in Figure 2.1. The furnace contains two electrodes, one at the top and one at the bottom, between which an alternating voltage is applied, producing a large alternating current of up to 15000 A. The anthracite, in granular form, is added continuously around the top electrode and removed from the bottom via "scrapers", where the rate of removal by these scrapers determines the speed of the particles through the furnace. As the particles conduct the electric current between the two electrodes they experience Ohmic heating, causing temperatures within the calciner to range from room temperature to above 2500°C near the tip of the upper electrode [14].

Anthracite is chosen due to its very high carbon content, which is often between 92% and 98% and its low proportion of impurities. The goal of calcination is to

obtain a partly "graphitised" form of anthracite, that is, a material whose chemical properties resemble those of graphite. Graphite is an extremely desirable material in the metallurgy industry due to its superior ability to conduct electricity, however pure graphite is very expensive. By the heat treatment of anthracite, one can obtain a material that exhibits similar characteristics to graphite for a much lower price. The main objective is to produce a material that has a low resistivity and can withstand extremely high temperatures. The calcined anthracite is often used as a major component of electrodes and ramming pastes which are both vital elements in many metallurgical processes.

Anthracite undergoes various transformations during the calcination process, of which three critical processes are known to occur. The first of these is called "carbonisation", which is the pyrolysis of anthracite due to the expulsion of volatiles. Organic impurities naturally occur within anthracite, particularly sulphur, nitrogen and oxygen, along with other small traces that manifest as ash after heating. It is important to drive off as high a proportion of these volatiles as possible in order to maximise the purity of the final product.

The second critical process is called "densification" which describes the shrinkage of anthracite particles due to changes to its density. It is important that densification takes place within the calciner otherwise one runs the risk of producing an electrode or ramming paste that may undergo structural changes and contract when in use.

The third and final critical process is "graphitisation". This is the irreversible conversion of a material to produce a graphite-like crystal structure. Graphite has a planar structure composed of layers of graphene within which free electrons are responsible for high electrical conductivity. The crystal structure of anthracite is much more disordered, however high temperatures cause realignment so that it resembles the ordered layers of graphite. This in turn causes its resistivity to decrease dramatically.

We focus on mathematically modelling the aspect of the calcination that involves the transformation of anthracite from a material of low electrical conductivity to that of high conductivity, related most closely to the graphitisation process, therefore we neglect carbonisation and densification for the purpose of this thesis. However, we do not study this on an atomic level: we are not interested in the precise realignment of crystal structure, rather we correlate the degree of graphitisation with the temperature within the furnace and allow the electrical and thermal conductivity of the material to evolve appropriately. This is discussed in more detail in Chapter 3.

2.2 Literature review

The graphitisation of anthracite is critically dependent on the temperatures that the material has been exposed to, whereas the temperatures in the furnace are a consequence of electric current conducting through the particles. The heat generated by Ohmic heating causes the temperature to rise and hence the electrical and thermal conductivities of the anthracite to increase [17, 29, 32, 57, 78, 92], thereby affecting the electric field within the furnace. This interdependent nature of the electrical and thermal processes yields a highly coupled physical model which requires a sound understanding of current conduction, Ohmic heating and the evolution of the electrical and thermal conductivities. This is further complicated by the granular nature of the anthracite, therefore, simplifications are often implemented in order to obtain tangible results.

Within the relevant literature relating to the furnaces, the authors often discuss the concept of the bulk electrical conductivity of a granular material, or its inverse, the *bulk electrical resistivity*. This can only sensibly be defined as an average. For example consider a large cylinder of length L and cross-sectional area A containing granular material, then the bulk resistivity ρ features in the formula

$$V = \frac{\rho L}{A} I, \tag{2.1}$$

for the current I through the cylinder and voltage drop V between (perfectly conducting) ends. Thus the bulk electrical resistivity is affected by the resistivity of the particle material, the *contact resistance* between individual particles and the effect of any insulating voids or materials.

We define the contact resistance between particles as the resistance incurred by electric current conducting from one particle to another via a contact interface between them. A number of different phenomena contribute to the contact resistance which can be partitioned into "geometrical contact resistance" and "material contact resistance". The former is a direct consequence of the particle shape, size and orientation, for example the influence of contact sizes on current conduction. The latter relates to the material itself, for example resistance can be affected by the presence of thin oxide layers that coat the particles. We will return to these concepts in more detail below.

Understanding the bulk electrical resistivity of granular material composed of carbon was the focus of Eidem [32], who explored the behaviour primarily through experimental work. He developed an apparatus consisting of a refractory cylinder

built around two graphite electrodes of 304.8 mm diameter. Also within the cylinder was a packed bed of randomly distributed carbon particles. A maximum current of 1600 A was applied across the two cylinders and the voltage drop was measured via the four-point measurement principle. The voltage drop over the central part of the carbon bed was measured by molybdenum wires inserted through the wall, whereas the temperature at these positions was measured using thermocouples that were inserted through the top electrode. His findings suggest that the bulk resistivity decreases with an increase in temperature, conclusions that are also drawn in other sources of literature [28, 29, 91].

A key finding of Eidem's work was the critical dependence of electric current conduction on particle contacts. Eidem's experiments imply that contact resistance is of vital importance when considering bulk resistivity and in fact, 70–95% of the bulk resistance is attributed to the contacts at temperatures up to 1400°C and approximately 50% at 1600°C. When considering different metallurgical cokes, Eidem conducts a statistical analysis that suggests that the discrepancy between their resistivities is a consequence of the contact resistance between coke particles, as opposed to the material resistivity. Experimental observations of the dependencies of bulk resistivity is also discussed by Espinola et al. [34] who conduct experimental analyses to study the electrical resistivity of carbonaceous powders to deduce their suitability for use in electrodes. Their findings suggest a strong dependence of the bulk resistivity on contact resistance between the carbon grains. Taking a theoretical approach, Dhainaut [28] simulated electric current conduction between two idealised two-dimensional carbon particles in contact, concluding that the majority of the bulk resistance is attributed to contact resistance for small contacts, namely if the contact area is approximately two orders of magnitude smaller than the size of the particle.

Similar to electric current conduction, the material thermal conductivity and the particle contacts are extremely important in deducing the effective bulk thermal conductivity. This is discussed by Batchelor et al. [11] who study a packed bed of particles of large conductivity embedded in a matrix of lower conductivity and derive a general formula for the effective conductivity in terms of the average thermal dipole strength of a particle. They deduce that the thermal flux across the particle surface is concentrated close to the particle contacts and approximate the dipole strength as the weighted sum of the fluxes across areas close to the contact. Zhou et al. [105] refer to the drastic temperature variations near to contacts, thus justifying a need for very fine meshes when numerically evaluating the effective thermal conductivity of packed beds by a boundary element method. Aichlmayr and Kulacki [1] conduct

experimental analyses to compare several effective thermal conductivity models and thus emphasise the dominant effect of particle contacts on the effective conductivity. The comparable behaviour of electric current and heat is hardly surprising due to the similarity of the equations of electrical and thermal conduction. Many of the conclusions drawn for electrical transfer can be extended to the thermal problem, and vice versa.

With the majority of the bulk resistivity being attributed to the particle contacts, understanding the intricacies of the contact areas between particles is vital. We now focus our discussion on electric current conduction, bearing in mind that similar deductions can be extended to thermal conduction. Holm [46] describes an electrical contact as an interface between two conductors which is able to carry electric current. From experimental analysis and CT scans, discussed further in Chapter 5, we deduce that the contacts between particles are microscopic in size compared to the particles themselves, therefore as current conducts through the solid material, it is significantly constricted when it passes through these areas. This results in large current densities very close to contacts and hence large resistances, namely, *constriction resistance*. We consider such resistance to be a geometrical contact resistance.

However, Holm claims that the contacts between particles that we observe are rarely entirely electrically conducting. This is due to the surface topography of particles which may be nominally flat, however surface roughness will mean that the materials may only make contact at a finite number of asperities, as depicted in Figure 2.2. For an imperfect contact the actual contact area is made up of small electrical contacts and may be of a smaller order of magnitude than the apparent contact area, thus inducing what we term *asperity resistance*. This is effectively constriction resistance over multiple small contacts, thus can be considered as a geometrical contact

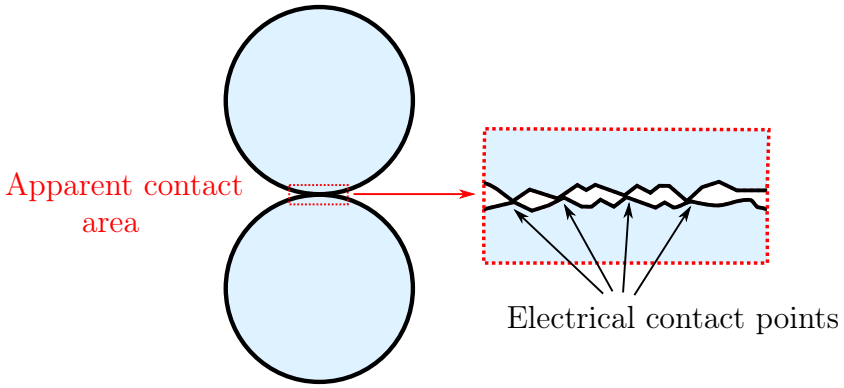


Figure 2.2: Schematic of the actual and apparent contact area. The former is likely made up of small electrical contacts; thus the actual area may be of a smaller order of magnitude.

resistance. However the quality of the particle surface is a property of the material.

Thus the constriction resistance due to the apparent contact area is likely greater than first perceived due to the microscopic asperities. Accurately accounting for such surface intricacies in a mathematical model is extremely difficult. Models by Greenwood and Williamson [38] and Bush et al. [15] describe rough surfaces as a collection of bumps where each of these is an electrical contact that experiences constriction resistance. We discuss these among other models in Chapter 6.

A further consequence of imperfect particle contacts is the concept of *oxide-layer resistance* which describes the resistance incurred whilst current tries to pass through a thin, highly resistive film or oxide-layer between two surfaces [46, 56, 89, 103]. Depending on the thickness and resistivity of the layer, this may significantly restrict current conduction between particles.

In conclusion, it is vital to understand not only the size of the particle contacts but also their nature, in particular their surface roughness and the presence of thin, resistive layers. We will further discuss contact resistance and its various attributions in Chapters 5 and 6.

There are no strong claims that the gas within the voids between anthracite particles in a calciner is ionised, even at the anticipated high temperatures. It is therefore acceptable to model current propagation purely by conduction through solid material with the gas acting as a perfect insulator. However heat transfer can occur through the gas-filled voids at high temperatures by radiation [18, 66, 96]. Tsotsas and Martin [98] use experimental and theoretical arguments to highlight the increase of heat transfer due to radiation at the elevated temperatures expected within a metallurgical furnace. Similarly, Zumbrunnen et al. [111] attribute the change in thermal conductance with particle size to be a consequence of the distance over which radiation can penetrate. Radiation can be complicated to include in thermal transfer models due to the complexity associated with its physical behaviour. Radiative transfer through a void depends on the temperature and orientation of the surrounding surfaces and hence involves a non-local, non-linear, integral condition [66, 71, 97]. Radiative transfer also depends on the optical depth of the gas in the void; for an optically thick medium, radiation travels only a short distance before being absorbed or scattered [47, 66, 71]. In this case it is possible to convert the integral relation for radiative transfer into a diffusion condition, similar to that for heat conduction. This approximation provides a significant simplification as energy transfer depends only on the local conditions and can be solved using standard numerical techniques such as finite-difference schemes. The Rosseland approximation is a well-known method for

diffusion approximation to the radiative transport equation [47, 84] and is used widely to include radiative contributions to the thermal conductivity of composite materials [24, 40, 73]. However this simplification is only valid in optically thick media where the radiation intensity is required to be nearly isotropic. In Chapter 4, we discuss the direct inclusion of the radiative integral condition for an optically thin medium.

2.3 Modelling techniques

Various approaches to model electrical and thermal conduction through granular or more general composite materials are present within the literature. We will focus on those that aim to derive effective electrical and thermal conductivities to describe the bulk. Describing the effective conductivity requires knowledge of the size, shape, distribution and conductivity of the particles themselves, along with the interaction between the particles and the behaviour in the gas-filled voids. For random structures this is very difficult to do. Many models impose the simplification of a periodic distribution of particles which are often approximated to be regular in shape. The majority of the prominent models in the literature focus on effective thermal conductivity, however we can again draw parallel arguments to the electrical problem. In this section we discuss some of these general models, noting that extensions to include more complicated phenomena such as radiation and contact resistance will be considered in Chapters 4 and 6 respectively.

Maxwell [63] proposed the first analytical expressions for effective conductivity of heterogeneous media by considering a dilute dispersion of conductive spherical particles embedded in a conductive continuous matrix. For a thermal problem, the effective conductivity was derived using far-field perturbations to solutions of the steady heat equation. These models are widely accepted for cases where the spherical inclusions are very small in comparison with the distances between the particles and can be extended to include radiative effects in the voids [55]. However general Maxwell models neglect the influence of contacts between particles due to the dilute assumption.

Crane and Vachon [26] focus on the effective thermal conductivity of a packed bed of particles via Ohm's Law models, simplifying the material as a repetitive geometry of idealised cubic particles arranged in a square array that are distributed to preserve the proper volume fractions of the physical system. The effective thermal conductivity is thereby determined by considering the equivalent electrical network model and applying Ohm's Law. Such an approach is further simplified by requiring one-dimensional heat transfer. From this analysis, the authors deduce upper and

lower bounds of the effective conductivity, accurate to within $\pm 20\%$ of experimental observations.

Zehner and Schlunder [102] consider a "point contact model", applicable to spherical, cylindrical and irregular particles. The authors deduce an analytical expression for the effective conductivity based upon a cylindrical unit cell comprising a solid sphere and surrounding fluid, each of which are thermally conductive. The expression is widely used in the literature, demonstrating satisfactory accuracy for particular solid-fluid thermal conductivity ratios. However, for higher ratios, namely $k_s/k_f > 10^3$ for solid conductivity k_s and fluid conductivity k_f, the Zehner-Schlunder model under predicts the effective conductivity [54]. Hsu et al. [51] postulate that this is a consequence of only considering point contacts between the solid spheres and obtain much better agreement with experimental data by considering finite contact areas between particles.

The above examples are all continuum models, however discrete models are often applied to consider the effective conductivity of granular material. In particular, discrete-element methods (DEM) consider each particle individually; electrical and thermal transfer is considered discretely within every entity in the bulk. This naturally leads to an extremely large number of equations to solve because a calciner is likely to contain over a million particles. Furthermore, such direct computer simulations require detailed geometrical and physical information about each particle, an endeavour that is likely to be impossible. Thus the computational solutions are infeasible and their accuracy is limited by the accuracy of the input data.

In this thesis, we focus on homogenisation methods such as the method of multiple scales [74, 76] to model the electrothermal behaviour of granular material. This technique exploits the discrepancy between the scales of the problem, namely the size of the particles is significantly smaller than the size of the bulk. This allows us to derive averaged equations on the particle scale, or microscale, that can be solved to obtain effective parameters, such as an effective conductivity, which is fed into a homogeneous model on the furnace scale, or macroscale. Therefore the microscopic heterogeneities are captured in the effective parameter rather than the geometry.

Homogenisation techniques are widely applied to heterogeneous matter. Pasternak and Mühlhaus [75] present two different homogenisation techniques to study a 1D granular material, namely homogenisation by differential expansion and homogenisation by integral transformation, where the former approach was found to produce accurate solutions to the model. Zhou et al. [106] propose a homogenisation technique to study thermal conduction through granular material in a vacuum, neglecting the

effect of radiation and verified their results against DEM simulations. Allaire et al. [5, 3, 4] employ the method of multiple scales on a geometry comprising a solid matrix with gaseous perforations and include the effect of radiation in their model. We discuss this further in Chapter 4.

The benefit of the method of multiple scales is the potential to include rapidly varying features of the problem, for example a rapidly oscillating conductivity function or a complicated microscopic geometry. When considering the electrothermal model on the scale of the furnace, it is extremely difficult to include variations on the particle scale due to their vastly different sizes. We have indicated in this chapter that particle contacts contribute overwhelmingly to the bulk electrical and thermal resistivities and therefore cannot be neglected. The method of multiple scales allows us to include such microscopic intricacies in the macroscopic model whilst still being numerically accurate and feasible. More detail into how we use the method of multiple scales is discussed in Chapters 3, 4 and 6.

2.4 Discussion

In conclusion, we wish to study the electrothermal behaviour of granular material within metallurgical furnaces. This involves understanding the coupling between electric current conduction and Ohmic heating to understand the effect such mechanisms have upon the material properties. Due to the multitude and geometrical complexity of the particles, our goal is to derive effective thermal and electrical conductivities for the granular material as a whole, whilst still capturing the vital influence of the microscopic particles on the behaviour of electric current and temperature. We have introduced the process of calcination which describes the heat treatment of anthracite particles as our case study, outlining the important phenomena and critical processes to consider. We then discussed the relevant literature, outlining the experimental and theoretical results related to electrical heating of granular material. After mentioning a few of the prominent modelling techniques, we introduced the method of multiple scales, a mathematically rigorous technique that we will implement throughout our analysis to derive the effective parameters of our model. We begin our study by considering steady current conduction within an idealised geometry of regular particles to demonstrate the suitability of this method.

Chapter 3

Homogenisation of electric current and heat flow

The purpose of the calcination process is to thermally manipulate the chemical and physical properties of anthracite to obtain a material that resembles graphite. The temperatures necessary for this transformation to take place are obtained in a calciner via Ohmic heating, that is, the heat induced due to the passing of an electric current through the conductive material. Therefore, to understand the graphitisation of anthracite within a calciner, it is necessary to deduce the temperature profile and to do so requires an understanding of electric current conduction throughout the material.

The propagation of electric current through a granular material depends on the material properties of the particles, in particular, the electrical conductivity. This is an intrinsic characteristic of the material itself, however, it can be altered depending on the environment to which the material is exposed. Graphite is renowned for its high electrical conductivity and as anthracite is exposed to high temperatures and graphitises, its electrical conductivity increases significantly [17, 29, 32, 78, 92]. Eidem [32] developed an experimental apparatus to measure the conductivity of anthracite at a range of temperatures and attributed some of the conductivity increase to volatiles being driven off via heating. He notes that the increase is moderate above 1000°C, compared with below 1000°C. Similar experimental analyses are carried out by Celzard et al. [17] on a variety of types of raw anthracites. Every anthracite exhibits a sharp rise in conductivity between 600 and 800°C, as also observed experimentally by Powell et al. [78], who furthermore reported an increase in the thermal conductivity. Sørlie et al. [92] study the cathode lining of industrial aluminium electrolysis cells, which are made from calcined anthracite and also observe an increase in the electrical conductivity with increased temperatures. Dijs et al. [29] consider

anthracite as a reducing agent within metallurgical processes and also observe the same critical dependence of the electrical conductivity on temperature.

Another intrinsic property of anthracite that undergoes a change due to high temperatures is the thermal conductivity, that is, the material's ability to conduct heat. Similar to the electrical conductivity, the thermal conductivity of anthracite increases with temperature, however, the increase is several orders of magnitude less than that of the electrical conductivity and is seen experimentally to be approximately linear [23, 78]. Hence as the temperature of the anthracite increases, the electric current distribution changes, altering the Ohmic heating, while the distribution of heat is simultaneously affected by the varying thermal diffusion. Understanding this tight coupling between effects is crucial to exploring the behaviour in a calciner.

Accurate computation of electric current and thermal propagation within a calciner is further complicated by the granular nature of the anthracite. As discussed in Chapter 2, a calciner comprises millions of irregular, angular particles, each of which make only a few, microscopic contacts with their neighbours. Electric current must therefore conduct through these tiny contacts, which increases the effective electrical resistance of the material. Throughout this thesis, we refer to this resistance as *contact resistance* and attribute it partly to the size of the contacts, termed *constriction resistance*, and also to imperfect contact surfaces, in particular *asperity resistance* and *oxide-layer resistance*. Perhaps surprisingly, this resistance may contribute the overwhelming majority of the total resistance of the bulk, granular material [32, 92]. Hence, understanding these particle contacts is imperative to the process.

Due to the interdependence of electrical and thermal processes, along with the complexity of a granular domain, we observe an extremely complicated and coupled system to describe the behaviour of electric current. However, because of the great discrepancy between the lengthscale of the particles and the lengthscale of the furnace, we can simplify the description of the problem. We consider behaviour of the process on the particle lengthscale, known henceforth as the microscopic scale and use this to define a model on the furnace scale, or the macroscopic scale. Instead of modelling every particle individually, we aim to obtain an effective conductivity of a homogeneous domain, which encompasses the effect of the actual heterogeneous domain. This is therefore an effective-medium model which captures the important features of the process whilst minimising the complexity.

In this chapter, we discuss the homogenisation technique known as the method of multiple scales and demonstrate the efficacy of this approach when solving the steady electric current conduction problem, along with the coupled transient thermal

conduction model. We compare the numerical solution of the homogenised model with numerical solutions of the full problem to validate the accuracy of homogenisation and illustrate the computational benefit.

3.1 Conductivity functions

Throughout our analysis we will need to define appropriate electrical and thermal conductivity functions to serve as inputs into our models. In this section we discuss the general form of such functions based upon what has been observed in the literature.

Electrical conductivity

From the literature, we expect the electrical conductivity σ of anthracite to be a sigmoid curve [23, 30, 88] that increases sharply from $\sigma = \alpha$ to $\sigma = \beta$ near a critical temperature T_c. It is expected that this critical temperature is between 700–1000°C [17, 32]. The experimental results of Celzard et al. [17] suggest using an electrical conductivity function based upon the logistic function,

$$\sigma(T) = \alpha \exp\left(\frac{\log(\beta/\alpha)}{1 + \exp\left(-\kappa(T - T_c)\right)}\right). \tag{3.1}$$

The parameter κ can be modified to control the slope of the increase from α to β. To demonstrate the behaviour of such a function with temperature, we choose example parameter values

$$\alpha = 1\,\mathrm{Sm}^{-1}, \qquad \beta = 120\,\mathrm{Sm}^{-1}, \qquad \kappa = 1.6 \times 10^{-2}\,(^{\circ}\mathrm{C})^{-1}, \qquad T_c = 700\,^{\circ}\mathrm{C}, \tag{3.2}$$

where S (for siemens) is the unit of electric conductance. We plot (3.1) as a function of temperature in Figure 3.1 We discuss the influence of the parameter values on the shape of (3.1) in Appendix A and Section 3.5.

We note that in reality, the electrical conductivity of anthracite is permanently altered by temperature, that is, the conductivity should increase with an increase in temperature as depicted in Figure 3.1, however will not decrease according to the same relationship. In other words, the electrical conductivity is a function of the highest temperature it has been exposed to, even once it has cooled down. We do not account for this phenomenon here but emphasise that the analysis outlined in this thesis is valid for any reasonable conductivity function σ.

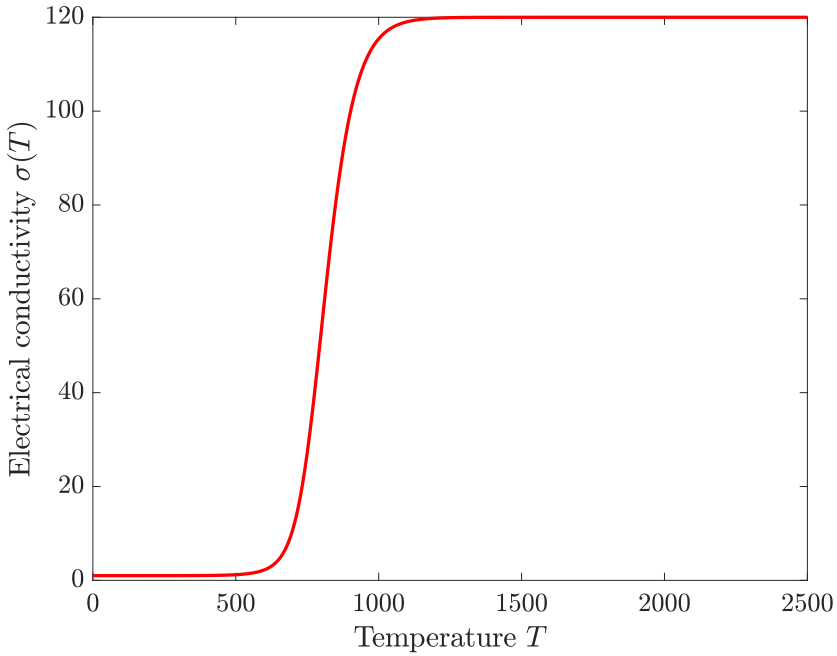


Figure 3.1: Electrical conductivity as a function of temperature described by (3.1) with parameters (3.2).

Thermal conductivity

From the literature, we expect the thermal conductivity to increase linearly with temperature [17, 23, 78]. The experimental results of [17] imply that the change in thermal conductivity of anthracite is negligible compared with the change in electrical conductivity, therefore we approximate the thermal conductivity to be a constant, in particular

$$k(T) = 0.7 \text{ Wm}^{-1}\text{K}^{-1}, \tag{3.3}$$

using Clendenin's results [23]. Note that for completeness, we will consider a general thermal conductivity $k(T)$ when outlining the mathematical model derivations to illustrate that any suitable conductivity function can be used, however we will conduct any numerical analysis using the constant value (3.3).

3.2 Method of multiple scales

The method of multiple scales [74, 76] allows us to extract homogeneous effective parameters from heterogeneous media. It is founded upon the separation of the macroscopic and microscopic lengthscales and subsequent treatment of the variables describing these lengthscales as independent. Hence at each point on the macroscale,

there is a microscale problem to consider. By solving the microscale problem, we can derive effective quantities on the macroscale, such as effective electrical and thermal conductivities. This simplifies the problem whilst still capturing the vital contribution of the microscale behaviour, such as the distribution of electrical current at contact points between particles.

Homogenisation methods have been used in the literature to understand the behaviour of granular materials [75]. In particular, Zhou et al. [106] simulate thermal conduction in a periodic granular material in a vacuum, obtaining the effective conductivity, effective specific heat capacity and other such quantities from a representative volume within the material. The accuracy of the homogenisation technique is then examined by comparison to simulations obtained via discrete element methods (DEM). Similar homogenisation techniques are prevalent within many sciences, for example, diffusive transport in heterogeneous media [13], modelling of fluid transport in tumours [20] and the improvement of filters using porosity gradients [27].

To begin our analysis of the calciner and to demonstrate the method of multiple scales we consider an isothermal material and just examine the electrical problem. Our aim is to derive the effective conductivity for electric current within granular material. This allows us to lay a framework that will be extended to include thermal transport behaviour.

3.3 Steady current conduction

Neglecting the influence of Ohmic heating, we will first consider a simple model describing electric current conduction through a stationary granular material to illustrate the homogenisation technique. Our approach will be to assume the material is composed of a periodic array of identical particles that are very much smaller than the region of interest.

We consider a domain $\tilde{\Omega}$ consisting of particulate material and gas-filled voids, where the size of $\tilde{\Omega}$ defines the macroscopic length scale L. We model the dimension of a typical particle to be $O(\delta L)$ for $\delta \ll 1$. We assume the gas to be electrically insulating, in other words, electric current can only pass through the solid material. We denote the region of solid material by $\tilde{\Omega}^S$ and the gas-filled voids by $\tilde{\Omega}^G$ and hence $\tilde{\Omega}^S = \tilde{\Omega} \backslash \tilde{\Omega}^G$. The external boundaries are denoted $\partial\tilde{\Omega}$ whereas the internal boundaries between solid particles and gas-filled voids are denoted $\tilde{\Gamma}_{W,i}$ for $i = 1, \cdots, N$ where $N \in \mathbb{Z}$ is the number of void boundaries. The particles make contact with their neighbours at an interface of width $\epsilon\delta L$ where $\epsilon < 1$. A schematic of a simplified

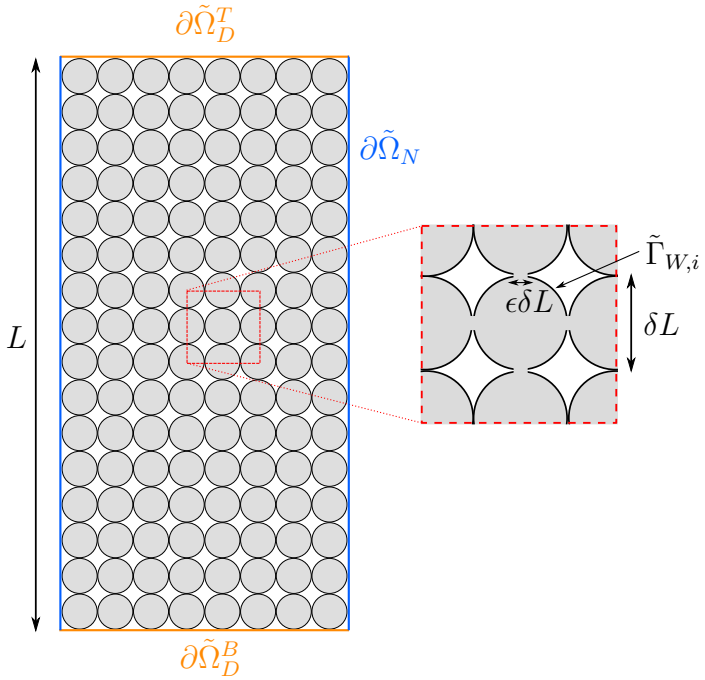


Figure 3.2: Simplified 2D representation of a regular, granular material comprised of truncated circular particles.

version of such a domain is given in Figure 3.2. Note that we expect particle contacts to be much smaller than this, namely $\epsilon \ll 1$, however we will discuss this further in Chapter 5.

We solve the following system of equations to understand how the electric potential $\tilde{\phi}(\tilde{\mathbf{x}})$ varies with spatial variable $\tilde{\mathbf{x}}$ within a material of electrical conductivity $\tilde{\sigma}(\tilde{\mathbf{x}})$, where the tilde-notation is used to indicate that the variables are dimensional,

$$\tilde{\nabla} \cdot (\tilde{\sigma}(\tilde{\mathbf{x}})\tilde{\nabla}\tilde{\phi}(\tilde{\mathbf{x}})) = 0, \qquad \tilde{\mathbf{x}} \in \tilde{\Omega}^S, \tag{3.4}$$

$$\tilde{\phi}(\tilde{\mathbf{x}}) = \phi_D(\tilde{\mathbf{x}}), \quad \tilde{\mathbf{x}} \in \partial\tilde{\Omega}_D, \tag{3.5}$$

$$\tilde{\nabla}\tilde{\phi}(\tilde{\mathbf{x}}) \cdot \mathbf{n} = 0, \qquad \tilde{\mathbf{x}} \in \partial\tilde{\Omega}_N \cup \tilde{\Gamma}_{W,i}\, \forall i, \tag{3.6}$$

where $\mathbf{n}$ is the outward normal vector to the domain. We split the external boundary $\partial\tilde{\Omega}$ into Neumann portion $\partial\tilde{\Omega}_N$ and Dirichlet portion $\partial\tilde{\Omega}_D$ and enforce a specified applied voltage $\phi_D(\tilde{\mathbf{x}})$ on the latter. We wish to find the electric current distribution resulting from an applied voltage across the domain, therefore we split $\partial\tilde{\Omega}_D = \partial\tilde{\Omega}_D^T \cup \partial\tilde{\Omega}_D^B$ and define $\phi_D(\tilde{\mathbf{x}})$ of (3.5) as

$$\phi_D(\tilde{\mathbf{x}}) = \begin{cases} \phi^T, & \tilde{\mathbf{x}} \in \partial\tilde{\Omega}_D^T, \\ \phi^B, & \tilde{\mathbf{x}} \in \partial\tilde{\Omega}_D^B, \end{cases} \tag{3.7}$$

for some prescribed, uniform voltages ϕ^T and ϕ^B where $\phi_B < \phi_T$.

Internally, we wish to differentiate between particle-to-particle and particle-to-gas interfaces. Recall that we attributed contact resistance to constriction resistance (small contacts), asperity resistance and oxide-layer resistance (imperfect contacts). In this chapter, we neglect surface imperfections and assume that the particles make perfect contacts of dimension $\epsilon\delta L$ with their neighbours, where $\epsilon < 1$. Therefore, rather than impose an explicit boundary condition here, we simply assume that contacts constitute a continuous extension of the solid domain. This is illustrated in Figure 3.2. On the other hand, to simulate the presence of non-conducting gas-filled voids, the remaining particle boundary, denoted $\tilde{\Gamma}_{W,i}$, is assumed to be insulating, therefore we enforce a zero-Neumann condition here. This indicates that electrical transfer is made via particle-to-particle contacts only.

Dimensionless equations

We scale our variables as follows:

$$\tilde{\mathbf{x}} = L\mathbf{x}, \qquad \tilde{\phi} = (\phi^T - \phi^B)\phi + \phi^B, \qquad \tilde{\sigma} = \beta\sigma, \tag{3.8}$$

where β is a characteristic size of the electrical conductivity $\tilde{\sigma}$ (in this case, the maximum value). We thereby obtain the dimensionless problem

$$\nabla \cdot (\sigma(\mathbf{x})\nabla\phi(\mathbf{x})) = 0, \quad \mathbf{x} \in \Omega^S, \tag{3.9}$$

$$\phi(\mathbf{x}) = 1, \quad \mathbf{x} \in \partial\Omega_D^T, \tag{3.10}$$

$$\phi(\mathbf{x}) = 0, \quad \mathbf{x} \in \partial\Omega_D^B, \tag{3.11}$$

$$\nabla\phi(\mathbf{x}) \cdot \mathbf{n} = 0, \quad \mathbf{x} \in \partial\Omega_N \cup \Gamma_{W,i}\, \forall i, \tag{3.12}$$

in domain Ω of size $O(1)$ with microstructure composed of particles of size δ and contact width $\epsilon\delta$.

3.3.1 Homogenisation via the method of multiple scales

The complexity of the problem is reduced by seeking a homogenised solution of the dimensionless governing equations (3.9)–(3.12) via the method of multiple scales. This involves obtaining an equation on the macroscale with an effective electrical conductivity that is valid within a simpler, homogeneous macroscopic domain and inherently captures the microscopic details. We closely follow the homogenisation methods presented in [76].

The purpose of homogenisation theory is to study equations (3.9)–(3.12) in the limit $\delta \to 0$, which physically represents the microscopic heterogeneities becoming

negligibly small. In other words, the goal is to replace the original, granular domain characterised by the coefficient $\sigma(\mathbf{x})$ and microscopic parameters δ and ϵ with an effective, homogeneous material which is characterised by tensor coefficient $\boldsymbol{\sigma}_{\text{eff}}$ that varies on the slow, macroscopic scale only.

We define the macroscopic and microscopic scale variables respectively as $\bar{\mathbf{x}} = \mathbf{x}$ and $\bar{\mathbf{y}} = \bar{\mathbf{x}}/\delta$. Since $\delta \ll 1$, $\bar{\mathbf{y}}$ varies much more quickly than $\bar{\mathbf{x}}$, therefore we can think of $\bar{\mathbf{x}}$ as constant when looking at the problem on the microscopic scale, in other words, we exploit scale separation and allow $\bar{\mathbf{x}}$ and $\bar{\mathbf{y}}$ to be independent variables. To implement the method of multiple scales we therefore assume that all terms depend explicitly on both the macroscopic scale $\bar{\mathbf{x}}$ and the microscopic scale $\bar{\mathbf{y}}$. This adds a degree of freedom that is removed by enforcing periodicity of the solution on the microscale. Validating this assumption is an important aspect of homogenisation theory and is beyond the scope of this exposition. More details can be found in [76]. In this example, we let the period of the microscale be δ, in other words, we assume one particle per periodic cell. The microscale variable $\bar{\mathbf{y}}$ is defined in the unit cell, $\omega(\bar{\mathbf{x}})$, as pictured in Figure 3.3.

Introducing the dependence of the problem on both the macroscale and the microscale, by the chain rule, the gradient operator becomes

$$\nabla_{\mathbf{x}} \to \nabla_{\bar{\mathbf{x}}} + \frac{1}{\delta}\nabla_{\bar{\mathbf{y}}}. \tag{3.13}$$

For convenience, we drop the over-bar notation. We look for an asymptotic expansion of $\phi = \phi(\mathbf{x}, \mathbf{y} = \mathbf{x}/\delta)$ in δ:

$$\phi \sim \phi_0(\mathbf{x}, \mathbf{y}) + \delta\phi_1(\mathbf{x}, \mathbf{y}) + \delta^2\phi_2(\mathbf{x}, \mathbf{y}) + O(\delta^3). \tag{3.14}$$

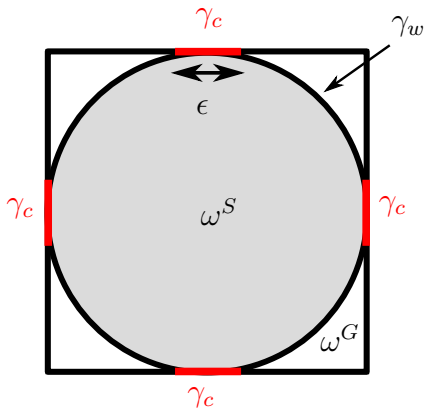


Figure 3.3: Unit cell domain $\omega = \omega^S \cup \omega^G$ in which we solve our cell problem (3.25)–(3.27), with contact interfaces γ_c and void interfaces γ_w.

As stated earlier, the microstructure has a periodic nature, hence we require that all of the terms in the expansion (3.14) are periodic in $\mathbf{y}$. Given this periodic microstructure, the separation of scales enforced above allows us to define a problem within a representative volume of the granular material, known as the unit cell and periodically extend this to the bulk material. Therefore (3.9)–(3.12) can be defined on the unit cell $\omega(\mathbf{x}) = \omega^S(\mathbf{x}) \cup \omega^G(\mathbf{x})$, with solid portion $\omega^S(\mathbf{x})$ and boundaries $\partial\omega^S(\mathbf{x}) = \gamma_w(\mathbf{x}) \cup \gamma_c(\mathbf{x})$, where γ_w represents the interface between particle and gas and γ_c represents where the particle makes contact with its neighbours. The problem is therefore written as

$$\nabla_{\mathbf{y}} \cdot (\sigma \nabla_{\mathbf{y}} \phi) + \delta[\nabla_{\mathbf{x}} \cdot (\sigma \nabla_{\mathbf{y}} \phi) + \nabla_{\mathbf{y}} \cdot (\sigma \nabla_{\mathbf{x}} \phi)] + \delta^2 \nabla_{\mathbf{x}} \cdot (\sigma \nabla_{\mathbf{x}} \phi) = 0, \tag{3.15}$$

for $\mathbf{y} \in \omega^S(\mathbf{x})$, with boundary conditions

$$(\delta \nabla_{\mathbf{x}} + \nabla_{\mathbf{y}}) \phi \cdot \mathbf{n} = 0, \quad \mathbf{y} \in \gamma_w(\mathbf{x}), \tag{3.16}$$

$$\phi \text{ periodic}, \quad \mathbf{y} \in \gamma_c(\mathbf{x}). \tag{3.17}$$

In writing down (3.15)–(3.17), we assume that the external boundary conditions, defined on $\partial\Omega_D$ and $\partial\Omega_N$ in (3.9)–(3.12) don't play any role in deriving the representative microscopic problem and only need to be considered when solving the resulting homogenised macroscopic problem. This is because the derivation of the homogenised problem is based on the analysis of local problems on the microscopic scale, in which the global boundaries are too far afield. The boundary conditions are important when proving the homogenisation theorem [76], however,this will not be discussed in this thesis. We include a note on boundary layers close to the external boundaries later in this chapter.

Leading-order problem

We substitute (3.14) into (3.15)–(3.17) and consider the leading-order term of ϕ,

$$\nabla_{\mathbf{y}} \cdot (\sigma \nabla_{\mathbf{y}} \phi_0) = 0, \qquad \mathbf{y} \in \omega^S \tag{3.18}$$

$$\nabla_{\mathbf{y}} \phi_0 \cdot \mathbf{n} = 0, \qquad \mathbf{y} \in \gamma_w, \tag{3.19}$$

$$\phi_0 \text{ periodic}, \qquad \mathbf{y} \in \gamma_c. \tag{3.20}$$

We conclude that ϕ_0 is independent of the microscale, or $\phi_0 = \phi_0(\mathbf{x})$. To see this, we multiply (3.18) by ϕ_0 and integrate over the solid portion of the cell, ω^S. Then, by the divergence theorem and boundary conditions (3.19)–(3.20), we find that $\nabla_{\mathbf{y}} \phi_0 = 0$. This tells us that the leading-order term is $\phi_0(\mathbf{x})$, which is the homogenised electric potential.

First-order problem

Consider now the first-order problem in δ from (3.15)–(3.17),

$$\nabla_{\mathbf{y}} \cdot (\sigma[\nabla_{\mathbf{x}}\phi_0 + \nabla_{\mathbf{y}}\phi_1]) = 0, \qquad \mathbf{y} \in \omega^S, \tag{3.21}$$

$$(\nabla_{\mathbf{x}}\phi_0 + \nabla_{\mathbf{y}}\phi_1) \cdot \mathbf{n} = 0, \qquad \mathbf{y} \in \gamma_w, \tag{3.22}$$

$$\phi_1 \text{ periodic}, \qquad \mathbf{y} \in \gamma_c. \tag{3.23}$$

Due to the linearity of (3.21), we write ϕ_1 in the form

$$\phi_1 = \mathbf{\Phi}(\mathbf{y}) \cdot \nabla_{\mathbf{x}}\phi_0(\mathbf{x}) + \hat{\phi}_1(\mathbf{x}), \tag{3.24}$$

where $\mathbf{\Phi}(\mathbf{y})$ is some vector function that must be found. The first term on the right-hand side of (3.24) is a particular integral and the second term is the complementary function. It will be shown in this analysis that the homogenised equation depends only on $\nabla_{\mathbf{y}}\phi_1$, therefore the value of $\hat{\phi}_1$ need not be considered. Putting (3.24) into (3.21)–(3.23) gives the cell problem as the following set of equations for the components $\Phi^{(i)}$ of $\mathbf{\Phi}$:

$$\nabla_{\mathbf{y}} \cdot \left(\sigma\left(\mathbf{e}_i + \nabla_{\mathbf{y}}\Phi^{(i)}\right)\right) = 0, \qquad \mathbf{y} \in \omega^S, \tag{3.25}$$

$$\left(\mathbf{e}_i + \nabla_{\mathbf{y}}\Phi^{(i)}\right) \cdot \mathbf{n} = 0, \qquad \mathbf{y} \in \gamma_w, \tag{3.26}$$

$$\Phi^{(i)} \text{ periodic}, \qquad \mathbf{y} \in \gamma_c, \tag{3.27}$$

where $\mathbf{e}_i$ denotes the basis vector in the relevant direction for $i = 1, 2, 3$ for a 3D problem.

Second-order problem

Finally, consider the second-order problem in δ,

$$\nabla_{\mathbf{x}} \cdot (\sigma[\nabla_{\mathbf{x}}\phi_0 + \nabla_{\mathbf{y}}\phi_1]) + \nabla_{\mathbf{y}} \cdot (\sigma[\nabla_{\mathbf{x}}\phi_1 + \nabla_{\mathbf{y}}\phi_2]) = 0, \qquad \mathbf{y} \in \omega^S, \tag{3.28}$$

$$(\nabla_{\mathbf{y}}\phi_2 + \nabla_{\mathbf{x}}\phi_1) \cdot \mathbf{n} = 0, \qquad \mathbf{y} \in \gamma_w, \tag{3.29}$$

$$\phi_2 \text{ periodic}, \qquad \mathbf{y} \in \gamma_c. \tag{3.30}$$

This is again a linear problem but only has a periodic solution if the non-homogeneous term in (3.28) has a particular form, due to the Fredholm alternative. We can find this condition by integrating (3.28) over the unit cell and integrating by parts:

$$\frac{1}{|\omega|}\int_{\omega^S} \nabla_{\mathbf{x}} \cdot (\sigma(\nabla_{\mathbf{x}}\phi_0 + \nabla_{\mathbf{y}}\phi_1))\,\mathrm{d}\mathbf{y} + \frac{1}{|\omega|}\int_{\partial\omega^S} (\sigma(\nabla_{\mathbf{x}}\phi_1 + \nabla_{\mathbf{y}}\phi_2)) \cdot \mathbf{n}\,\mathrm{d}S = 0. \tag{3.31}$$

The second term in (3.31) disappears due to the boundary conditions (3.29) and (3.30). Recalling that ϕ_1 takes the form (3.24), we obtain

$$\nabla_{\mathbf{x}} \cdot \left(\frac{1}{|\omega|} \int_{\omega^S} \sigma(\nabla_{\mathbf{x}}\phi_0 + \nabla_{\mathbf{y}}\mathbf{\Phi}\nabla_{\mathbf{x}}\phi_0)\, \mathrm{d}\mathbf{y} \right) = 0, \tag{3.32}$$

and so we find that ϕ_0 must satisfy

$$\nabla_{\mathbf{x}} \cdot \left(\left\{ \frac{1}{|\omega|} \int_{\omega^S} \sigma(\mathbf{I} + \nabla_{\mathbf{y}}\mathbf{\Phi})\, \mathrm{d}\mathbf{y} \right\} \nabla_{\mathbf{x}}\phi_0 \right) = 0. \tag{3.33}$$

Note that we define the gradient of vector function $\mathbf{\Phi}$ as

$$(\nabla_{\mathbf{y}}\mathbf{\Phi})_{ij} = \partial_i \Phi^{(j)}. \tag{3.34}$$

Homogenised problem

From the above analyses we conclude that, in place of the complicated heterogeneous problem (3.9)–(3.12), we need only consider the homogenised problem

$$\nabla_{\mathbf{x}} \cdot (\boldsymbol{\sigma}_{\text{eff}} \nabla_{\mathbf{x}}\phi_0) = 0, \qquad \mathbf{x} \in \Omega, \tag{3.35}$$

$$\phi_0 = \phi_D(\mathbf{x}), \qquad \mathbf{x} \in \partial\Omega_D, \tag{3.36}$$

$$\nabla\phi_0 \cdot \mathbf{n} = 0, \qquad \mathbf{x} \in \partial\Omega_N, \tag{3.37}$$

in the homogeneous domain Ω with effective conductivity defined from (3.33) as

$$\boldsymbol{\sigma}_{\text{eff}} = \frac{1}{|\omega|} \int_{\omega^S} \sigma(\mathbf{I} + \nabla_{\mathbf{y}}\mathbf{\Phi})\, \mathrm{d}\mathbf{y}. \tag{3.38}$$

The effective conductivity is a tensor that describes how easily electric current can conduct in each direction within the granular material. For systems of particles with many geometrical symmetries such as the one we are considering, $\boldsymbol{\sigma}_{\text{eff}}$ is symmetric, in fact, it is a multiple of the identity matrix. If we were to consider a non-symmetric unit cell with evident anisotropy, we would expect the off-diagonal terms of (3.38) to be non-zero and for the diagonal terms to be different from each other. Examples of such cell domains will be discussed in Chapter 7.

In practice, we need to solve (3.25)–(3.27) to determine the cell solution $\mathbf{\Phi}$. This allows us to calculate the effective conductivity (3.38) so that we can solve the steady electric current conduction problem within a homogeneous domain, knowing that the effect of the microstructure on electric current conduction is still captured and accounted for.

A note on boundary layers

An important issue in the classical homogenisation approach outlined above is that the right-hand side of expansion (3.14) does not satisfy the Dirichlet boundary conditions (3.10)–(3.11) which we wish to impose on the true solution. The approximation (3.14) can be improved, at least near to the Dirichlet boundary $\partial\Omega_D$ by considering a boundary layer. This involves the introduction of supplementary terms in the expansion of $\phi(\mathbf{x})$, namely

$$\phi(\mathbf{x}) \sim \phi_0(\mathbf{x},\mathbf{y}) + \delta\left[\phi_1(\mathbf{x},\mathbf{y}) + \phi_1^{bl}(\mathbf{x})\right] + \delta^2\left[\phi_2(\mathbf{x},\mathbf{y}) + \phi_2^{bl}(\mathbf{x})\right] + O(\delta^3), \tag{3.39}$$

where each function $\phi_i^{bl}(\mathbf{x})$ satisfies

$$\nabla\cdot(\sigma(\mathbf{x})\nabla\phi_i^{bl}(\mathbf{x})) = 0, \qquad \mathbf{x}\in\Omega^S, \tag{3.40}$$

$$\phi_i^{bl}(\mathbf{x}) = -\phi_i(\mathbf{x},\mathbf{y}), \quad \mathbf{x}\in\partial\Omega_D, \tag{3.41}$$

$$\nabla\phi_i^{bl}(\mathbf{x})\cdot\mathbf{n} = 0, \qquad \mathbf{x}\in\partial\Omega_N\cup\Gamma_{W,i}\,\forall i. \tag{3.42}$$

We note that $\phi_i^{bl}(\mathbf{x})$ is heavily dependent on δ, however is not a function of $\mathbf{y}=\mathbf{x}/\delta$. The advantage of (3.39) over (3.14) is that $\phi_i+\phi_i^{bl}$ satisfies a Dirichlet boundary condition. Due to the homogenisation method above, we are only interested in the first-order boundary layer behaviour, ϕ_1^{bl}, which requires solving the problem

$$\nabla\cdot(\sigma(\mathbf{x})\nabla\phi_1^{bl}(\mathbf{x})) = 0, \qquad \mathbf{x}\in\Omega^S, \tag{3.43}$$

$$\phi_1^{bl}(\mathbf{x}) = -\boldsymbol{\Phi}(\mathbf{y})\cdot\nabla_{\mathbf{x}}\phi_0 - \hat{\phi}(\mathbf{x}), \quad \mathbf{x}\in\partial\Omega_D, \tag{3.44}$$

$$\nabla\phi_1^{bl}(\mathbf{x})\cdot\mathbf{n} = 0, \qquad \mathbf{x}\in\partial\Omega_N\cup\Gamma_{W,i}\,\forall i. \tag{3.45}$$

To incorporate boundary layers in this way improves the convergence of the homogenised solution to the actual solution. However, to obtain the asymptotic behaviour of ϕ_1^{bl}, namely, to homogenise (3.43)–(3.45) is a very difficult problem that is usually studied only for particular domains Ω, therefore we will not include boundary layers in this analysis. Instead, we will enforce the same external boundary conditions for the homogenised solution ϕ_0 as defined for exact solution ϕ. More details on the inclusion of boundary layers are discussed in [2, 59, 67].

3.3.2 Numerical results

For a simple geometry we can solve the dimensionless steady electric current conduction problem (3.9)–(3.12) both directly and by the homogenisation method outlined

above. We include some two-dimensional results to illustrate the validity of our homogenisation model and its ability to accurately approximate the direct solution.

To approximate a 2D furnace, we define our dimensional domain as a rectangle of dimensions $\tilde{\Omega} = [0, L/5] \times [0, L]$ where the height:width ratio has been chosen to resemble the dimensions observed in reality. We take the microstructure to be a periodic array of truncated circles of width δL and contact width $\epsilon\delta L$ to approximate the anthracite particles, as depicted in Figure 3.2. Thus the dimensionless domain according to the scaling (3.8) is $\Omega = [0, 0.2] \times [0, 1]$.

We must also define the portions of the boundary on which to enforce Dirichlet and Neumann conditions. For the purpose of this analysis, we simply enforce Dirichlet conditions on the top and bottom edges of the domain, namely

$$\partial\Omega_D^T = \{(x, y) \in \partial\Omega : y = 1\}, \qquad \partial\Omega_D^B = \{(x, y) \in \partial\Omega : y = 0\}, \tag{3.46}$$

therefore on $\partial\Omega_D$ we enforce (3.10)–(3.11). The remainder of the domain is $\partial\Omega_N = \partial\Omega \backslash \partial\Omega_D$, upon which we enforce the zero-flux condition (3.12).

Definition of electrical conductivity

We must define a suitable electrical conductivity function $\sigma(\mathbf{x})$. As discussed in Section 3.1, the electrical conductivity of anthracite increases with temperature, therefore we enforce that the spatial variation of $\sigma(\mathbf{x})$ is caused by a spatially-varying temperature function $T(\mathbf{x})$, which we will prescribe within the domain. Given that we expect temperatures from room temperature $T_{\min} = 37°\text{C}$ to $T_{\max} = 2500°\text{C}$, we define the following temperature profile such that the hottest point is the centre of the domain,

$$\tilde{T}(\tilde{x}, \tilde{y}) = T_{\min} + (T_{\max} - T_{\min}) \sin\left(\frac{\pi\tilde{y}}{L}\right) \sin\left(\frac{5\pi\tilde{x}}{L}\right). \tag{3.47}$$

A heat map of this profile is given by Figure 3.4. We scale temperature such that

$$\tilde{T} = (T_c - T_{\min})T + T_{\min}, \tag{3.48}$$

and thus our dimensionless temperature profile is

$$T(x, y) = \frac{T_{\max} - T_{\min}}{T_c - T_{\min}} \sin(\pi y) \sin(5\pi x). \tag{3.49}$$

As discussed in Section 3.1, we choose our electrical conductivity function to be

$$\tilde{\sigma}(\tilde{T}) = \alpha \exp\left(\frac{\log(\beta/\alpha)}{1 + \exp(-\kappa(\tilde{T} - T_c))}\right). \tag{3.50}$$

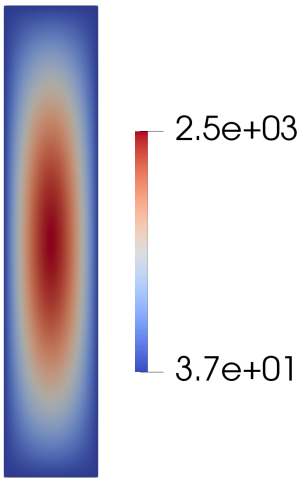


Figure 3.4: Temperature profile given by (3.47) such that the furnace is hottest at its centre.

Intuitively, α defines the lowest conductivity value and β the highest, whereas T_c denotes the critical temperature where we observe the greatest increase in conductivity and κ can be used to modify the sharpness of this increase. We will use this conductivity function in our homogenisation analysis with parameter values

$$\alpha = 1\,\mathrm{Sm}^{-1}, \qquad \beta = 120\,\mathrm{Sm}^{-1}, \qquad \kappa = 10^{-3}\,(^{\circ}\mathrm{C})^{-1}, \qquad T_c = 700\,^{\circ}\mathrm{C}. \tag{3.51}$$

We choose these parameters for numerical simplicity; in our homogenisation analysis we assume that σ does not vary on the scale of a particle, therefore for very sharp electrical conductivity increases (for example $\kappa = 10^{-2}$), we require the macro-microscale ratio δ to be extremely small. Thus comparing the homogenised and direct solutions for such a conductivity function requires us to solve the problem directly for many more particles than we can handle numerically. This highlights another merit of the homogenisation model which can be solved for an expanse of conductivity functions of varying complexity.

By enforcing the scalings (3.8) and (3.48), the dimensionless electrical conductivity is

$$\sigma(T) = \frac{\alpha}{\beta}\exp\left(\frac{\log\left(\beta/\alpha\right)}{1+\exp(-\kappa(T_c - T_{\min})(T-1))}\right). \tag{3.52}$$

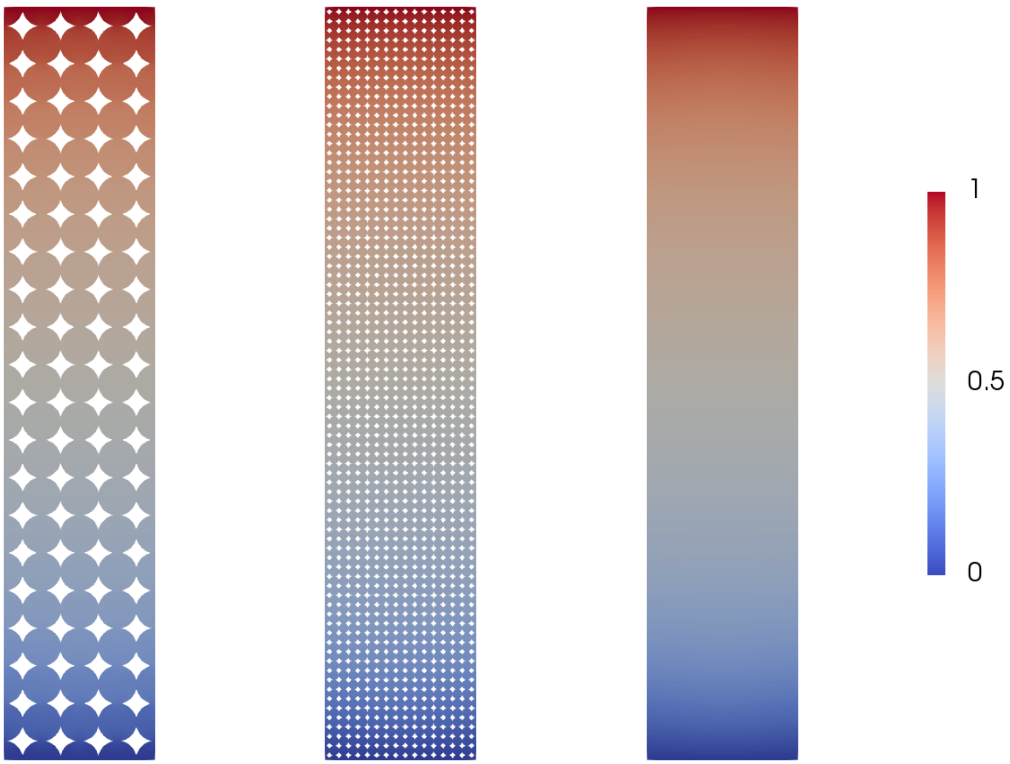
We solve (3.9)–(3.12) using piecewise affine finite elements in `FEniCS` [6] on a mesh of triangles. To illustrate the computational cost of direct simulation, we solve the problem directly for a range of different values of δ and observe that the computational cost increases significantly as δ is decreased, ultimately becoming infeasible as we

approach realistic values of δ. Note that we choose δ to ensure there are integer values of particles within the domain. We set the contact width $\epsilon = 0.2$ (recalling that ϵ is a fraction of δ), which is also larger than we would expect, but results in a computational problem that we can solve on a single, large workstation.

Results

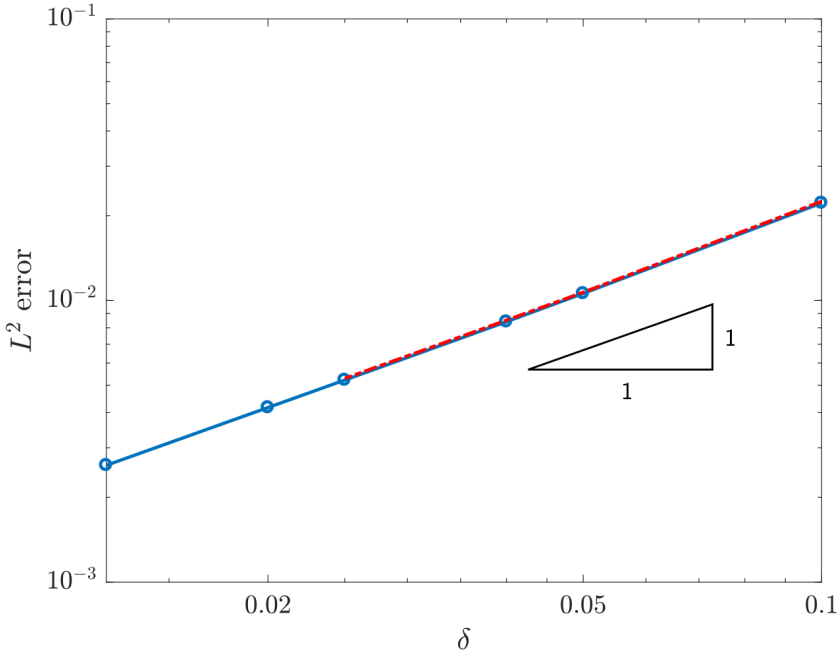
We include colour maps of the direct solution for two different δ along with the homogenised solution in Figure 3.5. This gives us a visual representation of how the homogenised solution is an approximation of the direct solution.

We quantify the error between the direct and homogenised solutions by interpolating the homogenised solution onto the heterogeneous domain Ω^S and calculating the L^2–error between them. We plot this error versus δ in Figure 3.6a. We consider two meshes, where the red, dashed line represents the error between solutions obtained on a mesh with twice as many mesh elements as for the blue, solid line to demonstrate mesh independence of our solutions. We note that the direct problem could only be solved for a minimum $\delta = 0.025$ on the finer mesh. A portion of the

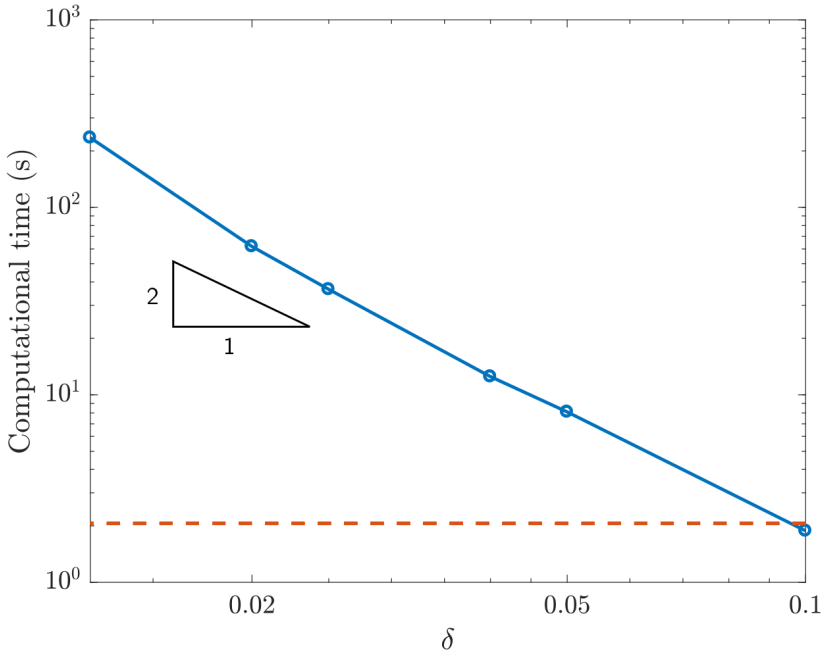


(a) $\delta = 0.05$. (b) $\delta = 0.0125$. (c) Homogenised.

Figure 3.5: Colour maps of the direct solution ϕ of (3.9)–(3.12) for (a) $\delta = 0.05$, (b) $\delta = 0.0125$ and (c) the homogenised solution ϕ_0 of (3.35)–(3.37).



(a) L^2-error between homogenised and direct solution with δ. The dashed red line represents the results for further refined meshes to demonstrate the accuracy of the solver.



(b) Computational time of solving the problem directly (blue solid line) with δ, along with the time to solve homogenisation problem, namely 2.06 s (dashed orange line).

Figure 3.6: L^2-error and computational time associated with the direct and homogenised solutions.

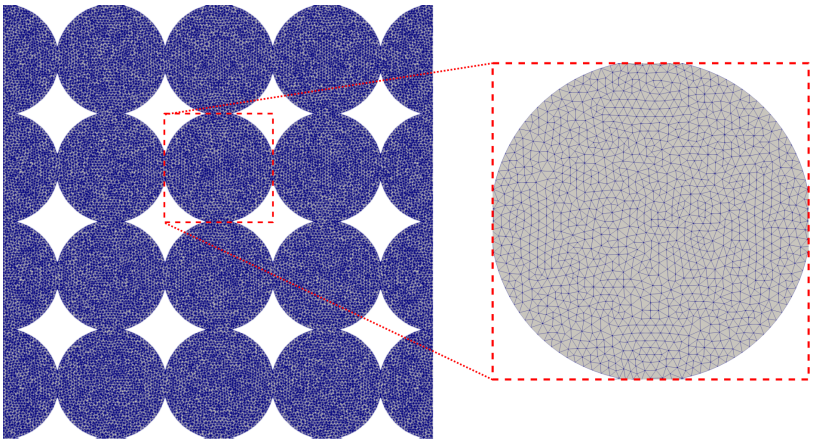


Figure 3.7: Portion of the mesh on which we solve the problem directly.

mesh corresponding to the blue, solid line is shown in Figure 3.7. For the rest of the numerical simulations in this thesis we use the mesh corresponding to the blue, solid line under the assumption that this same level of accuracy extends to future results.

We see that the approximation error of the homogenised solution scales as we would expect, that is, the error between the direct and homogenised solution is $O(\delta)$. This implies that as $\delta \to 0$, the homogenised solution is an accurate approximation of the direct solution.

We also plot the computational time as a function of δ in Figure 3.6b and observe that the direct computational time increases with decreasing δ, in particular it approximately follows a $O(\delta^{-2})$ trend. We note that for three-dimensional particles, which is of course what we are interested in, the computational time will increase as $O(\delta^{-3})$, at best. We also include a dashed line to represent the time to obtain the homogenised solution, namely 2.06 seconds.

It is clear from these results that as δ decreases, the homogenised solution accurately approximates the direct solution while simultaneously the direct solution becomes extremely computationally expensive. Even for this simple, two-dimensional example, we could not obtain a direct solution for $\delta < 0.0125$ on our workstation. Given that we expect $\delta = O(10^{-3})$ in reality, it is evident that direct computational solutions will be intractable without significantly more computational power and will take an infeasible length of time to simulate. We can therefore appreciate the computational benefit and sufficient accuracy of homogenisation methods.

We note that for $\delta = 0.1$, solving the problem directly was more computationally efficient than by homogenisation, however,this corresponds to a domain consisting of 20 particles. We recall that the homogenisation method is appropriate for extremely

small δ and involves studying the problem as $\delta \to 0$. Further noting the L^2-error associated with $\delta = 0.1$, we conclude that the homogenised solution is not an adequate approximation to the true solution for large δ.

Discussion

In conclusion, the homogenisation method of multiple scales allows us to analyse a complicated problem on a microscopic scale in order to reduce the complexity. By solving the cell problem (3.25)–(3.27) once for a given function σ, we can calculate an effective conductivity tensor which therefore allows us to solve the homogenised macroscopic problem (3.35)–(3.37). As demonstrated, we can use this technique to understand electric current conduction within the calciner, however,these ideas are easily extended to include the thermal problem. The metallurgical furnaces in which we are interested contain extremely large numbers of small, angular particles, and in particular, the nature of the contacts between particles is highly significant for electrical and thermal conduction throughout the furnace. Through the use of multiple scales methods, we can incorporate such vital effects without the computational expense of solving the problem within every particle. In a realistic model of a calciner, δ is $O(10^{-3})$. The results in this section have demonstrated that for such small δ, solving the full problem is computationally infeasible and that the homogenised solution provides a very good approximation to the solution of the full problem.

3.4 Coupled electrothermal conduction

We now wish to incorporate the thermal influences present within electric furnaces such as the calciner. This is done by introducing the phenomenon of Ohmic heating [57, 71], defined as a process where an electric current is passed through a material such that heat is internally generated due to the material's electrical resistance. Such heating is prevalent within the metallurgy industry [32, 41, 62] and is particularly utilised within the food industry [42, 58, 95]. A simple application of Ohmic heating is the thermistor which is a temperature-dependent resistor [35, 49, 50] often used for fuses. Fowler et al. study a positive temperature characteristic (PTC) thermistor whose electrical conductivity decreases with temperature. Such a thermistor is used as a fuse to prevent short circuiting and surges in current.

The mathematical models we aim to implement are nearly identical to those that are used for the well-studied topic of thermistors. Steady electric current conduction

within a thermistor follows the same law as outlined in Section 3.3, namely

$$\nabla \cdot (\sigma(T)\nabla\phi) = 0, \tag{3.53}$$

for electric potential ϕ, where the electrical conductivity σ depends on temperature T. According to Ohm's law, the current density $\mathbf{j}$ is related to the electric potential by

$$\mathbf{j} = -\sigma(T)\nabla\phi. \tag{3.54}$$

Assuming a local version for power generation $P = VI = V^2/R$, we write

$$-\mathbf{j} \cdot \nabla\phi = \sigma\nabla\phi \cdot \nabla\phi, \tag{3.55}$$

which therefore serves as a source term in the heat equation, henceforth referred to as the Ohmic heating term. We thereby solve the following equation for temperature,

$$\rho c_p \frac{\partial T}{\partial t} - \nabla \cdot (k\nabla T) - \sigma\nabla\phi \cdot \nabla\phi = 0. \tag{3.56}$$

3.4.1 Homogenisation of Ohmic heating term

Consider again electric current conduction throughout a granular domain $\tilde{\Omega}$ (such as Figure 3.2) but now consider the effect of temperature with a heat source due to Ohmic heating. We consider the steady thermal problem, however this analysis is easily extended to include time-dependence. The electric potential $\tilde{\phi}$ and the temperature field $\tilde{T}$ satisfy the following system of equations:

$$\tilde{\nabla} \cdot (\tilde{\sigma}(\tilde{T})\tilde{\nabla}\tilde{\phi}(\tilde{\mathbf{x}})) = 0, \quad \tilde{\mathbf{x}} \in \tilde{\Omega}^S, \tag{3.57}$$

$$\tilde{\nabla} \cdot (\tilde{k}(\tilde{T})\tilde{\nabla}\tilde{T}(\tilde{\mathbf{x}})) + \tilde{\sigma}(\tilde{T})\tilde{\nabla}\tilde{\phi}(\tilde{\mathbf{x}}) \cdot \tilde{\nabla}\tilde{\phi}(\tilde{\mathbf{x}}) = 0, \quad \tilde{\mathbf{x}} \in \tilde{\Omega}^S, \tag{3.58}$$

$$\tilde{\phi}(\tilde{\mathbf{x}}) = \phi_D(\mathbf{x}), \quad \tilde{\mathbf{x}} \in \partial\tilde{\Omega}_D, \tag{3.59}$$

$$\tilde{T}(\tilde{\mathbf{x}}) = T_D(\mathbf{x}), \quad \tilde{\mathbf{x}} \in \partial\tilde{\Omega}_D, \tag{3.60}$$

$$\tilde{\nabla}\tilde{\phi}(\tilde{\mathbf{x}}) \cdot \mathbf{n} = \tilde{\nabla}\tilde{T}(\tilde{\mathbf{x}}) \cdot \mathbf{n} = 0, \quad \tilde{\mathbf{x}} \in \partial\tilde{\Omega}_N \cup \tilde{\Gamma}_{W,i}, \ \forall i, \tag{3.61}$$

where $\tilde{k}$ is the thermal conductivity and $\tilde{\sigma}$ is the electrical conductivity which are both dependent on temperature. We again consider mixed Neumann-Dirichlet external boundary conditions, along with zero-Neumann internal boundary conditions between particles and the gas-filled voids. This is a simplifying assumption for the thermal problem, as we expect thermal transfer via radiation in these regions, as well as possibly conduction and convection. We consider radiative transfer as an extension in Chapter 4, however, we assume conduction and convection are negligible

throughout this thesis. For notational simplicity and the purpose of demonstrating the homogenisation method, we define Dirichlet conditions for the electric potential and temperature on the same boundary portions $\partial\tilde{\Omega}_D = \partial\tilde{\Omega}_D^T \cup \partial\tilde{\Omega}_D^B$, and enforce homogeneous Neumann conditions elsewhere on $\partial\tilde{\Omega}_N$. We could of course consider different boundary regions for the electrical and thermal problems, however it does not affect the homogenisation method we wish to demonstrate. In fact, the special case that we have chosen can be solved using an alternative method, as outlined in Section 3.5.

Similar to Section 3.3, we define the Dirichlet conditions as a voltage drop in the electrical potential, however, we consider the temperature to take the same value on each of the Dirichlet portions of the external surface, namely

$$\phi_D(\tilde{\mathbf{x}}) = \begin{cases} \phi^T, & \tilde{\mathbf{x}} \in \partial\tilde{\Omega}_D^T, \\ \phi^B, & \tilde{\mathbf{x}} \in \partial\tilde{\Omega}_D^B, \end{cases} \qquad T_D(\tilde{\mathbf{x}}) = T_{\min}, \quad \tilde{\mathbf{x}} \in \partial\tilde{\Omega}_D^T \cup \partial\tilde{\Omega}_D^B. \tag{3.62}$$

Dimensionless equations

We scale our variables as follows:

$$\tilde{\mathbf{x}} = L\mathbf{x}, \qquad \tilde{\phi} = (\phi^T - \phi^B)\phi + \phi^B, \qquad \tilde{T} = \zeta T + T_{\min}, \qquad \tilde{\sigma} = \beta\sigma, \qquad \tilde{k} = \xi k, \tag{3.63}$$

where β and ξ are some characteristic sizes of the electrical and thermal conductivities respectively and ζ is to be determined. The steady-state heat equation (3.58) becomes

$$\frac{\xi\zeta}{L^2}\nabla\cdot(k\nabla T) + \frac{\beta(\phi^T - \phi^B)^2}{L^2}\sigma\nabla\phi\cdot\nabla\phi = 0, \tag{3.64}$$

therefore we choose

$$\zeta = \frac{\beta(\phi^T - \phi^B)^2}{\xi}. \tag{3.65}$$

We thereby obtain the dimensionless problem

$$\nabla\cdot(\sigma(T)\nabla\phi(\mathbf{x})) = 0, \quad \mathbf{x} \in \Omega^S, \tag{3.66}$$

$$\nabla\cdot(k(T)\nabla T(\mathbf{x})) + \sigma(T)\nabla\phi(\mathbf{x})\cdot\nabla\phi(\mathbf{x}) = 0, \quad \mathbf{x} \in \Omega^S, \tag{3.67}$$

$$T(\mathbf{x}) = 0, \quad \phi(\mathbf{x}) = 1, \quad \mathbf{x} \in \partial\Omega_D^T, \tag{3.68}$$

$$T(\mathbf{x}) = 0, \quad \phi(\mathbf{x}) = 0, \quad \mathbf{x} \in \partial\Omega_D^B, \tag{3.69}$$

$$\nabla T(\mathbf{x})\cdot\mathbf{n} = 0, \quad \nabla\phi(\mathbf{x})\cdot\mathbf{n} = 0, \quad \mathbf{x} \in \partial\Omega_N \cup \Gamma_{W,i}\,\forall i, \tag{3.70}$$

in the same domain as for the electrical problem with microstructure composed of particles of size δ and contact width $\epsilon\delta$. Again we will consider the limit $\delta \to 0$ to study the microscopic heterogeneities becoming negligibly small.

Homogenisation via the method of multiple scales

Following the same homogenisation procedure as in Section 3.3 and concentrating on the same simplified geometry. We consider two scales, the macroscopic scale $\mathbf{x}$ and the microscopic scale $\mathbf{y} = \mathbf{x}/\delta$. We asymptotically expand the electric potential and temperature,

$$\phi(\mathbf{x}, \mathbf{y}) \sim \phi_0(\mathbf{x}, \mathbf{y}) + \delta\phi_1(\mathbf{x}, \mathbf{y}) + \delta^2\phi_2(\mathbf{x}, \mathbf{y}) + O(\delta^3), \tag{3.71}$$

$$T(\mathbf{x}, \mathbf{y}) \sim T_0(\mathbf{x}, \mathbf{y}) + \delta T_1(\mathbf{x}, \mathbf{y}) + \delta^2 T_2(\mathbf{x}, \mathbf{y}) + O(\delta^3), \tag{3.72}$$

where each ϕ_i and T_i and their normal derivatives are assumed to be spatially periodic on the microscopic scale. Due to the temperature dependence of the thermal and electrical conductivities, we also asymptotically expand $k(T)$ and $\sigma(T)$ for small δ,

$$k(T) \sim k(T_0) + \delta T_1 k'(T_0) + \frac{\delta^2}{2}(2T_2 k'(T_0) + T_1^2 k''(T_0)) + O(\delta^3), \tag{3.73}$$

$$\sigma(T) \sim \sigma(T_0) + \delta T_1 \sigma'(T_0) + \frac{\delta^2}{2}(2T_2 \sigma'(T_0) + T_1^2 \sigma''(T_0)) + O(\delta^3), \tag{3.74}$$

where k', k'', σ', σ'' denote derivatives of the functions with respect to T. Note that we have assumed here that the conductivities and their derivatives are $O(1)$. There may be cases where this is not true, in which case our asymptotic expansions might break down, however we do not discuss these cases in this thesis. For ease of notation, we will denote $k_0 = k(T_0)$ and $\sigma_0 = \sigma(T_0)$. Therefore, by considering these expansions in (3.66)–(3.70), we obtain systems for each order of δ.

Leading-order problem

The system at leading-order in δ is

$$\nabla_{\mathbf{y}} \cdot (\sigma_0 \nabla_{\mathbf{y}} \phi_0) = 0, \qquad \mathbf{y} \in \omega^S, \tag{3.75}$$

$$\nabla_{\mathbf{y}} \cdot (k_0 \nabla_{\mathbf{y}} T_0) + \sigma_0 \nabla_{\mathbf{y}} \phi_0 \cdot \nabla_{\mathbf{y}} \phi_0 = 0, \qquad \mathbf{y} \in \omega^S, \tag{3.76}$$

$$\nabla_{\mathbf{y}} \phi_0 \cdot \mathbf{n} = \nabla_{\mathbf{y}} T_0 \cdot \mathbf{n} = 0, \qquad \mathbf{y} \in \gamma_w, \tag{3.77}$$

$$\phi_0,\ T_0 \text{ periodic}, \qquad \mathbf{y} \in \gamma_c. \tag{3.78}$$

As discussed in Section 3.3, ϕ_0 is independent of the microscopic variable and thus the second term on the left-hand side of (3.76) is zero, therefore we conclude that T_0 is also independent of $\mathbf{y}$,

$$\phi_0 = \phi_0(\mathbf{x}), \qquad T_0 = T_0(\mathbf{x}). \tag{3.79}$$

First-order problem

At first-order in δ, we have

$$\nabla_{\mathbf{y}} \cdot (\sigma_0[\nabla_{\mathbf{x}}\phi_0 + \nabla_{\mathbf{y}}\phi_1]) = 0, \qquad \mathbf{y} \in \omega^S, \tag{3.80}$$

$$\nabla_{\mathbf{y}} \cdot (k_0[\nabla_{\mathbf{x}}T_0 + \nabla_{\mathbf{y}}T_1]) = 0, \qquad \mathbf{y} \in \omega^S, \tag{3.81}$$

$$(\nabla_{\mathbf{x}}\phi_0 + \nabla_{\mathbf{y}}\phi_1) \cdot \mathbf{n} = 0, \qquad \mathbf{y} \in \gamma_w, \tag{3.82}$$

$$(\nabla_{\mathbf{x}}T_0 + \nabla_{\mathbf{y}}T_1) \cdot \mathbf{n} = 0, \qquad \mathbf{y} \in \gamma_w, \tag{3.83}$$

$$\phi_1,\, T_1 \text{ periodic}, \qquad \mathbf{y} \in \gamma_c. \tag{3.84}$$

In a similar way to Section 3.3, we again find cell problems for unknown vector functions $\mathbf{\Phi}(\mathbf{y})$ and $\mathbf{\Psi}(\mathbf{y})$, where

$$\phi_1 = \mathbf{\Phi}(\mathbf{y}) \cdot \nabla_{\mathbf{x}}\phi_0(\mathbf{x}) + \hat{\phi}_1(\mathbf{x}), \qquad T_1 = \mathbf{\Psi}(\mathbf{y}) \cdot \nabla_{\mathbf{x}}T_0(\mathbf{x}) + \hat{T}_1(\mathbf{x}). \tag{3.85}$$

As discussed previously, the homogenised equation only involves $\nabla_{\mathbf{y}}\phi_1$ and $\nabla_{\mathbf{y}}T_1$, therefore we don't need to consider the values of $\hat{\phi}_1$ and $\hat{T}_1$. Noting that $\sigma_0 = \sigma(T_0)$ $k_0 = k(T_0)$ are functions of the macroscale only, we define the cell problem for the components $\Phi^{(i)}$ and $\Psi^{(i)}$ of $\mathbf{\Phi}$ and $\mathbf{\Psi}$ respectively as

$$\nabla^2_{\mathbf{y}}\Phi^{(i)} = 0, \qquad \mathbf{y} \in \omega^S, \tag{3.86}$$

$$\left(\mathbf{e}_i + \nabla_{\mathbf{y}}\Phi^{(i)}\right) \cdot \mathbf{n} = 0, \qquad \mathbf{y} \in \gamma_w, \tag{3.87}$$

$$\Phi^{(i)} \text{ periodic}, \qquad \mathbf{y} \in \gamma_c, \tag{3.88}$$

$$\nabla^2_{\mathbf{y}}\Psi^{(i)} = 0, \qquad \mathbf{y} \in \omega^S, \tag{3.89}$$

$$\left(\mathbf{e}_i + \nabla_{\mathbf{y}}\Psi^{(i)}\right) \cdot \mathbf{n} = 0, \qquad \mathbf{y} \in \gamma_w, \tag{3.90}$$

$$\Psi^{(i)} \text{ periodic}, \qquad \mathbf{y} \in \gamma_c, \tag{3.91}$$

where $\mathbf{e}_i$ is the unit vector in the i^{th} direction. We now note that the cell problems for $\mathbf{\Phi}$ and $\mathbf{\Psi}$ are identical. By the uniqueness principle for the Poisson equation, the solutions to the cell problems (3.86)–(3.88) and (3.89)–(3.91) differ by a constant but have a unique gradient, therefore, we can write

$$\nabla_{\mathbf{y}}\mathbf{\Psi} = \nabla_{\mathbf{y}}\mathbf{\Phi}. \tag{3.92}$$

Second-order problem

Finally, at second-order in δ, we have the following equations for ϕ_2 and T_2 respectively, defined within ω^S,

$$\begin{aligned}\nabla_{\mathbf{y}} \cdot (\sigma_0[\nabla_{\mathbf{x}}\phi_1 + \nabla_{\mathbf{y}}\phi_2] + T_1\sigma_0'[\nabla_{\mathbf{x}}\phi_0 + \nabla_{\mathbf{y}}\phi_1]) \\ +\nabla_{\mathbf{x}} \cdot (\sigma_0[\nabla_{\mathbf{x}}\phi_0 \nabla_{\mathbf{y}}\phi_1]) = 0,\end{aligned} \tag{3.93}$$

$$\begin{aligned}\nabla_{\mathbf{y}} \cdot (T_1 k'(T_0)[\nabla_{\mathbf{x}}T_0 + \nabla_{\mathbf{y}}T_1] + k_0[\nabla_{\mathbf{x}}T_1 + \nabla_{\mathbf{y}}T_2]) \\ +\nabla_{\mathbf{x}} \cdot (k_0[\nabla_{\mathbf{x}}T_0 + \nabla_{\mathbf{y}}T_1]) + \sigma_0(\nabla_{\mathbf{x}}\phi_0 + \nabla_{\mathbf{y}}\phi_1) \cdot (\nabla_{\mathbf{x}}\phi_0 + \nabla_{\mathbf{y}}\phi_1) = 0,\end{aligned} \tag{3.94}$$

with boundary conditions

$$(\nabla_{\mathbf{x}}\phi_1 + \nabla_{\mathbf{y}}\phi_2) \cdot \mathbf{n} = 0, \qquad \mathbf{y} \in \gamma_w, \tag{3.95}$$

$$(\nabla_{\mathbf{x}}T_1 + \nabla_{\mathbf{y}}T_2) \cdot \mathbf{n} = 0, \qquad \mathbf{y} \in \gamma_w, \tag{3.96}$$

$$\phi_2,\, T_2 \text{ periodic}, \qquad \mathbf{y} \in \gamma_c. \tag{3.97}$$

Applying the Fredholm alternative by integrating (3.93) over ω and applying boundary conditions (3.95)–(3.97) yields the solvability condition

$$\nabla_{\mathbf{x}} \cdot \left(\left\{ \frac{\sigma_0}{|\omega|} \int_{\omega^S} (\mathbf{I} + \nabla_{\mathbf{y}}\mathbf{\Phi}) \mathrm{d}\mathbf{y} \right\} \nabla_{\mathbf{x}}\phi_0 \right) = 0, \tag{3.98}$$

and doing the same for (3.94) gives

$$\begin{aligned}\nabla_{\mathbf{x}} \cdot \left(\left\{ \frac{k_0}{|\omega|} \int_{\omega^S} (\mathbf{I} + \nabla_{\mathbf{y}}\mathbf{\Psi}) \mathrm{d}\mathbf{y} \right\} \nabla_{\mathbf{x}}T_0 \right) \\ + \nabla_{\mathbf{x}}\phi_0 \cdot \left(\frac{\sigma_0}{|\omega|} \int_{\omega^S} (\mathbf{I} + \nabla_{\mathbf{y}}\mathbf{\Phi})^{\top} (\mathbf{I} + \nabla_{\mathbf{y}}\mathbf{\Phi}) \mathrm{d}\mathbf{y} \right) \nabla_{\mathbf{x}}\phi_0 = 0,\end{aligned} \tag{3.99}$$

where $\mathbf{I}$ is the identity matrix.

Homogenised problem

From the analysis above, the dimensionless macroscale electrothermal conduction equations (3.66)–(3.70) can be approximated as a homogenised problem,

$$\nabla_{\mathbf{x}} \cdot (\boldsymbol{\sigma}_{\text{eff}} \nabla_{\mathbf{x}}\phi_0(\mathbf{x})) = 0, \qquad \mathbf{x} \in \Omega, \tag{3.100}$$

$$\nabla_{\mathbf{x}} \cdot (\boldsymbol{k}_{\text{eff}} \nabla_{\mathbf{x}}T_0(\mathbf{x})) + q_{\text{eff}} = 0, \qquad \mathbf{x} \in \Omega, \tag{3.101}$$

$$T_0(\mathbf{x}) = 0, \quad \phi_0(\mathbf{x}) = 1 \qquad \mathbf{x} \in \partial\Omega_D^T, \tag{3.102}$$

$$T_0(\mathbf{x}) = 0, \quad \phi_0(\mathbf{x}) = 0 \qquad \mathbf{x} \in \partial\Omega_D^B, \tag{3.103}$$

$$\nabla\phi_0(\mathbf{x}) \cdot \mathbf{n} = \nabla T_0(\mathbf{x}) \cdot \mathbf{n} = 0, \qquad \mathbf{x} \in \partial\Omega_N, \tag{3.104}$$

where $\boldsymbol{\sigma}_{\text{eff}}$ is the effective electrical conductivity, $\boldsymbol{k}_{\text{eff}}$ is the effective thermal conductivity and q_{eff} is the effective Ohmic heating term, defined by

$$\boldsymbol{k}_{\text{eff}} = \frac{k(T_0)}{|\omega|}\int_{\omega^S}(\mathbf{I}+\nabla_{\mathbf{y}}\boldsymbol{\Psi})\mathrm{d}\mathbf{y} = \frac{k(T_0)}{|\omega|}\int_{\omega^S}(\mathbf{I}+\nabla_{\mathbf{y}}\boldsymbol{\Phi})\mathrm{d}\mathbf{y}, \tag{3.105}$$

$$\boldsymbol{\sigma}_{\text{eff}} = \frac{\sigma(T_0)}{|\omega|}\int_{\omega^S}(\mathbf{I}+\nabla_{\mathbf{y}}\boldsymbol{\Phi})\mathrm{d}\mathbf{y}, \tag{3.106}$$

$$q_{\text{eff}} = \nabla_{\mathbf{x}}\phi_0 \cdot \left(\frac{\sigma(T_0)}{|\omega|}\int_{\omega^S}(\mathbf{I}+\nabla_{\mathbf{y}}\boldsymbol{\Phi})^{\top}(\mathbf{I}+\nabla_{\mathbf{y}}\boldsymbol{\Phi})\mathrm{d}\mathbf{y}\right)\nabla_{\mathbf{x}}\phi_0. \tag{3.107}$$

Analysing the effective tensors

Given that the Ohmic heating term for electric potential ϕ and tensor electrical conductivity $\boldsymbol{\sigma}$ is given by $\nabla\phi\cdot\boldsymbol{\sigma}\nabla\phi$, we might have expected the effective Ohmic heating term q_{eff} to depend on ϕ_0 and $\boldsymbol{\sigma}_{\text{eff}}$ in this way. We will now analyse the integrals (3.106) and (3.107) to show that this is true.

Let us consider the integral in (3.107) and denote it $\bar{\mathcal{J}}$:

$$\bar{\mathcal{J}} = \frac{1}{|\omega|}\int_{\omega^S}\left(\mathbf{I}+\nabla_{\mathbf{y}}\boldsymbol{\Phi}\right)^{\top}\left(\mathbf{I}+\nabla_{\mathbf{y}}\boldsymbol{\Phi}\right)\mathrm{d}\mathbf{y}. \tag{3.108}$$

We note that both the effective electrical and thermal conductivities include the following integral

$$\mathcal{J} = \frac{1}{|\omega|}\int_{\omega^S}\left(\mathbf{I}+\nabla_{\mathbf{y}}\boldsymbol{\Phi}\right)\mathrm{d}\mathbf{y}. \tag{3.109}$$

Proposition 1. *Consider the two integrals* (3.108) *and* (3.109)*. For* $\boldsymbol{\Phi}$ *satisfying the cell problems* (3.86)–(3.88)*, we claim that*

$$\bar{\mathcal{J}} = \mathcal{J}. \tag{3.110}$$

Proof. We begin by expanding the right-hand side of (3.108),

$$|\omega|\bar{\mathcal{J}} = \int_{\omega^S}(\mathbf{I}+\nabla_{\mathbf{y}}\boldsymbol{\Phi})\mathrm{d}\mathbf{y} + \int_{\omega^S}\nabla_{\mathbf{y}}\boldsymbol{\Phi}^{\top}\mathrm{d}\mathbf{y} + \int_{\omega^S}\nabla_{\mathbf{y}}\boldsymbol{\Phi}^{\top}\nabla_{\mathbf{y}}\boldsymbol{\Phi}\mathrm{d}\mathbf{y}. \tag{3.111}$$

We write the third integral in Einstein summation convention and apply integration by parts and the divergence theorem to give

$$\left(\int_{\omega^S}\nabla_{\mathbf{y}}\boldsymbol{\Phi}^{\top}\nabla_{\mathbf{y}}\boldsymbol{\Phi}\mathrm{d}\mathbf{y}\right)_{ij} = \int_{\omega^S}(\partial_k\Phi_i)(\partial_k\Phi_j)\,\mathrm{d}\mathbf{y}, \tag{3.112}$$

$$= \int_{\omega^S}\partial_k(\Phi_i\partial_k\Phi_j) - \Phi_i\partial_k\partial_k\Phi_j\,\mathrm{d}\mathbf{y}, \tag{3.113}$$

$$= \int_{\partial\omega}\Phi_i\partial_k\Phi_j n_k\,\mathrm{d}S - \int_{\omega^S}\Phi_i\partial_k\partial_k\Phi_j\,\mathrm{d}\mathbf{y}, \tag{3.114}$$

where $\mathbf{n} = (n_k)$ is the outward-facing normal vector. Recall the cell problem (3.86)–(3.88) for $\boldsymbol{\Phi}$ in index notation,

$$\partial_k \partial_k \Phi_j = 0, \qquad \text{in } \omega^S, \tag{3.115}$$

$$\partial_k \Phi_j n_k + n_j = 0, \qquad \text{on } \gamma_w, \tag{3.116}$$

$$\Phi_j \text{ periodic}, \qquad \text{on } \gamma_c. \tag{3.117}$$

Therefore, the volume integral in (3.114) disappears due to (3.115) and we split the boundary integral into γ_c and γ_w,

$$\int_{\partial\omega} \Phi_i \partial_k \Phi_j n_k \,\mathrm{d}S = -\int_{\gamma_w} \Phi_i n_j \,\mathrm{d}S + \int_{\gamma_c} \Phi_i \partial_k \Phi_j n_k \,\mathrm{d}S, \tag{3.118}$$

$$= -\int_{\partial\omega} \Phi_i n_j \,\mathrm{d}S, \tag{3.119}$$

$$= -\int_{\omega^S} \partial_j \Phi_i \,\mathrm{d}\mathbf{y}, \tag{3.120}$$

noting that the second integral on the right-hand side of (3.118) is zero by periodicity of Φ_i. Therefore, the third integral in (3.111) can be written

$$\left(\int_{\omega^S} \nabla_{\mathbf{y}} \boldsymbol{\Phi}^\top \nabla_{\mathbf{y}} \boldsymbol{\Phi} \mathrm{d}\mathbf{y}\right)_{ij} = -\int_{\omega^S} \partial_j \Phi_i \,\mathbf{dy}, \tag{3.121}$$

$$= \left(-\int_{\omega^S} \nabla_{\mathbf{y}} \boldsymbol{\Phi}^\top \,\mathrm{d}\mathbf{y}\right)_{ij}, \tag{3.122}$$

and hence (3.111) simplifies to

$$|\omega|\bar{\mathcal{J}} = \int_{\omega^S} (\mathbf{I} + \nabla_{\mathbf{y}} \boldsymbol{\Phi}) \mathbf{dy} + \int_{\omega^S} \nabla_{\mathbf{y}} \boldsymbol{\Phi}^\top \mathbf{dy} - \int_{\omega^S} \nabla_{\mathbf{y}} \boldsymbol{\Phi}^\top \,\mathbf{dy}, \tag{3.123}$$

$$= |\omega|\mathcal{J}. \tag{3.124}$$

□

Therefore, recalling (3.92), the effective quantities (3.105)–(3.107) are

$$\boldsymbol{k}_{\text{eff}} = k(T_0)\mathcal{J}. \tag{3.125}$$

$$\boldsymbol{\sigma}_{\text{eff}} = \sigma(T_0)\mathcal{J}, \tag{3.126}$$

$$q_{\text{eff}} = \nabla_{\mathbf{x}} \phi_0 \cdot \boldsymbol{\sigma}_{\text{eff}} \nabla_{\mathbf{x}} \phi_0. \tag{3.127}$$

We can thereby solve the homogenised problem (3.100)–(3.104) for the coupled electrothermal conduction in a homogeneous domain using the effective parameters above to capture the microscopic heterogeneities. We follow the same numerical procedure as in Section 3.3.

3.4.2 Numerical results

We consider the same simple geometry Ω as in Section 3.3 and solve the dimensionless steady electrothermal conduction problem (3.66)–(3.70) both directly and by the homogenisation method outlined above. We include some two-dimensional results for illustration.

We use the same electrical conductivity function (3.1) as before, with parameter values $\alpha = 1\,\mathrm{Sm}^{-1}$, $\beta = 120\,\mathrm{Sm}^{-1}$, $\kappa = 10^{-3}\,(^{\circ}\mathrm{C})^{-1}$, $T_c = 700\,^{\circ}\mathrm{C}$, however, non-dimensionalising according to the scalings (3.63) yields

$$\sigma(T) = \frac{\alpha}{\beta}\exp\left(\frac{\log(\beta/\alpha)}{1+\exp(-\kappa(\zeta T + T_{\min} - T_c))}\right), \qquad \zeta = \frac{\beta(\phi^T - \phi^B)^2}{\xi}. \tag{3.128}$$

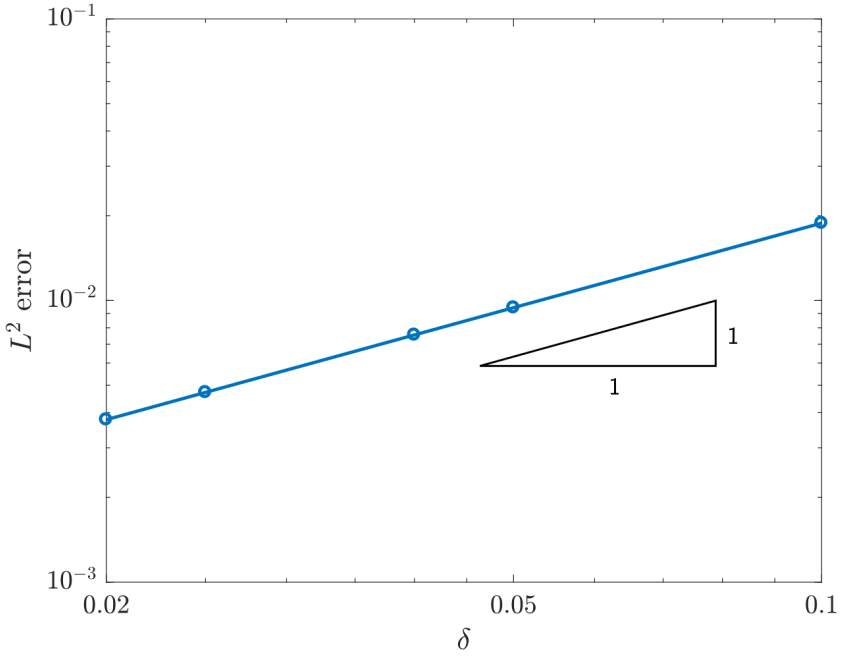
As discussed in Section 3.1, the change in thermal conductivity is insignificant in comparison with the increase in the electrical conductivity, therefore we approximate the thermal conductivity as a constant, namely,

$$\tilde{k} = 0.7\,\mathrm{Wm}^{-1}\mathrm{K}^{-1}, \quad \Rightarrow \quad \xi = 0.7\,\mathrm{Wm}^{-1}\mathrm{K}^{-1},\ k = 1. \tag{3.129}$$

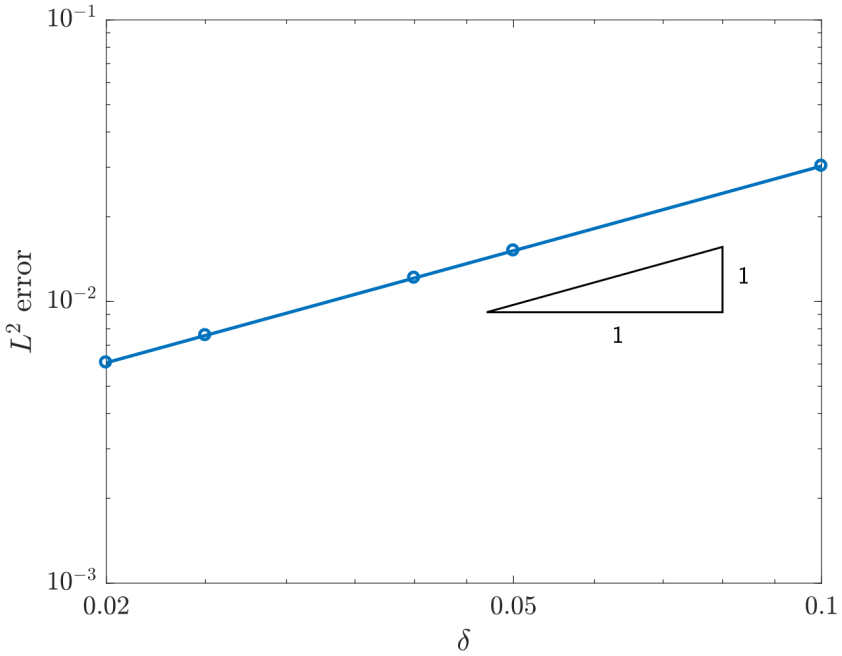
Similar to before, we solve (3.66)–(3.70) using piecewise affine finite elements in `FEniCS` [6] on a mesh of triangles and illustrate the computational cost of direct simulation by solving the problem directly for a range of different values of δ.

Results

We plot a graph of the L^2–error versus δ between the homogenised and direct solutions for both ϕ and T in Figure 3.8, along with the computational time of the direct solutions in Figure 3.9. Again we observe the expected trend for the approximation error, namely the error between the direct and homogenised solution is $O(\delta)$. The computational time, in the best case, is $O(\delta^{-2})$, however we notice that this trend is not consistent for all δ. This is hardly surprising as quadratic behaviour requires the time the solver takes to obtain the solution to scale linearly with the number of cells in the mesh. The homogenised solution was obtained in 7.54 seconds. We note again that the homogenisation technique is preferable for very small δ, as we would expect in a furnace, due to the significantly reduced computational time and the small approximation error.



(a) Electric potential



(b) Temperature

Figure 3.8: L^2-error between homogenised and direct solutions for (a) electric potential ϕ and (b) temperature T for different values of δ.

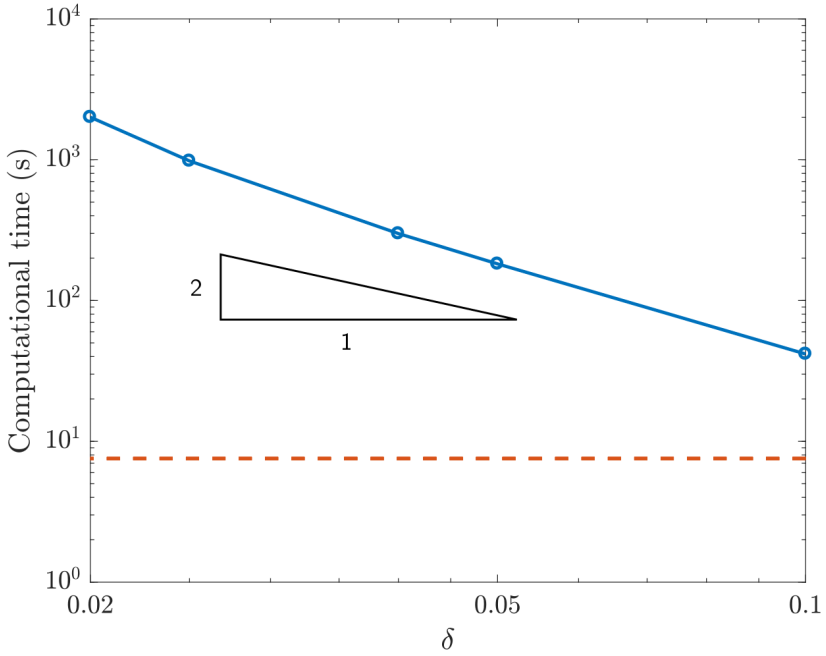


Figure 3.9: Computational time of solving the problem directly (blue solid line) with δ, along with the time to solve homogenisation problem, namely 7.54 s (dashed orange line).

3.5 Temperature as a function of electric potential

We mentioned previously that by considering the Dirichlet and Neumann conditions for the electric potential and temperature to be defined on the same boundary portions, we were studying a special case of the problem that could be solved using alternative methods. In particular, the equations for the coupled electrothermal conduction problem has been considered by Cimatti and Howison [22, 48] and they show it can be reduced to a single nonlinear elliptic problem together with a nonlinear ODE. In this section, we will show how we reach this conclusion.

Consider again the dimensionless, coupled, steady-state electrothermal problem of Ohmic heating in a granular material:

$$\nabla \cdot (\sigma(T)\nabla\phi(\mathbf{x})) = 0, \quad \mathbf{x} \in \Omega^S, \tag{3.130}$$

$$\nabla \cdot (k(T)\nabla T(\mathbf{x})) + \sigma(T)\nabla\phi(\mathbf{x}) \cdot \nabla\phi(\mathbf{x}) = 0, \quad \mathbf{x} \in \Omega^S, \tag{3.131}$$

$$T(\mathbf{x}) = 0, \quad \phi(\mathbf{x}) = 1, \quad \mathbf{x} \in \partial\Omega_D^T, \tag{3.132}$$

$$T(\mathbf{x}) = 0, \quad \phi(\mathbf{x}) = 0, \quad \mathbf{x} \in \partial\Omega_D^B, \tag{3.133}$$

$$\nabla T(\mathbf{x}) \cdot \mathbf{n} = 0, \quad \nabla\phi(\mathbf{x}) \cdot \mathbf{n} = 0, \quad \mathbf{x} \in \partial\Omega_N \cup \Gamma_{W,i}\, \forall i. \tag{3.134}$$

Given that both electric potential and temperature Dirichlet conditions are applied along the same portion of the boundary, $\partial\Omega_D$ and similarly for Neumann conditions on $\partial\Omega_N$, the level curves for ϕ are identical to the level curves for T on these boundaries. Hence following the method in [48], we assume that this relationship between the level curves is true everywhere and can consider temperature as a function of electric potential,

$$T = f(\phi), \tag{3.135}$$

where f is to be determined. Expanding (3.131) in terms of $f(\phi)$, we obtain

$$k'\left(\frac{\mathrm{d}f}{\mathrm{d}\phi}\right)^2 \nabla\phi\cdot\nabla\phi + k\frac{\mathrm{d}^2 f}{\mathrm{d}\phi^2}\nabla\phi\cdot\nabla\phi + k\frac{\mathrm{d}f}{\mathrm{d}\phi}\nabla^2\phi + \sigma\nabla\phi\cdot\nabla\phi = 0, \tag{3.136}$$

where $k' = \mathrm{d}k/\mathrm{d}T$. Expanding (3.130) in the same way provides us with an expression for $\nabla^2\phi$,

$$\nabla^2\phi = -\frac{\sigma'}{\sigma}\frac{\mathrm{d}f}{\mathrm{d}\phi}\nabla\phi\cdot\nabla\phi, \tag{3.137}$$

which we can substitute into (3.136), leaving us with the ODE

$$\frac{k}{\sigma}\frac{\mathrm{d}^2 f}{\mathrm{d}\phi^2} + \left(\frac{k'\sigma - k\sigma'}{\sigma^2}\right)\left(\frac{\mathrm{d}f}{\mathrm{d}\phi}\right)^2 + 1 = 0, \tag{3.138}$$

which can be written as

$$\frac{\mathrm{d}}{\mathrm{d}\phi}\left(\frac{k(f)}{\sigma(f)}\frac{\mathrm{d}f}{\mathrm{d}\phi}\right) = -1. \tag{3.139}$$

This is a nonlinear ODE with boundary conditions

$$f(1) = f(0) = 0. \tag{3.140}$$

We observe that the dependence of T on ϕ relies only on the ratio between $k(T)$ and $\sigma(T)$, rather than the two functions independently. Integrating (3.139) twice and applying the boundary conditions (3.140), we obtain

$$\int_0^{f(\phi)} \frac{k(t)}{\sigma(t)}\mathrm{d}t = \frac{1}{2}\phi\left(1-\phi\right), \tag{3.141}$$

The ODE for $T = f(\phi)$ given by (3.139)-(3.140) has a unique solution. To see this, assume that there exist two solutions, $f(\phi)$ and $g(\phi)$ and consider (3.141), namely

$$\int_0^{f(\phi)} \frac{k(t)}{\sigma(t)}\mathrm{d}t - \int_0^{g(\phi)} \frac{k(t)}{\sigma(t)}\mathrm{d}t = 0, \tag{3.142}$$

$$\int_{g(\phi)}^{f(\phi)} \frac{k(t)}{\sigma(t)}\mathrm{d}t = 0, \tag{3.143}$$

for all ϕ. Thus by the first mean value theorem for definite integrals, if $k(t)/\sigma(t)$ is continuous, there exists $h(\phi) \in (g, f)$ such that

$$\frac{k(h)}{\sigma(h)}(f(\phi) - g(\phi)) = 0, \tag{3.144}$$

therefore, for $k(T)/\sigma(T) \neq 0$, we have

$$f(\phi) = g(\phi), \tag{3.145}$$

hence the solution is unique. The two requirements, namely that k/σ is continuous and non-zero are always true in our case. Considering k/σ to be zero would imply that either the solid is entirely thermally insulating or the electrical conductivity is infinite, neither of which are physical cases we are interested in.

Numerical solution

We can solve (3.139)–(3.140) numerically using piecewise affine finite elements in `FEniCS` [6]. To illustrate the behaviour of the solutions, we consider solving the problem for the special case of the non-dimensional conductivities

$$\sigma(T) = \frac{\alpha}{\beta}\exp\left(\frac{\log(\beta/\alpha)}{1 + \exp(-\kappa(\zeta T + T_{\min} - T_c))}\right), \qquad k = 1, \tag{3.146}$$

for parameters

$$\begin{gathered}\alpha = 1\,\mathrm{Sm}^{-1}, \quad \beta = 120\,\mathrm{Sm}^{-1}, \quad \kappa = 1.6 \times 10^{-2}\,(^{\circ}\mathrm{C})^{-1}, \quad \phi^T = 56\,\mathrm{V}, \\ \phi^B = 0\,\mathrm{V}, \quad T_{\min} = 37\,^{\circ}\mathrm{C}, \quad T_c = 700\,^{\circ}\mathrm{C}, \quad \xi = 0.7\,\mathrm{Wm}^{-1}\mathrm{K}^{-1},\end{gathered} \tag{3.147}$$

and

$$\zeta = \frac{\beta(\phi^T - \phi^B)^2}{\xi}. \tag{3.148}$$

The resulting numerical solution for $T = f(\phi)$ is plotted in Figure 3.10. It seems that $f(\phi)$ exhibits different regions of behaviour, in particular there are three regions for the solution: one with a shallow gradient, another that is much narrower with a very steep gradient and finally the transition region between them. The shallow gradient regions correspond to when T is less than the critical temperature T_c, whereas the steep gradient corresponds to $T > T_c$. The sharp transition regions occur when T is close to T_c. The range of ϕ over which the transition takes place is dictated by the parameter values α, β and κ, as is the maximum value of $f(\phi)$.

To illustrate the changing behaviour of $T = f(\phi)$ with the parameter values we vary β and κ in Figures 3.11–3.12. We notice that for smaller β, which can alternatively be thought of as a smaller difference between the maximum and minimum

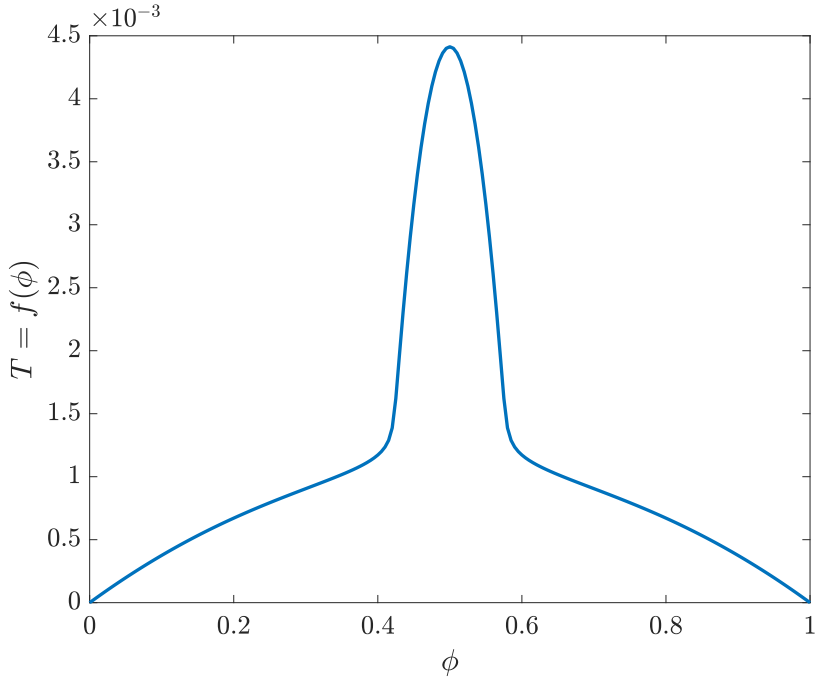


Figure 3.10: Solution to ODE (3.139)–(3.140) for $k(T)$ and $\sigma(T)$ given by (3.146) with parameters (3.147).

electrical conductivity values, for example $\beta = 30$ in Figure 3.11, the shape of $f(\phi)$ resembles a parabola. Yet increasing β causes the maximum temperature to decrease and the shape to change, namely a protrusion near $\phi = 0.5$ begins to form. Interestingly, as we increase β further, this protrusion grows and the maximum temperature increases again.

In Figure 3.12 we vary κ where the smaller the value of κ, the sharper the increase of electrical conductivity from its minimum to maximum value. We notice that the maximum temperature increases as κ decreases and for $\kappa < 0.02$, the shape resembles a parabola. As κ decreases, a protrusion appears and grows significantly. We conduct an analytical analysis to further explore the shape of $f(\phi)$ in Appendix A.

The benefit of this approach is that now, we need only solve the electrical problem for ϕ and subsequently can deduce the solution for T by solving the ODE (3.139)–(3.140).

Extension to the homogenised problem

Now that we have shown that the exact solutions ϕ and T of the coupled problem (3.130)–(3.134) satisfy the relationship $T = f(\phi)$, we expect that this relationship

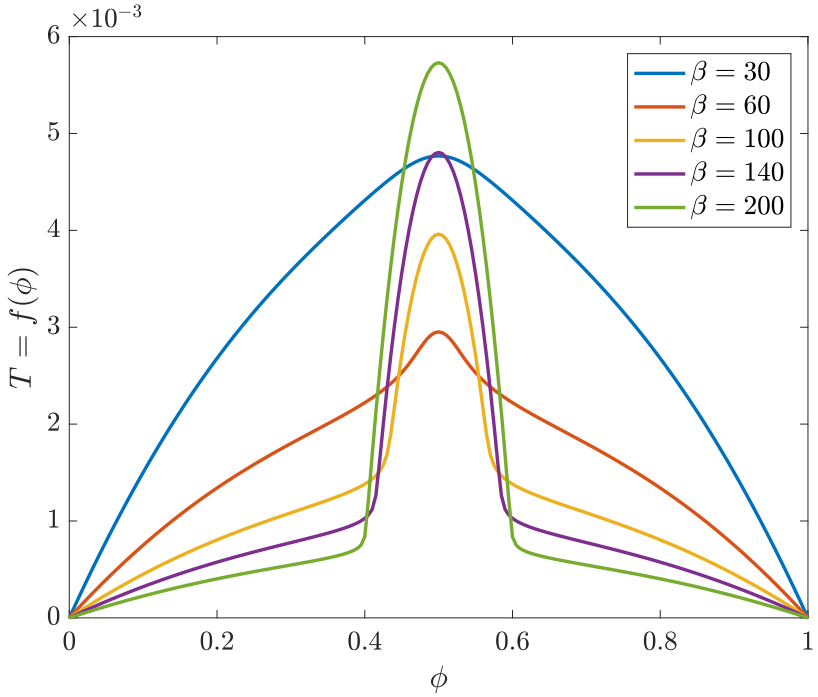


Figure 3.11: Solution to ODE (3.139)–(3.140) for $k(T)$ and $\sigma(T)$ given by (3.146) with parameters (3.147) but different β values.

can be extended to the homogenised solutions, namely,

$$T = f(\phi) \Rightarrow T_0 = f(\phi_0). \tag{3.149}$$

For completion, we show that this is expectation is valid.

Consider the homogenised steady state problem

$$\nabla_{\mathbf{x}} \cdot (\boldsymbol{\sigma}_{\text{eff}} \nabla_{\mathbf{x}} \phi_0(\mathbf{x})) = 0, \qquad \mathbf{x} \in \Omega, \tag{3.150}$$

$$\nabla_{\mathbf{x}} \cdot (\boldsymbol{k}_{\text{eff}} \nabla_{\mathbf{x}} T_0(\mathbf{x})) + q_{\text{eff}} = 0, \qquad \mathbf{x} \in \Omega, \tag{3.151}$$

$$T_0(\mathbf{x}) = 0, \quad \phi_0(\mathbf{x}) = 1, \qquad \mathbf{x} \in \partial\Omega_D^T, \tag{3.152}$$

$$T_0(\mathbf{x}) = 0, \quad \phi_0(\mathbf{x}) = 0, \qquad \mathbf{x} \in \partial\Omega_D^B, \tag{3.153}$$

$$\nabla\phi_0(\mathbf{x}) \cdot \mathbf{n} = \nabla T_0(\mathbf{x}) \cdot \mathbf{n} = 0, \qquad \mathbf{x} \in \partial\Omega_N, \tag{3.154}$$

with effective quantities

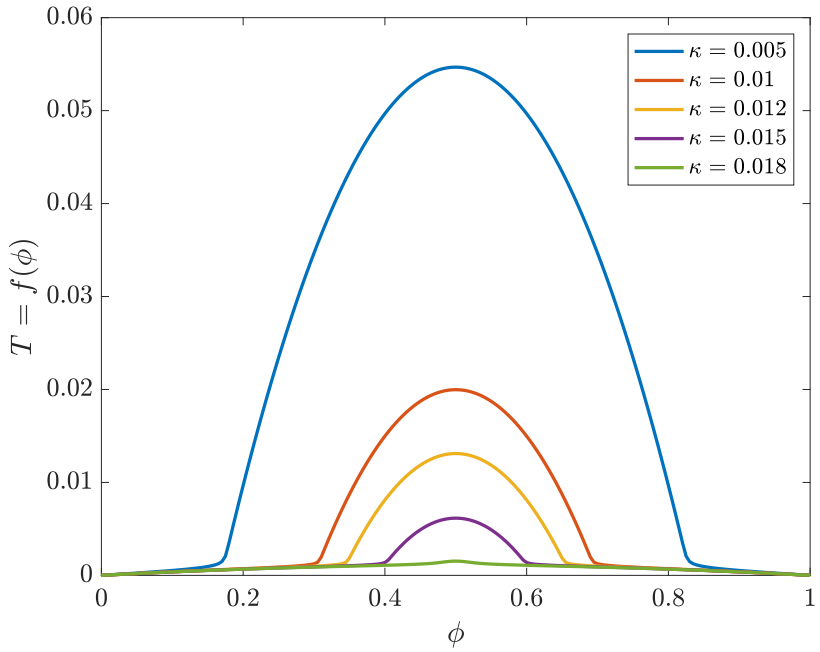
$$\boldsymbol{k}_{\text{eff}} = k(T_0)\mathcal{J}, \tag{3.155}$$

$$\boldsymbol{\sigma}_{\text{eff}} = \sigma(T_0)\mathcal{J}, \tag{3.156}$$

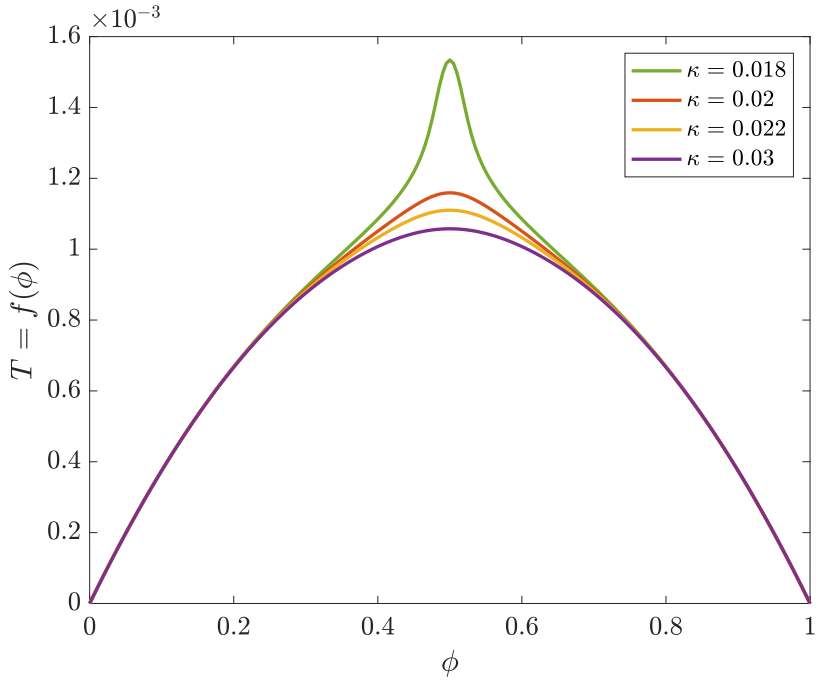
$$q_{\text{eff}} = \nabla_{\mathbf{x}}\phi_0 \cdot \boldsymbol{\sigma}_{\text{eff}} \nabla_{\mathbf{x}} \phi_0. \tag{3.157}$$

where

$$\mathcal{J} = \frac{1}{|\omega|} \int_{\omega^S} (\mathbf{I} + \nabla_{\mathbf{y}} \boldsymbol{\Phi}) \, \mathrm{d}\mathbf{y}. \tag{3.158}$$



(a) Similar shapes but great variation in magnitude for $\kappa < 0.015$.



(b) For $\kappa > 0.018$ the variation in magnitude is reduced.

Figure 3.12: Solution to ODE (3.139)–(3.140) for $k(T)$ and $\sigma(T)$ given by (3.146) with parameters (3.147) but different κ values.

Let us write T_0 as a function of ϕ_0,

$$T_0 = g(\phi_0). \tag{3.159}$$

Therefore, (3.151) becomes

$$\nabla_{\mathbf{x}} \cdot \left(k(T_0)\mathcal{J}\frac{\mathrm{d}g}{\mathrm{d}\phi}\nabla_{\mathbf{x}}\phi_0 \right) + \sigma(T_0)\nabla_{\mathbf{x}}\phi_0 \cdot \mathcal{J}\nabla_{\mathbf{x}}\phi_0 = 0. \tag{3.160}$$

The first term on the left-hand side of (3.160) becomes

$$\begin{aligned} \nabla_{\mathbf{x}} \cdot \left(k\mathcal{J}\frac{\mathrm{d}g}{\mathrm{d}\phi}\nabla_{\mathbf{x}}\phi_0 \right) = k\frac{\mathrm{d}g}{\mathrm{d}\phi}\nabla_{\mathbf{x}} \cdot (\mathcal{J}\nabla_{\mathbf{x}}\phi_0) \\ + \left(k\frac{\mathrm{d}^2 g}{\mathrm{d}\phi^2} + k' \left(\frac{\mathrm{d}g}{\mathrm{d}\phi} \right)^2 \right) \nabla_{\mathbf{x}}\phi_0 \cdot \mathcal{J}\nabla_{\mathbf{x}}\phi_0. \end{aligned} \tag{3.161}$$

In a similar way, we write (3.150) as

$$\nabla_{\mathbf{x}} \cdot (\sigma\mathcal{J}\nabla_{\mathbf{x}}\phi_0) = \sigma\nabla_{\mathbf{x}} \cdot (\mathcal{J}\nabla_{\mathbf{x}}\phi_0) + \sigma'\frac{\mathrm{d}g}{\mathrm{d}\phi}\nabla_{\mathbf{x}}\phi_0 \cdot \mathcal{J}\nabla_{\mathbf{x}}\phi_0 = 0. \tag{3.162}$$

By substituting (3.162) and (3.161) into (3.160), we obtain

$$\left(k\frac{\mathrm{d}^2 g}{\mathrm{d}\phi^2} + \left(k' - \frac{k\sigma'}{\sigma} \right) \left(\frac{\mathrm{d}g}{\mathrm{d}\phi} \right)^2 + \sigma \right) \nabla_{\mathbf{x}}\phi_0 \cdot \mathcal{J}\nabla_{\mathbf{x}}\phi_0 = 0, \tag{3.163}$$

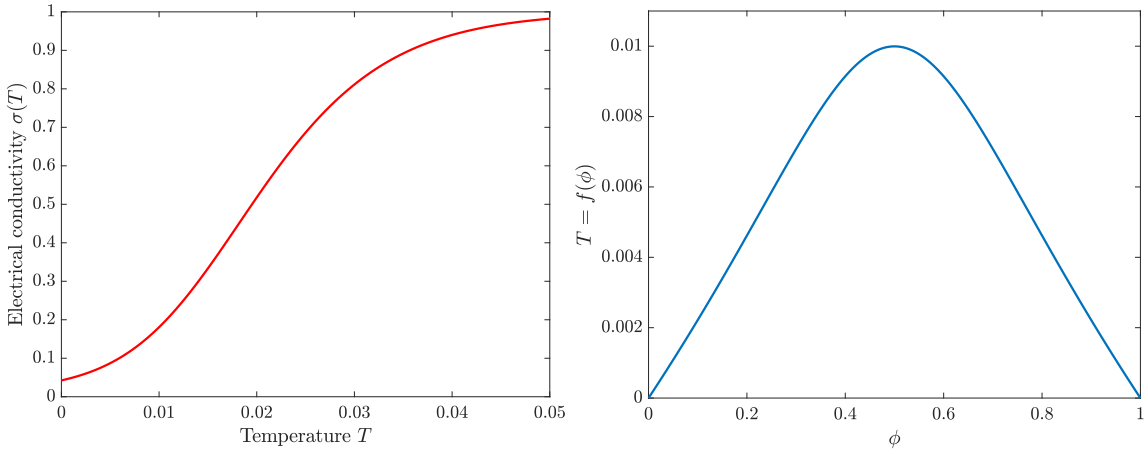
therefore, g satisfies the same nonlinear ODE (3.139) as f. By the uniqueness of (3.139), it is clear that $T = f(\phi) \Rightarrow T_0 = f(\phi_0)$. For this special case of boundary conditions, we need only solve the steady current conduction problem by homogenisation and can then deduce the temperature profile by solving the ODE (3.139)–(3.140).

3.5.1 Numerical results

We again solve the coupled model (3.130)–(3.134), both by homogenisation and directly, using piecewise affine finite elements in `FEniCS` [6] on a mesh of triangles. For illustration, we compare the two solutions for non-dimensional thermal conductivity $k = 1$ and non-dimensional electrical conductivity function (3.146) with parameter values

$$\begin{gathered} \alpha = 1\,\mathrm{Sm}^{-1}, \qquad \beta = 120\,\mathrm{Sm}^{-1}, \qquad \kappa = 10^{-3}\,(^\circ\mathrm{C})^{-1}, \qquad \phi^T = 27\,\mathrm{V}, \\ \phi^B = 0\,\mathrm{V}, \qquad T_c = 700\,^\circ\mathrm{C}, \qquad \xi = 0.7\,\mathrm{Wm}^{-1}\mathrm{K}^{-1}, \end{gathered} \tag{3.164}$$

The electrical conductivity function is plotted in Figure 3.13a and the solution to the ODE (3.139)–(3.140) in Figure 3.13b. Recall from Section 3.3 that we choose



(a) Electrical conductivity. (b) Solution to ODE.

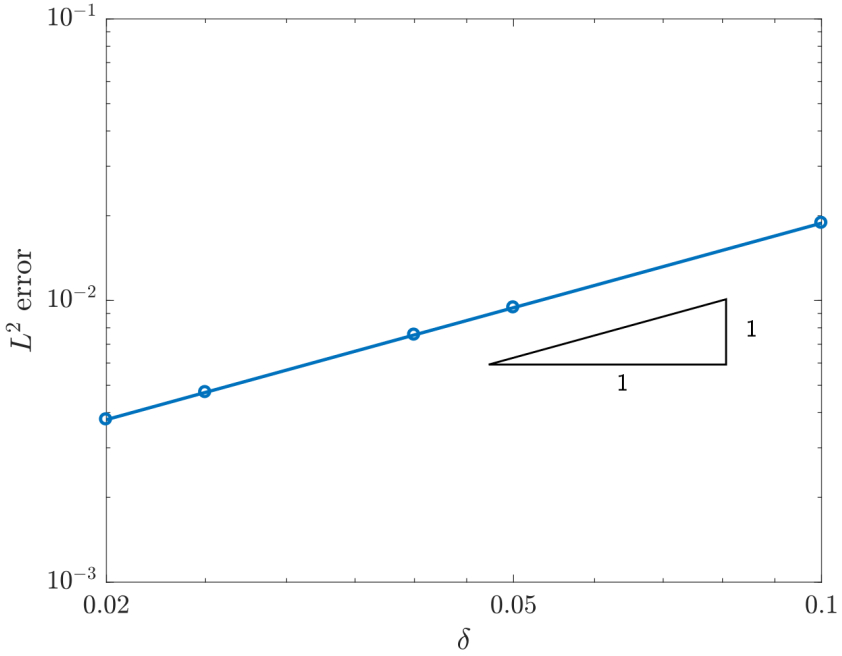
Figure 3.13: Electrical conductivity and solution to ODE (3.139)–(3.140) for $k(T)$ and $\sigma(T)$ given by (3.146) with parameters (3.164).

these parameters due to the numerical limitations involved with accurately solving the direct problem.

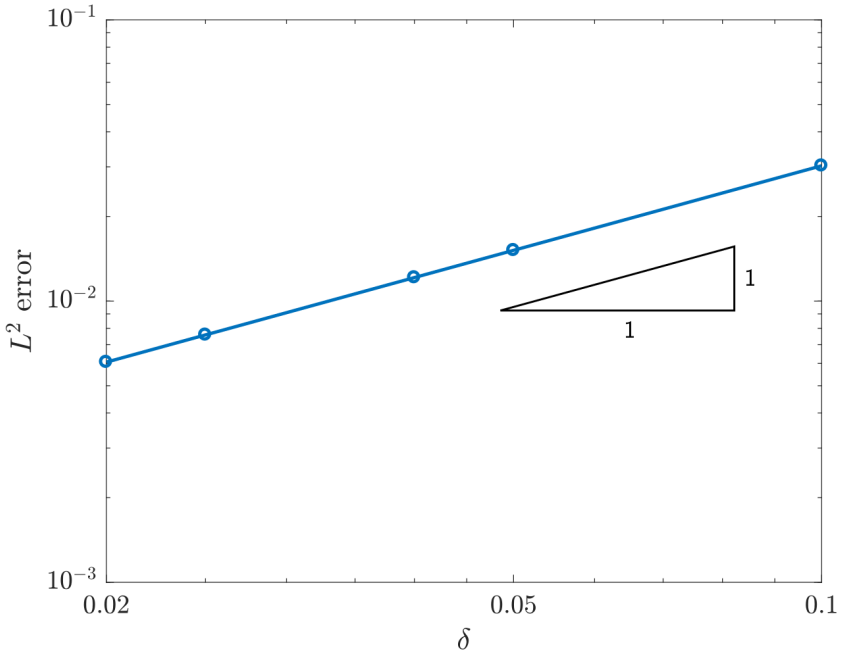
As with the models discussed previously, we plot a graph of the L^2–error versus δ between the homogenised and direct solutions for both ϕ and T in Figure 3.14 and plot the direct solution computational time in Figure 3.15. We again observe the expected $O(\delta)$ trend for the approximation error and $O(\delta^{-2})$ behaviour for the computational time. In this case, the homogenised solution was obtained in 7.43 seconds.

3.6 Discussion

In this chapter, we have discussed how to apply the homogenisation method of multiple scales to study current conduction and Ohmic heating through a regular granular material within a furnace. We highlighted that the microstructure is vital to correctly capture how current conducts throughout the bulk, however accounting for a multitude of tiny particles directly is infeasibly expensive and numerical methods struggle to solve the electrothermal conduction model within domains that accurately represent a furnace. The benefit of homogenisation is that we can reduce the computational complexity involved with this multiscale problem and by considering behaviour within the microstructure independently of the macrostructure, we obtained an effective conductivity that can be used as a parameter within a homogeneous macroscale model. The microscopic geometrical intricacies are therefore captured in this effective



(a) Electric potential



(b) Temperature

Figure 3.14: L^2-error between homogenised and direct solutions for (a) electric potential ϕ and (b) temperature T for different values of δ.

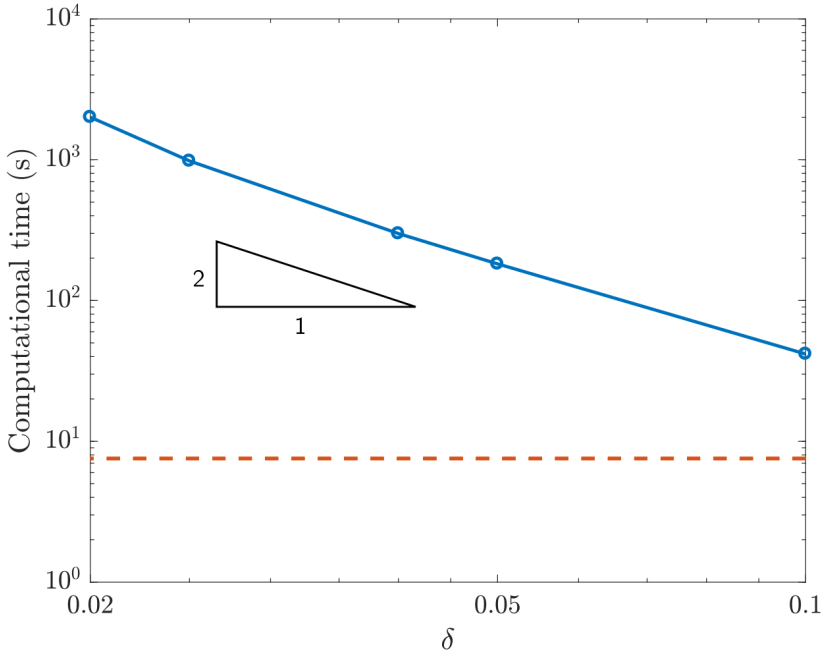


Figure 3.15: Computational time of solving the problem directly (blue solid line) with δ, along with the time to solve homogenisation problem, namely 7.43 s (dashed orange line).

parameter, hence we have simplified the problem whilst still capturing the essential microscopic influence.

To demonstrate this technique numerically, we made some simplifying assumptions. First of all, we assumed a regular, uniform domain of truncated circles. The methods described in this thesis are applicable to a vast range of more complicated geometries, in particular to three-dimensional domains. Furthermore, this work can be extended to include more irregularity in the microstructure. For example, we could expand our unit cell domain to include a collection of particles of different shapes and sizes, so long as we retain the periodicity constraint. This is discussed in more detail in Chapter 7.

Another simplification was that we assumed perfect particle contacts whose size of a similar order of magnitude as the particle size. As mentioned in Chapter 2, in reality we expect particles to be several orders of magnitude smaller than the particle size and comprise asperities due to rough surfaces and thin, resistive layers between particles. Each of these will interfere with electric current conduction through contacts. We study the effects of minute particle contacts via asymptotic analyses in Chapter 5, followed by the influence of surface imperfections in Chapter 6.

The functions we used for the electric and thermal conductivities were chosen for numerical accessibility, however it is clear from the analysis presented above that the model can take any suitable function as an input, therefore this work can be easily applied to different granular materials and for a variety of operating parameters.

Chapter 4

Radiative transfer

The thermal conduction models discussed so far neglect an important heat transfer phenomenon, that is, radiation between solid particles through the gas-filled voids [85, 99, 100]. Both experimental and theoretical analyses into the thermal conductivity of packed beds are discussed by Tsotsas and Martin [98]. Their findings indicate an increase in thermal conductivity with elevated temperatures, especially in particle beds with larger particles, due to intensification of heat transfer by radiation. The authors emphasise the dominance of radiation for high-temperature regimes. Similarly, the overall thermal conductance of a packed bed of granular, opaque particles was investigated experimentally and via a one-dimensional thermal conductance model by Zumbrunnen et al. [111], who found a proportional relationship between thermal conductance and particle size as a consequence of radiation and the distance over which radiation can penetrate.

There are many further industrial and natural applications where radiation within gas-filled voids between conducting solids has significant impact on the effective thermal conductivity of composite materials. Examples of these include multilayer thermal insulation systems [94], open-celled metal alloy foams [104] and Earth materials within the mantle [87]. The effective conductivities of alumina, graphite and nickel, each perforated with both spherical and cylindrical voids, were investigated by Francl and Kingery [36]. The findings suggest a dependence upon void orientation, especially when the temperatures exceed 500°C. Experimental exploration of the conductivity of a variety of porous materials was conducted by Luikov et al. [60]. For some materials the conductivities plateau for high temperatures, whilst for others, the conductivities appear to grow indefinitely. Thus the behaviour of the effective thermal conductivity with temperature is non-trivial and depends not only on the material of interest but also the material geometry.

A common theme in the aforementioned references is that radiation is most relevant in high-temperature regimes such as the heat treatment of anthracite in a calciner furnace. These high temperatures render experimental analysis extremely difficult, which supports the need for informative mathematical models that can accurately predict the effective thermal conductivity of granular and composite materials. However, including radiative transfer within mathematical models is extremely challenging due to the non-locality of the radiative boundary condition. This increases the numerical complexity when studying radiative transfer in the millions of voids between particles in the furnace. Appropriate simplifications must be taken to ensure the accurate yet feasible inclusion of radiation.

Tiihonen [97] studied radiation on non-convex surfaces and proved the existence and uniqueness of the conductive-radiative problem. Kiradjiev et al. [55] generalised Maxwell models to account for radiative transfer for a dilute pore distribution. The authors derived a relationship between the effective thermal conductivity and temperature and concluded that the effective thermal conductivity saturates with increasing temperature, or rather the rate of increase of the conductivity slows down as the temperature increases for the dilute distribution. Homogenisation and multiscale methods have been applied to the conductive-radiative thermal transfer in porous materials. Allaire, El Ganaoui and Habibi [3, 4, 5] study the thermal transfer within nuclear reactors, more specifically, conductive and radiative transfer throughout periodic, perforated domains. The authors consider thermal conduction throughout a solid matrix and enforce a radiative boundary condition on the interface between the solid and gaseous perforations. These works introduce the implementation of multiple scales techniques to problems involving non-local radiative boundary conditions, however differ from the methods discussed in this thesis as they analyse the weak form of the problem. Similar works are presented by Ma and Cui [61]. However, the standard method of multiple scales discussed in Chapter 3 is not suitable for this problem because there is a complication associated with approximating integrals on the interfaces. A naïve approach results in an incorrect homogenised model, as discussed by Chapman and McBurnie [19, 64]. Therefore careful adaptation of the multiple scales analysis to allow for slow-scale macroscale variation is necessary to deal with the radiative boundary condition.

In this chapter we discuss how to mathematically model radiative transfer in the voids between conducting particles and the adaptation of the standard multiple scales technique necessary for accurate inclusion in the homogenised model.

4.1 Modelling thermal radiation

An informative review of radiative heat transfer theory can be found in [66]. Radiative transfer between surfaces depends on the orientation of the surfaces relative to each other as well as their temperatures and radiative properties. By the Stefan-Boltzmann law, the radiative flux emitted per unit area at a point $\mathbf{x}$ on a void surface Γ is

$$q_{\text{emitted}}(\mathbf{x}) = \epsilon^* \sigma^* T^4(\mathbf{x}), \tag{4.1}$$

where ϵ^* is the surface emissivity and σ^* is the Stefan-Boltzmann constant. The incident flux on $\mathbf{x} \in \Gamma$ from all points $\mathbf{z}$ elsewhere on the surface is given in [66] as

$$q_{\text{incident}}(\mathbf{x}) = \int_\Gamma \epsilon^* \sigma^* T^4(\mathbf{z}) F(\mathbf{z}, \mathbf{x}) \, \mathrm{d}S, \tag{4.2}$$

where $F(\mathbf{z}, \mathbf{x})$ is known as the view-factor for the surface Γ, a geometrical property introduced to account for the effects of surface orientation on radiative transfer. The view-factor (depicted in Figure 4.1) describes the proportion of the radiation emitted from point $\mathbf{z}$ that strikes point $\mathbf{x}$ and is defined as

$$F(\mathbf{z}, \mathbf{x}) = \frac{\cos\theta(\mathbf{z}, \mathbf{x}) \cos\theta'(\mathbf{z}, \mathbf{x})}{\pi |\mathbf{z} - \mathbf{x}|^2}, \tag{4.3}$$

where $\theta(\mathbf{z}, \mathbf{x})$ is the angle between the surface normal at $\mathbf{z}$ and the line of sight from $\mathbf{z}$ to $\mathbf{x}$, and $\theta'(\mathbf{z}, \mathbf{x})$ is the angle between the surface normal at $\mathbf{x}$ and the line of sight. The view factor exhibits an inverse-square law and hence captures how the intensity of radiation at the receiving surface is inversely proportional to the square of the distance from the source. For closed surfaces, the view factor satisfies

$$\int_\Gamma F(\mathbf{z}, \mathbf{x}) \, \mathrm{d}S = 1. \tag{4.4}$$

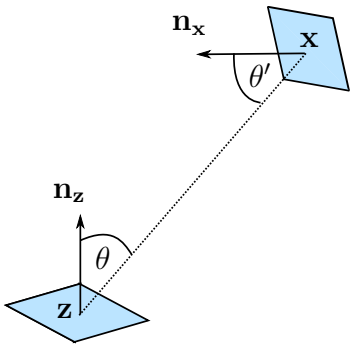


Figure 4.1: Schematic to demonstrate the orientation between two surfaces and the derivation of the view factor (4.3).

In the case of a sphere of radius R, one can deduce through simple trigonometry [47] that the view factor is

$$F_{\text{sphere}}(\mathbf{z}, \mathbf{x}) = \frac{1}{4\pi R^2}. \tag{4.5}$$

For ease of illustration and numerical calculations, we will consider spherical voids throughout this chapter, however the analysis is easily extended to account for more general voids with more complex view factors.

4.2 Homogenisation of integral constraints

To demonstrate homogenisation of the radiative boundary condition by the method of multiple scales, we consider a simple geometry $\tilde{\Omega}$ of size L with periodic microstructure of period δL where $\delta \ll 1$. The domain consists of a solid matrix $\tilde{\Omega}^S$ with N uniformly distributed spherical perforations of radius $\tilde{R} = \delta L R$ filled with a gas of negligible thermal conductivity, as in Figure 4.2. We note that $R = O(1)$ and $R < 1$ so that the periodic cell is defined as a cube perforated by a spherical void.

To capture radiative effects, we must amend the original heat flux condition defined on the interfaces between the conducting solid and gas, $\tilde{\Gamma}_i$, $i = 1, \cdots, N$, to include the Stefan-Boltzmann law. This boundary condition is based upon the conservation of energy, hence is defined as the difference between the flux emitted (4.1)

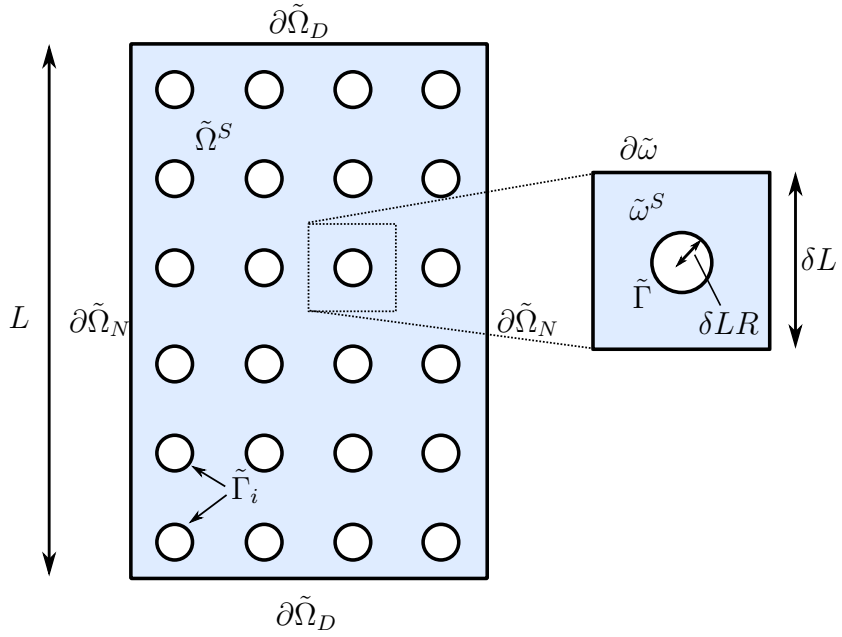


Figure 4.2: Solid matrix with uniformly distributed spherical perforations in which we solve heat transfer problem.

and the incident flux (4.2). Typically in industrial applications involving heat radiation, the material surfaces are not perfectly black, hence some of the radiation hitting the surface is reflected rather than absorbed. For simplicity, we assume that the solid material is a black-body object, thus, the thermal emissivity $\epsilon^* = 1$. The approach outlined in this thesis can be extended to include grey-diffuse surfaces, however this is not necessary to demonstrate homogenisation of the radiative operator. Furthermore, we also assume that the gas-filled void behaves like a vacuum, namely there is no heat transfer by conduction nor absorption of radiation within the void.

We wish to solve the following dimensional system of equations for temperature $\tilde{T}$ with spatial variable $\tilde{\mathbf{x}}$ within the solid portion of the domain $\tilde{\Omega}^S$ which has temperature-dependent thermal conductivity $\tilde{k}(\tilde{T})$,

$$\tilde{\nabla} \cdot (\tilde{k}(\tilde{T})\tilde{\nabla}\tilde{T}(\tilde{\mathbf{x}})) = 0, \qquad \tilde{\mathbf{x}} \in \tilde{\Omega}^S, \tag{4.6}$$

$$-\tilde{k}(\tilde{T})\nabla\tilde{T}(\tilde{\mathbf{x}}) \cdot \mathbf{n} = \sigma^*\tilde{T}^4(\tilde{\mathbf{x}}) - \frac{\sigma^*}{4\pi\tilde{R}^2}\int_{\tilde{\Gamma}_i} \tilde{T}^4(\tilde{\mathbf{z}})\mathrm{d}S, \qquad \tilde{\mathbf{x}} \in \tilde{\Gamma}_i \,\forall i, \tag{4.7}$$

$$\tilde{\nabla}\tilde{T}(\tilde{\mathbf{x}}) \cdot \mathbf{n} = 0, \qquad \tilde{\mathbf{x}} \in \partial\tilde{\Omega}_N, \tag{4.8}$$

$$\tilde{T}(\tilde{\mathbf{x}}) = T_D(\tilde{\mathbf{x}}), \qquad \tilde{\mathbf{x}} \in \partial\tilde{\Omega}_D, \tag{4.9}$$

where $T_D(\tilde{\mathbf{x}})$ is a given function on the Dirichlet portion of the outer boundary $\partial\tilde{\Omega}_D$ and the remainder of the outer boundary is denoted $\partial\tilde{\Omega}_N$.

Our challenge in this chapter is to correctly account for the radiative boundary condition (4.7) in the multiple scales methodology. We will see that the standard method is insufficient when dealing with an integral, thus care must be taken to account for the variation of the macroscale.

4.2.1 Variation of the slow scale

In standard multiple scales expansions such as those discussed in Chapter 3, an often ignored issue is that the macroscale $\mathbf{x}$ should vary over a single cell. For the vast majority of cases, it is perfectly reasonable to assume a constant value of the macroscale when analysing the microscopic cell problem. Strictly speaking, when we write the relationship between the two scales $\mathbf{x}$ and $\mathbf{y}$ as $\mathbf{y} = \mathbf{x}/\delta$, we actually mean

$$\mathbf{y} = \mathbf{x}/\delta - \lfloor \mathbf{x}/\delta \rfloor, \tag{4.10}$$

where we refer to the component-wise floor function, or alternatively

$$\mathbf{y} = \mathbf{x}/\delta \bmod 1. \tag{4.11}$$

These definitions neglect to account for which periodic cell we are concentrating on, namely, we are not concerned about the macroscopic position within the domain, only the periodic microscopic behaviour is relevant. For this reason, the slow-scale variable is taken to be constant when studying the microscale problem. However, the non-locality of the integral condition (4.7) means that variation of the slow-scale within the periodic cell matters and thereby cannot be taken to be constant. Further detail can be found in [19, 64]. To illustrate when slow-scale variation must be accounted for, we discuss some simple examples that compare internal boundaries, Dirichlet boundary conditions and integral constraints.

Boundary within a periodic cell

Let a surface within a periodic cell be defined by the function

$$f(\mathbf{x}, \mathbf{y}) = 0, \tag{4.12}$$

where $\mathbf{x}$ denotes the set of macroscopic points on the boundary and $\mathbf{y}$ denotes the set of microscopic points on the boundary, related by

$$\mathbf{y} = \mathbf{x}/\delta - \lfloor \mathbf{x}/\delta \rfloor, \tag{4.13}$$

for $\delta \ll 1$. We wish to show that the boundary remains unchanged if we use $\mathbf{x}$ or just a general $\hat{\mathbf{x}}$ within a cell, which will allow us to conclude that it is appropriate to use whichever value of the macroscale variable we want within a cell, more specifically, we can choose $\mathbf{x}$ to be constant. We write

$$\mathbf{x} = \hat{\mathbf{x}} + \delta(\mathbf{y} - \mathbf{b}), \tag{4.14}$$

where $\hat{\mathbf{x}}$ is an arbitrary point within the periodic cell and $\mathbf{b} = \hat{\mathbf{x}}/\delta - \lfloor \hat{\mathbf{x}}/\delta \rfloor$ is the shift between $\hat{\mathbf{x}}$ and the origin of the periodic cell. We thus obtain

$$f(\mathbf{x}, \mathbf{y}) = f(\hat{\mathbf{x}}, \mathbf{y}) + \delta(\mathbf{y} - \mathbf{b}) \cdot \nabla_{\mathbf{x}} f(\hat{\mathbf{x}}, \mathbf{y}) + O(\delta^2) = 0. \tag{4.15}$$

At leading order,

$$f(\hat{\mathbf{x}}, \mathbf{y}) = 0, \tag{4.16}$$

from which we conclude that if $f(\mathbf{x}, \mathbf{y}) = 0$ for some points $(\mathbf{x}, \mathbf{y})$ on the boundary, then $f(\hat{\mathbf{x}}, \mathbf{y}) = 0$ holds for all values of $\hat{\mathbf{x}}$ within the periodic cell, so long as $\mathbf{y}$ is within the set of microscopic boundary points. Therefore we can choose any value of the macroscale variable within the unit cell.

Furthermore, the $O(\delta)$ equation tells us

$$(\mathbf{y}-\mathbf{b})\cdot\nabla_{\mathbf{x}}f(\hat{\mathbf{x}},\mathbf{y})=0, \tag{4.17}$$

which is immediately satisfied due to (4.16) being true for all values of $\hat{\mathbf{x}}$ within the periodic cell. The derivative with respect to $\mathbf{x}$ in (4.17) is a partial derivative of the first argument of $f(\mathbf{x},\mathbf{y})$ and (4.16) implies that f is constant in this variable for a fixed $\mathbf{y}$ on the boundary.

Therefore we conclude that to define an internal boundary on the microscale in multiple scales form, we can neglect slow-scale variation and need only consider the microscale variable, namely, the macroscale variable can be taken to be constant.

Dirichlet condition on an internal boundary

Consider now a Dirichlet condition defined on internal boundary Γ given by

$$u(\mathbf{x},\mathbf{y})=0, \tag{4.18}$$

where $\mathbf{x}$ and $\mathbf{y}$ are the macroscopic and microscopic points on Γ respectively. The following analysis is very similar to that above, except that u is a dependent variable in our problem and $u\sim u_0+\delta u_1+O(\delta^2)$. Again, writing

$$\mathbf{x}=\hat{\mathbf{x}}+\delta(\mathbf{y}-\mathbf{b}),\qquad \mathbf{b}=\hat{\mathbf{x}}/\delta-\lfloor\hat{\mathbf{x}}/\delta\rfloor, \tag{4.19}$$

for $\hat{\mathbf{x}}$ an arbitrary point within the periodic cell and $\mathbf{b}$ the shift between $\hat{\mathbf{x}}$ and the origin of the periodic cell, we obtain

$$u(\mathbf{x},\mathbf{y})=u_0(\hat{\mathbf{x}},\mathbf{y})+\delta(u_1(\hat{\mathbf{x}},\mathbf{y})+(\mathbf{y}-\mathbf{b})\cdot\nabla_{\mathbf{x}}u_0(\hat{\mathbf{x}},\mathbf{y}))+O(\delta^2)=0. \tag{4.20}$$

At leading order, we find

$$u_0(\hat{\mathbf{x}},\mathbf{y})=0, \tag{4.21}$$

which tells us that the leading order boundary condition is independent of the choice of macroscopic variable $\mathbf{x}$ within the cell. At $O(\delta)$,

$$u_1(\hat{\mathbf{x}},\mathbf{y})+(\mathbf{y}-\mathbf{b})\cdot\nabla_{\mathbf{x}}u_0(\hat{\mathbf{x}},\mathbf{y})=0. \tag{4.22}$$

The second term on the left-hand side is zero due to (4.21), namely that $u_0(\mathbf{x},\mathbf{y})=0$ for any $\mathbf{x}$ as long as $\mathbf{y}$ is evaluated on the boundary. This is essential to understand why $\nabla_{\mathbf{x}}u_0\neq 0$ in general, only when u_0 is evaluated on the microscale boundary within the periodic cell. Thus, at $O(\delta)$,

$$u_1(\hat{\mathbf{x}},\mathbf{y})=0, \tag{4.23}$$

for all $\hat{\mathbf{x}}$ in the cell when $\mathbf{y}$ is on the boundary.

We can prove that $u_k(\hat{\mathbf{x}}, \mathbf{y}) = 0$ for all $k \in \mathbb{Z}^+$ by induction. For analytical ease, we demonstrate the argument in 1D, but the argument is true for higher dimensions. Consider $u(x, y)$ where x and y are the 1D macroscale and microscale variables lying on interface Γ respectively and expand in small δ where $x = \hat{x} + \delta(y - b)$ and $b = \hat{x}/\delta - \lfloor \hat{x}/\delta \rfloor$, thus

$$u(\hat{x} + \delta(y - b), y) = \sum_{n=0}^{\infty} (\delta(y - b))^n \frac{\partial^n u}{\partial x^n}(\hat{x}, y), \tag{4.24}$$

where

$$u = \sum_{k=0}^{\infty} \delta^k u_k. \tag{4.25}$$

Considering (4.24) and (4.25) in (4.18), we obtain

$$\sum_{k=0}^{\infty} \sum_{n=0}^{\infty} \delta^{k+n} (y - b)^n \frac{\partial^n u_k}{\partial x^n}(\hat{x}, y) = 0, \tag{4.26}$$

and by writing $m = n + k$, we deduce that

$$\sum_{m=0}^{\infty} \delta^m \sum_{n=0}^{m} (y - b)^n \frac{\partial^n u_{m-n}}{\partial x^n}(\hat{x}, y) = 0. \tag{4.27}$$

Recall that our goal is to show $u_i(\hat{x}, y) = 0$ for all i. The result is true for $i = 0$ following from (4.21). We proceed with the induction method by assuming $u_i(\hat{x}, y) = 0$ for all integers i such that $0 \leq i \leq N - 1$. We then consider the $O(\delta^N)$ equation, namely

$$\sum_{n=0}^{N} (y - b)^n \frac{\partial^n u_{N-n}}{\partial x^n}(\hat{x}, y) = 0. \tag{4.28}$$

Given $u_i(\hat{x}, y) = 0$ for $i \leq N - 1$, these terms vanish, leaving only the $n = 0$ term, thus

$$u_N(\hat{x}, y) = 0, \tag{4.29}$$

as required, thereby completing the proof by induction.

Therefore, extending this proof to higher dimensions, we conclude that

$$u(\hat{\mathbf{x}}, \mathbf{y}) = 0, \tag{4.30}$$

for any macroscopic variable $\hat{\mathbf{x}}$, so long as microscopic $\mathbf{y} \in \Gamma$.

Integral constraints on an internal boundary

We now consider an integral constraint defined on an internal boundary Γ within the periodic cell, such as

$$\int_\Gamma u(\mathbf{x},\mathbf{y})\,\mathrm{d}S(\mathbf{y}) = 0, \tag{4.31}$$

where $\mathbf{x}$ and $\mathbf{y}$ are macroscopic and microscopic points respectively on Γ. Again, writing

$$\mathbf{x} = \hat{\mathbf{x}} + \delta(\mathbf{y}-\mathbf{b}), \qquad \mathbf{b} = \hat{\mathbf{x}}/\delta - \lfloor \hat{\mathbf{x}}/\delta \rfloor, \tag{4.32}$$

for $\hat{\mathbf{x}}$ an arbitrary point within the periodic cell and $\mathbf{b}$ the shift between $\hat{\mathbf{x}}$ and the origin of the periodic cell, we obtain

$$\int_\Gamma \left\{ u_0(\hat{\mathbf{x}},\mathbf{y}) + \delta[u_1(\hat{\mathbf{x}},\mathbf{y}) + (\mathbf{y}-\mathbf{b})\cdot\nabla_{\mathbf{x}} u_0(\hat{\mathbf{x}},\mathbf{y})] + O(\delta^2) \right\} \mathrm{d}S(\mathbf{y}) = 0. \tag{4.33}$$

At $O(1)$,

$$\int_\Gamma u_0(\hat{\mathbf{x}},\mathbf{y})\,\mathrm{d}S(\mathbf{y}) = 0, \tag{4.34}$$

which tells us that the leading order expansion of constraint (4.31) is satisfied irrespective of where the macroscale coordinate is evaluated within the periodic cell. Therefore,

$$\nabla_{\mathbf{x}} \int_\Gamma u_0(\hat{\mathbf{x}},\mathbf{y})\,\mathrm{d}S(\mathbf{y}) = 0. \tag{4.35}$$

At $O(\delta)$, we have

$$\int_\Gamma u_1(\hat{\mathbf{x}},\mathbf{y})\,\mathrm{d}S(\mathbf{y}) = -\int_\Gamma \mathbf{y}\cdot\nabla_{\mathbf{x}} u_0(\hat{\mathbf{x}},\mathbf{y})\,\mathrm{d}S(\mathbf{y}) + \mathbf{b}\cdot\nabla_{\mathbf{x}} \int_\Gamma u_0(\hat{\mathbf{x}},\mathbf{y})\,\mathrm{d}S(\mathbf{y}). \tag{4.36}$$

Contrary to the previous case, we don't necessarily have $\nabla_{\mathbf{x}} u_0(\hat{\mathbf{x}},\mathbf{y}) = 0$, but rather, by (4.35), the constraint for $u_1(\hat{\mathbf{x}},\mathbf{y})$ is

$$\int_\Gamma u_1(\hat{\mathbf{x}},\mathbf{y})\,\mathrm{d}S(\mathbf{y}) = -\int_\Gamma \mathbf{y}\cdot\nabla_{\mathbf{x}} u_0(\hat{\mathbf{x}},\mathbf{y})\,\mathrm{d}S(\mathbf{y}), \tag{4.37}$$

which can be evaluated for any value of the macroscale variable $\hat{\mathbf{x}}$ within the periodic cell.

From this analysis, it is clear that

$$\int_\Gamma u(\mathbf{x},\mathbf{y})\,\mathrm{d}S(\mathbf{y}) = 0 \not\Rightarrow \int_\Gamma u(\hat{\mathbf{x}},\mathbf{y})\,\mathrm{d}S(\mathbf{y}) = 0, \tag{4.38}$$

therefore we cannot take the macroscopic variable to be constant when writing an integral in multiple scales form. We must take extra care when analysing the radiative boundary condition (4.7) as the standard method is not valid. We outline the appropriate handling of the integral constraint in the multiple scales analysis of the radiation problem (4.6)–(4.9).

4.3 Extended multiple scales analysis

Dimensionless equations

We will scale our variables using the same scaling as in Chapter 3, namely

$$\tilde{\mathbf{x}} = L\mathbf{x}, \qquad \tilde{T} = \zeta T + T_{\min}, \qquad \tilde{k} = \xi k, \tag{4.39}$$

where we note that ζ will be chosen to be $\zeta = \beta(\phi^T - \phi^B)^2/\xi$ when we couple the thermal problem with the electrical problem in Section 4.5. Therefore, the radiative boundary condition becomes

$$-k\nabla T(\mathbf{x}) \cdot \mathbf{n} = \frac{\sigma^* \zeta^3 L}{\xi} \left((T(\mathbf{x}) + \tau)^4 - \frac{1}{4\pi\delta^2 R^2} \int_{\Gamma_i} (T(\mathbf{z}) + \tau)^4 \mathrm{d}S \right), \tag{4.40}$$

where $\tau = T_{\min}/\zeta$. We want to consider the case where heat transfer by conduction and radiation are in balance on the microscale. To deduce the conditions necessary for this regime, we rescale the spatial variable

$$\mathbf{x} = \delta \mathbf{y}, \tag{4.41}$$

where δ is the period of the microscale. Therefore, the dimensionless radiative boundary condition (4.40) becomes

$$-\frac{k}{\delta}\nabla_{\mathbf{y}} T(\mathbf{y}) \cdot \mathbf{n} = \frac{\sigma^* \zeta^3 L}{\xi} \left((T(\mathbf{y}) + \tau)^4 - \frac{1}{4\pi R^2} \int_{\Gamma} (T(\mathbf{z}) + \tau)^4 \mathrm{d}S \right), \tag{4.42}$$

where Γ is the boundary of the microscopic void of radius R. Thus we obtain the dimensionless parameter $\lambda = \sigma^* \zeta^3 \delta L/\xi$. We note the different regimes that can be captured due to the magnitude of λ; if $\lambda \gg 1$, then radiation dominates on the particle length-scale, which essentially replaces the void with a perfect conductor. On the other hand, if $\lambda \ll 1$, conduction dominates on the particle length-scale, thus the void is in effect a perfect insulator. We have a balance between conduction and radiation when $\lambda = O(1)$, therefore throughout this thesis, we consider the case where

$$\lambda = \frac{\sigma^* \zeta^3 \delta L}{\xi} = O(1). \tag{4.43}$$

We thus rewrite the dimensionless radiative boundary condition (4.40) as

$$-k\nabla T(\mathbf{x}) \cdot \mathbf{n} = \frac{\lambda}{\delta} \left((T(\mathbf{x}) + \tau)^4 - \frac{1}{4\pi\delta^2 R^2} \int_{\Gamma_i} (T(\mathbf{z}) + \tau)^4 \mathrm{d}S \right), \tag{4.44}$$

and the full, dimensionless problem with the new radiative boundary condition becomes

$$\nabla \cdot (k(T)\nabla T(\mathbf{x})) = 0, \qquad \mathbf{x} \in \Omega^S, \quad (4.45)$$

$$-k\nabla T(\mathbf{x}) \cdot \mathbf{n} = \frac{\lambda}{\delta}\left((T(\mathbf{x})+\tau)^4 - \frac{1}{4\pi\delta^2 R^2}\int_{\Gamma_i}(T(\mathbf{z})+\tau)^4 \mathrm{d}S\right), \qquad \mathbf{x} \in \Gamma_i \,\forall i, \quad (4.46)$$

$$\nabla T(\mathbf{x}) \cdot \mathbf{n} = 0, \qquad \mathbf{x} \in \partial\Omega_N, \quad (4.47)$$

$$T(\mathbf{x}) = T_D(\mathbf{x}), \qquad \mathbf{x} \in \partial\Omega_D. \quad (4.48)$$

For ease of notation, we write (4.46) as

$$-k\nabla T(\mathbf{x}) \cdot \mathbf{n} = \frac{\lambda}{\delta} G_i((T+\tau)^4)(\mathbf{x}), \qquad \mathbf{x} \in \Gamma_i \,\forall i, \quad (4.49)$$

where

$$G_i(f)(\mathbf{x}) = f(\mathbf{x}) - \frac{1}{4\pi\delta^2 R^2}\int_{\Gamma_i} f(\mathbf{z})\mathrm{d}S, \quad (4.50)$$

and Γ_i is defined in terms of the macroscopic variable $\mathbf{x}$. We note some properties of G_i, namely

$$1\cdot \quad G_i(f+g)(\mathbf{x}) = G_i(f)(\mathbf{x}) + G_i(g)(\mathbf{x}), \quad (4.51)$$

$$2\cdot \quad G_i(\alpha)(\mathbf{x}) = 0 \text{ for } \alpha \text{ independent of } \mathbf{x}, \quad (4.52)$$

$$3\cdot \quad \int_{\Gamma_i} G_i(f)(\mathbf{x})\mathrm{d}S = 0. \quad (4.53)$$

The first of these is linearity which is clearly understood from the definition of G_i given by (4.50). The second property states that $G_i(\cdot)(\mathbf{x})$ is zero when applied to a quantity independent of $\mathbf{x}$ whereas the final property makes use of (4.4) to say that the integral over G_i on the appropriate surface Γ_i is 0. We continue with the multiple scales analysis of the thermal conductive-radiative problem (4.45)–(4.48).

Multiple scales expansion of heat equation

We begin by implementing the multiple scales expansion for the heat equation (4.45), where we set

$$\mathbf{x} = \hat{\mathbf{x}} + \delta(\mathbf{y} - \mathbf{b}), \qquad \nabla \to \nabla_{\mathbf{x}} + \frac{1}{\delta}\nabla_{\mathbf{y}}, \quad (4.54)$$

where δ is the period of the microscale, $\hat{\mathbf{x}}$ is an arbitrary point within the periodic cell and $\mathbf{b} = \hat{\mathbf{x}}/\delta - \lfloor \hat{\mathbf{x}}/\delta \rfloor$ is the shift between $\hat{\mathbf{x}}$ and the origin of the periodic cell. Note that we could consider the standard expansion here, namely $\mathbf{x} = \delta\mathbf{y}$, due to the locality of the equation, however we use the extended expansion (4.54) to avoid any

confusion associated with using different expansions for the heat equation (4.45) and the boundary condition (4.49). We asymptotically expand T and thus k:

$$T(\mathbf{x},\mathbf{y}) \sim T_0(\mathbf{x},\mathbf{y}) + \delta T_1(\mathbf{x},\mathbf{y}) + \delta^2 T_2(\mathbf{x},\mathbf{y}) + O(\delta^3), \tag{4.55}$$

$$k(T) \sim k_0(T_0) + \delta k_1(T_0,T_1) + \delta^2 k_2(T_0,T_1,T_2) + O(\delta^3), \tag{4.56}$$

where

$$k_0 = k(T_0), \qquad k_1 = T_1 k'(T_0), \qquad k_2 = T_2 k'(T_0) + \frac{1}{2}T_1^2 k''(T_0). \tag{4.57}$$

For ease of notation, let $f = \nabla\cdot(k\nabla T)$. Thus,

$$f(\mathbf{x},\mathbf{y}) = f(\hat{\mathbf{x}},\mathbf{y}) + \delta(\mathbf{y}-\mathbf{b})\cdot\nabla_{\mathbf{x}} f(\hat{\mathbf{x}},\mathbf{y}) + \frac{\delta^2}{2}(\mathbf{y}-\mathbf{b})^2\nabla^2_{\mathbf{x}} f(\hat{\mathbf{x}},\mathbf{y}) + \ldots = 0, \tag{4.58}$$

for $\mathbf{y}\in\omega^S$, as depicted in Figure 4.3, where we write

$$f(\hat{\mathbf{x}},\mathbf{y}) = \frac{1}{\delta^2}f_0(\hat{\mathbf{x}},\mathbf{y}) + \frac{1}{\delta}f_1(\hat{\mathbf{x}},\mathbf{y}) + f_2(\hat{\mathbf{x}},\mathbf{y}) + O(\delta), \tag{4.59}$$

for

$$f_0(\hat{\mathbf{x}},\mathbf{y}) = \nabla_{\mathbf{y}}\cdot(k_0\nabla_{\mathbf{y}}T_0), \tag{4.60}$$

$$f_1(\hat{\mathbf{x}},\mathbf{y}) = \nabla_{\mathbf{y}}\cdot(k_0(\nabla_{\mathbf{y}}T_1 + \nabla_{\mathbf{x}}T_0) + k_1\nabla_{\mathbf{y}}T_0) + \nabla_{\mathbf{x}}\cdot(k_0\nabla_{\mathbf{y}}T_0), \tag{4.61}$$

$$\begin{aligned} f_2(\hat{\mathbf{x}},\mathbf{y}) = {}& \nabla_{\mathbf{y}}\cdot(k_0(\nabla_{\mathbf{y}}T_2 + \nabla_{\mathbf{x}}T_1) + k_1(\nabla_{\mathbf{y}}T_1 + \nabla_{\mathbf{x}}T_0) + k_2\nabla_{\mathbf{y}}T_0) \\ & + \nabla_{\mathbf{x}}\cdot(k_0(\nabla_{\mathbf{y}}T_1 + \nabla_{\mathbf{x}}T_0) + k_1\nabla_{\mathbf{y}}T_0). \end{aligned} \tag{4.62}$$

Therefore, we consider equation (4.58) in ω^S for each order of δ, namely

$$O(\delta^{-2}): \quad f_0 = 0, \tag{4.63}$$

$$O(\delta^{-1}): \quad f_1 + (\mathbf{y}-\mathbf{b})\cdot\nabla_{\mathbf{x}} f_0 = 0 \quad \Rightarrow \quad f_1 = 0, \tag{4.64}$$

$$O(1): \quad f_2 + (\mathbf{y}-\mathbf{b})\cdot\nabla_{\mathbf{x}} f_1 + \frac{1}{2}(\mathbf{y}-\mathbf{b})^2\nabla^2_{\mathbf{x}} f_0 = 0 \quad \Rightarrow \quad f_2 = 0. \tag{4.65}$$

As expected, this is the same result that we would obtain if we had considered the standard multiple scales expansion, $\mathbf{x} = \delta\mathbf{y}$, in (4.45).

Multiple scales expansion of integral constraint

We expand the integral constraint (4.49) in terms of the two scales using (4.54) by considering the left and right-hand sides separately.

Consider first the left-hand side. In a similar method as before, let $Q = -k\nabla T\cdot\mathbf{n}$, thus

$$Q(\mathbf{x},\mathbf{y}) = Q(\hat{\mathbf{x}},\mathbf{y}) + \delta(\mathbf{y}-\mathbf{b})\cdot\nabla_{\mathbf{x}} Q(\hat{\mathbf{x}},\mathbf{y}) + \frac{\delta^2}{2}(\mathbf{y}-\mathbf{b})^2\nabla^2_{\mathbf{x}} Q(\hat{\mathbf{x}},\mathbf{y}) + \ldots, \tag{4.66}$$

for $\mathbf{y} \in \Gamma$, where we write

$$Q(\hat{\mathbf{x}}, \mathbf{y}) = \frac{1}{\delta} Q_0(\hat{\mathbf{x}}, \mathbf{y}) + Q_1(\hat{\mathbf{x}}, \mathbf{y}) + \delta Q_2(\hat{\mathbf{x}}, \mathbf{y}) + \dots, \tag{4.67}$$

for

$$Q_0 = -k_0 \nabla_{\mathbf{y}} T_0 \cdot \mathbf{n}, \tag{4.68}$$

$$Q_1 = -[k_0(\nabla_{\mathbf{y}} T_1 + \nabla_{\mathbf{x}} T_0) + k_1 \nabla_{\mathbf{y}} T_0] \cdot \mathbf{n}, \tag{4.69}$$

$$Q_2 = -[k_0(\nabla_{\mathbf{y}} T_2 + \nabla_{\mathbf{x}} T_1) + k_1(\nabla_{\mathbf{y}} T_1 + \nabla_{\mathbf{x}} T_0) + k_2 \nabla_{\mathbf{y}} T_0] \cdot \mathbf{n}. \tag{4.70}$$

Thus, the left-hand side of the boundary condition (4.49) for $\mathbf{y} \in \Gamma$ in the unit cell ω^S can be written for every order of δ, namely

$$O(\delta^{-1}) : \text{LHS} = -k_0 \nabla_{\mathbf{y}} T_0 \cdot \mathbf{n}, \tag{4.71}$$

$$O(1) : \quad \text{LHS} = -[k_0(\nabla_{\mathbf{y}} T_1 + \nabla_{\mathbf{x}} T_0) + k_1 \nabla_{\mathbf{y}} T_0 + (\mathbf{y} - \mathbf{b}) \cdot \nabla_{\mathbf{x}}(k_0 \nabla_{\mathbf{y}} T_0)] \cdot \mathbf{n}, \tag{4.72}$$

$$\begin{aligned} O(\delta) : \quad \text{LHS} = -[&k_0(\nabla_{\mathbf{y}} T_2 + \nabla_{\mathbf{x}} T_1) + k_1(\nabla_{\mathbf{y}} T_1 + \nabla_{\mathbf{x}} T_0) + k_2 \nabla_{\mathbf{y}} T_0 \\ &+ (\mathbf{y} - \mathbf{b}) \cdot \nabla_{\mathbf{x}}(k_0(\nabla_{\mathbf{y}} T_1 + \nabla_{\mathbf{x}} T_0) + k_1 \nabla_{\mathbf{y}} T_0) \\ &+ \frac{1}{2}(\mathbf{y} - \mathbf{b})^2 \nabla_{\mathbf{x}}^2 (k_0 \nabla_{\mathbf{y}} T_0)] \cdot \mathbf{n}. \end{aligned} \tag{4.73}$$

Now we consider the right-hand side of (4.49), namely

$$\text{RHS} \ = \frac{\lambda}{\delta} G_i((T + \tau)^4)(\mathbf{x}). \tag{4.74}$$

Consider the integral within $G_i(\cdot)(\mathbf{x})$, given by

$$\mathcal{I}_i(\mathbf{x}) = \frac{1}{4\pi\delta^2 R^2} \int_{\Gamma_i} (T + \tau)^4 \mathrm{d}S(\mathbf{x}). \tag{4.75}$$

Recall that the boundary within the periodic, unit cell ω^S is denoted Γ, therefore we replace general Γ_i in (4.75). We proved in Section 4.2.1 that an internal boundary Γ

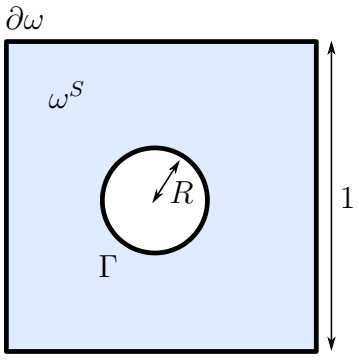


Figure 4.3: Unit cell in which we solve the cell problem (4.103)–(4.105)

.

within a periodic cell can be evaluated for any value of the macroscale $\mathbf{x}$, thus the freedom of choice of $\mathbf{x}$ allows us to write

$$\mathrm{d}S(\mathbf{x}) = \delta^2 \mathrm{d}S(\mathbf{y}), \tag{4.76}$$

and we thus consider the right-hand side as

$$\begin{aligned} \text{RHS} &= \frac{\lambda}{\delta} G((T(\mathbf{x},\mathbf{y})+\tau)^4)(\mathbf{y}), && (4.77)\\ &= \frac{\lambda}{\delta}\left((T(\mathbf{x},\mathbf{y})+\tau)^4 - \frac{1}{4\pi R^2}\int_\Gamma (T(\mathbf{x},\mathbf{z})+\tau)^4 \mathrm{d}S(\mathbf{z})\right). && (4.78)\end{aligned}$$

We note that the variable $T(\mathbf{x},\mathbf{y})$ within the integral cannot be expanded for any arbitrary $\mathbf{x}$ and we must conduct the appropriate multiple scales analysis for the integrand outlined in Section 4.2.1. Using the multiple scales expansion (4.54), we obtain

$$\begin{aligned} \text{RHS } = \frac{\lambda}{\delta} G((T(\hat{\mathbf{x}},\mathbf{y})+\tau)^4 &+ \delta(\mathbf{y}-\mathbf{b})\cdot\nabla_{\mathbf{x}}(T(\hat{\mathbf{x}},\mathbf{y})+\tau)^4 \\ &+ \frac{\delta^2}{2}(\mathbf{y}-\mathbf{b})^2\nabla_{\mathbf{x}}^2(T(\hat{\mathbf{x}},\mathbf{y})+\tau)^4)(\mathbf{y}). \end{aligned} \tag{4.79}$$

We thereby write the RHS of (4.49) as

$$\text{RHS} = \frac{\lambda}{\delta} G(\tau_0 + \delta\tau_1 + \delta^2\tau_2 + O(\delta^3))(\mathbf{y}), \tag{4.80}$$

where τ_i are given by

$$\begin{aligned} \tau_0 &= (T_0+\tau)^4, && (4.81)\\ \tau_1 &= 4(T_0+\tau)^3(T_1 + (\mathbf{y}-\mathbf{b})\cdot\nabla_{\mathbf{x}}T_0), && (4.82)\\ \tau_2 &= 2(T_0+\tau)^2(3T_1^2 + 2(T_0+\tau)T_2 + (\mathbf{y}-\mathbf{b})\cdot[6T_1\nabla_{\mathbf{x}}T_0 + 2(T_0+\tau)\nabla_{\mathbf{x}}T_1] \\ &\qquad + (\mathbf{y}-\mathbf{b})^2[3(\nabla_{\mathbf{x}}T_0)^2 + (T_0+\tau)\nabla_{\mathbf{x}}^2 T_0]). && (4.83)\end{aligned}$$

Leading-order problem

We combine (4.63), (4.71) and (4.80) along with the periodicity of T_0 to obtain the leading-order problem, namely

$$\begin{aligned} \nabla_{\mathbf{y}}\cdot(k_0\nabla_{\mathbf{y}}T_0) &= 0, && \mathbf{y}\in\omega^S, && (4.84)\\ -k_0\nabla_{\mathbf{y}}T_0\cdot\mathbf{n} &= \lambda G((T_0+\tau)^4)(\mathbf{y}), && \mathbf{y}\in\Gamma, && (4.85)\\ T_0 &\text{ periodic}, && \mathbf{y}\in\partial\omega. && (4.86)\end{aligned}$$

By multiplying (4.84) by $(T_0+\tau)$ and integrating over ω^S, we obtain

$$\int_{\omega^S} k_0 \nabla_{\mathbf{y}} T_0 \cdot \nabla_{\mathbf{y}} T_0 \,\mathrm{d}\mathbf{y} + \int_\Gamma \lambda G((T_0+\tau)^4)(\mathbf{y})(T_0+\tau)\,\mathrm{d}S = 0, \tag{4.87}$$

where the boundary integral over $\partial\omega$ vanishes due to periodicity (4.86). Let us analyse the Γ-boundary integral in (4.87). For ease of notation, we write

$$\hat{T}_0 = T_0 + \tau, \tag{4.88}$$

thus

$$\int_\Gamma \lambda G(\hat{T}_0^4)(\mathbf{y})\hat{T}_0\,\mathrm{d}S = \lambda \int_\Gamma \left(\hat{T}_0^4(\cdot,\mathbf{y}) - \frac{1}{4\pi R^2}\int_\Gamma \hat{T}_0^4(\cdot,\mathbf{z})\,\mathrm{d}S(\mathbf{z})\right)\hat{T}_0(\cdot,\mathbf{y})\,\mathrm{d}S(\mathbf{y}), \tag{4.89}$$

$$= \lambda\left(\int_\Gamma \hat{T}_0^5(\cdot,\mathbf{y})\mathrm{d}S(\mathbf{y}) - \frac{1}{4\pi R^2}\int_\Gamma \hat{T}_0^4(\cdot,\mathbf{z})\,\mathrm{d}S(\mathbf{z})\int_\Gamma \hat{T}_0(\cdot,\mathbf{y})\,\mathrm{d}S(\mathbf{y})\right). \tag{4.90}$$

We note the interesting form of (4.90) and its resemblance to the integral Chebyshev inequality, therefore we explore the boundedness of (4.90).

Lemma 4.3.1. *For a spherical surface Γ of radius R and $\hat{T}_0 \geq 0$,*

$$\int_\Gamma \hat{T}_0^5(\cdot,\mathbf{y})\mathrm{d}S(\mathbf{y}) - \frac{1}{4\pi R^2}\int_\Gamma \hat{T}_0^4(\cdot,\mathbf{z})\,\mathrm{d}S(\mathbf{z})\int_\Gamma \hat{T}_0(\cdot,\mathbf{y})\,\mathrm{d}S(\mathbf{y}) \geq 0. \tag{4.91}$$

Proof. Consider the inequality

$$\left(\hat{T}_0^4(\cdot,\mathbf{y}) - \hat{T}_0^4(\cdot,\mathbf{z})\right)\left(\hat{T}_0(\cdot,\mathbf{y}) - \hat{T}_0(\cdot,\mathbf{z})\right) \geq 0. \tag{4.92}$$

Integrating (4.92) over Γ for $\mathbf{y}$ and $\mathbf{z}$, we deduce

$$\int_\Gamma\int_\Gamma \left(\hat{T}_0^4(\cdot,\mathbf{y}) - \hat{T}_0^4(\cdot,\mathbf{z})\right)\left(\hat{T}_0(\cdot,\mathbf{y}) - \hat{T}_0(\cdot,\mathbf{z})\right)\mathrm{d}S(\mathbf{y})\mathrm{d}S(\mathbf{z}) \geq 0, \tag{4.93}$$

$$2\int_\Gamma\int_\Gamma \hat{T}_0^5(\cdot,\mathbf{y})\mathrm{d}S(\mathbf{y})\mathrm{d}S(\mathbf{z}) - 2\int_\Gamma\int_\Gamma \hat{T}_0^4(\cdot,\mathbf{z})\hat{T}_0(\cdot,\mathbf{y})\mathrm{d}S(\mathbf{y})\mathrm{d}S(\mathbf{z}) \geq 0, \tag{4.94}$$

$$2|\Gamma|\int_\Gamma \hat{T}_0^5(\cdot,\mathbf{y})\mathrm{d}S(\mathbf{y}) - 2\int_\Gamma \hat{T}_0^4(\cdot,\mathbf{z})\mathrm{d}S(\mathbf{z})\int_\Gamma \hat{T}_0(\cdot,\mathbf{y})\mathrm{d}S(\mathbf{y}) \geq 0. \tag{4.95}$$

Given that $|\Gamma| = 4\pi R^2$ for a spherical surface, we conclude the proof. □

Using the Lemma above, (4.90) becomes

$$\int_\Gamma \lambda G((T_0+\tau)^4)(\mathbf{y})(T_0+\tau)\,\mathrm{d}S \geq 0, \tag{4.96}$$

thus forcing the first term on the left-hand side of (4.87) to be non-positive, namely

$$\int_{\omega^S} k_0 \nabla_{\mathbf{y}} T_0 \cdot \nabla_{\mathbf{y}} T_0 \,\mathrm{d}\mathbf{y} \leq 0, \tag{4.97}$$

$$\Rightarrow \nabla_{\mathbf{y}} T_0 = 0. \tag{4.98}$$

Therefore, we conclude that $T_0 = T_0(\mathbf{x})$ is independent of the microscale $\mathbf{y}$.

First-order problem

Noting the cancellation of the $\nabla_{\mathbf{y}} T_0$ terms, we combine (4.64), (4.72) and (4.80) along with the periodicity of T_1 to write the first-order problem as

$$\nabla_{\mathbf{y}} \cdot (k_0(\nabla_{\mathbf{y}} T_1 + \nabla_{\mathbf{x}} T_0)) = 0, \quad \mathbf{x} \in \omega^S, \tag{4.99}$$

$$-k_0(\nabla_{\mathbf{y}} T_1 + \nabla_{\mathbf{x}} T_0) \cdot \mathbf{n} = \lambda G(4(T_0 + \tau)^3 [T_1 + (\mathbf{y} - \mathbf{b}) \cdot \nabla_{\mathbf{x}} T_0])(\mathbf{y}), \quad \mathbf{x} \in \Gamma, \tag{4.100}$$

$$T_1 \text{ periodic}, \quad \mathbf{x} \in \partial\omega. \tag{4.101}$$

In a similar analysis to that of Chapter 3, we introduce the vector function $\mathbf{\Psi}(\mathbf{y})$ such that

$$T_1 = \mathbf{\Psi}(\mathbf{y}) \cdot \nabla_{\mathbf{x}} T_0(\mathbf{x}) + \hat{T}_1(\mathbf{x}), \tag{4.102}$$

thus substituting this into (4.99)–(4.101) and noting that $k_0 = k(T_0)$ is independent of the microscale $\mathbf{y}$, we obtain the cell problem

$$\nabla_{\mathbf{y}}^2 \mathbf{\Psi} = 0, \qquad \mathbf{x} \in \omega^S, \tag{4.103}$$

$$-k_0(\nabla_{\mathbf{y}} \mathbf{\Psi} + \mathbf{I}) \cdot \mathbf{n} = 4\lambda(T_0 + \tau)^3 G(\mathbf{\Psi} + \mathbf{y})(\mathbf{y}), \qquad \mathbf{x} \in \Gamma, \tag{4.104}$$

$$\mathbf{\Psi} \text{ periodic}, \qquad \mathbf{x} \in \partial\omega. \tag{4.105}$$

We include the simplification of the right-hand side of (4.100) according to (4.51)–(4.53):

$$G(4(T_0 + \tau)^3 [T_1 + (\mathbf{y} - \mathbf{b}) \cdot \nabla_{\mathbf{x}} T_0])(\mathbf{y}) \tag{4.106}$$

$$= 4(T_0 + \tau)^3 G(\mathbf{\Psi} \cdot \nabla_{\mathbf{x}} T_0 + (\mathbf{y} - \mathbf{b}) \cdot \nabla_{\mathbf{x}} T_0)(\mathbf{y}), \tag{4.107}$$

$$= 4(T_0 + \tau)^3 G(\mathbf{\Psi} + (\mathbf{y} - \mathbf{b}))(\mathbf{y}) \cdot \nabla_{\mathbf{x}} T_0, \tag{4.108}$$

$$= 4(T_0 + \tau)^3 [G(\mathbf{\Psi} + \mathbf{y})(\mathbf{y}) - G(\mathbf{b})(\mathbf{y})] \cdot \nabla_{\mathbf{x}} T_0, \tag{4.109}$$

$$= 4(T_0 + \tau)^3 G(\mathbf{\Psi} + \mathbf{y})(\mathbf{y}) \cdot \nabla_{\mathbf{x}} T_0. \tag{4.110}$$

We notice that the cell problem (4.103)–(4.105) is similar to that studied in Chapter 3, however this time we have a non-zero right-hand side of the boundary condition between the particle and the gas-filled void.

Second-order problem

Finally, we combine (4.65), (4.73) and (4.80) along with the periodicity of T_2 to obtain the second-order problem, given by

$$\begin{aligned} \nabla_{\mathbf{y}} \cdot (k_0(\nabla_{\mathbf{y}} T_2 + \nabla_{\mathbf{x}} T_1) + k_1(\nabla_{\mathbf{y}} T_1 + \nabla_{\mathbf{x}} T_0) \\ + \nabla_{\mathbf{x}} \cdot (k_0(\nabla_{\mathbf{y}} T_1 + \nabla_{\mathbf{x}} T_0)) = 0, \end{aligned} \qquad \mathbf{x} \in \omega^S, \tag{4.111}$$

$$\begin{aligned} -[k_0(\nabla_{\mathbf{y}} T_2 + \nabla_{\mathbf{x}} T_1) + k_1(\nabla_{\mathbf{y}} T_1 + \nabla_{\mathbf{x}} T_0)] \cdot \mathbf{n} \\ -(\mathbf{y} - \mathbf{b}) \cdot \nabla_{\mathbf{x}} (k_0(\nabla_{\mathbf{y}} T_1 + \nabla_{\mathbf{x}} T_0)) \cdot \mathbf{n} = \lambda G(\tau_2)(\mathbf{y}), \end{aligned} \qquad \mathbf{x} \in \Gamma, \tag{4.112}$$

$$T_2 \text{ periodic}, \qquad \mathbf{x} \in \partial\omega, \tag{4.113}$$

where τ_2 is given by (4.83). By the Fredholm alternative, we seek a solvability condition by integrating (4.111) over ω^S and applying the divergence theorem to obtain

$$\begin{aligned} \nabla_{\mathbf{x}} \cdot \left(\frac{1}{|\omega|} \int_{\omega^S} k_0(\nabla_{\mathbf{y}} T_1 + \nabla_{\mathbf{x}} T_0) \, \mathrm{d}\mathbf{y} \right) \\ + \frac{1}{|\omega|} \int_{\partial\omega^S} [k_0(\nabla_{\mathbf{y}} T_2 + \nabla_{\mathbf{x}} T_1) + k_1(\nabla_{\mathbf{y}} T_1 + \nabla_{\mathbf{x}} T_0)] \cdot \mathbf{n} \, \mathrm{d}S = 0. \end{aligned} \tag{4.114}$$

The boundary integral on the left-hand side of (4.114) can be written as the sum of the integral over Γ and the integral over $\partial\omega$, however the latter vanishes by periodicity of T_1 and T_2 and their normal derivatives. Therefore we focus on the integral over Γ. Using (4.112), we can write the boundary integral in (4.114) as

$$\begin{aligned} \int_\Gamma [k_0(\nabla_{\mathbf{y}} T_2 + \nabla_{\mathbf{x}} T_1) + k_1(\nabla_{\mathbf{y}} T_1 + \nabla_{\mathbf{x}} T_0)] \cdot \mathbf{n} \, \mathrm{d}S \\ = - \int_\Gamma \left[(\mathbf{y} - \mathbf{b}) \cdot \nabla_{\mathbf{x}} (k_0(\nabla_{\mathbf{y}} T_1 + \nabla_{\mathbf{x}} T_0) \cdot \mathbf{n}) + \lambda G(\tau_2)(\mathbf{y}) \right] \mathrm{d}S. \end{aligned} \tag{4.115}$$

Note that, from (4.53), we have

$$\int_\Gamma G(\tau_2)(\mathbf{y}) \mathrm{d}S = 0, \tag{4.116}$$

and from the first-order boundary condition (4.100), that

$$- \int_\Gamma (\mathbf{y} - \mathbf{b}) \cdot \nabla_{\mathbf{x}} (k_0(\nabla_{\mathbf{y}} T_1 + \nabla_{\mathbf{x}} T_0) \cdot \mathbf{n}) \, \mathrm{d}S = \nabla_{\mathbf{x}} \cdot \left(4\lambda (T_0 + \tau)^3 \int_\Gamma \mathbf{y} \, G(T_1 + \mathbf{y} \cdot \nabla_{\mathbf{x}} T_0)(\mathbf{y}) \, \mathrm{d}S \right). \tag{4.117}$$

Therefore, recalling (4.102), (4.114) becomes

$$\nabla_{\mathbf{x}} \cdot \left(\frac{1}{|\omega|} \int_{\omega^S} k_0 (\nabla_{\mathbf{y}} T_1 + \nabla_{\mathbf{x}} T_0) \, \mathrm{d}\mathbf{y} \right) + \nabla_{\mathbf{x}} \cdot \left(\frac{4\lambda (T_0 + \tau)^3}{|\omega|} \int_{\Gamma} \mathbf{y} \, G(T_1 + \mathbf{y} \cdot \nabla_{\mathbf{x}} T_0)(\mathbf{y}) \, \mathrm{d}S \right) = 0, \tag{4.118}$$

$$\nabla_{\mathbf{x}} \cdot \left(\frac{1}{|\omega|} \left[k_0 \int_{\omega^S} (\mathbf{I} + \nabla_{\mathbf{y}} \boldsymbol{\Psi}) \, \mathrm{d}\mathbf{y} + 4\lambda (T_0 + \tau)^3 \int_{\Gamma} \mathbf{y} G(\boldsymbol{\Psi} + \mathbf{y})(\mathbf{y}) \, \mathrm{d}S \right] \nabla_{\mathbf{x}} T_0 \right) = 0, \tag{4.119}$$

where

$$\left(\mathbf{y} G(\boldsymbol{\Psi} + \mathbf{y})(\mathbf{y}) \right)_{ij} = y_i G(\Psi_j + y_j)(\mathbf{y}), \tag{4.120}$$

$$= y_i \left(\Psi_j + y_j - \frac{1}{4\pi R^2} \int_{\Gamma} \Psi_j + y_j \, \mathrm{d}S \right). \tag{4.121}$$

Hence we arrive at the homogenised problem

$$\nabla_{\mathbf{x}} \cdot (\boldsymbol{k}_{\text{eff}} \nabla_{\mathbf{x}} T_0(\mathbf{x})) = 0, \qquad \mathbf{x} \in \Omega, \tag{4.122}$$

$$\nabla_{\mathbf{x}} T_0(\mathbf{x}) \cdot \mathbf{n} = 0, \qquad \mathbf{x} \in \partial\Omega_N, \tag{4.123}$$

$$T_0(\mathbf{x}) = T_D(\mathbf{x}), \qquad \mathbf{x} \in \partial\Omega_D, \tag{4.124}$$

where

$$\boldsymbol{k}_{\text{eff}} = \frac{1}{|\omega|} \left(k(T_0) \int_{\omega^S} (\mathbf{I} + \nabla_{\mathbf{y}} \boldsymbol{\Psi}) \, \mathrm{d}\mathbf{y} + 4\lambda (T_0 + \tau)^3 \int_{\Gamma} \mathbf{y} G(\boldsymbol{\Psi} + \mathbf{y})(\mathbf{y}) \, \mathrm{d}S \right), \tag{4.125}$$

and

$$G(f(\mathbf{x}, \mathbf{y}))(\mathbf{y}) = f(\mathbf{x}, \mathbf{y}) - \frac{1}{4\pi R^2} \int_{\Gamma} f(\mathbf{x}, \mathbf{z}) \, \mathrm{d}S, \tag{4.126}$$

and $\boldsymbol{\Psi}$ satisfies the cell problem (4.103)–(4.105).

4.4 Numerical results

As with the electrical and thermal conduction models in Chapter 3, our goal is to demonstrate the efficiency and accuracy of the homogenisation method using a two-dimensional example. We will validate it by comparing the homogenised solution with the numerical solution of the exact model (4.45)–(4.48) for a range of δ to illustrate convergence, whilst also comparing the computational cost of the two methods.

We solve the homogenised problem (4.122)–(4.124) in the domain $\Omega = [1.0, 1.0]$ where the Dirichlet boundary is given by $\partial\Omega_D = \partial\Omega_D^T \cup \partial\Omega_D^B$ for

$$\partial\Omega_D^T = \{(x, y) \in \partial\Omega : y = 1\}, \qquad \partial\Omega_D^B = \{(x, y) \in \partial\Omega : y = 0\}, \tag{4.127}$$

on which we define

$$T_D(\mathbf{x}) = \begin{cases} 1, & \mathbf{x} \in \partial\Omega_D^T, \\ 0, & \mathbf{x} \in \partial\Omega_D^B. \end{cases} \tag{4.128}$$

The remainder of the boundary is denoted $\partial\Omega_N$ where zero-flux conditions are enforced.

For the direct solution to (4.45)–(4.48), we consider a solid matrix Ω^S perforated with i circular voids with boundaries Γ_i and apply the same external boundary conditions (4.128) as the homogenised model.

For simplicity, we consider a constant thermal conductivity $k = 1$ and a void radius $R = 0.1$. We recall that our analysis was conducted as $\delta \to 0$ with $\lambda = O(1)$, therefore we solve the models for $\lambda = 1$. Note that for a two-dimensional disk D of radius R, the view factor between $\mathbf{x}$ and $\mathbf{z}$ on ∂D is

$$F(\mathbf{x}, \mathbf{z}) = \frac{1}{2\pi R}, \tag{4.129}$$

which replaces the spherical view-factor $1/4\pi R^2$ for the purpose of the numerical analysis.

Homogenisation algorithm

A critical difference between this homogenisation model and those discussed in Chapter 3 is the dependence of the cell solution $\boldsymbol{\Psi}$ on the homogenised temperature T_0, indicated by the presence of T_0 in the cell problem boundary condition (4.104). We must therefore adapt our homogenisation procedure. We propose the following algorithm for solving the homogenised problem:

1. solve the cell problem (4.103)–(4.105) for a variety of T_0;
2. calculate the effective conductivity tensor $\boldsymbol{k}_{\text{eff}}$ (4.125) for each value of T_0;
3. interpolate the effective conductivity values by a cubic spline to obtain an estimation of function $\boldsymbol{k}_{\text{eff}}(T_0)$ valid for every T_0 within a given range;
4. solve the (nonlinear) homogenised problem (4.122)–(4.124) with effective conductivity function $\boldsymbol{k}_{\text{eff}}(T_0)$ for homogenised temperature T_0.

We solve the cell, homogenised and direct problems using piecewise quadratic finite elements in `Firedrake` [80] on a mesh of triangles. We use the `Scipy` [53] package `interpolate` to fit the spline to the calculated values of $\boldsymbol{k}_{\text{eff}}$.

Results

There is significant numerical complexity associated with solving the nonlinear condition (4.46) on the void boundary, thus considering large numbers of such voids renders the direct solution infeasible if δ is very small. Therefore we include results for only $\delta = 1.0, 0.5, 0.25$ to demonstrate convergence of the homogenised solution to the direct solution and the computational superiority of the former.

By interpolating the homogenised solution onto the heterogeneous domain Ω^S, we calculate the L^2-error in Ω^S between the homogenised and direct solutions, which we plot against δ in Figure 4.4a. We see that the error decreases approximately as $O(\delta)$ as expected, indicating that as δ decreases, the homogenised solution accurately approximates the "true" solution and can thereby be used to estimate the behaviour of thermal conduction in a solid domain perforated with periodically distributed gas-filled voids. In Figure 4.4b, we plot the computational time of solving the problem directly for δ and see that, in the best case, the computational time scales like $O(\delta^{-2})$.

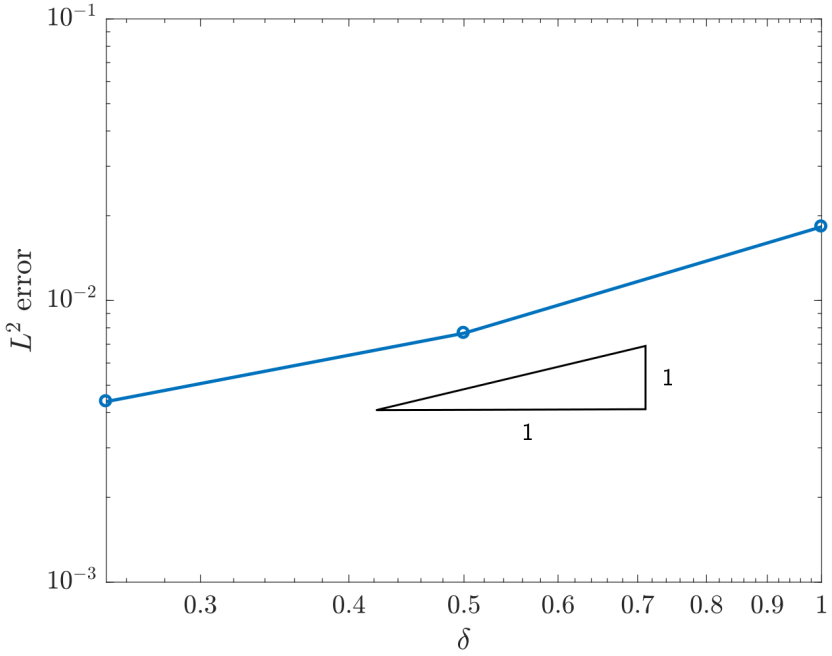
Effective conductivity with temperature

We are interested in how the void radius R affects the effective conductivity tensor $\boldsymbol{k}_{\text{eff}}$. Similar to the discussion in Chapter 3, the symmetry of the unit cell ω means that $\boldsymbol{k}_{\text{eff}}$ is a scalar multiple of the identity matrix, namely

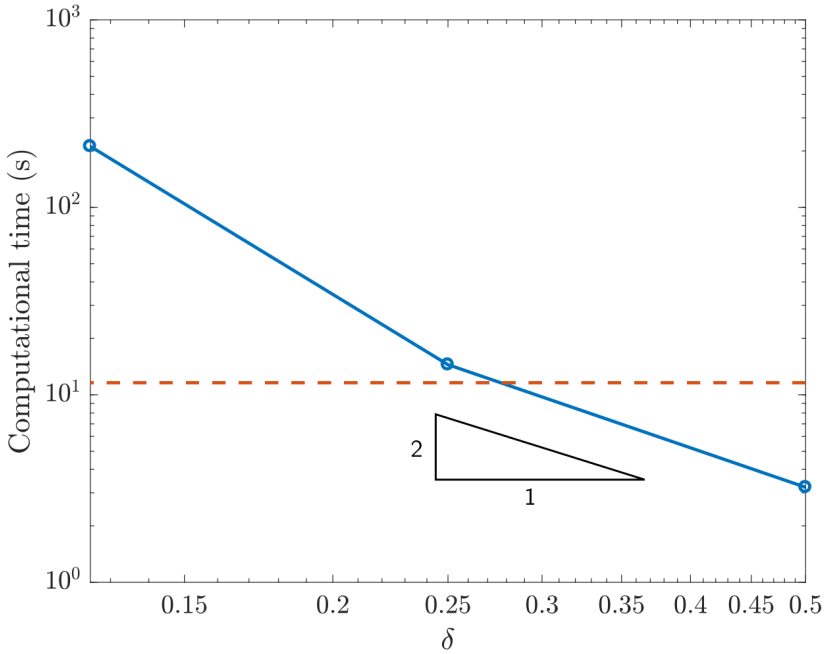
$$\boldsymbol{k}_{\text{eff}} = k_{\text{eff}}\,\mathbf{I}. \tag{4.130}$$

We repeat steps 1–3 of the homogenisation algorithm above for different R and plot the corresponding effective conductivity scalar multiple k_{eff} against T_0 in Figure 4.5b. Although the trend exhibited for each radius is similar, as observed by comparing Figure 4.5a to the purple, dash-dot line for $R = 0.4$ in Figure 4.5b, we notice a significant difference in the magnitude of the effective conductivity. In particular, for $T_0 \in [0, 4]$, the conductivity for $R = 0.1$ ranges from 0.98 to 1.09, as depicted in Figure 4.5a, whereas the conductivity for $R = 0.4$ ranges from 1.02 to 6.10.

We conjecture that this behaviour can be understood by considering the form of the effective conductivity (4.125). The larger the void, the greater the influence of radiative transfer, or rather, the greater the contribution of the integral over the void boundary Γ, which is multiplied by T_0^3. Therefore, for larger radii, the temperature dependence is more prominent and has a greater impact on the effective conductivity $\boldsymbol{k}_{\text{eff}}$.

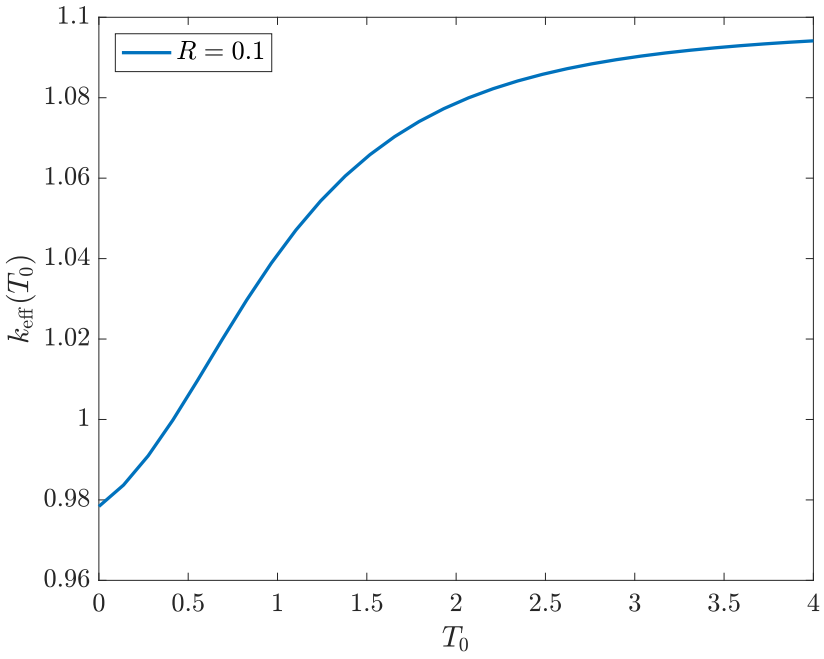


(a) L^2-error between homogenised solutions and direct solution for different values of δ.

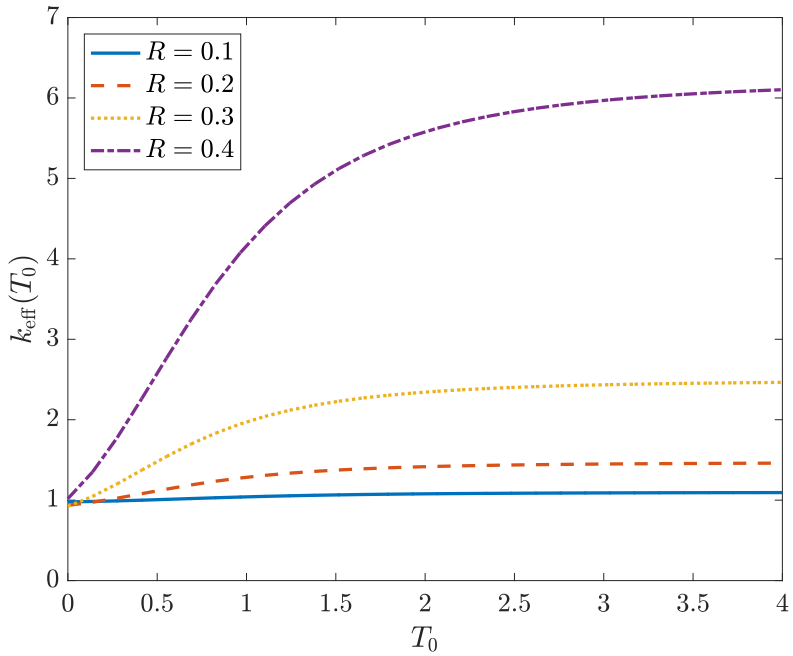


(b) Computational time of solving the problem directly (blue solid line) with δ, along with the time to solve homogenisation problem, namely 11.8 s (dashed orange line).

Figure 4.4: L^2-error and computational time associated with the direct and homogenised solutions.



(a) Void radius $R = 0.1$.



(b) Void radii $R = 0.1$, 0.2, 0.3 and 0.4.

Figure 4.5: Relationship between scalar effective conductivity k_{eff} and homogenised temperature T_0 for different void radii.

For every void-size, we observe saturation in the effective conductivity at high temperatures, behaviour that is attributed partly to the solid material. As the temperature gets very large, the radiative condition means that the voids act as perfect conductors, thus the solid is the rate-limiting factor. Similar observations were reported by Kiradjiev [55] for the case of very small voids solved using Maxwell-type models. Therefore, due to the geometry, radiation does not dominate over conduction for high temperatures.

4.5 Coupling with the electrical problem

We consider the non-dimensional steady-state coupled electrothermal problem with radiative heating,

$$\nabla \cdot (\sigma(T)\nabla\phi(\mathbf{x})) = 0, \quad \mathbf{x} \in \Omega^S, \tag{4.131}$$

$$\nabla \cdot (k(T)\nabla T(\mathbf{x})) + \sigma(T)\nabla\phi(\mathbf{x}) \cdot \nabla\phi(\mathbf{x}) = 0, \quad \mathbf{x} \in \Omega^S, \tag{4.132}$$

$$\nabla\phi(\mathbf{x}) \cdot \mathbf{n} = 0, \quad \mathbf{x} \in \Gamma_i \, \forall i, \tag{4.133}$$

$$-k(T)\nabla T(\mathbf{x}) \cdot \mathbf{n} = \frac{\lambda}{\delta} G_i((T(\mathbf{x}) + \tau)^4)(\mathbf{x}), \quad \mathbf{x} \in \Gamma_i \, \forall i, \tag{4.134}$$

$$T(\mathbf{x}) = 0, \quad \phi(\mathbf{x}) = 1, \quad \mathbf{x} \in \partial\Omega_D^T, \tag{4.135}$$

$$T(\mathbf{x}) = 0, \quad \phi(\mathbf{x}) = 0, \quad \mathbf{x} \in \partial\Omega_D^B, \tag{4.136}$$

$$\nabla\phi(\mathbf{x}) \cdot \mathbf{n} = \nabla T(\mathbf{x}) \cdot \mathbf{n} = 0, \quad \mathbf{x} \in \partial\Omega_N. \tag{4.137}$$

Following the analysis outlined above and in Chapter 3, the coupled homogenisation problem is written as

$$\nabla_{\mathbf{x}} \cdot (\boldsymbol{\sigma}_{\text{eff}} \nabla_{\mathbf{x}} \phi_0(\mathbf{x})) = 0, \qquad \mathbf{x} \in \Omega, \tag{4.138}$$

$$\nabla_{\mathbf{x}} \cdot (\boldsymbol{k}_{\text{eff}} \nabla_{\mathbf{x}} T_0(\mathbf{x})) + q_{\text{eff}} = 0, \qquad \mathbf{x} \in \Omega, \tag{4.139}$$

$$T_0(\mathbf{x}) = 0, \quad \phi_0(\mathbf{x}) = 0, \qquad \mathbf{x} \in \partial\Omega_D^T, \tag{4.140}$$

$$T_0(\mathbf{x}) = 0, \quad \phi_0(\mathbf{x}) = 0, \qquad \mathbf{x} \in \partial\Omega_D^B, \tag{4.141}$$

$$\nabla_{\mathbf{x}}\phi_0(\mathbf{x}) \cdot \mathbf{n} = \nabla_{\mathbf{x}} T_0(\mathbf{x}) \cdot \mathbf{n} = 0, \qquad \mathbf{x} \in \partial\Omega_N, \tag{4.142}$$

where

$$\boldsymbol{\sigma}_{\text{eff}} = \frac{\sigma(T_0)}{|\omega|} \int_{\omega^S} (\mathbf{I} + \nabla_{\mathbf{y}} \boldsymbol{\Phi}) \, \mathrm{d}\mathbf{y}, \tag{4.143}$$

$$q_{\text{eff}} = \nabla_{\mathbf{x}}\phi_0 \cdot \boldsymbol{\sigma}_{\text{eff}} \nabla_{\mathbf{x}}\phi_0, \tag{4.144}$$

$$\boldsymbol{k}_{\text{eff}} = \frac{1}{|\omega|} \left(k(T_0) \int_{\omega^S} (\mathbf{I} + \nabla_{\mathbf{y}} \boldsymbol{\Psi}) \, \mathrm{d}\mathbf{y} + 4\lambda(T_0 + \tau)^3 \int_{\Gamma} \mathbf{y} G(\boldsymbol{\Psi} + \mathbf{y})(\mathbf{y}) \, \mathrm{d}S \right), \tag{4.145}$$

for $\boldsymbol{\Phi}$ and $\boldsymbol{\Psi}$ solutions to the cell problems

$$\nabla_{\mathbf{y}}^2 \boldsymbol{\Phi} = 0, \qquad \mathbf{y} \in \omega^S, \tag{4.146}$$

$$(\nabla_{\mathbf{y}} \boldsymbol{\Phi} + \mathbf{I}) \cdot \mathbf{n} = 0, \qquad \mathbf{y} \in \Gamma, \tag{4.147}$$

$$\boldsymbol{\Phi} \text{ periodic}, \qquad \mathbf{y} \in \partial\omega, \tag{4.148}$$

$$\nabla_{\mathbf{y}}^2 \boldsymbol{\Psi} = 0, \qquad \mathbf{y} \in \omega^S, \tag{4.149}$$

$$-k_0(\nabla_{\mathbf{y}} \boldsymbol{\Psi} + \mathbf{I}) \cdot \mathbf{n} = 4\lambda(T_0 + \tau)^3 G(\boldsymbol{\Psi} + \mathbf{y})(\mathbf{y}), \qquad \mathbf{y} \in \Gamma, \tag{4.150}$$

$$\boldsymbol{\Psi} \text{ periodic}, \qquad \mathbf{y} \in \partial\omega, \tag{4.151}$$

and $G(\cdot)(\mathbf{y})$ is given by

$$G(f(\mathbf{x}, \mathbf{y}))(\mathbf{y}) = f(\mathbf{x}, \mathbf{y}) - \frac{1}{4\pi R^2} \int_\Gamma f(\mathbf{x}, \mathbf{z}) \, \mathrm{d}S. \tag{4.152}$$

By comparing the steady-state conductive-only electrothermal problem (3.57)–(3.61) with the steady-state conductive-radiative electrothermal problem (4.131)–(4.136) for spatially-independent $k = k(T)$, $\sigma = \sigma(T)$, we notice that the homogenised problems (3.100)–(3.103) and (4.138)–(4.141) are identical, the only difference lying within the effective thermal conductivities.

4.6 Discussion

In this chapter, we explored the influence of radiative effects on the thermal transfer within a solid matrix with gaseous perforations or voids. The presence of a nonlinear, integral boundary condition in the governing equations posed a computational complication, however with careful consideration of the multiple scales methodology, we extended the standard homogenisation technique to include the nonlocal condition. From this, we derived a homogenised model and effective thermal conductivity tensor. We compared the homogenised solution to that obtained directly and observed that the approximation error of the former decreases with microstructure period δ, thereby verifying that our homogenisation model can accurately approximate conductive-radiative transfer within the domain. By noting the computational costs for each of the solutions, we conclude that as the number of voids increases, obtaining a solution by direct solve becomes intractable and, in fact, the homogenised solution is a very good approximation for the solution.

Interestingly, the conduction-radiation effective conductivity tensor is very similar to that corresponding to the conduction-only problem, namely the former is the latter

plus a radiative term. The separation of the two thermal contributions within (4.145) allows us to qualitatively understand their respective effects. It is clear from the presence of the third power of homogenised temperature T_0 in the radiative term of (4.145) that as T_0 increases, radiation plays a larger role in determining the effective conductivity, however we deduced numerically that the conductivity saturates for large temperatures, therefore the radiation does not dominate over conduction, rather the conducting solid is the limiting factor.

Chapter 5

Steady current conduction through small contact points

The efficiency of the heat treatment of carbon is critically dependent on electric current propagation through the granular material. Electric current conduction is itself governed by the electrical resistance of the system, in particular, the bulk resistivity of the material. We understand the bulk resistivity of the coke bed to be the overall resistivity of the collection of particles as a whole and to depend on both the resistivity of the particulate material as well as the contact resistance between particles. Due to the emphasis on the importance of contact resistance in the literature [28, 32, 34, 46], we turn now to the study of electric current conduction due to varying properties of the contacts between particles.

As discussed by Holm [46], we consider contact resistance to comprise constriction resistance and a resistance due to imperfect contacts, termed asperity resistance and oxide-layer resistance. In our analysis thus far, we have included perfect particle contacts that are of a similar order of magnitude to the size of the particle itself, thereby underestimating the constriction resistance and neglecting oxide-layer resistance entirely. However from the literature [39, 46, 103], we know that in reality the contacts are rough and imperfect and results following CT scans presented in this chapter indicate that the particle contacts are significantly smaller than the size of the particle itself. To correctly capture the current conduction throughout a granular material, we must incorporate such effects into our mathematical model.

In this chapter, we focus on the latter extension, that is, the effect of having small (but perfect) particle contacts. We wish to understand the impact of such small contacts on the behaviour of the electric potential with the goal of quantifying the importance of constriction resistance within the full system.

This chapter is structured as follows: to motivate our interest in small contacts, we first consider a CT scan analysis of a collection of anthracite particles. The scans demonstrate the minuteness of particle contacts in contrast with particle size whilst also highlighting the limited number of contacts per particle. We then consider steady current conduction throughout idealised repeating geometries in two and three dimensions with very small contacts, with the goal of analytically determining a relationship between the electric potential and the size of the particle contact. We begin by studying current conduction within an infinite two-dimensional strip with contacts centred on each boundary and through the use of complex analysis techniques, we obtain an explicit solution for the electric potential $\phi(\mathbf{x})$ within the strip. As an explicit solution is not always possible for more complicated domains, we then solve the same problem via the method of matched asymptotics to demonstrate that both approaches yield the same answer. Following this validation, we extend our analysis to three-dimensional domains. We solve the steady-current conduction problem within a unit cube with circular contact areas on its boundary surface. In both the two- and three-dimensional cases, we obtain a relationship between total current J passing through the contact and the size ϵ of the contact. This allows us to deduce how the electric potential behaves as we move away from the contacts; the variations in electric potential far from the contacts become negligible compared with those close to the contacts. Finally, we show that the solution obtained via matched asymptotics can be used to correctly approximate the solution to the homogenisation cell problem, defined in Chapter 3, therefore allowing us to extend our conclusions about the effect of constriction resistance to our mathematical model for current conduction throughout granular material.

5.1 CT scan of anthracite particles

In order to gain some insight into how particles make contact with one another inside the calciner, we collected a sample of calcined anthracite in a cylindrical container of height 30 mm and diameter 25 mm. Using a CT scanner, we obtained various cross-sectional images [93] of the sample, known henceforth as "slices", taken at 0.025 mm intervals. The sample was imaged from above and also from the side, therefore in theory these slices should allow us to observe how particles are interacting with each other at nearly every point within the sample. A schematic illustrating these slices is presented in Figure 5.1 and an example of the CT images is displayed in Figure 5.2.

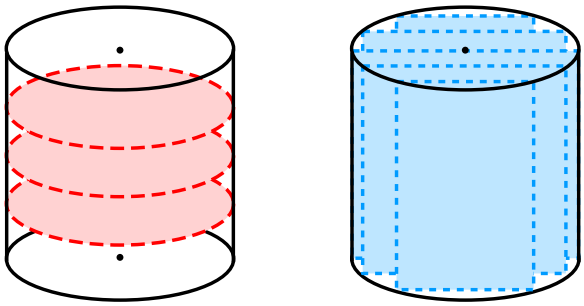


Figure 5.1: Schematic of the CT images of the sample as viewed from above (left) and from the side (right).

We are particularly interested in the size of the contacts, but also the number of contacts per particle and their nature. For example, we might expect to see many point-to-plane contacts, that is when a sharp asperity of one particle touches a planar face of another particle. We may also observe edge-to-plane contacts, or perhaps edge-to-edge contacts. These properties will have significant impact on the electrical contact resistance and hence the bulk resistivity of the sample.

When studying the CT scans, we notice that there seem to be very few visible contacts per image. When considering a single slice, some particles appear to be surrounded entirely by free space, making no contacts with the surrounding particles. Of course, the particle is making contact with its neighbours but such contacts are

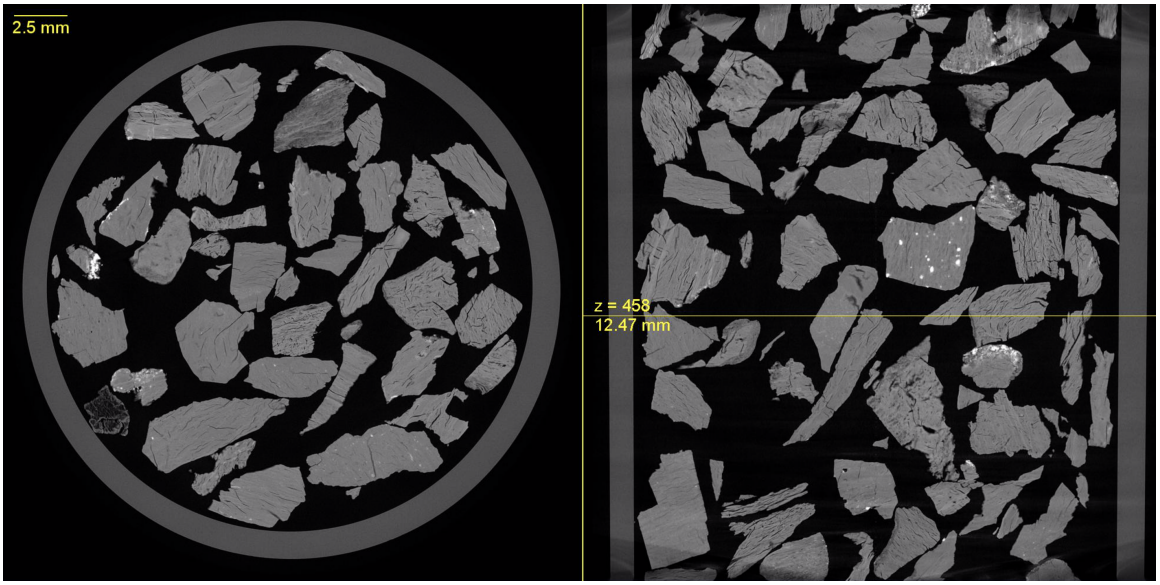


Figure 5.2: CT scans of anthracite particles using data from [93]. The left image is a cross-sectional top-view at a height of 12.47 mm above the bottom of the cylinder, as indicated by the right image, which is a cross-sectional side-view of the sample.

present on different planes to the one we are considering. This implies that each particle makes very few contacts with its neighbours. Thus we estimate the number of contacts a particle makes with its neighbours to be around four to five. We also notice that the angular, irregular nature of the particles means that most of the visible contacts are due to the corners or points of the particles. As a consequence, the contact area is very small and the total contact area per particle is significantly smaller than the particle itself. By studying the CT scans, we estimate that a contact is approximately 100 times smaller than the size of the particle.

In conclusion, although informative in a qualitative sense, the CT images do not allow us to draw quantitative conclusions on how current might propagate through a two-dimensional domain. The contacts between particles in the images are not well defined and therefore we cannot expect current to behave in a matter that approximates true current conduction. However, we conclude that since each particle shares very few contacts with its neighbours and the contacts themselves are microscopic compared with the size of the particle, we expect large current densities near to the contacts, hence resulting in a large constriction resistance, as observed in the literature. We are therefore motivated to mathematically explore the behaviour of electric potential close to such small contacts.

5.2 Explicit solution in two dimensions

In order to analyse the effect of small particle contacts on the behaviour of current conduction, we begin by considering a simple two-dimensional example. We wish to study steady current conduction throughout a representative particle, where the current enters through a small contact and exits through another. We approximate a particle as an infinite, two-dimensional strip of width 2δ and apply mixed Dirichlet-Neumann boundary conditions. We enforce that the Dirichlet portions are centred at $x = 0$ for $y = \pm\delta$ and are of width $\epsilon\delta$ where $\epsilon \ll 1$, thus representing the small particle contacts. Upon the remaining portion, we enforce zero-flux conditions to represent the boundary between the conducting solid particle and the insulating gas-filled void. We choose this domain for analytical ease, in particular an infinite strip is more easily dealt with using complex analysis than a finite domain. We consider $\epsilon \ll 1$ as this allows us to capture the effects of a contact that is very small in comparison with the particle.

Scaling the spatial variable by δ, we consider the strip in Figure 5.3. We study steady current conduction with a uniform conductivity $\sigma = 1$ throughout the domain.

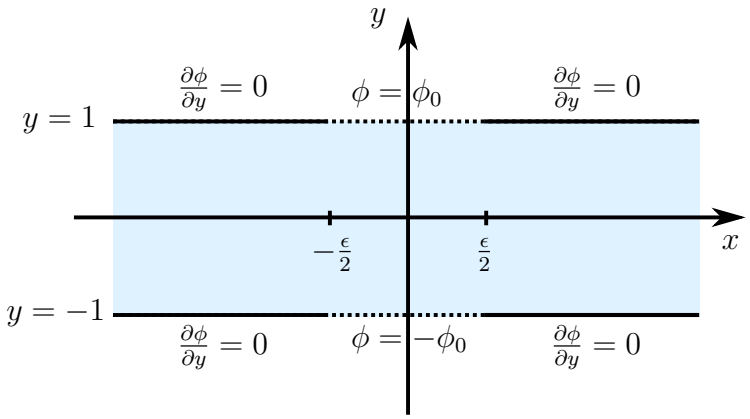


Figure 5.3: Schematic of infinite strip in which we solve (5.1)–(5.4).

Therefore the problem is

$$\nabla^2\phi = 0, \qquad -1 \leq y \leq 1, \tag{5.1}$$

$$\phi = \phi_0, \qquad |x| \leq \epsilon/2,\ y = 1, \tag{5.2}$$

$$\phi = -\phi_0, \quad |x| \leq \epsilon/2,\ y = -1, \tag{5.3}$$

$$\nabla\phi \cdot \mathbf{n} = 0 \qquad |x| \geq \epsilon/2,\ y = \pm 1, \tag{5.4}$$

where ϕ_0 is a prescribed, uniform voltage and $\mathbf{n}$ is the outwards unit normal to the domain. We note that we could have scaled ϕ by ϕ_0 so that this parameter no longer appears in the problem, however we choose to retain this throughout our analysis as it helps to understand the final (dimensional) relationship. We note the mixed boundary conditions result in singularities at $(\pm\epsilon/2, \pm 1)$. We use complex analysis and the notion of conformal maps to analyse the problem.

Complex analysis

Complex analysis provides a powerful method for solving two-dimensional Laplace problems due to the connection between complex functions and harmonic functions. A harmonic function, i.e. a solution to the Laplace equation, can be written as the real part of a holomorphic function. In other words it can be represented by convergent power series and hence is infinitely differentiable.

As an overview, we use complex analysis to rewrite the problem in terms of a complex potential $w(z)$ and in particular consider the hodograph variable $w'(z)$ associated with the problem [21]. We then use conformal maps to obtain a relationship between the hodograph variable and the complex spatial variable z, from which we can obtain the complex potential and hence the electric potential, defined as the real part of $w(z)$.

We can consider every point (x, y) in a two-dimensional domain in terms of the complex variable $z = x + \mathrm{i}y$. Since $\phi(z)$ is a harmonic function and the infinite strip is simply connected, there exists a harmonic function $\psi(z)$ such that

$$w(z) = \phi(z) + \mathrm{i}\psi(z) \tag{5.5}$$

is holomorphic [16]. We will refer to $\psi(z)$ as the stream function and $w(z)$ as the complex potential. The goal is to find an expression for the complex potential $w(z)$ in terms of complex variable z from which we can deduce ϕ by taking the real part of w. In order to find an expression for $w(z)$, we must first understand how the stream function $\psi(z)$ behaves within the strip.

The potential and stream function ϕ and ψ are harmonic conjugates and satisfy the Cauchy–Riemann equations,

$$\frac{\partial \phi}{\partial x} = \frac{\partial \psi}{\partial y}, \qquad \frac{\partial \phi}{\partial y} = -\frac{\partial \psi}{\partial x}. \tag{5.6}$$

Using these equations, we can write the steady current conduction equation (5.1) in terms of ψ, namely

$$\nabla^2 \psi = 0, \quad -1 \leq y \leq 1. \tag{5.7}$$

Similarly, we can convert the zero-flux condition for ϕ (5.4) into a condition for ψ. Along the Neumann boundary portion $\{(x, y) : |x| \geq \epsilon/2, y = \pm 1\}$,

$$\nabla \phi(x, \pm 1) \cdot \mathbf{n} = \frac{\partial \phi}{\partial y}(x, \pm 1) = 0, \quad \Rightarrow \quad \frac{\partial \psi}{\partial x}(x, \pm 1) = 0 \tag{5.8}$$

$$\Rightarrow \quad \psi(x, \pm 1) = \text{constant}. \tag{5.9}$$

At this point it is helpful to note the symmetries of the problem: ϕ is even in x and odd in y, hence

$$\frac{\partial \phi}{\partial x} = \frac{\partial \psi}{\partial y} \text{ odd in } x \text{ and } y, \tag{5.10}$$

$$-\frac{\partial \phi}{\partial y} = \frac{\partial \psi}{\partial x} \text{ even in } x \text{ and } y. \tag{5.11}$$

Taking $\psi(0, y) = 0$ along with (5.10)–(5.11), we deduce that ψ is odd in x and even in y. In summary, for $|x| \geq \epsilon/2$,

$$\psi(x, 1) = -\psi(-x, 1), \qquad \psi(x, 1) = \psi(x, -1). \tag{5.12}$$

To find the constant value that ψ takes along each Neumann boundary portion, (reminder, we label this the Neumann portion due to the original problem for ϕ

(5.1)–(5.4)), consider the total current J through the particle contact. Recall that the total current through a surface S is

$$J = \int_S \mathbf{j} \cdot \mathbf{n} \, \mathrm{d}S, \tag{5.13}$$

where $\mathbf{j}$ is the current density given by $\mathbf{j} = \sigma \mathbf{E} = -\sigma \nabla \phi$, and $\mathbf{n}$ is the unit normal vector to the surface. Since we assume constant conductivity $\sigma = 1$ within the strip, the total current passing through the top contact into the strip is given by

$$J = -\int_{-\epsilon/2}^{\epsilon/2} \nabla \phi \cdot \mathbf{n}|_{y=1} \, \mathrm{d}x, \tag{5.14}$$

where we take $\mathbf{n} = (0, -1)^T$. Therefore, recalling the Cauchy–Riemann equations (5.6) and symmetries (5.12), the total current through the top contact is

$$\begin{aligned} J &= -\int_{-\epsilon/2}^{\epsilon/2} \left(-\frac{\partial \phi}{\partial y} \right) \Big|_{y=1} \mathrm{d}x, && (5.15) \\ &= -\int_{-\epsilon/2}^{\epsilon/2} \frac{\partial \psi}{\partial x} \Big|_{y=1} \mathrm{d}x, && (5.16) \\ &= -[\psi(\epsilon/2, 1) - \psi(-\epsilon/2, 1)], && (5.17) \\ &= -2\psi(\epsilon/2, 1), && (5.18) \end{aligned}$$

hence, given that ψ is constant on the boundary $|x| \geq \epsilon/2$, along with the fact that ψ is even in y and odd in x we deduce that

$$\psi(x, \pm 1) = \begin{cases} -\frac{J}{2}, & x \geq \epsilon/2, \\ \frac{J}{2}, & x \leq -\epsilon/2. \end{cases} \tag{5.19}$$

Along the Dirichlet portion of the strip, the potential ϕ is constant in x, therefore

$$\begin{aligned} \phi(x, \pm 1) = \pm \phi_0 \quad &\Rightarrow \quad \frac{\partial \phi}{\partial x}(x, \pm 1) = 0, && (5.20) \\ &\Rightarrow \quad \frac{\partial \psi}{\partial y}(x, \pm 1) = 0. && (5.21) \end{aligned}$$

We have deduced how ψ behaves within the strip (5.7) and defined the appropriate boundary conditions (5.19) and (5.21).

Finally, to simplify the problem further, we exploit the symmetries of the problem to consider only one quadrant of the domain. Without loss of generality, we choose the upper-right quadrant, along with the added boundary conditions deduced from the symmetry properties of ϕ and ψ,

$$\begin{aligned} \phi(x, 0) = 0, \quad \frac{\partial \psi}{\partial y}(x, 0) &= 0, \qquad x > 0, && (5.22) \\ \frac{\partial \phi}{\partial x}(0, y) = 0, \qquad \psi(0, y) &= 0, \qquad 0 < y < 1. && (5.23) \end{aligned}$$

Note that (5.23) comes from the fact $\partial\psi/\partial y(0,y) = 0 \Rightarrow \psi(0,y) = 0$, chosen so that ψ is odd in x.

Therefore we are interested in solving the following problems:

$$\nabla^2\phi = 0, \qquad \nabla^2\psi = 0, \qquad x \geq 0,\ 0 \leq y \leq 1, \tag{5.24}$$

$$\phi = \phi_0, \qquad \frac{\partial\psi}{\partial y} = 0, \qquad |x| \leq \epsilon/2,\ y = 1, \tag{5.25}$$

$$\phi = 0, \qquad \frac{\partial\psi}{\partial y} = 0, \qquad y = 0, \tag{5.26}$$

$$\frac{\partial\phi}{\partial y} = 0, \qquad \psi = -\frac{J}{2}, \qquad x \geq \epsilon/2,\ y = 1, \tag{5.27}$$

$$\frac{\partial\phi}{\partial x} = 0, \qquad \psi = 0, \qquad x = 0. \tag{5.28}$$

We now have a problem for the complex potential $w(z) = \phi + \mathrm{i}\psi$ within the complex plane z. From (5.24)–(5.28) we can define $\partial\phi/\partial x$ or $\partial\phi/\partial y$ on every boundary, therefore we proceed by considering the hodograph variable $w'(z)$ and look for a conformal mapping between w' and z.

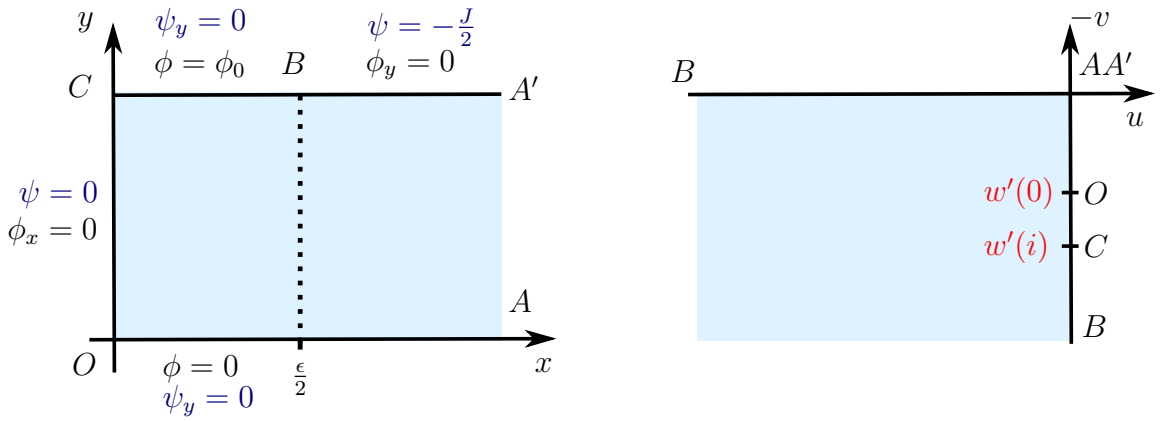
Conformal mapping of the hodograph and spatial variables

A conformal map is a function that preserves angles locally [16] and is useful for transforming inconvenient geometries into more desirable ones. Since we understand the behaviour of $\partial\phi/\partial x$ and $\partial\phi/\partial y$ along each boundary in the complex plane z, presented in Figure 5.4a, we consider the derivative of the complex potential, namely, the hodograph variable, given by

$$w'(z) = \frac{\partial\phi}{\partial x} - \mathrm{i}\frac{\partial\phi}{\partial y} = u(z) - \mathrm{i}v(z), \tag{5.29}$$

which is depicted in Figure 5.4b. We note that the hodograph variable satisfies $\mathrm{Re}(w') \leq 0$ and $\mathrm{Im}(w') \leq 0$ due to the maximum principle of Laplace's equation; the maximum value $\phi(x,y) = \phi_0$ is given by boundary condition (5.25) and allows us to deduce that $\phi_x \leq 0$ and $\phi_y \geq 0$.

By finding a conformal map between the two planes, we can obtain a relationship between the hodograph variable w' and the physical variable z, therefore we can integrate to find an expression for the complex potential $w(z)$. We can do this by mapping both the complex plane z and the hodograph plane w' to the upper half plane and finding the Möbius transformation to relate them.



(a) Physical plane, $z = x + \mathrm{i}y$.

(b) Hodograph plane, $w'(z) = u - \mathrm{i}v$.

Figure 5.4: Schematic of the physical and hodograph planes between which we obtain a conformal mapping.

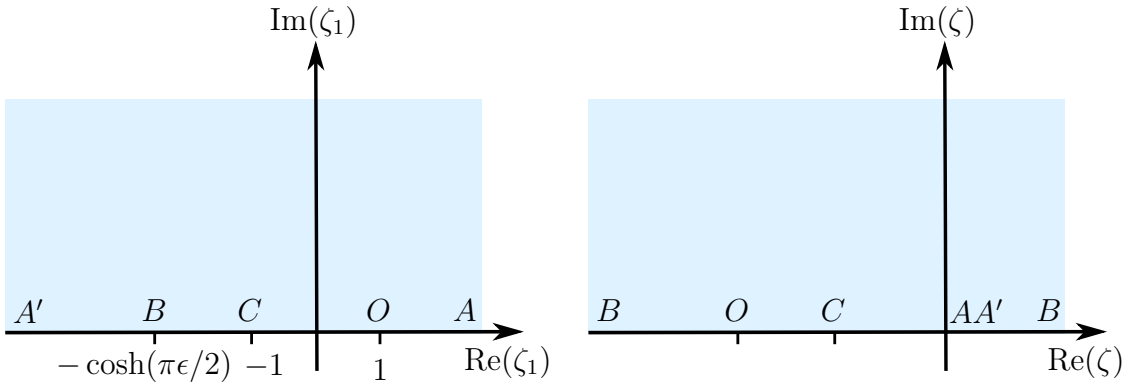
We consider a conformal map from the physical plane to the upper half plane using hyperbolic function $\cosh(\cdot)$, chosen suitably for the angle-opening property of the exponential function. Hence, we define

$$\zeta_1 = \cosh(\pi z). \tag{5.30}$$

We map the hodograph plane to the upper half plane using the transformation

$$\zeta = (w')^2. \tag{5.31}$$

The half planes ζ_1 and ζ are depicted in Figure 5.5. To obtain a correspondence



(a) $\zeta_1 = \cosh(\pi z)$.

(b) $\zeta = (w')^2$.

Figure 5.5: Half-planes obtained by applying the conformal mappings (5.30) and (5.31) to the physical and hodograph planes respectively.

between ζ_1 and ζ, we apply the Möbius transformation

$$\zeta = \frac{-\alpha^2}{\zeta_1 + \cosh(\pi\epsilon/2)}, \tag{5.32}$$

$$(w')^2 = \frac{-\alpha^2}{\cosh(\pi z) + \cosh(\pi\epsilon/2)}, \tag{5.33}$$

where α is some real, positive constant to be determined. Equation (5.33) relates w' to z, as desired. To find w' in terms of z, we take the square root of (5.33) and get

$$w' = \frac{\mathrm{i}\alpha}{\sqrt{\cosh(\pi z) + \cosh(\pi\epsilon/2)}}. \tag{5.34}$$

Note, we must carefully consider which branch of the square root is appropriate. Approximating $\cosh(\pi\epsilon/2) = 1$ for $\epsilon \ll 1$, we identify branch points of $\sqrt{\cosh(\pi z) + 1}$ at $z = n\mathrm{i}$, for n odd and non-zero. As discussed previously, the hodograph variable satisfies

$$\mathrm{Re}(w') \leq 0, \qquad \mathrm{Im}(w') \leq 0, \tag{5.35}$$

in other words

$$-\pi \leq \arg(w') \leq -\frac{\pi}{2}. \tag{5.36}$$

We choose the branch cuts that restrict

$$0 \leq \arg\left(\sqrt{\cosh(\pi z) + \cosh(\pi\epsilon/2)}\right) \leq \frac{\pi}{2}, \tag{5.37}$$

to ensure that $\sqrt{\cosh(\pi z) + \cosh(\pi\epsilon/2)}$ always has positive real and imaginary parts and write (5.34) as

$$w' = \frac{-\mathrm{i}\alpha}{\sqrt{\cosh(\pi z) + \cosh(\pi\epsilon/2)}}, \tag{5.38}$$

where the minus sign in the numerator has been introduced to ensure negative imaginary and real parts of w'. We illustrate this by taking a particular point in z. With reference to the physical and hodograph planes of Figure 5.4, we know that $w'(0) = -\mathrm{i}\beta$ for some real $\beta > 0$. By approximating $\cosh(\pi\epsilon/2) \sim 1$, we have

$$w'(0) = \frac{-\mathrm{i}\alpha}{\sqrt{\cosh(0) + 1}}, \tag{5.39}$$

$$w'(0) = \frac{-\mathrm{i}\alpha}{\sqrt{2}}. \tag{5.40}$$

We can now integrate (5.38) and recall that $w(0) = 0$ to find the complex potential,

$$w(z) = -\int_0^z \frac{\mathrm{i}\alpha}{\sqrt{\cosh(\pi z') + \cosh(\pi\epsilon/2)}}\mathrm{d}z'. \tag{5.41}$$

The final step is to deduce the value of α. Using the boundary conditions (5.25) and (5.27) we are left to solve the following integral expressions,

$$\phi_0 = \int_0^{\mathrm{i}} \frac{-\mathrm{i}\alpha}{\sqrt{\cosh(\pi z') + \cosh(\pi\epsilon/2)}} \mathrm{d}z', \tag{5.42}$$

$$\phi_0 - \mathrm{i}\frac{J}{2} = \int_0^{\mathrm{i}+\epsilon/2} \frac{-\mathrm{i}\alpha}{\sqrt{\cosh(\pi z') + \cosh(\pi\epsilon/2)}} \mathrm{d}z'. \tag{5.43}$$

Using the path independence of complex integrals, we deduce that (5.42) and (5.43) imply

$$\frac{J}{2} = \int_{\mathrm{i}}^{\mathrm{i}+\epsilon/2} \frac{\alpha}{\sqrt{\cosh(\pi z') + \cosh(\pi\epsilon/2)}} \mathrm{d}z'. \tag{5.44}$$

The integral expressions (5.42) and (5.44) hold for all $\epsilon > 0$. To study the behaviour of the electric potential as the contact interfaces become increasingly small, we will now consider $\epsilon \to 0$.

Limiting behaviour of ϵ

First, consider (5.44). Enforcing the scaling $\epsilon\eta/2 = z - \mathrm{i}$, we obtain

$$\frac{J}{2\alpha} = \int_0^1 \frac{1}{\sqrt{-\cosh(\pi\epsilon\eta/2) + \cosh(\pi\epsilon/2)}} \frac{\epsilon}{2} \mathrm{d}\eta. \tag{5.45}$$

Since $\epsilon \ll 1$, we can asymptotically expand the terms in the denominator. Considering an $O(\epsilon^2)$ expansion of $\cosh(\cdot)$, we find

$$\frac{J}{\alpha} \sim \int_0^1 \frac{\epsilon}{\sqrt{(-1 - \frac{\pi^2\eta^2}{8}\epsilon^2) + (1 + \frac{\pi^2}{8}\epsilon^2)}} \mathrm{d}\eta, \tag{5.46}$$

$$\sim \frac{2\sqrt{2}}{\pi} \int_0^1 \frac{1}{\sqrt{1-\eta^2}} \mathrm{d}\eta = \sqrt{2}. \tag{5.47}$$

Hence we deduce that $\alpha \sim J/\sqrt{2}$ and we write our explicit solution as

$$w(z) \sim -\frac{\mathrm{i}J}{\sqrt{2}} \int_0^z \frac{1}{\sqrt{\cosh(\pi z') + \cosh(\pi\epsilon/2)}} \mathrm{d}z', \tag{5.48}$$

where the electric potential $\phi(z)$ is given by the real part of (5.48).

5.2.1 Electric potential close to small contacts

We now have an explicit solution for the electric potential (5.48), albeit rather complicated. What is most interesting to us now is the behaviour of this solution close to the small contact. We start by obtaining a relationship between J and ϵ to use in (5.48).

We rewrite (5.42), given we know $\alpha = J/\sqrt{2}$, as

$$\phi_0 = -\frac{\mathrm{i}J}{\sqrt{2}} \int_0^{\mathrm{i}} \frac{1}{\sqrt{\cosh(\pi z') + \cosh(\pi\epsilon/2)}} \mathrm{d}z', \tag{5.49}$$

which after applying the change of variables $z' = \mathrm{i}\hat{\eta}$ is written as

$$\phi_0 = \frac{J}{\sqrt{2}} \int_0^1 \frac{1}{\sqrt{\cos(\pi\hat{\eta}) + \cosh(\pi\epsilon/2)}} \mathrm{d}\hat{\eta}. \tag{5.50}$$

It is clear from (5.50) that we have a singularity at $\hat{\eta} = 1$ as $\epsilon \to 0$. We claim that the major contribution of the integrand is close to this singularity, therefore, we assume that the integrand is negligible for $\hat{\eta} < 1 - \gamma$ for some small parameter γ, such that $\epsilon \ll \gamma \ll 1$. We can write (5.50) as

$$\frac{\sqrt{2}}{J}\phi_0 = \underbrace{\int_0^{1-\gamma} \frac{1}{\sqrt{\cos(\pi\hat{\eta}) + \cosh(\pi\epsilon/2)}} \mathrm{d}\hat{\eta}}_{I_{\mathrm{out}}(\epsilon)} + \underbrace{\int_{1-\gamma}^1 \frac{1}{\sqrt{\cos(\pi\hat{\eta}) + \cosh(\pi\epsilon/2)}} \mathrm{d}\hat{\eta}}_{I_{\mathrm{in}}(\epsilon)}, \tag{5.51}$$

where $I_{\mathrm{out}}(\epsilon)$ and $I_{\mathrm{out}}(\epsilon)$ denote the negligible (outer) and major (inner) contributions of the integral respectively. We consider these integrals separately.

Inner integral

Consider the behaviour close to $\hat{\eta} = 1$ and apply the scaling $\hat{\eta} = 1 - \epsilon\xi$ to give,

$$I_{\mathrm{in}}(\epsilon) = \int_0^{\frac{\gamma}{\epsilon}} \frac{\epsilon}{\sqrt{-\cos(\pi\epsilon\xi) + \cosh(\pi\epsilon/2)}} \mathrm{d}\xi. \tag{5.52}$$

In a similar way as before, we consider asymptotic expansions for small ϵ and hence obtain

$$I_{\mathrm{in}}(\epsilon) \sim \frac{\sqrt{2}}{\pi} \int_0^{\frac{\gamma}{\epsilon}} \frac{1}{\sqrt{\xi^2 + 1/4}} \mathrm{d}\xi, \tag{5.53}$$

$$= \frac{\sqrt{2}}{\pi} \left[\log\left(2\xi + \sqrt{4\xi^2 + 1}\right) \right]_0^{\frac{\gamma}{\epsilon}}, \tag{5.54}$$

$$\sim \frac{\sqrt{2}}{\pi} \left(2\log 2 + \log\gamma - \log\epsilon + O(\epsilon^2)\right). \tag{5.55}$$

Outer integral

Now we consider the outer behaviour $I_{\text{out}}(\epsilon)$ of (5.51) away from $\hat{\eta} = 1$ by taking the leading order asymptotic expansion of $\cosh(\pi\epsilon/2)$ and expanding for small γ,

$$I_{\text{out}}(\epsilon) = \int_0^{1-\gamma} \frac{1}{\sqrt{\cos(\pi\hat{\eta}) + 1}} \mathrm{d}\hat{\eta}, \tag{5.56}$$

$$= \frac{1}{\sqrt{2}} \int_0^{1-\gamma} \frac{1}{\cos(\frac{\pi}{2}\hat{\eta})} \mathrm{d}\hat{\eta}, \tag{5.57}$$

$$= \frac{1}{\pi\sqrt{2}} \left(\log\left(1 + \cos\left(\frac{\pi}{2}\gamma\right)\right) - \log\left(1 - \cos\left(\frac{\pi}{2}\gamma\right)\right)\right), \tag{5.58}$$

$$\sim \frac{\sqrt{2}}{\pi} \left(2\log 2 - \log\pi - \log\gamma + O(\gamma^2)\right). \tag{5.59}$$

Relationship between current and contact size

Combining the inner and outer solutions, (5.55) and (5.59) in (5.51), we find to leading order

$$J = \frac{\pi\phi_0}{4\log 2 - \log\pi - \log\epsilon} + O(\epsilon). \tag{5.60}$$

Equation (5.60) illustrates a very interesting relationship between total current J and applied potential ϕ_0 at a contact. It tells us that as the contact interface gets infinitesimally small, the total current passing through the contact also gets small, as one would expect. However, one might expect the current to decrease linearly as the width of the gap decreases, when in fact the current J decays like

$$J = O\left(\frac{1}{\log\epsilon}\right). \tag{5.61}$$

Considering Ohm's law $V = JR$ for voltage $V = \phi_0$, resistance R and current J defined as (5.60), we deduce that the constriction resistance due to a gap of size ϵ behaves like

$$R = O(\log\epsilon), \tag{5.62}$$

where the resistance gradients close to the contacts are substantial. From this insight, when considering a material conductivity of order of magnitude 1 and contacts of size $\epsilon \ll 1$, we have shown that the constriction resistance due to small contact points dominates over the material resistivity.

Since this is a simple domain, we are able to find an explicit solution, however in general, an explicit solution is not always possible. Instead, we can solve such problems using the method of matched asymptotics. We illustrate the effectiveness of this approach by applying matched asymptotics to this same problem to obtain the same result as above.

5.3 Solution by matched asymptotics

Due to the presence of a very small parameter ϵ in our problem, it is natural to aim to approximate the solution in the limiting case of $\epsilon = 0$, however, doing so in our situation would violate the boundary condition $\phi(\mathbf{x}) = \pm\phi_0$ for $|\mathbf{x}| \leq \epsilon/2$, $y = \pm 1$. This can be thought of as a singularly perturbed problem and can be dealt with using the method of matched asymptotics [45], which involves separating the domain into two subdomains. In one of these regions, labelled the "outer region", we treat the problem as a regular perturbation and obtain an approximation for the solution here. Within the other subdomain, or the "inner region", this approximation is not valid. Therefore a new approximation is obtained by treating the inner region as a separate perturbation problem. The outer and inner solutions are then combined by "matching" , resulting in an approximate solution that is valid throughout the entire domain. The method of matched asymptotics can be outlined as follows:

1. determine the scaling of the inner region,
2. rescale the spatial variable within the inner region,
3. find the asymptotic expansion of the solution within the inner region using relevant boundary conditions,
4. find the asymptotic expansion of the solution within the outer region using relevant boundary conditions,
5. match the inner and outer solutions.

Therefore, we can appropriately account for small contacts with respect to a comparatively large domain. We will demonstrate this technique on the same reduced problem for ϕ (5.24)–(5.28) within the upper-right quadrant of the infinite strip, where our inner region will be close to the top contact and the outer region will be elsewhere in the quadrant. Symmetry will allow us to deduce the solution elsewhere.

5.3.1 Two dimensional problem

Consider the problem (5.24)–(5.28) for ϕ. To proceed with the method of matched asymptotics, we study an inner problem localised near the top contact by enforcing the scaling

$$z = -\frac{\epsilon}{2}Z + \mathrm{i}, \tag{5.63}$$

We refer to $z = x + \mathrm{i}y$ as the "outer variable" and $Z = X + \mathrm{i}Y$ as the "inner variable". We shall consider the problem in terms of each variable separately, then match these solutions asymptotically.

Inner problem

The inner problem is very similar to the earlier "full" problem, however it is easier because it is defined within a semi-infinite region. We solve the following system of equations for Φ where $\Phi(X, Y) = \phi(x, y)$,

$$\nabla^2 \Phi = 0, \qquad X \leq 0,\, Y \geq 0, \tag{5.64}$$

with boundary conditions

$$\Phi(X, 0) = \phi_0, \quad -1 \leq X \leq 0, \tag{5.65}$$

$$\frac{\partial \Phi}{\partial Y}(X, 0) = 0, \qquad X \leq -1, \tag{5.66}$$

$$\frac{\partial \Phi}{\partial X}(0, Y) = 0, \qquad Y \geq 0. \tag{5.67}$$

We note that this is equivalent to solving the following system of equations for Ψ, the complex conjugate of Φ,

$$\nabla^2 \Psi = 0, \qquad X \leq 0,\, Y \geq 0, \tag{5.68}$$

with boundary conditions

$$\frac{\partial \Psi}{\partial Y}(X, 0) = 0, \quad -1 \leq X \leq 0 \tag{5.69}$$

$$\Psi(X, 0) = -\frac{J}{2}, \qquad X \leq -1, \tag{5.70}$$

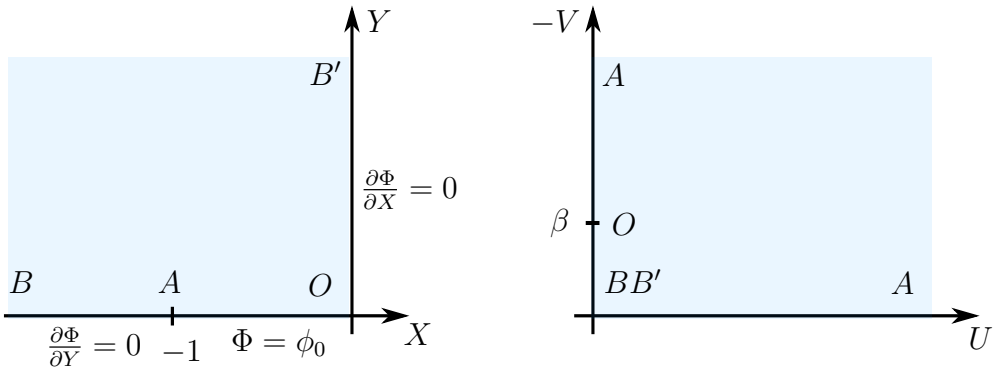
$$\Psi(0, Y) = 0, \qquad Y \geq 0. \tag{5.71}$$

Similar to the analysis in Section 5.2, we seek to find a conformal mapping between the hodograph plane, depicted in Figure 5.6b, given by

$$W'(Z) = \frac{\partial \Phi}{\partial X} - \mathrm{i}\frac{\partial \Phi}{\partial Y} = U - \mathrm{i}V, \tag{5.72}$$

and the physical plane $Z = X + \mathrm{i}Y$, depicted in Figure 5.6a. In a similar argument as before, the hodograph variable satisfies $\mathrm{Im}(W') \geq 0$ and $\mathrm{Re}(W') \geq 0$ due to the maximum principle of Laplace's equation and the boundary condition (5.65). We wish to map both domains to the upper-half plane and apply a Möbius transform to obtain a relationship between W' and Z. By applying

$$\zeta_1 = -Z^2, \qquad \zeta = (W')^2, \tag{5.73}$$



(a) Physical plane, $Z = X + \mathrm{i}Y$. (b) Hodograph plane, $W'(Z) = U - \mathrm{i}V$.

Figure 5.6: Schematic of the physical and hodograph planes between which we obtain a conformal mapping.

to each of the domains, and using the Möbius transform $\zeta = -\beta^2/(\zeta_1 + 1)$, we obtain the relationship

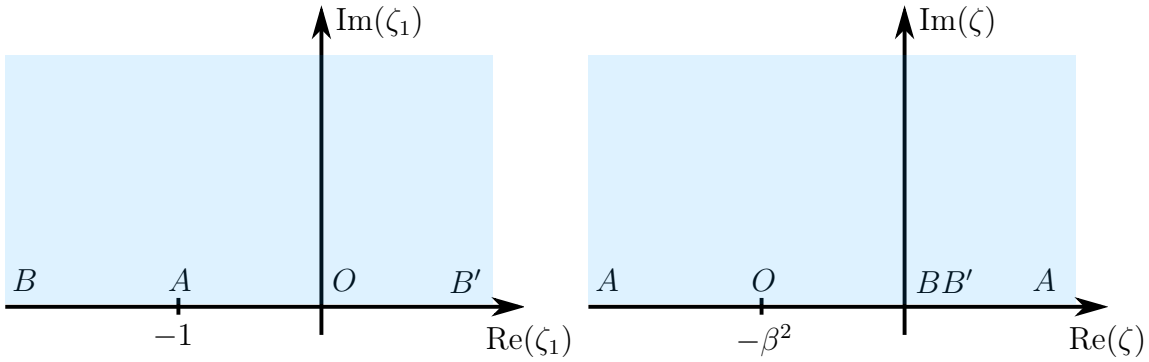
$$(W')^2 = \frac{\beta^2}{Z^2 - 1}, \tag{5.74}$$

for some real, positive constant β to be determined. Taking the square root, we find W' in terms of Z to be

$$W'(Z) = \frac{\beta}{\sqrt{Z^2 - 1}}. \tag{5.75}$$

The denominator of (5.75) is a multivalued function, therefore we must be careful to define which branch of $\sqrt{Z^2 - 1}$ we are interested in. We can write

$$\sqrt{Z^2 - 1} = (r_1 r_2)^{\frac{1}{2}} e^{\frac{\mathrm{i}}{2}(\theta_1 + \theta_2)}, \tag{5.76}$$



(a) $\zeta_1 = -Z^2$. (b) $\zeta = (W')^2$.

Figure 5.7: Half planes obtained by applying the conformal mappings (5.73) to the physical and hodograph planes respectively.

where

$$r_1 = |Z-1|, \qquad r_2 = |Z+1|, \qquad \theta_1 = \arg(Z-1), \qquad \theta_2 = \arg(Z+1). \tag{5.77}$$

It is straightforward to verify that $\sqrt{Z^2-1}$ has branch points at $Z = \pm 1$. We can uniquely define $\sqrt{Z^2-1}$ by enforcing bounds on θ_1 and θ_2, hence defining a branch cut between $Z = 1$ and $Z = -1$. We choose the branch cut that extends along the real axis on the intervals $(-\infty, -1]$ and $[1, \infty)$, as illustrated in Figure 5.8. This branch cut occurs when θ_1 and θ_2 are restricted such that

$$0 \leq \arg(Z-1) < 2\pi, \qquad -\pi < \arg(Z+1) \leq \pi. \tag{5.78}$$

Returning to (5.75), we are reminded that

$$\mathrm{Re}(W') \geq 0, \qquad \mathrm{Im}(W') \geq 0. \tag{5.79}$$

Given (5.78) and that $\pi/2 \leq \arg(Z) \leq \pi$, we restrict

$$\frac{\pi}{2} \leq \arg(\sqrt{Z^2+1}) \leq \pi. \tag{5.80}$$

to ensure that $\sqrt{Z^2+1}$ always has a positive imaginary part but a negative real part. Therefore we write (5.75) as

$$W'(Z) = \frac{-\beta}{\sqrt{Z^2-1}}, \tag{5.81}$$

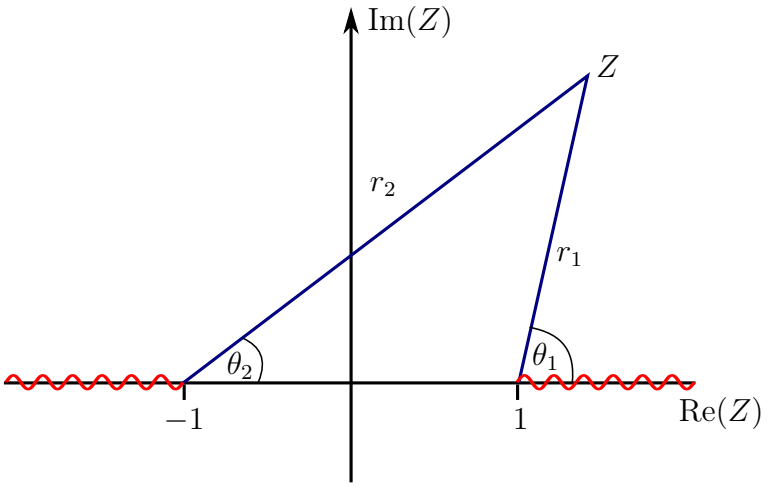


Figure 5.8: Schematic of the branch cut of $\sqrt{Z^2-1}$ that connects -1 to 1 through infinity.

where the minus sign in the numerator has been introduced to ensure positive real and imaginary parts of W' given (5.80). To demonstrate this, recall that $W'(0) = \mathrm{i}\beta$. Therefore

$$W'(0) = \frac{-\beta}{\sqrt{-1}} = \frac{-\beta}{\mathrm{i}} = \mathrm{i}\beta. \tag{5.82}$$

To find the complex potential $W(Z) = \Phi(Z) + \mathrm{i}\Psi(Z)$, we integrate (5.81) to obtain

$$W(Z) = -\beta \log\left(Z + \sqrt{Z^2 - 1}\right) + C. \tag{5.83}$$

With an appropriate branch of log and by enforcing the boundary condition $W(0) = \phi_0$, we find that

$$C = \phi_0 + \beta\frac{\mathrm{i}\pi}{2}, \tag{5.84}$$

noting that $\log(\sqrt{-1}) = \log(\mathrm{i}) = \mathrm{i}\pi/2$. We next consider the boundary condition $W(-1) = \phi_0 - \mathrm{i}J/2$ which gives

$$-\frac{\mathrm{i}J}{2} = -\beta\left(\log(-1) - \frac{\mathrm{i}\pi}{2}\right). \tag{5.85}$$

In order to define $\log(-1)$, we must consider how we are approaching $Z = -1$ in the complex plane. From Figure 5.6a, we notice that $\mathrm{Im}(Z) \geq 0$, therefore, given our chosen branch of the square-root, we must have $\mathrm{Im}(Z + \sqrt{Z^2 - 1}) \geq 0$. Thus we approach $Z = -1$ from above, thereby $\log(-1) = \mathrm{i}\pi$. We now conclude that $\beta = J/\pi$, hence the inner solution is

$$W(Z) = -\frac{J}{\pi}\left(\log\left(Z + \sqrt{Z^2 - 1}\right) - \frac{\mathrm{i}\pi}{2}\right) + \phi_0. \tag{5.86}$$

This is the leading order complex potential close to the upper contact.

Outer problem

For the outer or "far-field" problem, the contacts are so small in comparison to the size of the domain, we approximate the contacts as point sources and sinks on the boundary. When studying this problem, we do not consider the reduced problem, but rather we solve Laplace's equation in the original infinite strip $-1 \leq y \leq 1$ for which we have $\partial\phi/\partial y = 0$ (equivalent to $\psi = \pm J/2$ as before) on the boundary and point sources/sinks at $(0, \pm 1)$. Consider a source/sink of strength q at the top contact $(0, 1)$ where q is to be determined. Conservation of charge tells us that the strength of the source/sink at the bottom contact must be $-q$. Thus the problem we wish to solve can be written in terms of potential ϕ or its complex conjugate ψ, namely

$$\nabla^2\phi = 0, \qquad \nabla^2\psi = 0, \qquad -1 \leq y \leq 1, \tag{5.87}$$

with boundary conditions

$$\frac{\partial \phi}{\partial y}(x, \pm 1) = 0, \qquad \psi(x, \pm 1) = \begin{cases} -\frac{J}{2}, & x > 0, \\ \frac{J}{2}, & x < 0. \end{cases} \tag{5.88}$$

We can apply the conformal map

$$\zeta = \mathrm{i} e^{\frac{\pi z}{2}}, \tag{5.89}$$

to transform our domain to the upper half plane as shown in Figure 5.9, where for $\mathrm{Im}(\zeta) = 0$, there exist point sources/sinks $q = \mp 1$ at $\mathrm{Re}(\zeta) = \pm 1$ respectively, and $\psi = -J/2$ for $|\mathrm{Re}(\zeta)| > 1$ and $\psi = J/2$ for $|\mathrm{Re}(\zeta)| < 1$. The theory of electric potential with respect to point a source/sink allows us to write down the general solution to the complex potential problem

$$w(\zeta) = \frac{q}{2\pi} \left(\log(\zeta + 1) - \log(\zeta - 1) \right) + c, \tag{5.90}$$

where $q \sim q_0 + \epsilon q_1 + O(\epsilon^2)$ and c is some constant to be determined.

From the symmetry of the full outer problem, we realise that $\phi = \psi = 0$ for $z = 0$, therefore $\zeta(\mathrm{i}) = 0$. Hence

$$0 = \frac{q}{2\pi} \left(\log(\mathrm{i} + 1) - \log(\mathrm{i} - 1) \right) + c, \tag{5.91}$$

$$= \frac{q}{2\pi} \log(-\mathrm{i}) + c \tag{5.92}$$

and we deduce that $c = \mathrm{i}q/4$. The outer solution is thereby

$$w(z) = \frac{q}{2\pi} \left(\log\left(\mathrm{i} e^{\frac{\pi z}{2}} + 1\right) - \log\left(\mathrm{i} e^{\frac{\pi z}{2}} - 1\right) + \frac{\mathrm{i}\pi}{2} \right). \tag{5.93}$$

This is the complex potential far from the contacts.

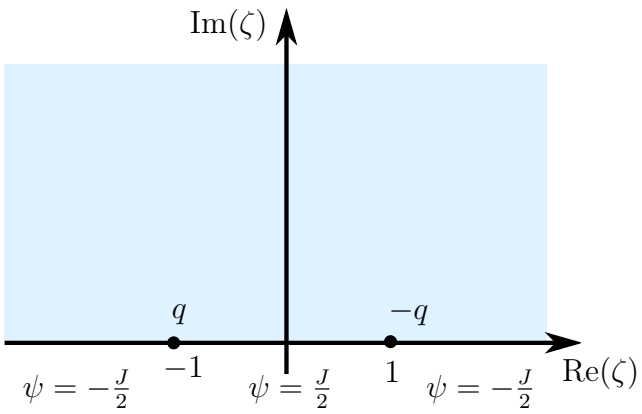


Figure 5.9: Schematic of the upper-half plane following the application of conformal map $\zeta = \mathrm{i} e^{\pi z/2}$ to the infinite strip.

Van Dyke's matching principle

We want to match the outer solution $w(z)$ given by (5.93) with the inner solution at the top contact $W(Z)$ given by (5.86) to ensure that the two solutions agree within the transition region between them. In this region, the two solutions will be equal, namely

$$\lim_{Z\to\infty} W(Z) \sim \lim_{z\to \mathrm{i}} w(z). \tag{5.94}$$

We will match our solutions using Van Dyke's matching rule [45]. This involves firstly asymptotically expanding the inner solution for small ϵ to m terms (known as the "m-term inner") and then converting inner variables to outer variables. From this, we retain n terms. Similarly, we expand the outer solution to n terms (known as the "n-term outer") and then convert to inner variables, retaining m terms. We then require that the m-term inner written in n-term outer variables is identical to the n-term outer written in m-term inner variables. This sounds complicated when written in words, however we will demonstrate the technique on this example and show that we obtain the same result as for the explicit solution method in Section 5.2.

Matching

Recall the scaling $z = -\epsilon Z/2 + \mathrm{i}$. The inner solution (5.86) is our 1-term inner, or $m = 1$. We write the inner solution in outer variables z, expanded to 1 term, or $n = 1$,

$$W(z) = -\frac{J}{\pi}\left(\log\left(\mathrm{i} - z + \sqrt{(\mathrm{i}-z)^2 - \epsilon^2/4}\right) + \log 2 - \log\epsilon - \frac{\mathrm{i}\pi}{2}\right) + \phi_0, \tag{5.95}$$

$$\sim -\frac{J}{\pi}\left(\log\left(2(\mathrm{i}-z) - \frac{\epsilon^2}{8(\mathrm{i}-z)} + \dots\right) + \log 2 - \log\epsilon - \frac{\mathrm{i}\pi}{2}\right) + \phi_0, \tag{5.96}$$

$$\sim -\frac{J_0}{\pi}\left(2\log 2 + \log(\mathrm{i}-z) - \log\epsilon - \frac{\mathrm{i}\pi}{2}\right) + \phi_0 + O(\epsilon), \tag{5.97}$$

where we expand $J \sim J_0 + \epsilon J_1 + O(\epsilon^2)$. We note that when using Van Dyke's matching principle, logarithms are treated as $O(1)$.

The 1-term outer solution is (5.93) and noting $\mathrm{i}e^{\frac{\pi}{2}(-\frac{\epsilon}{2}Z+\mathrm{i})} = -e^{-\frac{\pi Z}{4}\epsilon}$, we find that

$$w(Z) = \frac{q}{2\pi}\left(\log\left(-e^{-\frac{\pi Z}{4}\epsilon} + 1\right) - \log\left(-e^{-\frac{\pi Z}{4}\epsilon} - 1\right) + \frac{\mathrm{i}\pi}{2}\right), \tag{5.98}$$

$$\sim \frac{q}{2\pi}\left(\log\left(\frac{\pi Z}{4}\epsilon\right) - \log\left(-2 + \frac{\pi Z}{4}\epsilon\right) + \frac{\mathrm{i}\pi}{2}\right) + \dots, \tag{5.99}$$

$$\sim \frac{q_0}{2\pi}\left(-3\log 2 + \log Z + \log\pi + \log\epsilon - \frac{\mathrm{i}\pi}{2}\right) + O(\epsilon), \tag{5.100}$$

where again $\log(-1) = \mathrm{i}\pi$ from the earlier reasoning and $q \sim q_0 + \epsilon q_1 + O(\epsilon)$.

To match these two solutions (5.97) and (5.100), we rewrite (5.97) in the variable Z:

$$W(Z) = -\frac{J_0}{\pi}\left(\log 2 + \log Z - \frac{\mathrm{i}\pi}{2}\right) + \phi_0 + O(\epsilon), \tag{5.101}$$

and compare with (5.100). Immediately we see that $q_0 = -2J_0$, which can then be extended to deduce $q = -2J$ therefore allowing us to derive the expression for total current J in terms of ϕ_0:

$$J = \frac{\pi\phi_0}{4\log 2 - \log\pi - \log\epsilon} + O(\epsilon). \tag{5.102}$$

We obtain the same relationship as we did via the explicit solution, (5.60).

Composite solution

Rather than having an inner and outer solution, we would like a uniformly valid expression that encompasses both behaviours and is valid for all values of x and y. One way to construct this "composite solution" is to add the inner and outer solutions together and subtract the expansion in the overlap region which would otherwise be counted twice. We choose to express this solution in terms of outer variables z. The solutions corresponding to the region close to the top contact and the rest of the strip respectively are

$$W_{\text{inner}}(z) = -\frac{J}{\pi}\left(\log 2 - \log\epsilon + \log\left(\mathrm{i} - z + \sqrt{(\mathrm{i}-z)^2 - \epsilon^2/4}\right) - \frac{\mathrm{i}\pi}{2}\right) + \phi_0 + O(\epsilon), \tag{5.103}$$

$$w_{\text{outer}}(z) = -\frac{J}{\pi}\left(\log\left(\mathrm{i}e^{\frac{\pi z}{2}} + 1\right) - \log\left(\mathrm{i}e^{\frac{\pi z}{2}} - 1\right) + \frac{\mathrm{i}\pi}{2}\right) + O(\epsilon), \tag{5.104}$$

and the overlap solution is

$$W_{\text{overlap}}(z) = -\frac{J}{\pi}\left(2\log 2 - \log\epsilon + \log(\mathrm{i}-z) - \frac{\mathrm{i}\pi}{2}\right) + \phi_0 + O(\epsilon). \tag{5.105}$$

The composite solution is constructed as

$$\begin{aligned} w_{\text{comp}}(z) = -\frac{J}{\pi}\Big(&\log\left(\mathrm{i} - z + \sqrt{(\mathrm{i}-z)^2 - \epsilon^2/4}\right) - \log(\mathrm{i}-z) \\ &+ \log\left(\mathrm{i}e^{\frac{\pi z}{2}} + 1\right) - \log\left(\mathrm{i}e^{\frac{\pi z}{2}} - 1\right) - \log 2 + \frac{\mathrm{i}\pi}{2}\Big) + O(\epsilon). \end{aligned} \tag{5.106}$$

We note that this solution is valid in the upper-right quadrant of the infinite strip and can be extended to correctly approximate behaviour throughout the rest of the strip through symmetry.

5.3.2 Extension to three dimensions

The two-dimensional analysis above provides intuition into how the electric potential behaves close to small contacts, therefore a natural extension is to think about similar contacts in a simple three-dimensional domain. We again employ the method of matched asymptotics to obtain an inner solution close to the top contact which we match with the outer solution defined within the region far from the contacts. This analysis allows us to obtain a three-dimensional relationship between current and contact width analogous to that obtained for the two-dimensional case described in Section 5.3.1

We consider the electric potential $\phi(\mathbf{x})$ for the spatial variable $\mathbf{x} = (x, y, z)$ within a unit cube Ω of electrical conductivity $\sigma = 1$ and represent particle contacts by circular regions of diameter ϵ, denoted $\partial\Omega_t$ and $\partial\Omega_b$ (for the top and bottom respectively), where $\epsilon \ll 1$. These regions are centred at $\mathbf{x}_t$ and $\mathbf{x}_b$, the centre points of the top and bottom faces respectively. Within these regions, we enforce Dirichlet boundary conditions, whereas on the remaining boundary surface, we enforce zero-flux conditions to represent the boundary between the conducting solid particle and the insulating gas-filled void. We can visualise this with the help of Figure 5.10. Again, we stress that our analysis is focused on understanding the behaviour of electric potential close to small contacts, therefore we can justify considering such a simple particle geometry by ensuring $\epsilon \ll 1$.

We wish to solve the following system of equations for steady current conduction

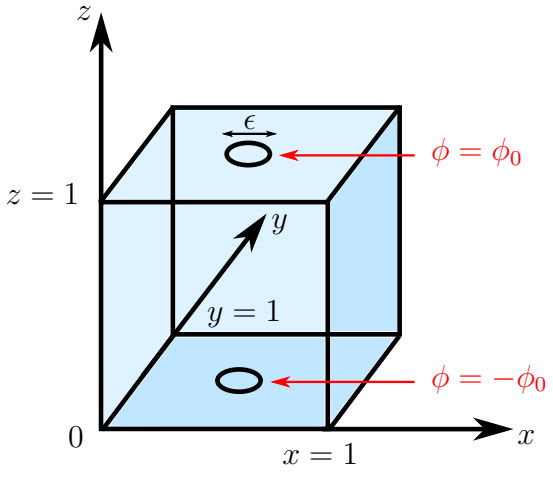


Figure 5.10: Unit cube in which we solve the steady current conduction problem (5.107)–(5.110) where we represent particle contacts as small circles of diameter $\epsilon \ll 1$.

within the unit cube:

$$\nabla^2\phi(\mathbf{x}) = 0, \qquad \mathbf{x} \in \Omega, \tag{5.107}$$

$$\phi(\mathbf{x}) = \phi_0, \qquad \mathbf{x} \in \partial\Omega_t, \tag{5.108}$$

$$\phi(\mathbf{x}) = -\phi_0, \qquad \mathbf{x} \in \partial\Omega_b, \tag{5.109}$$

$$\nabla\phi(\mathbf{x}) \cdot \mathbf{n} = 0, \qquad \mathbf{x} \in \partial\Omega \backslash (\partial\Omega_t \cup \partial\Omega_b). \tag{5.110}$$

Inner problem

We wish to study the behaviour of the electric potential close to the top contact, $\mathbf{x}_t = (1/2, 1/2, 1)$, therefore we introduce inner variables $\mathbf{X} = (X, Y, Z)$, where

$$\mathbf{x} = -\epsilon\mathbf{X} + \mathbf{x}_t. \tag{5.111}$$

The inner problem thereby involves solving Laplace's equation for $\bar{\Phi}(\mathbf{X}) = \phi(\mathbf{x})$ in the positive half-space with mixed Dirichlet-Neumann boundary conditions on the boundary surface $Z = 0$, in particular, the equipotential boundary condition $\bar{\Phi} = \phi_0$ is enforced upon a unit disk centred at $\mathbf{X} = \mathbf{0}$ and the remainder of the surface $Z = 0$ is subject to the zero-flux condition. We write the inner problem as

$$\nabla^2\bar{\Phi} = 0, \qquad Z \geq 0, \tag{5.112}$$

$$\bar{\Phi} = \phi_0, \qquad X^2 + Y^2 \leq 1,\ Z = 0, \tag{5.113}$$

$$\nabla\bar{\Phi} \cdot \mathbf{n} = 0, \qquad X^2 + Y^2 > 1,\ Z = 0, \tag{5.114}$$

along with the matching condition for $Z \to \infty$ which we will discuss later.

Oblate spheroidal coordinates, denoted $\boldsymbol{\mu} = (\mu, \nu, \theta)$ are ideal for analysing this problem because the Laplace equation is separable in this coordinate system and the degenerate limit $\mu \to 0$ of an oblate spheroid is a disk, much like $\partial\Omega_t$, the region where we have an equipotential condition (5.113). We define the oblate spheroidal coordinate system as

$$X = \cosh\mu\cos\nu\cos\theta, \qquad Y = \cosh\mu\cos\nu\sin\theta, \qquad Z = \sinh\mu\sin\nu, \tag{5.115}$$

where

$$0 \leq \mu < \infty, \qquad 0 \leq \nu \leq \pi/2, \qquad -\pi \leq \theta \leq \pi. \tag{5.116}$$

A plot of μ and ν in the X–Z plane are shown in Figure 5.11. Note that we must restrict $0 \leq \nu \leq \pi/2$ to ensure $Z \geq 0$. We therefore write the inner problem (5.112)–

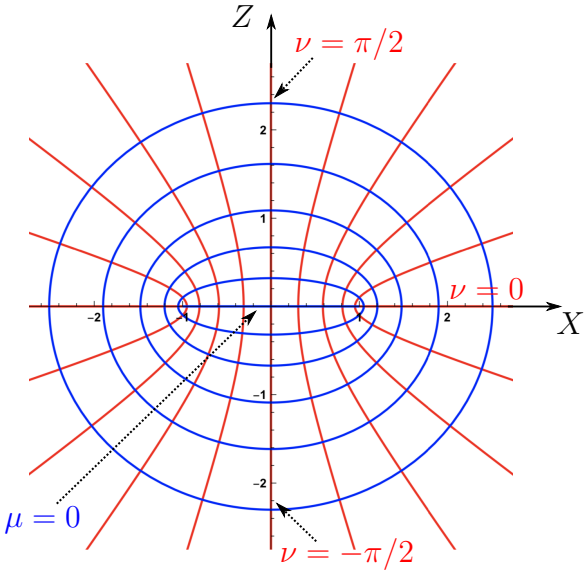


Figure 5.11: Plot of oblate spheroidal coordinates μ and ν in X–Z plane. The blue ellipses are curves of constant μ and θ the red half-hyperbolae are curves of constant ν and θ.

(5.114) for $\Phi(\boldsymbol{\mu}) = \bar{\Phi}(\mathbf{X})$ in oblate spheroidal coordinates, namely,

$$\frac{1}{\sinh^2\mu + \sin^2\nu}\left[\frac{1}{\cosh\mu}\frac{\partial}{\partial\mu}\left(\cosh\mu\frac{\partial\Phi}{\partial\mu}\right) + \frac{1}{\cos\nu}\frac{\partial}{\partial\nu}\left(\cos\nu\frac{\partial\Phi}{\partial\nu}\right)\right] + \frac{1}{\cosh^2\mu\cos^2\nu}\frac{\partial^2\Phi}{\partial\theta^2} = 0, \tag{5.117}$$

with boundary conditions

$$\Phi = \phi_0, \qquad \mu = 0, \tag{5.118}$$

$$\frac{\partial\Phi}{\partial\nu} = 0, \qquad \nu = 0. \tag{5.119}$$

Due to the separability of $\Phi(\boldsymbol{\mu}) = M(\mu)N(\nu)\Theta(\theta)$, if a surface of constant μ is an equipotential surface, then the potential off the surface is a function of μ only and the problem becomes 1-dimensional. Due to (5.118), the surface $\mu = 0$ is an equipotential surface, thus given $\Phi \to 0$ as $\mu \to \infty$, the problem (5.117) reduces to

$$\frac{\mathrm{d}}{\mathrm{d}\mu}\left(\cosh\mu\frac{\mathrm{d}\Phi}{\mathrm{d}\mu}\right) = 0, \tag{5.120}$$

therefore $\Phi(\mu)$ is of the form

$$\Phi(\mu) = A\tan^{-1}(\sinh\mu) + B, \tag{5.121}$$

where A and B are constants to be determined. From the boundary condition (5.118) we deduce $B = \phi_0$. To deduce A, we again calculate the total current passing through the top contact in an analogous method to that described in Section 5.2. In physical variables $\mathbf{x}$, this is found by integrating the current density over the contact domain, namely

$$J = \iint_{\partial\Omega_t} \mathbf{j}(\mathbf{x}) \cdot \mathbf{n} \, \mathrm{d}S, \tag{5.122}$$

for current density $\mathbf{j}(\mathbf{x}) = -\nabla_{\mathbf{x}}\phi(\mathbf{x})$. Combining the inner scaling (5.111) and oblate spheroidal scaling (5.115), we can write $\mathbf{j}$ in terms of oblate spheroidal coordinates,

$$\mathbf{j}(\boldsymbol{\mu}) = -\nabla_{\boldsymbol{\mu}}\Phi(\mu) = -\frac{\hat{e}_\mu}{\epsilon\sqrt{\sinh^2\mu + \sin^2\nu}} \frac{A}{\cosh\mu}, \tag{5.123}$$

where $\hat{e}_\mu$ is the unit vector for coordinate μ. The surface element perpendicular to the μ-coordinate is given by

$$\mathrm{d}S = \epsilon^2 \cosh\mu \cos\nu \sqrt{\sinh^2\mu + \sin^2\nu} \; \mathrm{d}\nu\mathrm{d}\theta. \tag{5.124}$$

The contact domain corresponds to $\mu = 0$, therefore by taking the normal vector in the direction of current flow $\mathbf{n} = \hat{e}_\mu$, we determine the total current J passing through the top contact to be

$$J = -\epsilon A \int_0^{\frac{\pi}{2}} \int_{-\pi}^{\pi} \cos\nu \, \mathrm{d}\theta\mathrm{d}\nu. \tag{5.125}$$

We therefore deduce the relationship

$$A = -\frac{J}{2\pi\epsilon}. \tag{5.126}$$

The inner solution $\Phi(\mu)$ in spheroidal coordinates near to the top contact hole is given by

$$\Phi(\mu) = -\frac{J}{2\pi\epsilon} \tan^{-1}(\sinh\mu) + \phi_0. \tag{5.127}$$

Outer problem

Consider the outer problem where our domain is the unit cube with point sinks/sources positioned at points $\mathbf{x}_t$ and $\mathbf{x}_b$ on the boundary and allow the strength of the top sink/source to be q, whose value is to be determined. We know from conservation of charge that the strength of the bottom sink/source is $-q$. Hence, the outer problem involves solving Laplace's equation for electric potential $\phi(\mathbf{x})$ in the unit cube, denoted Ω with homogeneous Neumann boundary conditions except for the presence of point sinks/sources on the boundary surface.

The electric potential due to a point sink/source positioned at $\mathbf{x}_0$ is

$$\phi(\mathbf{x}) \sim \frac{q}{2\pi}\left(\frac{1}{|\mathbf{x}-\mathbf{x}_0|}\right). \tag{5.128}$$

Recall that $\mathbf{x}_t = (1/2, 1/2, 1)$ is the position of the point sink/source of strength q on the bottom face and $\mathbf{x}_b = (1/2, 1/2, 0)$ is the position of the point sink/source of strength $-q$ on the bottom face. The method of images allows us to write the total potential as

$$\phi(\mathbf{x}) = \frac{q}{2\pi}\left(\frac{1}{|\mathbf{x}-\mathbf{x}_t|} + \sum_{m,n,p=-\infty}^{\infty}{}' \left(\frac{(-1)^p}{|\mathbf{x}-\mathbf{x}_t+(m,n,p)|}\right)\right), \tag{5.129}$$

where the $\sum'$ notation denotes the summation where the term $m = n = p = 0$ is excluded.

Matching

To match solutions (5.127) and (5.129), we must consider the limiting behaviour of the inner solution as we move away from the top contact and match this with the limiting behaviour of the outer solution as we move towards to top contact. This corresponds to

$$\mu \to \infty, \qquad \mathbf{x} \to \mathbf{x}_t. \tag{5.130}$$

We rewrite the inner solution (5.127)

$$\Phi(\mu) = -\frac{J}{2\pi\epsilon}\left(\frac{\mathrm{i}}{2}\log\left(\frac{1-\frac{\mathrm{i}}{2}(e^{\mu}-e^{-\mu})}{1+\frac{\mathrm{i}}{2}(e^{\mu}-e^{-\mu})}\right)\right)+\phi_0, \tag{5.131}$$

$$= -\frac{\mathrm{i}J}{4\pi\epsilon}\log\left(\frac{-\frac{\mathrm{i}}{2}+e^{-\mu}+\frac{\mathrm{i}}{2}e^{-2\mu}}{\frac{\mathrm{i}}{2}+e^{-\mu}-\frac{\mathrm{i}}{2}e^{-2\mu}}\right)+\phi_0. \tag{5.132}$$

For large μ, $e^{-\mu}$ is very small, therefore we can asymptotically expand the denominator within the log to obtain

$$\Phi(\mu) \sim -\frac{\mathrm{i}J}{4\pi\epsilon}\log\left(\left(-\frac{\mathrm{i}}{2}+e^{-\mu}+\frac{\mathrm{i}}{2}e^{-2\mu}\right)\left(-2\mathrm{i}+4e^{-\mu}+6\mathrm{i}e^{-2\mu}+\dots\right)\right)+\phi_0, \tag{5.133}$$

$$\sim -\frac{\mathrm{i}J}{4\pi\epsilon}\log\left(-1-4\mathrm{i}e^{-\mu}+\dots\right)+\phi_0, \tag{5.134}$$

$$\sim -\frac{\mathrm{i}J}{4\pi\epsilon}(-\mathrm{i}\pi+4\mathrm{i}e^{-\mu}+\dots)+\phi_0. \tag{5.135}$$

For large μ, the inner solution behaves as

$$\Phi(\mu) = \frac{J}{\pi\epsilon}\left(e^{-\mu}-\frac{\pi}{4}\right)+\phi_0. \tag{5.136}$$

Consider the transformation from inner cartesian coordinates into oblate spheroidal coordinates (5.115). We write

$$X^2 + Y^2 + Z^2 = \cosh^2\mu\cos^2\nu + \sinh^2\mu\sin^2\nu, \tag{5.137}$$

and notice that for the limiting behaviour $\mu \to \infty$, both $\cosh\mu$, $\sinh\mu \sim \frac{1}{2}e^{\mu}$, therefore, we can write

$$e^{-\mu} \sim \frac{1}{2\sqrt{X^2+Y^2+Z^2}}, \qquad \text{as } \mu \to \infty. \tag{5.138}$$

Hence, from equation (5.136), the inner solution as we move away from the top contact is

$$\Phi(\mathbf{X}) = \frac{J}{\pi\epsilon}\left(\frac{1}{2\sqrt{X^2+Y^2+Z^2}} - \frac{\pi}{4}\right) + \phi_0, \tag{5.139}$$

where $J \sim J_0 + \epsilon J_1 + O(\epsilon^2)$.

Recall the outer solution given by (5.129). To match with the inner solution near the top contact, we must consider the behaviour as $\mathbf{x} \to \mathbf{x}_t$, i.e. the behaviour near the point sink/source singularity. By recalling the scaling (5.111) we can write

$$\frac{1}{|\mathbf{x}-\mathbf{x}_t|} = \frac{1}{\sqrt{\epsilon^2X^2 + \epsilon^2Y^2 + \epsilon^2Z^2}}, \tag{5.140}$$

and approximate

$$\frac{1}{|\mathbf{x}-\mathbf{x}_t+(m,n,p)|} \sim \frac{1}{\sqrt{m^2+n^2+p^2}} + O(\epsilon), \tag{5.141}$$

thus we write the outer solution (5.129) in inner variables $\mathbf{X}$,

$$\phi(\mathbf{X}) \sim \frac{q}{2\pi}\left(\frac{1}{\epsilon\sqrt{X^2+Y^2+Z^2}} + \sum_{m,n,p=-\infty}^{\infty}{}' \frac{(-1)^p}{\sqrt{m^2+n^2+p^2}} + O(\epsilon)\right), \tag{5.142}$$

where $q \sim q_0 + \epsilon q_1 + O(\epsilon^2)$. The summation in (5.142) is known as a lattice sum and has been proven to be convergent, in particular, its value is approximately equal to -0.774, [70, 110, 109]. We will denote this constant as α for the remainder of the calculation.

By considering $O(\epsilon^{-1})$ matching of (5.139) and (5.142), we find

$$q_0 = J_0. \tag{5.143}$$

By considering the next order expansion, we write

$$\frac{J_0+\epsilon J_1}{\pi\epsilon}\left(\frac{1}{2\sqrt{X^2+Y^2+Z^2}} - \frac{\pi}{4}\right) + \phi_0 = \frac{J_0+\epsilon q_1}{2\pi}\left(\frac{1}{\epsilon\sqrt{X^2+Y^2+Z^2}} + \alpha\right), \tag{5.144}$$

hence $q_1 = J_1$. Therefore we deduce the relationship

$$J = \left(\frac{4\pi\epsilon}{\pi + 2\alpha\epsilon} \right) \phi_0, \tag{5.145}$$

and we can write the potential in the cube as

$$\phi(\mathbf{x}) = \frac{2\epsilon\,\phi_0}{\pi + 2\alpha\epsilon} \sum_{m,n,p=-\infty}^{\infty} \left(\frac{(-1)^{p+1}}{|\mathbf{x} - \mathbf{x}_t + (m,n,p)|} \right). \tag{5.146}$$

Relationship between current and contact radius

From (5.145), we notice that as the contact gets small, $\epsilon \to 0$, then the current decays like

$$J = O(\epsilon). \tag{5.147}$$

We draw the reader's attention to the interesting behaviour of the current; the area decreases as $O(\epsilon^2)$, however the current as $O(\epsilon)$. This result agrees with the analysis of Holm [46].

We note that this analysis studies quite a specific geometry, namely one with two circular contacts placed symmetrically at the centres of the top and bottom faces. However, we claim that this has a generic structure than can be easily extended to more complicated arrangements of contacts. The linearity of Laplace's equation allows us to consider current flow in the x, y and z directions separately, such that we can take the sum of the solutions. Therefore, if we have contacts on opposing sides, we can consider this potential drop in isolation to any other contacts on adjacent faces and solve the problem as above, so long as we consider very small contacts of diameter $\epsilon \ll 1$. If the contacts are sufficiently small, the approximation error associated with neglecting the adjacent contacts is negligibly small. The positions of the contacts on the faces are also easily handled by an appropriate scaling into oblate spheroidal coordinates, such that the resulting problem is identical to the one we solved above.

5.4 Comparing matched asymptotics with the numerical solution to the 2D cell problem

Having studied the behaviour of the electric potential due to small contact points analytically, we would like to validate our findings within the homogenisation framework, namely, we would like to verify that the effect of small contacts on the electric potential deduced asymptotically is reflective of the behaviour within our model to

study electric current conduction throughout granular material. We will do this by considering a two-dimensional problem where the unit cell has a simple geometry, namely a long rectangle with symmetrically aligned contacts, as in Figure 5.12. This geometry should give a potential that is roughly approximated by the one found in the infinite strip we considered in our asymptotic analysis. Hence the unit cell is a rectangle whose width is significantly bigger than the width of the contact. After solving the homogenisation cell problem within this geometry, we will compare the behaviour of the current at the top contact deduced both numerically and asymptotically to verify agreement between the two solutions. From this analysis, the analytical expressions relating current to contact size will be relevant within our homogenisation cell problem and we can further emphasise the importance of accurately modelling the process on a particle-scale in order to understand the furnace-scale behaviour.

Homogenisation cell problem

Consider the cell problem (3.25)–(3.27) corresponding to the steady current conduction problem outlined in Chapter 3 and assume uniform material conductivity, namely

$$\nabla_{\mathbf{y}}^2 \Phi^{(i)} = 0, \qquad \mathbf{y} \in \omega^S, \tag{5.148}$$

$$\left(\mathbf{e}_i + \nabla_{\mathbf{y}} \Phi^{(i)}\right) \cdot \mathbf{n} = 0, \qquad \mathbf{y} \in \gamma, \tag{5.149}$$

$$\Phi^{(i)} \text{ periodic}, \qquad \mathbf{y} \in \partial\omega_c^S, \tag{5.150}$$

where $\Phi^{(i)}(\mathbf{y})$ are the components of the vector function $\mathbf{\Phi}(\mathbf{y})$. We will restrict our analysis to the two-dimensional problem, thus $i = 1, 2$. We consider a rectangle of height 2δ and width $w \gg \delta$ to approximate the infinite strip studied in Section 5.3.1. Consider this rectangle to be centred at the origin with contact gaps of width $\epsilon\delta$ centred on the top and bottom boundaries, where $\epsilon \ll 1$. A schematic of this domain is given in Figure 5.12. We denote the contact boundaries $\partial\omega_c^S = \partial\omega_c^T \cup \omega_c^B$ and the remaining boundary γ. We can solve this problem using the matched asymptotics approach outlined in Section 5.3.1. To see this, we translate the vector function $\mathbf{\Phi}$ such that

$$\hat{\mathbf{\Phi}}(\mathbf{y}) = \mathbf{\Phi}(\mathbf{y}) + \mathbf{y}, \tag{5.151}$$

therefore the cell problem (5.148)–(5.150) in terms of $\hat{\mathbf{\Phi}}(\mathbf{y})$ is

$$\nabla_{\mathbf{y}}^2 \hat{\Phi}^{(i)} = 0, \qquad \mathbf{y} \in \omega^S, \tag{5.152}$$

$$\nabla_{\mathbf{y}} \hat{\Phi}^{(i)} \cdot \mathbf{n} = 0, \qquad \mathbf{y} \in \gamma, \tag{5.153}$$

$$(\hat{\Phi}^{(i)} - \mathbf{y} \cdot \mathbf{e}_i) \text{ periodic}, \qquad \mathbf{y} \in \partial\omega_c^S, \tag{5.154}$$

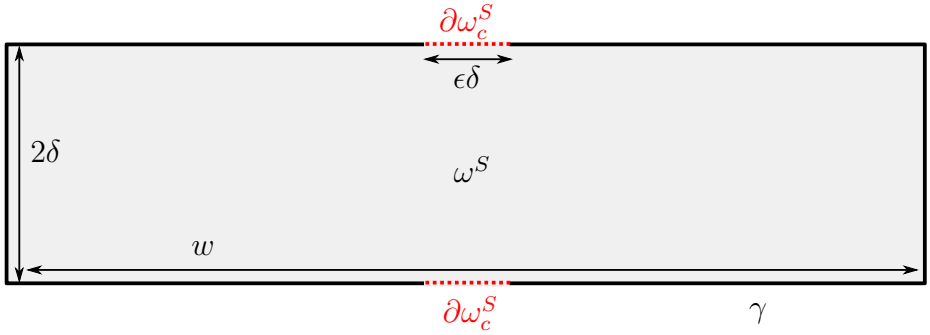


Figure 5.12: Schematic of a rectangular representative cell in which to solve the homogenisation cell problem.

where the final condition describes a voltage drop between the top and bottom contacts of magnitude equal to the height of the cell. Thus for a cell of height 2δ and contact width $\epsilon\delta$ such as that in Figure 5.12, we have the condition for $|x| < \epsilon\delta/2$,

$$\hat{\Phi}^{(2)}(x,\delta) - \delta = \hat{\Phi}^{(2)}(x,-\delta) + \delta, \tag{5.155}$$

$$\hat{\Phi}^{(2)}(x,\delta) - \hat{\Phi}^{(2)}(x,-\delta) = 2\delta. \tag{5.156}$$

Hence if we enforce that $\hat{\Phi}^{(2)}(x,-\delta) = -\delta$ for $|x| < \epsilon\delta/2$, we have $\hat{\Phi}^{(2)}(x,\delta) = \delta$. Note that we can fix $\hat{\mathbf{\Phi}}(x,-\delta)$ because we are primarily interested in $\nabla_{\mathbf{y}}\hat{\mathbf{\Phi}}$ rather than $\hat{\mathbf{\Phi}}$ itself.

Given the asymptotic analysis of the problem (5.1)–(5.4) in Section 5.3.1, we notice an analogy between that and the cell problem (5.152)–(5.154) for the second component of $\hat{\mathbf{\Phi}}$. As before, we scale the spatial variable with δ and rewrite the cell problem (5.152)–(5.154) as

$$\nabla_{\mathbf{y}}^2\hat{\Phi}^{(2)} = 0, \qquad \mathbf{y} \in \omega^S, \tag{5.157}$$

$$\nabla_{\mathbf{y}}\hat{\Phi}^{(2)} \cdot \mathbf{n} = 0, \qquad \mathbf{y} \in \gamma, \tag{5.158}$$

$$\hat{\Phi}^{(2)} = 1, \qquad \mathbf{y} \in \partial\omega_c^T, \tag{5.159}$$

$$\hat{\Phi}^{(2)} = -1, \qquad \mathbf{y} \in \partial\omega_c^B, \tag{5.160}$$

where we have fixed $\hat{\Phi}^{(2)}|_{\partial\omega_c^B} = -1$ to retrieve the boundary conditions (5.159)–(5.160) and $\partial\omega_c^T$ and $\partial\omega_c^B$ are the top and bottom contacts of width $\epsilon \ll 1$. By considering the width of the rectangle to be much greater than the height, we allow the behaviour of $\hat{\Phi}^{(2)}$ within this geometry to approximate that within the infinite strip analysed in Section 5.3.1. Therefore, the cell problem (5.157)–(5.160) for $\hat{\Phi}^{(2)}$ is analogous to solving Laplace's equation for ϕ in the infinite strip, as outlined by (5.1)-(5.4).

Comparing the matched asymptotics to the numerical solution

Recall that we derived a relationship between the current passing through the top contact of the infinite strip (5.102) from which we deduced that the total current J_ϕ varies with the contact width ϵ according to:

$$J_\phi = O\left(\frac{1}{\log \epsilon}\right). \tag{5.161}$$

By solving the homogenisation cell problem (5.148)–(5.150) for $\mathbf{\Phi}$ and using the translation (5.151), we can study the behaviour of the current J_Φ corresponding to the second component $\Phi^{(2)}$ close to the top contact. We will affirm the analogy between the two problems if the behaviour of currents J_ϕ and J_Φ satisfy the same relationship.

We solve the homogenisation cell problem (5.148)-(5.150) within a rectangular domain $\omega = [-3, 3] \times [-1, 1]$ for a range of ϵ values using finite elements in `FEniCS` [6]. From the solution, we calculate the current quantity J_Φ, given by

$$J_\Phi = -\int_{\epsilon/2}^{\epsilon/2} \nabla_{\mathbf{y}} \Phi^{(2)} \cdot \mathbf{n} \, \mathrm{d}\mathbf{y}, \tag{5.162}$$

where $\mathbf{n} = (0, -1)^T$. We plot the current J_Φ and J_ϕ corresponding to the numerical solution and asymptotic composite solution (5.106) respectively in Figure 5.13. We see that the numerical solution agrees very well with the asymptotic solution for $\epsilon < 0.3$. The deviation of the asymptotics from the numerics for $\epsilon > 0.3$ is not surprising since we derived the asymptotic solution for $\epsilon \ll 1$, hence would not expect this to be a good approximation for large ϵ. We conclude that the solution obtained via matched asymptotics can be used to infer the solution to the homogenisation cell problem and moreover provides us with analytical expressions to understand the behaviour of the electric potential due to small contact points.

5.5 Discussion

From the analysis outlined above, we have observed some interesting and perhaps non-intuitive behaviour of the electric current and electric potential when we consider the limiting behaviour of small contacts. We considered a two-dimensional domain with contact gap of width ϵ and a three-dimensional domain with contact circle of diameter ϵ. In each case, the current decays as $\epsilon \to 0$ according to

$$J_{2\mathrm{D}} = O\left(\frac{1}{\log \epsilon}\right), \qquad J_{3\mathrm{D}} = O(\epsilon). \tag{5.163}$$

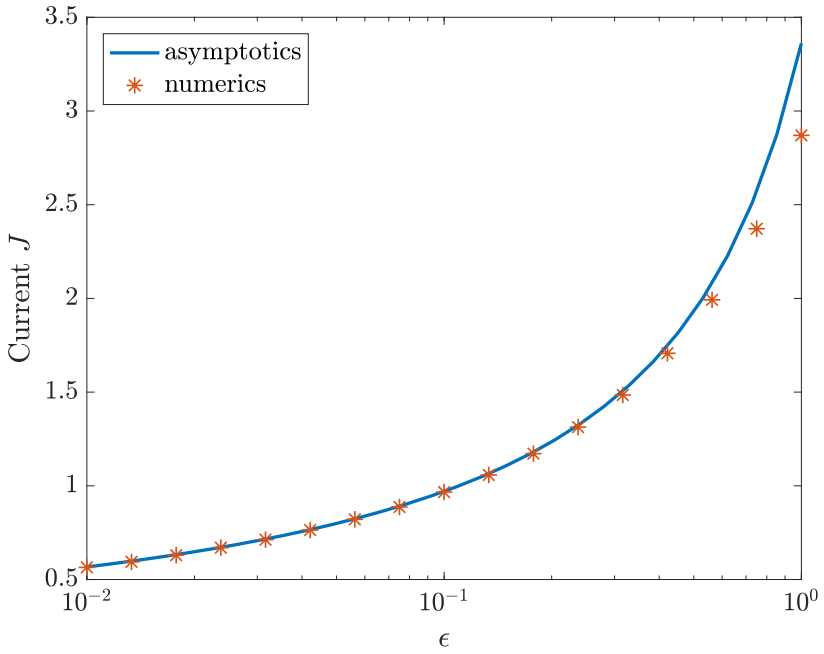


Figure 5.13: Current through the top contact versus ϵ for asymptotic solution (5.106) with $\phi_0 = 1$ (blue line) and the equivalent current quantity J_Φ for the numerical solution to (5.148)–(5.150) (orange stars).

By considering Ohm's law $V = JR$ for voltage V, current J and resistance R, we deduce that the constriction resistance due to small gaps must be

$$R_{2\mathrm{D}} = O(\log \epsilon), \qquad R_{3\mathrm{D}} = O\left(\epsilon^{-1}\right). \tag{5.164}$$

The resistance in the three-dimensional example agrees with the findings of Holm [46]. We verified that the two-dimensional homogenisation cell problem could be approximated by the asymptotic solution and hence satisfies the same relationships as above. Without proof, we infer that the three-dimensional homogenisation problem can also be approximated asymptotically and hence exhibits the relevant behaviour above.

Expressions (5.164) demonstrate that as the contact size becomes very small, the constriction resistance incurred by the electric current having to squeeze through such a gap becomes large. We therefore expect such a resistance to dominate over the material resistivity. The relevant solutions for the electric potential (5.106) and (5.146) imply that the potential gradient away from the contacts is negligible in comparison to that close to the contacts. We can consider physical analogies of the contact topologies studied in this chapter; the 2D contact could be thought of as a

long and thin contact of width ϵ which is very much smaller than its length. Such a contact might occur within a granular material if a sharp edge of one particle makes contact with a plane of another particle. The 3D, circular contact might be a sound approximation when a corner of one particle makes contact with a plane of another particle. Having approximations for long and thin contacts as well as circular contacts allows us to consider a variety of contacting behaviour when modelling the microscale in our homogenisation problem.

Due to the perceived dominance of constriction resistance over the material resistivity of the particle, we conjecture that by accurately capturing the small contacts, one can neglect geometrical details of the particle shape, namely, one can obtain sufficiently accurate solutions to the steady current conduction within a simplified particle geometry provided that the small contacts are accounted for appropriately.

The extreme influence of small contacts on the resistance of the system is in agreement with the literature, however we have only accounted for constriction resistance in this chapter. We extend our analysis into the influence of particle contacts on steady current conduction by considering the effect of the second component of contact resistance, that is, oxide-layer resistance which is attributed to imperfect contacts or infinitesimally close but untouching contacts.

Chapter 6

Contact resistance due to imperfect surfaces

In our analysis so far, we have considered perfect contacts represented as continuous media between particles. This neglects the components of contact resistance that we term asperity resistance and oxide-layer resistance, understood to be a consequence of imperfect contact interfaces.

In this chapter, we explore the influence of imperfect surfaces on electric current conduction through a granular material in the form of oxide-layer resistance. We begin by discussing models in the literature that attempt to capture asperity resistance, highlighting their complexity. We then briefly introduce how we expect to model oxide-layer resistance. We present some experimental results to explore the contribution of contact resistance to the overall resistance of two contacting particles subject to an applied load. The precise surface topography of anthracite particles in a furnace is extremely complex and irregular, therefore obtaining conclusive results from experiments conducted on such particles is extremely difficult. Instead, we consider half-cylinders made of graphite as we can manipulate the contacting surfaces to compare varying degrees of surface imperfection and its effect on the overall resistance of the system. To explain the experimental observations, we apply Hertzian and Holm theory [44, 46] to describe the influence of applied load on the resistance of the system and show that our experimental results do not agree with this prediction. We discuss similar trends observed in the literature and provide some possible explanations as to why our results differ from the theory.

We then introduce modelling adaptations to account for a thin, resistive layer between particles. The effect can be captured by a boundary condition between contacting particles and we briefly discuss the derivation of this condition. Following

this, we outline the homogenisation of the adapted problem, extending the methodology described in Chapter 3. The new boundary condition results in a discontinuous electric potential at the particle contacts which brings with it some numerical complexities. We discuss how to deal with such complexities in the homogenisation cell problem and solve the problem numerically.

6.1 Modelling imperfect surfaces

Contacts between nominally flat surfaces are understood to comprise a multitude of micro-contacts [39, 46]. This reduces the actual area through which current can conduct (a schematic of this effect is depicted in Figure 2.2). We refer to the influence of micro-contacts as surface roughness and the consequential resistance as asperity resistance. We recall the definition apparent contact area to describe the contact area perceived by the human eye, for example, the apparent contact area of two spherical particles is a circle. The actual contact area describes the total contact area due to the micro-contacts. It is likely that the actual contact area is several orders of magnitude smaller than the apparent contact, therefore the relationship for constriction-only resistance R_ϵ through a circular contact of diameter ϵ, namely $R_\epsilon = O(\epsilon^{-1})$ is rarely observed in reality. The resistance at a contact will be partly determined by the nature of these micro-contacts, however, capturing this mathematically is not an easy task. Furthermore, both apparent and actual contact areas are dependent on the force or pressure at the contact, thus whether the material experiences elastic and plastic deformation is relevant to accurately model these contacts.

Alongside asperity resistance, current conduction is also disrupted by thin, highly resistive layers between particles, termed oxide-layer resistance. For investigative ease, we will treat rough surfaces of micro-contacts and thin, resistive layers as two separate issues and discuss the relevant modelling techniques for each of them.

Rough surfaces

It is very difficult to include roughness in a mathematical model due to the complexity and randomness of the asperity distribution and because surfaces are often rough over multiple scales, somewhat like a fractal. Greenwood and Williamson [38] propose foundational models to show how contact deformation depends on the topography of the surface. They model a rough surface as a collection of spherical bumps of equal radius of curvature and allow their heights to follow a Gaussian distribution. This model predicts that the actual contact area, that is, the total area of all (deformed)

spherical contacts, is nearly proportional to the applied load. Bush et al. [15] derive a model in the same vein but approximate asperities as paraboloids whose heights are distributed randomly, then apply Hertzian contact theory. The authors also deduce that contact area and load are approximately proportional and claim that the constant of proportionality is linked to the Hertzian elastic modulus and the absolute mean slope of the surface profile. Jackson et al. [52] derive a multiscale model of the contact between rough surfaces by considering a surface consisting of smaller asperities located on top of larger asperities in repeated fashion. The authors similarly deduce that the real area of contact is proportional to the load and suggest that the mean contact pressure is determined by the surface topography, elastic constants and yield strength, instead of the applied load. They offer the explanation that increasing the load results in more asperities coming into contact, however, does not change the load supported per contact area.

Thin, resistive layers

Each of the rough-surface models above presents a complicated and intricate treatment of imperfect surfaces at the contact interfaces between particles. Given that we are already considering contacts that are several orders of magnitude smaller than the particles, which themselves are microscopic in comparison to the furnace, we choose not to model our contact as a collection of asperities and instead consider how to account for a highly resistive layer. We can model this phenomenon by studying current conduction through a very thin layer of given conductivity that is located between the two "contacting" particles. By considering the limiting behaviour of this thin layer, we obtain an electric current flux condition containing a parameter σ_c that represents the conductance at the contact interface, along with a jump condition for the the electric potential. The value of the contact conductance parameter should be chosen to approximate the resistance due to the layer itself, however, it could also be tactically chosen to approximately account for the resistance due to rough surfaces.

6.2 Resistance between contacting cylinders

Following our analysis of the importance of constriction resistance in Chapter 5, we wish to experimentally explore the total contact resistance between two particles and try to quantify the effect of apparent particle contact area upon the total resistance. We conduct a range of simple experiments where the basic idea is to pass a current between two materials in contact and measure the voltage drop to infer the total

resistance. By increasing the mechanical load on the system, we expect the contact area between the two materials to increase, thereby reducing the electrical resistance. By studying the resistance versus the load, we can compare the observed relationship to the theory presented by Hertz [44], who derives the expected contact area with respect to the applied load and Holm [46], who derives the expected constriction resistance with respect to contact area. Any difference between this resistance and that derived theoretically could potentially be attributed to imperfect contacts.

To gain preliminary results, we must enforce some simplifications. The first simplification is that we study the contact area between the curved surfaces of two half-cylinders, rather than angular particles that would be typical in a furnace. This is to allow us to approximate the contact area, a task that would be significantly more challenging, if not impossible, if we were to consider more general particles. The theory we hope to compare our results to is based upon Hertzian contact mechanics and the case of cylindrical surfaces in contact is well understood (for elastic deformations). We can also file, polish and gold-coat the cylindrical surfaces to reduce surface asperities, thereby diminishing resistance due to rough surfaces. We can then compare the resistance of such improved surfaces to untouched surfaces. However, we understand that these are highly ideal surfaces and will not necessarily reflect the contacts between particles in a calciner furnace, yet the rigorous Hertzian theory allows us to adopt a guideline as to the expected contact area between two general curved surfaces. This will allow us to better quantify the resistance as a function of contact area.

The second simplification is that we conduct the experiments using a highly isotropic material known as 2020 grade graphite, rather than the anthracite itself. Anthracite is extremely anisotropic, but we hope to attribute any resistance variation between experiments to differing contact areas and hence we consider 2020 grade graphite in the hope that the effect of anisotropy not significant.

Experimental apparatus

The experimental apparatus, as depicted in Figure 6.1, involves two half-cylinders of graphite of radius 10 mm that are positioned such that their curved surfaces are in contact with each other, while the opposing flat sides are in contact with copper plugs. We consider two cases, firstly where the cylinders' axes are perpendicular and secondly when they are in parallel, as in Figure 6.2. Together, the plugs and half-cylinders are placed between two metal plates, between which an electric current of $I = 0.011$ A is passed. We measure the voltage drop V between the two copper plugs

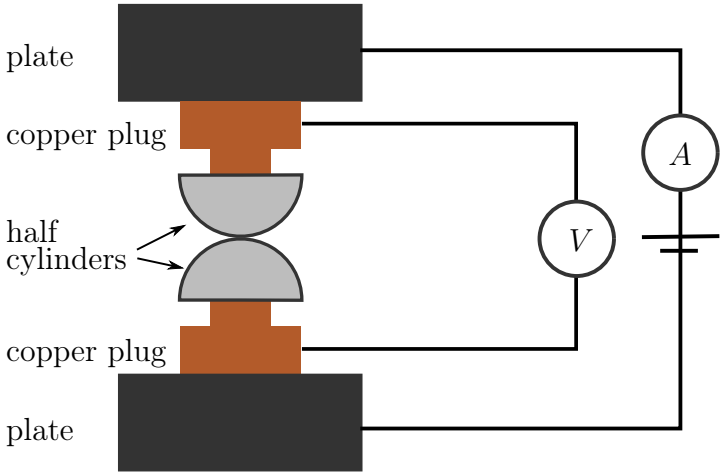
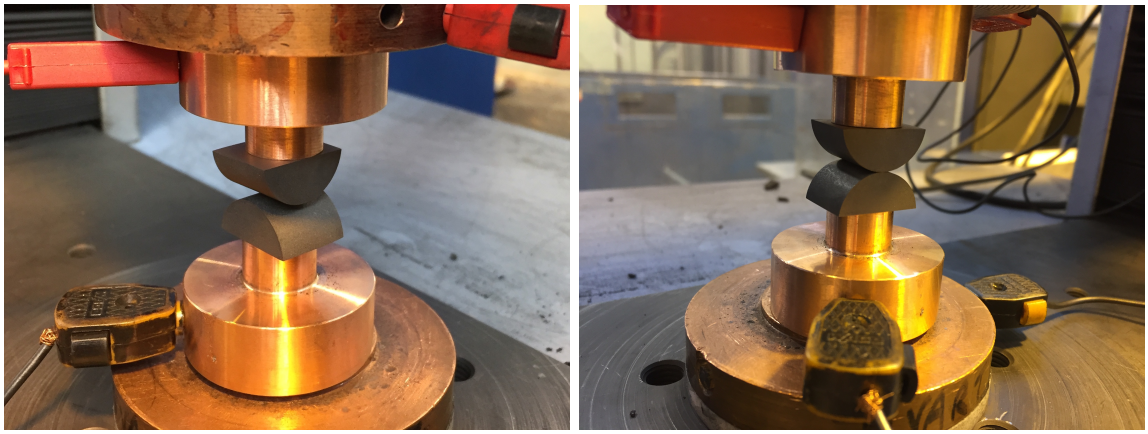


Figure 6.1: Schematic of the experimental apparatus used to conduct the experiments.

to allow us to calculate the resistance of the cylinders using Ohm's Law $R = V/I$. We note that we are only interested in the change in the resistance with load, therefore we can neglect the resistance of the copper plugs and the material resistivity of the graphite, as these contributions will remain constant throughout the experiment. We do, however, wish to minimise the contact resistance between the copper and the graphite, as any surface imperfections or oxide layers present here will affect the change in resistance with load. Copper is chosen for the plugs for this very reason, as it has an inherently low resistivity. We further minimise this interfacial resistance by filing, polishing and gold-coating the flat side of the half-cylinders. This should ensure a "clean" contact that is not subject to small fragments of insulating material



(a) Perpendicular axes. (b) Parallel axes.

Figure 6.2: Experimental set-up to analyse the current conduction through two half-cylinders with their curved surfaces in contact.

and reduces surface asperities. Gold has a very low resistivity, therefore coating the graphite surface with this material will reduce the contact resistance between the cylinder and the copper plug.

By continuously increasing the load on the particles and continuously recording the voltage, we observe how the resistance of the system changes with applied load. We obtain nearly 20,000 measurements per experiment and we repeat each experiment four times for each set-up (perpendicular and parallel). To further analyse the effect of contact resistance, we conduct the same experiments as above except the curved surfaces of the cylinder are also filed, polished and coated with gold. We are interested in this result since the discrepancy between the results of the regular contact and the gold-plated contact experiments should be solely due to diminishing some of the contact resistance between the cylinders.

Results

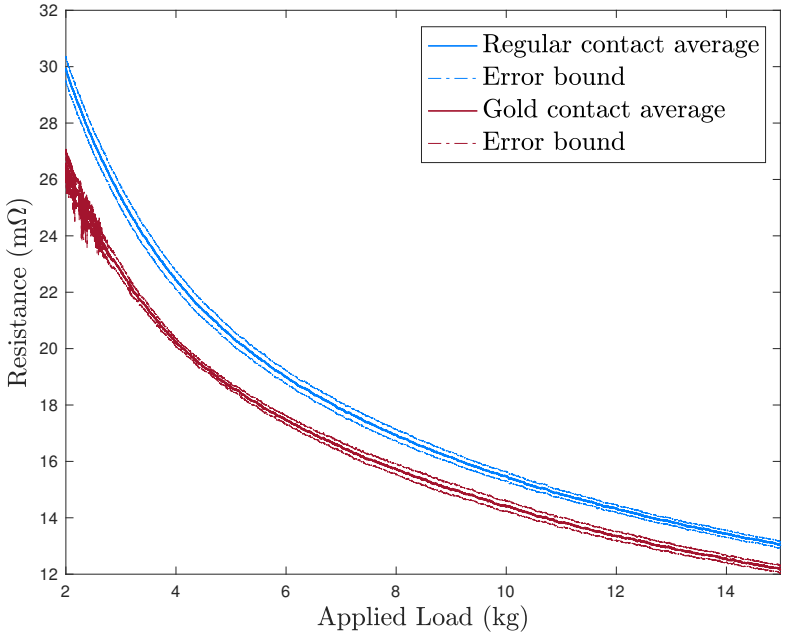
We plot the resistance in mΩ against the applied load in kg in Figure 6.3 for perpendicular and parallel alignment. The blue lines represent the results from the experiments conducted on regular contacts, whereas the red lines represent the gold-coated contacts. We plot the mean resistance along with error bounds given by one standard deviation from the mean deduced from repeating each experiment four times. Due to excessive noise for small loads, the horizontal axis representing the load begins at 2kg and increases to 15kg. We attribute the noise in Figure 6.3a, for the gold contacts, to stabilisation of the apparatus as the load is increased.

We notice a gradual decrease in the resistance of the system, as expected. As anticipated, the gold-coated experiment results in an overall lower resistance than the regular contact. The entirety of this decrease is due to dissipating some of the asperity or oxide-layer resistance, as we expect the contact area, and hence the constriction resistance, to be similar for the two experiments. The total resistance of the system reduces to around half of its initial value in each of the cases, indicating that the resistance due to particle contacts is extremely significant.

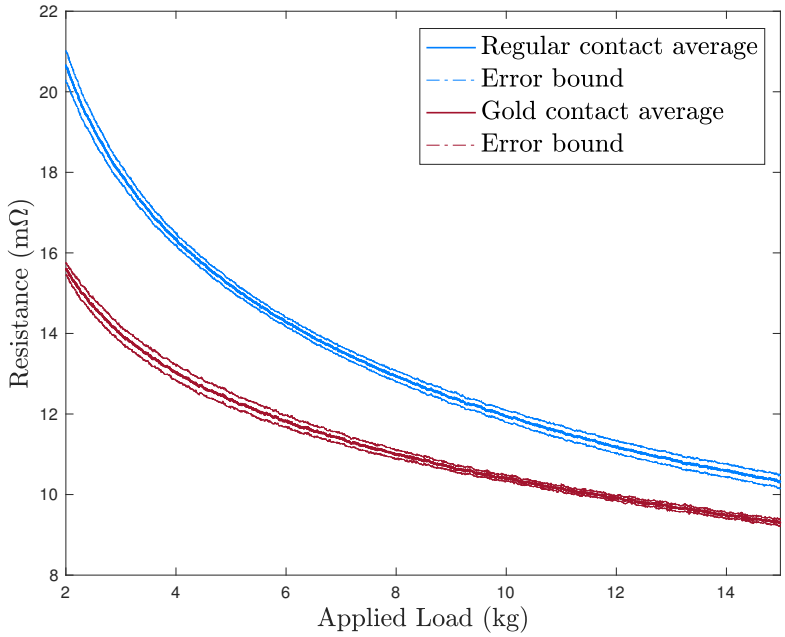
We now wish to study whether our experimental results can be explained by classical Hertzian theory.

6.2.1 Comparing Hertzian theory with experimental data

Consider two curved bodies of known radii of curvature in contact. Initially, the bodies touch at either a point (if perpendicular) or along a line (if parallel), however



(a) Axes aligned perpendicularly.



(b) Axes aligned in parallel.

Figure 6.3: Resistance versus applied load for cylinders in contact, repeated for gold-coated contact surfaces.

following the application of some load, elastic deformation enlarges these contacts into areas across which the loads are distributed. The analysis of this behaviour was first presented by Hertz [44], who imposes the following assumptions: (i) the surfaces are smooth, continuous, non-conforming and frictionless, (ii) the size of the contact area is much smaller than the characteristic dimensions of the contacting bodies, (iii) the strains caused by deformations are small and (iv) each solid can be assumed to behave as an elastic half-space.

Consider the experiment where the axes of the cylinders are positioned perpendicularly. When two cylinders both of radius R, length L, elastic moduli E_1 and E_2 and Poisson's ratios ν_1 and ν_2 are in contact with their axes perpendicular, subject to a load of magnitude W, as in Figure 6.4, Hertzian theory approximates the contact as a circle of radius a where

$$a = \left(\frac{3WR}{4LE^*}\right)^{\frac{1}{3}}, \tag{6.1}$$

and E^* is the reduced contact modulus, defined by

$$\frac{1}{E^*} = \frac{1-\nu_1^2}{E_1} + \frac{1-\nu_2^2}{E_2}. \tag{6.2}$$

Therefore, the applied load is proportional to the third power of the contact radius, namely,

$$W = O(a^3). \tag{6.3}$$

In order to include the relationship of contact area and electrical resistance, we couple Hertzian theory with Holm theory. Holm suggests that the constriction resistance R_c to current flowing through a circular contact between two surfaces behaves

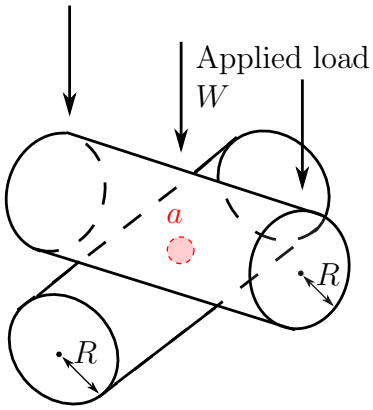


Figure 6.4: Perpendicular cylinders of radii R in contact at a circular region of radius a subject to applied load is denoted W.

like

$$R_c = O\left(a^{-1}\right), \tag{6.4}$$

where a is the radius of the contact, as also deduced via matched asymptotics in Section 5.3.2.

Therefore, combining the theories of Hertz and Holm suggests that the constriction resistance and the applied load are related by

$$R_c = O\left(W^{-\frac{1}{3}}\right). \tag{6.5}$$

To directly obtain an estimate for the relationship between the experimentally measured data for applied load and resistance we can conduct a linear regression analysis. By plotting the logarithm of the resistance R against the logarithm of the applied load W, the data reduces to almost a straight line. Using the `MATLAB` function `fitlm` to fit a linear regression model to the data, we obtain estimates for coefficients β_0 and β_2 in the linear relationship

$$\log R = \beta_0 + \beta_2 \log W, \tag{6.6}$$

therefore, we obtain the relationship

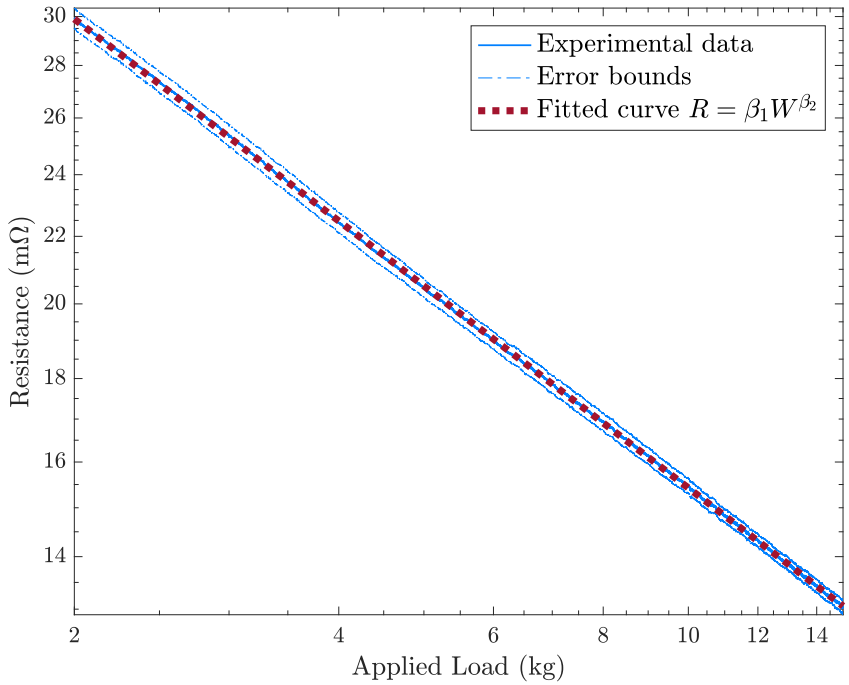
$$R = e^{\beta_0} W^{\beta_2} = \beta_1 W^{\beta_2}. \tag{6.7}$$

After conducting this linear regression analysis, we find that the results from our experiments demonstrate a different trend to (6.5), namely that the exponent $\beta_2 \approx -0.4$. The same trend is observed by Zeroukhi et al. [103] who carried out similar experiments on cylindrical copper wires of diameter 2.06 mm. Therefore, we claim that the experimentally measured resistance R_e is related to the load by

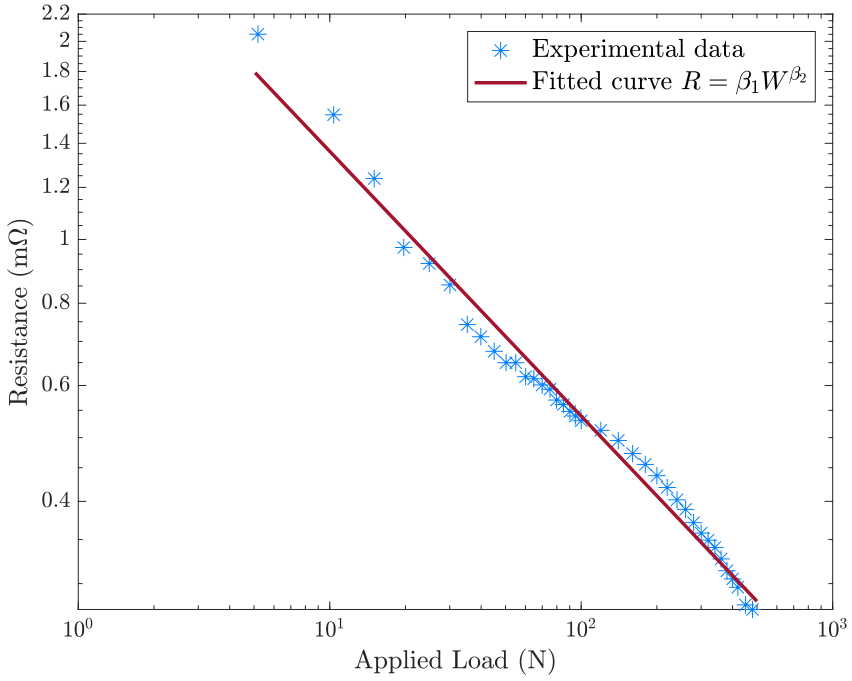
$$R_e = O\left(W^{-0.4}\right). \tag{6.8}$$

Our experimental results along with those of Zeroukhi et al. are represented graphically in Figure 6.5.

Zeroukhi et al. suggest an explanation to the shape of their experimental data, Figure 6.5b. They acknowledge that electrical contact resistance comprises more than just the constriction resistance explained by Holm and that oxide layer resistance is likely affecting the results. The authors also analyse the imprints on the wires due to the compressive force and claim that the imprint is invisible for loads less than 30 N, suggesting that the deformation is elastic. However, for forces greater than 30 N the imprint is visible, hence the deformation is plastic. This could be reason to reject Hertz analysis since to apply such theory we must assume that the materials are elastic.



(a) Log-log plot of experimental data for perpendicular cylinders as in Figure 6.2a fitted with a curve $R = \beta_1 W^{\beta_2}$ for $\beta_1 \approx 39.75$ mΩ/kg and $\beta_2 \approx -0.41$.



(b) Log-log plot of experimental data for perpendicular wires reproduced from [103] fitted with a curve $R = \beta_1 W^{\beta_2}$ for $\beta_1 \approx 3.44$ mΩ/N and $\beta_2 \approx -0.40$.

Figure 6.5: Experimental data fitted with $R = \beta_1 W^{\beta_2}$ curve.

6.2.2 Discussion

In conclusion, we observed how resistance varies with an applied load. We conducted experiments on a system of two half-cylinders which were placed in contact on their curved sides. We expected that increasing the load would result in a greater contact area between the cylinders and hence a reduction in the resistance. We observed such behaviour experimentally and compared it with the theoretical relationship between load and resistance outlined by Hertz and Holm for elastic bodies, however the theory did not correctly approximate the experiments. We speculate that the disagreement is a consequence of two main features: (1) the deformation of the materials is not elastic, as required by Hertz and (2) most surfaces are considered to be rough over many scales, similar to a fractal, therefore it is not always obvious how describe the actual contact area between materials. We chose to compare our results to Hertzian-Holm theory as it is rigorously explored and widely used in the literature, however it is not necessarily reflective of our physical experiments. We designed our experiments to be as appropriate as possible for comparison with this theory, namely, we manufactured cylinders so that we observed nearly perfect radii of curvature at the contacts and refined the surfaces to minimise roughness and oxide-layer influence. The disagreement of the data with the theory given these measures implies that the influence of contact resistance is very much more complicated than we expected, thereby it is very difficult to quantitatively include in our model.

However, despite an incomplete understanding of the precise contributions of different components of contact resistance, we can still confirm that the contact between particles has a great impact on the overall resistance of the system. This is evident from the substantial drop in the resistance as the load is increased and the contact area changes, as shown in Figures 6.3 and 6.5. This gives us further reason to believe that when considering the bulk resistivity of granular material, we should attribute a significant proportion of its resistance to the contacts between particles. The literature suggests that imperfect contacts contribute to the contact resistance, therefore we are compelled to include such behaviours in our homogenisation model.

6.3 Homogenisation of jump condition

In our homogenisation models outlined in Chapter 3, we have only included constriction resistance, thus neglecting any resistance due to imperfect contacts. As discussed in the introduction to the present chapter, we include thin, resistive layers at the contacts to capture the effect of imperfect contacts. Mathematically, this

involves modifying the boundary condition at the contacts to include a contact conductance parameter σ_c and allow the electric potential to jump from one particle to another.

Derivation of boundary condition

We consider a particle contact of size $\epsilon\delta L$ where the surfaces are separated by a very thin layer of width $\nu \ll \epsilon\delta L$ and conductivity σ_ν located between two particles of conductivity σ. Since the layer is extremely thin with respect to its other dimensions, we consider one-dimensional current conduction in this region. Consider the boundaries between the particles and the layer to be Γ^- and Γ^+, as in Figure 6.6. From continuity of current combined with Ohm's law within the thin layer, we deduce the following boundary conditions,

$$\sigma\nabla\phi\cdot\mathbf{n}|_{\Gamma^-} = \sigma_c[\phi]^+_-, \qquad \sigma\nabla\phi\cdot\mathbf{n}|_{\Gamma^+} = \sigma_c[\phi]^-_+, \tag{6.9}$$

where $\mathbf{n}$ is the outward normal to the relevant surface, $[\phi]^+_-$ denotes the jump in potential from Γ^- to Γ^+ and we term σ_c the contact conductance, given by

$$\sigma_c = \frac{\sigma_\nu}{\nu}. \tag{6.10}$$

We see that for very small σ_ν, the contact conductance σ_c is very small in comparison to σ, therefore the layer results in a large interfacial resistance.

We wish now to include this boundary condition within our homogenisation model outlined in Chapter 3. Although this may seem like a minor change to the mathematical model, it provokes significant modification of the numerical approach for the

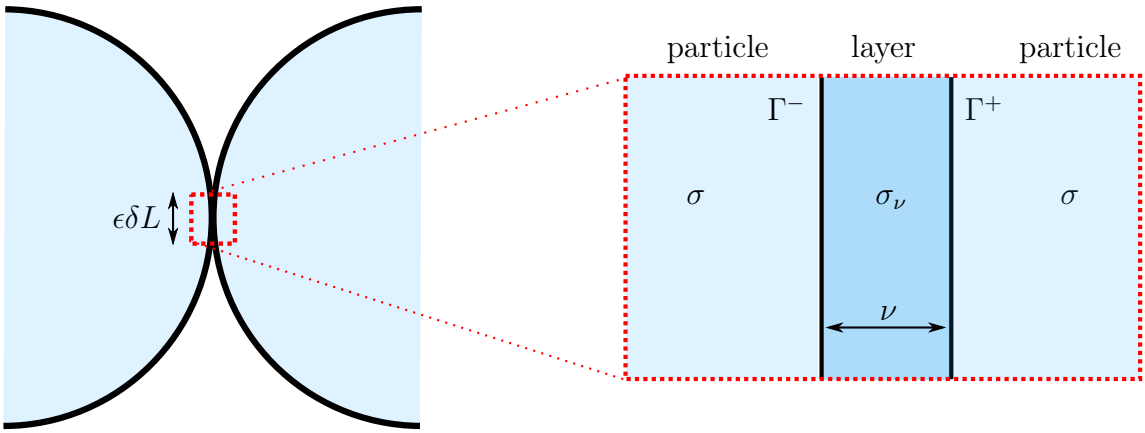


Figure 6.6: Schematic of a thin layer of conductivity σ_ν and width $\nu \ll \epsilon\delta L$ between two particles of conductivity σ.

cell problem, in particular, we need to include solution discontinuities on a periodic boundary. We follow the same methodology as before and discuss the extensions to consider the jump condition (6.9).

6.3.1 Problem adaptation

We again consider steady current conduction throughout the same domain as in Chapter 3, namely $\tilde{\Omega}$ of size L composed of solid particles $\tilde{\Omega}^S$ of conductivity $\tilde{\sigma}(\tilde{\mathbf{x}})$ and gas-filled voids as depicted in Figure 6.7. We consider the same boundary conditions as before except for the particle contacts $\tilde{\Gamma}_{C,j}$ for $j = 1, \ldots, M$ where M is the total number of particle contacts, where we enforce the jump conditions (6.9). The problem is thereby

$$\tilde{\nabla} \cdot (\tilde{\sigma}(\tilde{\mathbf{x}})\tilde{\nabla}\tilde{\phi}(\tilde{\mathbf{x}})) = 0, \qquad \tilde{\mathbf{x}} \in \tilde{\Omega}^S, \tag{6.11}$$

$$\tilde{\sigma}(\tilde{\mathbf{x}})\tilde{\nabla}\tilde{\phi}(\tilde{\mathbf{x}}) \cdot \mathbf{n} = \sigma_c[\tilde{\phi}(\tilde{\mathbf{x}})], \qquad \tilde{\mathbf{x}} \in \tilde{\Gamma}_{C,j}\, \forall j, \tag{6.12}$$

$$\tilde{\nabla}\tilde{\phi}(\tilde{\mathbf{x}}) \cdot \mathbf{n} = 0, \qquad \tilde{\mathbf{x}} \in \partial\tilde{\Omega}_N \cup \tilde{\Gamma}_{W,i}\, \forall i, \tag{6.13}$$

$$\tilde{\phi}(\tilde{\mathbf{x}}) = \phi_D(\tilde{\mathbf{x}}), \qquad \tilde{\mathbf{x}} \in \partial\tilde{\Omega}_D, \tag{6.14}$$

where $\mathbf{n}$ is the outwards normal to the surface and $[\tilde{\phi}]$ is the jump in the potential across the surface in the direction $\mathbf{n}$. We again prescribe $\phi_D(\tilde{\mathbf{x}})$ on $\partial\tilde{\Omega}_D = \partial\tilde{\Omega}_D^T \cup \partial\tilde{\Omega}_D^B$

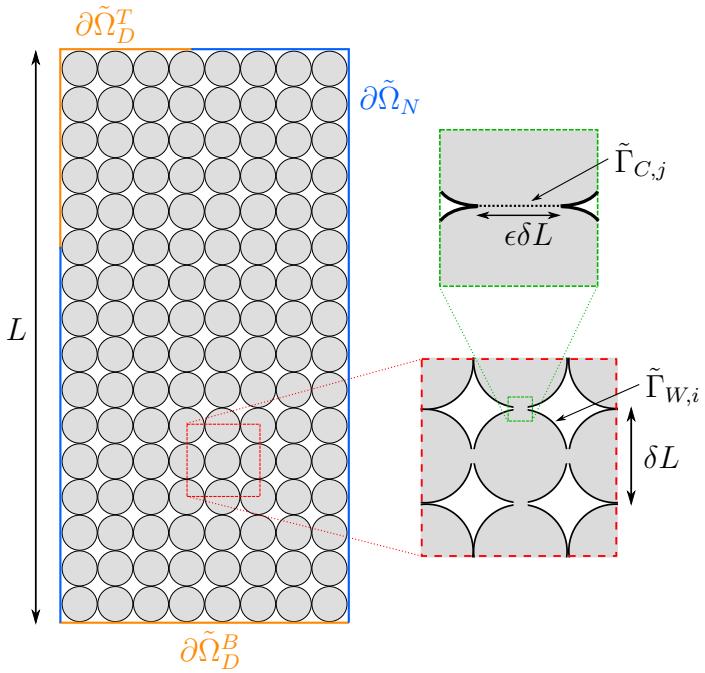


Figure 6.7: Simplified 2D representation of a regular, granular material comprised of truncated circular particles, as in Chapter 3 with particle contacts $\tilde{\Gamma}_{C,j}$ and the particle-gas boundaries $\tilde{\Gamma}_{W,i}$.

as

$$\phi_D(\tilde{\mathbf{x}}) = \begin{cases} \phi^T, & \tilde{\mathbf{x}} \in \partial\tilde{\Omega}_D^T, \\ \phi^B, & \tilde{\mathbf{x}} \in \partial\tilde{\Omega}_D^B, \end{cases} \tag{6.15}$$

and recall that σ_c is the contact conductance at the contact between particles.

Dimensionless equations

We scale our variables in the same way as in Chapter 3, namely,

$$\tilde{\mathbf{x}} = L\mathbf{x}, \qquad \tilde{\phi} = (\phi^T - \phi^B)\phi + \phi^B, \qquad \tilde{\sigma} = \beta\sigma, \tag{6.16}$$

where β is some characteristic size of the electrical conductivity. The contact boundary condition (6.12) becomes

$$\sigma(\mathbf{x})\nabla\phi(\mathbf{x}) \cdot \mathbf{n} = \frac{\sigma_c L}{\beta}[\phi(\mathbf{x})]. \tag{6.17}$$

The homogenisation technique that we wish to implement involves studying behaviour on the lengthscale of a particle. We rescale the spatial variable to account for this,

$$\mathbf{x} = \delta\mathbf{y}, \tag{6.18}$$

therefore (6.17) becomes

$$\sigma\nabla_{\mathbf{y}}\phi \cdot \mathbf{n} = \frac{\sigma_c \delta L}{\beta}[\phi]. \tag{6.19}$$

We label the prefactor $\lambda_c = \sigma_c\delta L/\beta$, and by considering its magnitude, we can capture the behaviour of the system according to different regimes. For example, $\lambda_c \gg 1$ corresponds to a very high contact conductance compared with the material conductivity. Recalling (6.10), we see that $\lambda_c \to \infty$ corresponds to the perfect contact scenario considered in Chapter 3. On the other hand, $\lambda_c \ll 1$ captures cases where the contact conductance is negligible in comparison with the material conductivity, therefore as $\lambda_c \to 0$, the contact becomes entirely insulating. This is a degenerate scenario, as it would result in zero current conduction from one particle to another. In the case where $\lambda_c = O(1)$, the material conductivity and contact conductance are of the same order of magnitude, hence we see a balance between the two. We wish to analyse the latter case, therefore throughout this chapter, we assume that

$$\lambda_c = \frac{\sigma_c \delta L}{\beta} = O(1). \tag{6.20}$$

We therefore write the dimensionless problem,

$$\nabla \cdot (\sigma(\mathbf{x})\nabla\phi(\mathbf{x})) = 0, \qquad \mathbf{x} \in \Omega^S, \tag{6.21}$$

$$\sigma(\mathbf{x})\nabla\phi(\mathbf{x}) \cdot \mathbf{n} = \frac{\lambda_c}{\delta}[\phi(\mathbf{x})], \qquad \mathbf{x} \in \Gamma_{C,j}\, \forall j, \tag{6.22}$$

$$\nabla\phi(\mathbf{x}) \cdot \mathbf{n} = 0, \qquad \mathbf{x} \in \partial\Omega_N \cup \Gamma_{W,i}\, \forall i, \tag{6.23}$$

$$\phi(\mathbf{x}) = 1, \qquad \mathbf{x} \in \partial\Omega_D^T, \tag{6.24}$$

$$\phi(\mathbf{x}) = 0, \qquad \mathbf{x} \in \partial\Omega_D^B. \tag{6.25}$$

6.3.2 Homogenisation of jump condition

We follow the same homogenisation procedure as in Chapter 3, namely we introduce the microscale $\mathbf{y} = \mathbf{x}/\delta$ where δ is the period of the microscale and expand the problem in terms of the two scales. The analysis is very similar to what we did before, therefore we will state the relevant results and only include detail into the new boundary condition at particle contacts. The reader should consult Chapter 3 for further explanation into the homogenisation technique.

Periodicity and the jump boundary condition

Throughout our homogenisation analysis in Chapter 3, we consider a representative microscopic volume that comprises a single particle, namely a truncated circle in 2D (as in Figure 3.3) or truncated sphere in 3D. Due to the periodic nature of the microstructure and how we choose our representative volume, the particle contacts lie on the cell boundary and thus the perfect contacts of Chapter 3 become periodic boundary conditions in the cell problem. We must take care when introducing the imperfect contact boundary condition (6.22) due to the jump in the electric potential. We claim that having the electric potential $\phi(\mathbf{x}, \mathbf{y})$ periodic in $\mathbf{y}$ is equivalent to having the potential jump from one contact boundary to its periodic partner on the opposite side of the cell. We illustrate this with a simple example.

Let us model an imperfect contact γ_c between particles of conductivity σ as a thin layer of width ν and conductivity σ_ν and suppose the electric potential at the centre of the layer is denoted ϕ^*, as in the left-hand diagram of Figure 6.8. Without loss of generality, we consider only one of the contacts for this analysis, however it can easily be extended to any particle contact. From the same analysis as above, the boundary conditions on γ_c^- and γ_c^+ can be derived as

$$\sigma\nabla\phi \cdot \mathbf{n}|_{\gamma_c^-} = 2\sigma_c[\phi]_-^*, \qquad \sigma\nabla\phi \cdot \mathbf{n}|_{\gamma_c^+} = 2\sigma_c[\phi]_+^*, \tag{6.26}$$

for $\mathbf{n}$, the outward normal vector to the relevant surface (in particular $\mathbf{n}|_{\gamma_c^-} = -\mathbf{n}|_{\gamma_c^+}$), contact conductance $\sigma_c = \sigma_\nu/\nu$ and $[\phi]_\pm^*$, the jump in the electric potential from $\gamma_c^\pm$ to the centre of the strip. Therefore, when applying the homogenisation technique and considering the problem on a representative, periodic, microscopic cell, such as the right-hand diagram of Figure 6.8, we consider the boundary conditions at the left and right contacts to be given by (6.26). The electric potential is still periodic at the contacts, namely, it takes the value ϕ^*, however there is a very thin region close to each boundary where the potential experiences a jump, as captured by the boundary condition.

We can show that for very thin layers, (6.26) can be written in terms of a jump $[\phi]_-^+$ from one side of the cell to the other, rather than in terms of the intermediate potential ϕ^*. Recalling conservation of current across the layer, namely

$$\sigma \nabla\phi \cdot \mathbf{n}|_{\gamma_c^-} = -\sigma \nabla\phi \cdot \mathbf{n}|_{\gamma_c^+}, \tag{6.27}$$

we deduce

$$2\phi^* = \phi^+ + \phi^-. \tag{6.28}$$

By using (6.28) in (6.26), we recover

$$\sigma \nabla\phi \cdot \mathbf{n}|_{\gamma_c^-} = \sigma_c [\phi]_-^+, \qquad \sigma \nabla\phi \cdot \mathbf{n}|_{\gamma_c^+} = \sigma_c [\phi]_+^-, \tag{6.29}$$

where $[\phi]_-^+$ denotes the jump in the potential from γ_c^- on the right-hand side of the particle to γ_c^+ on the left-hand side and vice versa for $[\phi]_+^-$. For negligibly thin layers, we enforce the following boundary condition at particle contacts γ_c:

$$\sigma \nabla\phi \cdot \mathbf{n} = \sigma_c [\phi], \tag{6.30}$$

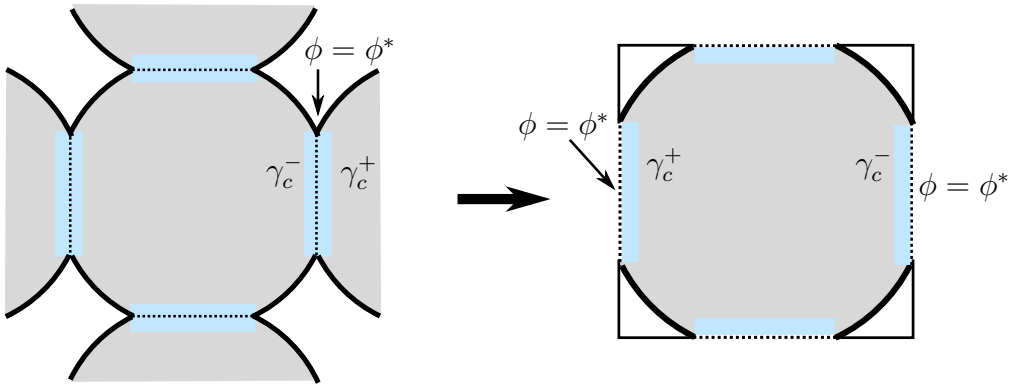


Figure 6.8: Schematic to explain the boundary conditions for the particle contacts in the unit cell.

where $[\phi]$ represents the jump in potential from one contact to its periodic partner on the other side of the cell. This may be intuitive when thinking about the periodic geometry and the boundary conditions defined on the macroscopic model, however we must be careful to follow the rules of the method of multiple scales [76] when writing down the microscopic model.

Homogenisation method

Considering both scales in our problem (6.21)–(6.25) and considering the analysis of the jumps in electric potential from one contact to another, we obtain the following governing equation:

$$\begin{aligned}\nabla_{\mathbf{y}} \cdot (\sigma \nabla_{\mathbf{y}} \phi_0) + \delta \left\{ \nabla_{\mathbf{y}} \cdot (\sigma(\nabla_{\mathbf{y}} \phi_1 + \nabla_{\mathbf{x}} \phi_0) + \nabla_{\mathbf{x}} \cdot (\sigma \nabla_{\mathbf{y}} \phi_0) \right\} \\ + \delta^2 \left\{ \nabla_{\mathbf{y}} \cdot (\sigma(\nabla_{\mathbf{y}} \phi_2 + \nabla_{\mathbf{x}} \phi_1)) + \nabla_{\mathbf{x}} \cdot (\sigma(\nabla_{\mathbf{y}} \phi_1 + \nabla_{\mathbf{x}} \phi_0)) \right\} = 0,\end{aligned} \tag{6.31}$$

defined within our unit cell ω^S in Figure 3.3, with boundary conditions

$$(\nabla_{\mathbf{y}} \phi_0 + \delta \left\{ \nabla_{\mathbf{y}} \phi_1 + \nabla_{\mathbf{x}} \phi_0 \right\} + \delta^2 \left\{ \nabla_{\mathbf{y}} \phi_2 + \nabla_{\mathbf{x}} \phi_1 \right\}) \cdot \mathbf{n} = 0, \tag{6.32}$$

defined for $\mathbf{y} \in \gamma_w$ and

$$\sigma(\nabla_{\mathbf{y}} \phi_0 + \delta \left\{ \nabla_{\mathbf{y}} \phi_1 + \nabla_{\mathbf{x}} \phi_0 \right\} + \delta^2 \left\{ \nabla_{\mathbf{y}} \phi_2 + \nabla_{\mathbf{x}} \phi_1 \right\}) \cdot \mathbf{n} = \lambda_c \left([\phi_0] + \delta [\phi_1] + \delta^2 [\phi_2] \right), \tag{6.33}$$

defined for $\mathbf{y} \in \gamma_c$, where $\mathbf{n}$ is the outward normal and $[\phi]$ denotes the jump in ϕ from contact γ_c to the contact on the opposing side of the cell. We consider the problem for each order of δ separately.

Leading-order problem

The leading-order problem is given by

$$\nabla_{\mathbf{y}} \cdot (\sigma \nabla_{\mathbf{y}} \phi_0) = 0, \qquad \mathbf{y} \in \omega^S, \tag{6.34}$$

$$\nabla_{\mathbf{y}} \phi_0 \cdot \mathbf{n} = 0, \qquad \mathbf{y} \in \gamma_w, \tag{6.35}$$

$$\sigma \nabla_{\mathbf{y}} \phi_0 \cdot \mathbf{n} = \lambda_c [\phi_0], \qquad \mathbf{y} \in \gamma_c. \tag{6.36}$$

As before, we multiply (6.34) by ϕ_0, integrate over ω^S and apply integration by parts to obtain

$$\int_{\omega^S} \nabla_{\mathbf{y}} \cdot (\sigma \nabla_{\mathbf{y}} \phi_0) \phi_0 \, \mathrm{d}\mathbf{y} = 0, \tag{6.37}$$

$$\int_{\omega^S} \sigma \nabla_{\mathbf{y}} \phi_0 \cdot \nabla_{\mathbf{y}} \phi_0 \, \mathrm{d}\mathbf{y} - \int_{\partial \omega^S} (\sigma \nabla_{\mathbf{y}} \phi_0 \cdot \mathbf{n}) \phi_0 \, \mathrm{d}S = 0, \tag{6.38}$$

where

$$\partial\omega^S = \gamma_w \cup \gamma_c. \tag{6.39}$$

Applying boundary conditions (6.35)–(6.36), we rewrite (6.38) as

$$\int_{\omega^S} \sigma \nabla_{\mathbf{y}} \phi_0 \cdot \nabla_{\mathbf{y}} \phi_0 \, \mathrm{d}\mathbf{y} - \int_{\gamma_c} \lambda_c[\phi_0]\phi_0 \, \mathrm{d}S = 0. \tag{6.40}$$

The surface integral in (6.40) must be dealt with carefully, since ϕ_0 is discontinuous here. Therefore, we must consider the integrand on both sides of the contact γ_c, namely γ_c^+ and γ_c^-. In particular, we write

$$\int_{\gamma_c} \lambda_c[\phi_0]\phi_0 \, \mathrm{d}S = \int_{\gamma_c} \left(\lambda_c[\phi_0]^+_- \phi_0^- + \lambda_c[\phi_0]^-_+ \phi_0^+ \right) \mathrm{d}S. \tag{6.41}$$

However, since the contacts γ_c lie on the boundary of the periodic cell, γ_c^+ for the contact on one side of the cell is equivalent to γ_c^- for the contact on the other side of the cell, as depicted in Figure 6.8. We must take care not to double-count the contribution of the particle contacts and thus we divide (6.41) by 2. From (6.41) we obtain

$$\int_{\gamma_c} \lambda_c[\phi_0]\phi_0 \, \mathrm{d}S = \frac{\lambda_c}{2} \int_{\gamma_c} [\phi_0]^+_- \left(\phi_0^- - \phi_0^+ \right) \mathrm{d}S, \tag{6.42}$$

$$= -\frac{\lambda_c}{2} \int_{\gamma_c} [\phi_0]^2 \, \mathrm{d}S. \tag{6.43}$$

Substituting (6.43) into (6.40), we obtain

$$\int_{\omega^S} \sigma \nabla_{\mathbf{y}} \phi_0 \cdot \nabla_{\mathbf{y}} \phi_0 \, \mathrm{d}\mathbf{y} + \frac{\lambda_c}{2} \int_{\gamma_c} [\phi_0]^2 \, \mathrm{d}S = 0. \tag{6.44}$$

For this to be true, we require

$$\nabla_{\mathbf{y}} \phi_0 = 0, \qquad [\phi_0] = 0, \tag{6.45}$$

therefore, the leading-order solution ϕ_0 is independent of the microscale $\mathbf{y}$, or rather

$$\phi_0 = \phi_0(\mathbf{x}). \tag{6.46}$$

First-order problem

The problem at first-order is given by

$$\nabla_{\mathbf{y}} \cdot (\sigma(\nabla_{\mathbf{y}} \phi_1 + \nabla_{\mathbf{x}} \phi_0)) = 0, \qquad \mathbf{y} \in \omega^S, \tag{6.47}$$

$$(\nabla_{\mathbf{y}} \phi_1 + \nabla_{\mathbf{x}} \phi_0) \cdot \mathbf{n} = 0, \qquad \mathbf{y} \in \gamma_w, \tag{6.48}$$

$$\sigma(\nabla_{\mathbf{y}} \phi_1 + \nabla_{\mathbf{x}} \phi_0) \cdot \mathbf{n} = \lambda_c[\phi_1], \qquad \mathbf{y} \in \gamma_c. \tag{6.49}$$

The cell problem is defined as

$$\nabla_{\mathbf{y}} \cdot (\sigma(\mathbf{I} + \nabla_{\mathbf{y}} \mathbf{\Phi})) = 0, \qquad \mathbf{y} \in \omega^S, \tag{6.50}$$

$$(\mathbf{I} + \nabla_{\mathbf{y}} \mathbf{\Phi}) \cdot \mathbf{n} = 0, \qquad \mathbf{y} \in \gamma_w, \tag{6.51}$$

$$\sigma(\mathbf{I} + \nabla_{\mathbf{y}} \mathbf{\Phi}) \cdot \mathbf{n} = \lambda_c \left[\mathbf{\Phi}\right], \qquad \mathbf{y} \in \gamma_c, \tag{6.52}$$

where we once again define $\phi_1 = \mathbf{\Phi} \cdot \nabla_{\mathbf{x}} \phi_0 + \hat{\phi}_1$.

Second-order problem

Finally, the second-order problem is given by

$$\nabla_{\mathbf{y}} \cdot (\sigma(\nabla_{\mathbf{y}} \phi_2 + \nabla_{\mathbf{x}} \phi_1)) + \nabla_{\mathbf{x}} \cdot (\sigma(\nabla_{\mathbf{y}} \phi_1 + \nabla_{\mathbf{x}} \phi_0)) = 0, \qquad \mathbf{y} \in \omega^S, \tag{6.53}$$

$$(\nabla_{\mathbf{y}} \phi_2 + \nabla_{\mathbf{x}} \phi_1) \cdot \mathbf{n} = 0, \qquad \mathbf{y} \in \gamma_w, \tag{6.54}$$

$$\sigma(\nabla_{\mathbf{y}} \phi_2 + \nabla_{\mathbf{x}} \phi_1) \cdot \mathbf{n} = \lambda_c[\phi_2], \qquad \mathbf{y} \in \gamma_c. \tag{6.55}$$

By integrating (6.53) over ω^S and applying integration by parts followed by boundary conditions (6.54)–(6.55), we obtain

$$\frac{1}{|\omega|} \int_{\gamma_c} \lambda_c[\phi_2] \, \mathrm{d}S + \nabla_{\mathbf{x}} \cdot \left(\left\{ \frac{1}{|\omega|} \int_{\omega^S} \sigma(\mathbf{I} + \nabla_{\mathbf{y}} \mathbf{\Phi}) \mathrm{d}\mathbf{y} \right\} \nabla_{\mathbf{x}} \phi_0 \right) = 0. \tag{6.56}$$

We again must take care to account for the discontinuity of ϕ_2 on particle contacts γ_c. In a similar analysis to the leading-order problem, we write

$$\int_{\gamma_c} \lambda_c[\phi_2] \, \mathrm{d}S = \frac{1}{2} \int_{\gamma_c} \lambda_c \left([\phi_2]^+_- + [\phi_2]^-_+ \right) \, \mathrm{d}S = 0, \tag{6.57}$$

since $[\phi_2]^+_- = -[\phi_2]^-_+$. Therefore, we arrive at the homogenised problem,

$$\nabla_{\mathbf{x}} \cdot (\boldsymbol{\sigma}_{\text{eff}} \nabla_{\mathbf{x}} \phi_0) = 0, \qquad \mathbf{x} \in \Omega, \tag{6.58}$$

$$\phi_0(\mathbf{x}) = 1, \qquad \mathbf{x} \in \partial\Omega_D^T, \tag{6.59}$$

$$\phi_0(\mathbf{x}) = 0, \qquad \mathbf{x} \in \partial\Omega_D^B, \tag{6.60}$$

$$\nabla \phi_0 \cdot \mathbf{n} = 0, \qquad \mathbf{x} \in \partial\Omega_N, \tag{6.61}$$

defined in the homogeneous domain Ω and with effective conductivity $\boldsymbol{\sigma}_{\text{eff}}$, given by

$$\boldsymbol{\sigma}_{\text{eff}} = \frac{1}{|\omega|} \int_{\omega^S} \sigma(\mathbf{I} + \nabla_{\mathbf{y}} \mathbf{\Phi}) \mathrm{d}\mathbf{y}, \tag{6.62}$$

for $\mathbf{\Phi}$ the solution to the cell problem (6.50)–(6.52). The homogenised problem and effective conductivity take the same form as the perfect contact problem (3.35)–(3.38) from Chapter 3, however, as discussed, the influence of the microstructure is captured in the cell problem, therefore imperfect contacts affect the value of the effective conductivity.

6.3.3 Deriving the variational form

The numerical procedure is identical to the perfect-contact case, namely, we solve the cell problem (6.50)–(6.52) within the representative unit cell, calculate the effective conductivity tensor (6.62) and finally solve the homogenised problem (6.58)–(6.61) in a homogeneous domain. However, an added complexity arises in the cell problem due to the jump in the vector function $\mathbf{\Phi}$. In order to include this jump in an efficient manner, we use discontinuous Galerkin (DG) methods, in particular the symmetric interior penalty Galerkin (SIPG) method [7, 31, 82, 101]. Similar to the continuous Galerkin (CG) methods used throughout this thesis, the DG method is a finite element scheme to solve a weak formulation of a mathematical model. In contrast to CG methods, the DG method involves a trial space of functions that are only piecewise continuous and therefore is very beneficial for problems where the solution experiences a jump along boundary facets.

DG methods are well understood and used in the literature [8, 25, 82], however, due to the complexity associated with our periodic domain, we include some notation and numerical detail.

Symmetric interior penalisation Galerkin method

The SIPG method for elliptic problems, first introduced by Arnold [7], Douglas and Dupont [31] and Wheeler [101], is an established discontinuous Galerkin method which uses penalties to weakly enforce continuity of both the solution and the boundary conditions. The method is attractive due to its enhanced flexibility afforded by discontinuous elements whilst also providing robust, high-order accurate approximations and is able to handle local mesh refinement and unstructured meshes [33].

The variational form for the SIPG method is found by integrating the equation over each mesh element and summing over all elements, followed by the addition of two "stabilisation" terms. The first of these stabilisation terms is a symmetrising term that corresponds to fluxes obtained after integration by parts, needed to ensure we get a symmetric bilinear form. The second is known as a penalisation term which enforces weak continuity of the solution where necessary. It is well understood that there exists a threshold penalty above which the bilinear form is coercive, hence the scheme is both stable and convergent [9, 10, 31]. One can regulate the degree of smoothness of the approximate solution through local variation of the penalisation term, thereby allowing closer approximation of solutions which vary in character throughout the domain. The penalisation parameter is chosen from the error analysis of the method.

We refer the reader to deterministic methods to deduce the threshold parameter [33, 83], however this will not be a focus of this thesis.

For the reasons outlined above, we choose to use the SIPG method for our numerical analysis and outline how we set up and solve this finite element scheme.

Domain and edge notation

Consider the cell domain ω^S in which we will solve our cell problem (6.50)–(6.52). We split this domain into a covering $\mathcal{T}$, known as the triangulation or the mesh, consisting of open triangles T, referred to henceforth as the elements. We write

$$\omega^S = \bigcup_{T \in \mathcal{T}} \bar{T}, \tag{6.63}$$

where the bar notation denotes closure. We denote the "skeleton" of the mesh by

$$\mathcal{F} = \bigcup_{T \in \mathcal{T}} \partial T, \tag{6.64}$$

which is divided up into various subgroups of edges or facets. We denote interior facets $\mathcal{F}_i$, particle wall facets $\mathcal{F}_w$ and particle contact facets $\mathcal{F}_c$, such that

$$\mathcal{F}_i = \mathcal{F} \setminus (\gamma_w \cup \gamma_c), \quad \mathcal{F}_w = \mathcal{F} \cap \gamma_w, \quad \mathcal{F}_c = \mathcal{F} \cap \gamma_c. \tag{6.65}$$

Let T^+ and T^- be two elements that share an edge in the interior, namely $e := T^+ \cap T^- \in \mathcal{F}_i$ with outward normal unit vectors $\mathbf{n}^+$ and $\mathbf{n}^-$ on e.

Jumps, averages and mesh size

For scalar function $\psi : \omega^s \to \mathbb{R}$ and vector function $\mathbf{v} : \omega^s \to \mathbb{R}^2$, let $\psi^\pm$ and $\mathbf{v}^\pm$ be the function values on the $T^\pm$ sides of edge e respectively. We define each function average on e as

$$\langle \psi \rangle = \frac{1}{2}\left(\psi^+ + \psi^-\right), \qquad \langle \mathbf{v} \rangle = \frac{1}{2}\left(\mathbf{v}^+ + \mathbf{v}^-\right), \tag{6.66}$$

and the jump in each function value across e as

$$[\![\psi]\!] = \left(\psi^+ - \psi^-\right)\mathbf{n}, \qquad [\![\mathbf{v}]\!] = \left(\mathbf{v}^+ - \mathbf{v}^-\right) \cdot \mathbf{n}, \tag{6.67}$$

where in this case $\mathbf{n} = \mathbf{n}^-$ represents the direction in which we are measuring the jump. If e is an outer boundary edge, i.e. e corresponds to only one element T^+, we define the averages to be $\langle \psi \rangle = \psi^+$, $\langle \mathbf{v} \rangle = \mathbf{v}^+$ and the jumps to be $[\![\psi]\!] = \psi^+ \mathbf{n}^+$, $[\![\mathbf{v}]\!] = \mathbf{v}^+ \cdot \mathbf{n}^+$.

Variational form

As aforementioned, discontinuous Galerkin methods use piecewise continuous basis functions within approximation spaces. Let $\mathcal{P}^k(T)$ denote the space of polynomials of degree k on element T. For $k \geq 1$ and triangulation $\mathcal{T}$ of ω^S, we introduce the discontinuous finite element space

$$V_k(\mathcal{T}) := \{v \in L^2(\omega^S) : v|_T \in \mathcal{P}^k(T), \forall T \in \mathcal{T}\}. \tag{6.68}$$

We are interested in deriving the variational form of the cell problem (6.50)–(6.52). For analytical simplicity, we consider the componentwise version of the cell problem, namely

$$\nabla_{\mathbf{y}} \cdot (\sigma(\mathbf{e}_i + \nabla_{\mathbf{y}}\Phi_i)) = 0, \qquad \mathbf{y} \in \omega^S, \tag{6.69}$$

$$(\mathbf{e}_i + \nabla_{\mathbf{y}}\Phi_i) \cdot \mathbf{n} = 0, \qquad \mathbf{y} \in \gamma_w, \tag{6.70}$$

$$\sigma(\mathbf{e}_i + \nabla_{\mathbf{y}}\Phi_i) \cdot \mathbf{n} = \lambda_c \left[\Phi_i\right], \qquad \mathbf{y} \in \gamma_c, \tag{6.71}$$

where Φ_i for $i = 1, 2$ are the components of the two-dimensional vector function $\mathbf{\Phi}$ and $\mathbf{e}_i$ is the relevant unit vector.

Let Ψ be a trial function in $V_k(\mathcal{T})$. We multiply (6.69) by Ψ and integrate by parts in each element $T \in \mathcal{T}$,

$$\int_T \sigma(\mathbf{e}_i + \nabla_{\mathbf{y}}\Phi_i) \cdot \nabla_{\mathbf{y}}\Psi \, \mathrm{d}\mathbf{y} - \int_{\partial T} \{\sigma(\mathbf{e}_i + \nabla_{\mathbf{y}}\Phi_i) \cdot \mathbf{n}\}\Psi \, \mathrm{d}S = 0, \tag{6.72}$$

where $\mathbf{n}$ denotes the outward normal to each element edge. By summing over all elements $T \in \mathcal{T}$ we obtain

$$\sum_{T\in\tau} \int_T \sigma(\mathbf{e}_i + \nabla_{\mathbf{y}}\Phi_i) \cdot \nabla_{\mathbf{y}}\Psi \, \mathrm{d}\mathbf{y} - \sum_{T\in\tau} \int_{\partial T} \{\sigma(\mathbf{e}_i + \nabla_{\mathbf{y}}\Phi_i) \cdot \mathbf{n}\}\Psi \, \mathrm{d}S = 0. \tag{6.73}$$

The terms defined on the element boundaries ∂T can be split according to the facet subspaces $\mathcal{F}_i$, $\mathcal{F}_w$ and $\mathcal{F}_c$, on which different conditions hold. We consider each of these subspaces separately.

Interior facets $\mathcal{F}_i$

Due to the piecewise continuity of the function space, the functions can take a different value on each side of every interior facet. To allow for this, we denote the function value on each side of edge e with $\pm$ superscript, therefore

$$\begin{aligned}\sum_{e\in\mathcal{F}_i} \int_e \{\sigma(\mathbf{e}_i + \nabla_{\mathbf{y}}\Phi_i) \cdot \mathbf{n}\}\Psi \mathrm{d}S = \sum_{e\in\mathcal{F}_i} \int_e (&\{\sigma^+(\mathbf{e}_i + \nabla_{\mathbf{y}}\Phi_i^+) \cdot \mathbf{n}^+\}\Psi^+ \\ &+ \{\sigma^-(\mathbf{e}_i + \nabla_{\mathbf{y}}\Phi_i^-) \cdot \mathbf{n}^-\}\Psi^-)\mathrm{d}S,\end{aligned} \tag{6.74}$$

By noting $\mathbf{n}^+ = -\mathbf{n}^-$, we can write

$$\sum_{e\in\mathcal{F}_i}\int_e \{\sigma(\mathbf{e}_i + \nabla_{\mathbf{y}}\Phi_i)\cdot\mathbf{n}\}\Psi \mathrm{d}S = \sum_{e\in\mathcal{F}_i}\int_e [\![\sigma(\mathbf{e}_i + \nabla_{\mathbf{y}}\Phi_i)\Psi]\!]\mathrm{d}S. \tag{6.75}$$

We use the identity

$$[\![\mathbf{v}\psi]\!] = \langle\mathbf{v}\rangle\cdot[\![\psi]\!] + \langle\psi\rangle[\![\mathbf{v}]\!], \tag{6.76}$$

for vector $\mathbf{v}$ and scalar ψ, which can be easily verified using (6.66)–(6.67), to expand (6.75) as

$$\begin{aligned}\sum_{e\in\mathcal{F}_i}\int_e \{\sigma(\mathbf{e}_i + \nabla_{\mathbf{y}}\Phi_i)\cdot\mathbf{n}\}\Psi \mathrm{d}S = \sum_{e\in\mathcal{F}_i}\int_e (&\langle\sigma(\mathbf{e}_i + \nabla_{\mathbf{y}}\Phi_i)\rangle\cdot[\![\Psi]\!] \\ &+ \langle\Psi\rangle[\![\sigma(\mathbf{e}_i + \nabla_{\mathbf{y}}\Phi_i)]\!])\mathrm{d}S.\end{aligned} \tag{6.77}$$

Note that in the interior of the domain, the following must hold,

$$[\![\nabla_{\mathbf{y}}\Phi_i]\!] = 0, \qquad \text{(continuity of flux)}, \tag{6.78}$$

$$[\![\Phi_i]\!] = 0, \qquad \text{(continuity of solution)}, \tag{6.79}$$

therefore, the second term on the right-hand side of (6.77) is zero by continuity of flux which yields

$$\sum_{e\in\mathcal{F}_i}\int_e \{\sigma(\mathbf{e}_i + \nabla_{\mathbf{y}}\Phi_i)\cdot\mathbf{n}\}\Psi \mathrm{d}S = \sum_{e\in\mathcal{F}_i}\int_e \langle\sigma(\mathbf{e}_i + \nabla_{\mathbf{y}}\Phi_i)\rangle\cdot[\![\Psi]\!]\mathrm{d}S. \tag{6.80}$$

Following the SIPG procedure [7, 31, 82, 101], more precisely since (6.80) does not give rise to a positive-definite operator, we must include stabilisation terms, namely the symmetrising term and the penalisation term. From continuity of solution (6.79), we observe

$$\sum_{e\in\mathcal{F}_i}\int_e \langle\sigma(\mathbf{e}_i + \nabla_{\mathbf{y}}\Psi)\rangle\cdot[\![\Phi_i]\!]\mathrm{d}S = 0, \tag{6.81}$$

assuming that Ψ is smooth enough, hence we can symmetrise (6.80) by adding (6.81).

We also add a penalty term to impose weak continuity on the solution across the interior boundaries. The penalty term is given by

$$-\sum_{e\in\mathcal{F}_i}\int_e \frac{\alpha_e}{|e|^\beta}[\![\Phi_i]\!][\![\Psi]\!]\mathrm{d}S, \tag{6.82}$$

where α_e is a positive number associated with the edge e of length $|e|$ and $\beta \geq 1$ is a real number. By including both stabilisation terms (6.81) and (6.82) in (6.80), we

find that the boundary term of (6.73) according to the interior facets is

$$\begin{aligned}\sum_{e\in\mathcal{F}_i}\int_e\{\sigma(\mathbf{e}_i+\nabla_{\mathbf{y}}\Phi_i)\cdot\mathbf{n}\}\Psi\mathrm{d}S=\sum_{e\in\mathcal{F}_i}\int_e(\langle\sigma(\mathbf{e}_i+\nabla_{\mathbf{y}}\Phi_i)\rangle\cdot[\![\Psi]\!]\\+\sum_{e\in\mathcal{F}_i}\int_e(\langle\sigma(\mathbf{e}_i+\nabla_{\mathbf{y}}\Psi)\rangle\cdot[\![\Phi_i]\!])\mathrm{d}S\\-\sum_{e\in\mathcal{F}_i}\int_e\frac{\alpha_e}{|e|^\beta}[\![\Phi_i]\!][\![\Psi]\!]\mathrm{d}S.\end{aligned}\tag{6.83}$$

Expression (6.83) gives rise to a positive-definite bilinear form if $\alpha_e/|e|^\beta$ is large enough. The penalty parameter α_e is a positive constant on each facet e whereas the parameter β is a global constant that is generally chosen to be $d-1$ where $d=1,2$ is the dimension. If $\beta>d-1$, the SIPG method is said to be superpenalised [82]. The choice of the penalisation parameter α_e arises from the error analysis of the method.

Contact facets $\mathcal{F}_c$

Due to the periodicity of the unit cell we treat the contact facets in a similar way as the interior facets outlined above. In a non-periodic problem, there would be no concept of a function value on the outer side of these facets, however through periodicity, the outer side of a boundary facet on the right-hand side of the cell is identical to the inner side of the corresponding boundary facet on the left-hand side of the cell. Therefore we obtain the following expression for the contact facet terms in the variational form,

$$\begin{aligned}\sum_{e\in\mathcal{F}_c}\int_e\{\sigma(\mathbf{e}_i+\nabla_{\mathbf{y}}\Phi_i)\cdot\mathbf{n}\}\Psi\mathrm{d}S=\sum_{e\in\mathcal{F}_c}\int_e(\langle\sigma(\mathbf{e}_i+\nabla_{\mathbf{y}}\Phi_i)\rangle\cdot[\![\Psi]\!]\\+\langle\Psi\rangle[\![\sigma(\mathbf{e}_i+\nabla_{\mathbf{y}}\Psi)]\!])\mathrm{d}S.\end{aligned}\tag{6.84}$$

However our continuity conditions are different for the contact facets, namely the following must hold,

$$[\![\nabla_{\mathbf{y}}\Phi_i]\!]=0,\qquad\text{(continuity of flux)},\tag{6.85}$$

$$\sigma(\mathbf{e}_i+\nabla_{\mathbf{y}}\Phi_i)\cdot\mathbf{n}=\lambda_c\,[\Phi_i]\,,\qquad\text{(jump in solution)}.\tag{6.86}$$

As with the interior facets, the second term on the right-hand side of (6.84) is zero due to continuity of flux, whereas the integrand of the first term can be written as

$$\langle \sigma(\mathbf{e}_i + \nabla\Phi_i)\rangle \cdot [\![\Psi]\!] = \frac{1}{2}\left(\sigma^+(\mathbf{e}_i^+ + \nabla_{\mathbf{y}}\Phi_i^+) + \sigma^-(\mathbf{e}_i^- + \nabla_{\mathbf{y}}\Phi_i^-)\right)\cdot \mathbf{n}[\Psi]_-^+, \tag{6.87}$$

$$= \frac{\lambda_c}{2}([\Phi_i]_-^+ - [\Phi_i]_+^-)[\Psi]_-^+, \tag{6.88}$$

$$= \lambda_c[\Phi_i][\Psi]. \tag{6.89}$$

Hence the boundary term of (6.73) according to the contacts is

$$\sum_{e\in\mathcal{F}_c}\int_e \{\sigma(\mathbf{e}_i + \nabla_{\mathbf{y}}\Phi_i)\cdot\mathbf{n}\}\Psi \mathrm{d}S = \sum_{e\in\mathcal{F}_c}\int_e \lambda_c[\Phi_i][\Psi]\mathrm{d}S. \tag{6.90}$$

Note that we do not include any penalisation term here as the solution is discontinuous along the contact facets.

Wall facets $\mathcal{F}_w$

Finally, the boundary term of (6.73) according to the particle walls is

$$\sum_{e\in\mathcal{F}_w}\int_e \{\sigma(\mathbf{e}_i + \nabla_{\mathbf{y}}\Phi_i)\cdot\mathbf{n}\}\Psi \mathrm{d}S = 0, \tag{6.91}$$

easily deduced from the boundary condition (6.70).

Variational form of cell problem

Hence, combining (6.83), (6.90) and (6.91) into (6.73), the variational form of the componentwise cell problem (6.69)–(6.71) is

$$\begin{aligned}\sum_{T\in\tau}\int_T \sigma(\mathbf{e}_i + \nabla_{\mathbf{y}}\Phi_i)\cdot\nabla_{\mathbf{y}}\Psi\,\mathrm{d}\mathbf{y}& \\ - \sum_{e\in\mathcal{F}_i}\int_e (\langle\sigma(\mathbf{e}_i+\nabla\Phi_i)\rangle\cdot[\![\Psi]\!] + \langle\sigma(\mathbf{e}_i+\nabla\Psi)\rangle\cdot[\![\Phi_i]\!])\mathrm{d}S& \\ + \sum_{e\in\mathcal{F}_i}\int_e \frac{\alpha_e}{|e|^\beta}[\![\Phi_i]\!][\![\Psi]\!]\mathrm{d}S - \sum_{e\in\mathcal{F}_c}\int_e \lambda_c[\Phi_i][\Psi]\mathrm{d}S = 0.&\end{aligned} \tag{6.92}$$

for all Ψ in $V_k(\mathcal{T})$ given by (6.68).

6.3.4 Numerical results

In this section, we demonstrate the efficacy of homogenisation when solving the non-dimensional model for steady current conduction with contact resistance (6.21)–(6.25), followed by a study of the influence of the contact conductance parameter

λ_c on the effective conductivity $\boldsymbol{\sigma}_{\text{eff}}$. We begin by solving the problem for fixed $\lambda_c = 1$ via homogenisation and comparing the solution with that obtained directly, along with the comparison of the corresponding computational costs. We consider the same domain $\Omega = [0, 0.2] \times [0, 1]$ as in Chapter 3, comprising a periodic array of truncated circular particles of period δ, where the width of the contact interface between particles is $\epsilon\delta$. For our numerical analysis, we consider δ ranging from 10^{-2} to 10^{-1} and let $\epsilon = 0.2$, recalling that ϵ is a fraction of δ.

To study the effect of λ_c on the effective conductivity, we solve the homogenisation cell problem for a variety of λ_c and calculate the corresponding $\boldsymbol{\sigma}_{\text{eff}}$. We consider λ_c ranging from 10^{-1} to 10^{1}, keeping in mind that we conducted our homogenisation analysis for $\lambda = O(1)$ and repeat this analysis for three different contact sizes ϵ ranging from 0.1 to 0.4.

We note the presence of the electrical conductivity σ in the cell problem boundary condition (6.52). Here we will consider the case where the electrical conductivity is constant in a cell, in particular $\sigma = 1$. However, if coupled with the thermal problem, we would consider a temperature-dependent conductivity, therefore we would need to include it in the cell problem as $\sigma(T_0)$, where T_0 is the homogenised temperature. This would prompt us to adapt our homogenisation procedure to allow for a cell problem that depends on the homogenised solution, which is identical to the discussion in Chapter 4 in the context of radiation.

Given a constant electrical conductivity and a symmetric unit cell ω, our effective conductivity tensor (6.62) will be a scalar multiple of the identity matrix. Therefore, in order to include the influence of this tensor when comparing our homogenised solution to the direct solution, we consider a source term $f(\mathbf{x}, \mathbf{y})$ in our steady current conduction equation (6.21) to ensure that the effective conductivity does not drop out of the problem. The adaptation necessary to include $f(\mathbf{x}, \mathbf{y})$ in the homogenisation analysis affects the method at higher orders, for example at $O(\delta^2)$ [74, 76], therefore the homogenised problem becomes

$$\nabla_{\mathbf{x}} \cdot (\boldsymbol{\sigma}_{\text{eff}} \nabla_{\mathbf{x}} \phi_0) = f_{\text{eff}}, \qquad \mathbf{x} \in \Omega, \tag{6.93}$$

$$\phi_0 = \phi_D(\mathbf{x}), \qquad \mathbf{x} \in \partial\Omega_D, \tag{6.94}$$

$$\nabla \phi_0 \cdot \mathbf{n} = 0, \qquad \mathbf{x} \in \partial\Omega_N, \tag{6.95}$$

where the effective conductivity $\boldsymbol{\sigma}_{\text{eff}}$ is given by (6.62) and the effective source term f_{eff} is defined as

$$f_{\text{eff}} = \frac{1}{|\omega|} \int_{\omega} f(\mathbf{x}, \mathbf{y}) \, \mathrm{d}\mathbf{y}. \tag{6.96}$$

For simplicity we consider a source term that depends only on the macroscale $\mathbf{x}$, in particular we let $f(\mathbf{x}) = x$.

We define the same simple boundary conditions as in Chapter 3, namely we enforce Dirichlet conditions on the top and bottom edges of the domain:

$$\partial\Omega_D^T = \{(x, y) \in \partial\Omega : y = 1\}, \qquad \partial\Omega_D^B = \{(x, y) \in \partial\Omega : y = 0\}. \tag{6.97}$$

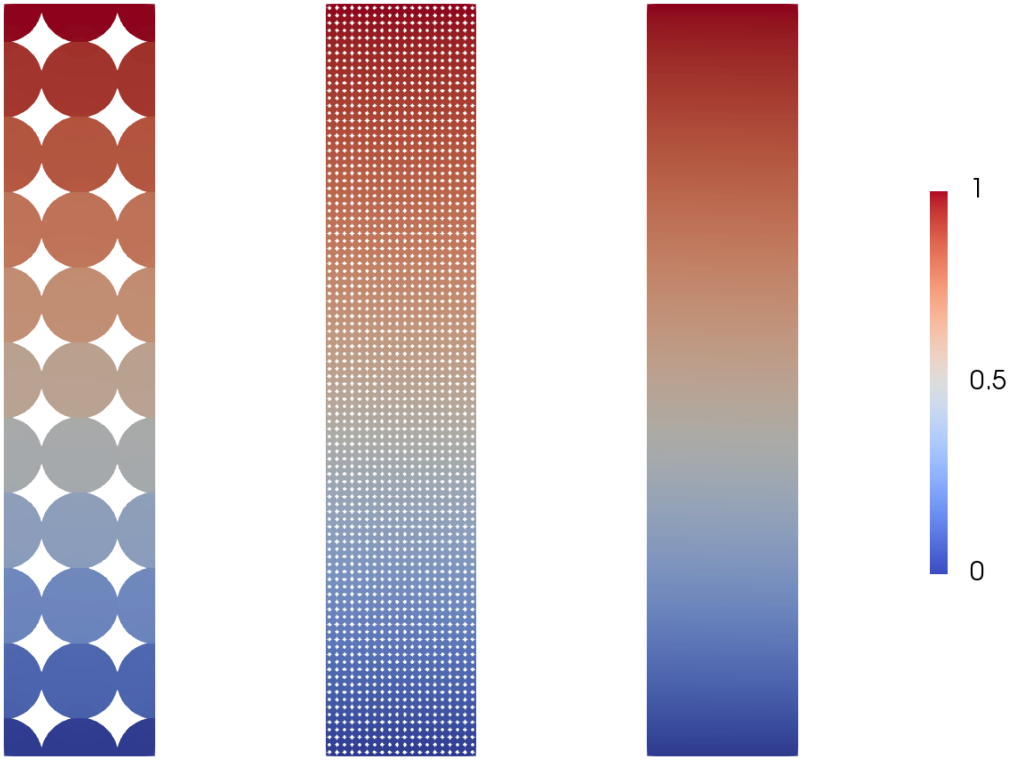
where we enforce

$$\phi_D(\mathbf{x}) = \begin{cases} 1, & \mathbf{x} \in \partial\Omega_D^T, \\ 0, & \mathbf{x} \in \partial\Omega_D^B, \end{cases} \tag{6.98}$$

The remainder of the boundary is $\partial\Omega_N = \partial\Omega \backslash \partial\Omega_D$, on which we enforce the zero-flux condition.

Results

We solve the coupled model (6.21)–(6.25) via homogenisation and directly using piecewise quadratic finite elements in `Firedrake` [80] on a mesh of triangles. We include colour-maps of the direct solution for $\delta = 0.1$ and $\delta = 0.01$ alongside the homogenised



(a) $\delta = 0.1$. (b) $\delta = 0.01$. (c) Homogenised.

Figure 6.9: Colour maps of the direct solution ϕ of (6.21)–(6.25) for (a) $\delta = 0.1$, (b) $\delta = 0.01$ and (c) the homogenised solution ϕ_0 of (6.93)–(6.95).

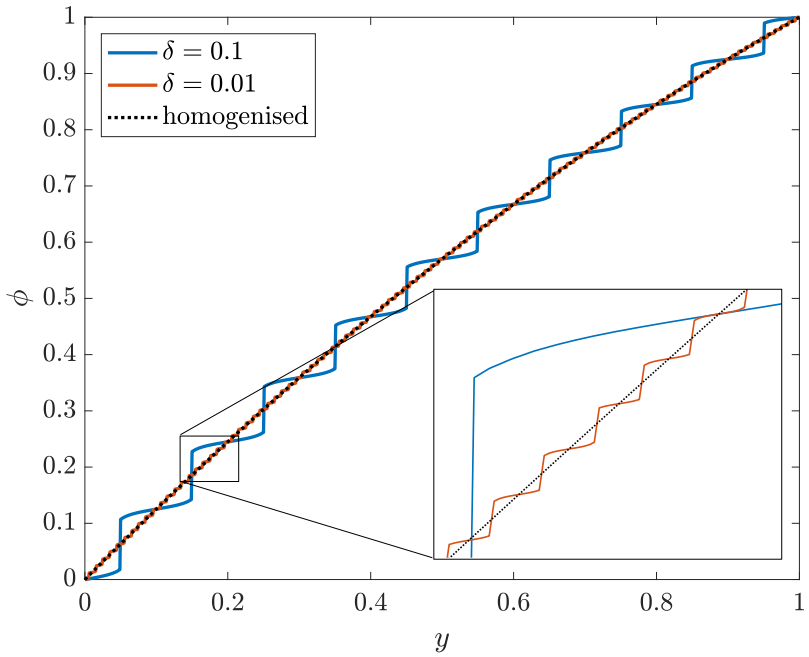


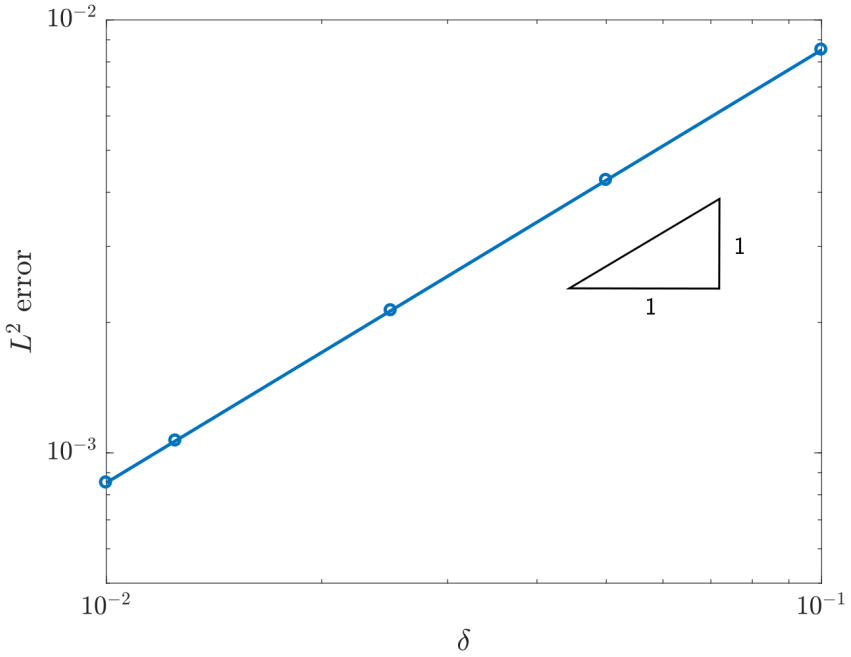
Figure 6.10: Electric potential ϕ along the line $x = 0.1$ when solved directly for $\delta = 0.1$ and $\delta = 0.01$, along with the homogenised solution.

solution in Figure 6.9 for a visual representation of how the homogenised solution approximates the direct solution. In Figure 6.9a we can see how the solution jumps at particle interfaces.

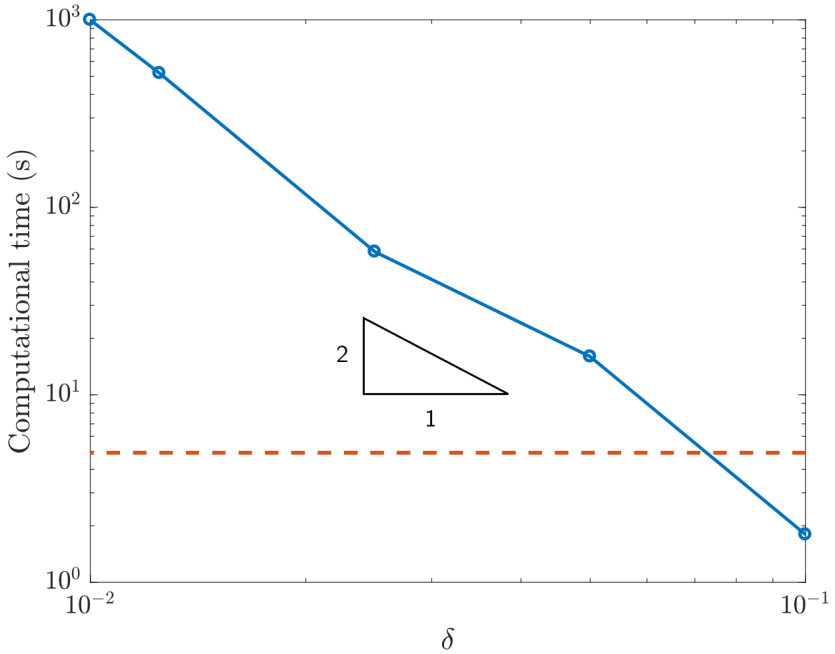
By plotting a line graph of the solutions along $x = 0.1$ in Figure 6.10, we observe the behaviour of ϕ along the length of the domain. We see that for $\delta = 0.1$, given by the blue, solid line, the solution experiences substantial jumps at contact interfaces, whereas for $\delta = 0.01$, given by the orange, solid line, the jumps are comparably smaller but more regular. Although the homogenised solution, given by the black, dotted line, does not capture this fluctuation in the electric potential, it is evident that as $\delta \to 0$, the homogenised solution becomes a better approximation for the direct solution.

We quantify the approximation error between the homogenised and direct solutions in Figure 6.11a where we calculate the L^2-error for a variety of δ in the same way as described in the previous chapters and plot the result on a log-log graph. From Figure 6.11a we see that the approximation error is $O(\delta)$, as expected, indicating clear convergence of the homogenised solution to the "true" solution as $\delta \to 0$.

We include in Figure 6.11b the direct solution computational time as a function of δ and observe that, in the best case, the direct computational time is $O(\delta^{-2})$. The



(a) L^2-error between homogenised solutions and direct solution for different values of δ.



(b) Computational time of solving the problem directly (blue solid line) with δ, along with the time to solve homogenisation problem, namely 4.91 s (dashed orange line).

Figure 6.11: L^2-error and computational time associated with the direct and homogenised solutions.

homogenised solution was obtained in 4.91 seconds, as indicated by the dashed line in Figure 6.11b.

Considering Figures 6.11a and 6.11b together, we have demonstrated increasing levels of accuracy of the homogenised solution as δ decreases where simultaneously the computational cost of direct solutions becomes less feasible. We note again that for three-dimensional problems, the computational cost will increase, in the best case, as $O(\delta^{-3})$ whilst the error should follow the same $O(\delta)$ trend. One can further appreciate the computational benefit of homogenisation for such problems.

We recall that due to the symmetries associated with this example, the effective conductivity tensor $\boldsymbol{\sigma}_{\text{eff}}$ is a scalar multiple of the identity matrix, namely

$$\boldsymbol{\sigma}_{\text{eff}} = \sigma_{\text{eff}} \mathbf{I}. \tag{6.99}$$

We are interested in how the scalar quantity σ_{eff} depends on the contact conductance parameter λ_c, therefore we solve the cell problem (6.50)–(6.52) for λ_c ranging from 10^{-1} to 10^{1} and plot the results in Figure 6.12. We do this for a variety of contact widths ϵ. We notice that for $\lambda_c = O(1)$ the relationship between σ_{eff} and λ_c is almost linear, as indicated by the triangle on the plot. Thus the contact conductance parameter has a significant impact on current conduction through granular material.

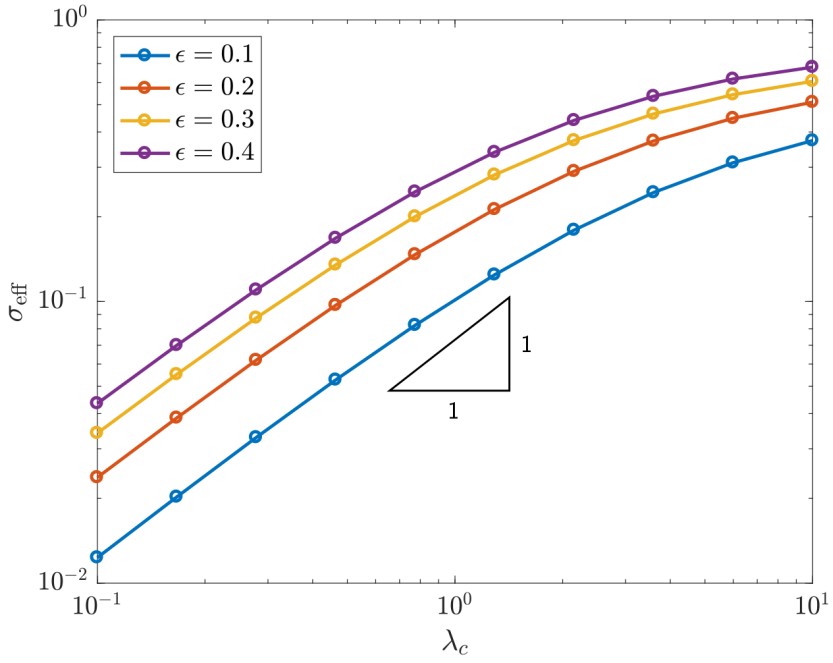


Figure 6.12: Variation in the effective conductivity with contact conductance parameter λ_c for different contact sizes ϵ.

The same trend is observed for each ϵ, however the overall effective conductivity is higher for larger contact widths, as expected. We recall the result from Chapter 5 that the effective conductivity tensor depends on ϵ as $O(1/\log\epsilon)$. Combining the effect of small contacts with the effect of imperfect contacts, it is evident that the nature of particle contacts has a significant influence on the effective conductivity and major impact on electric current conduction through a granular material.

6.4 Discussion

Motivated by the prominent influence of particle contacts on the effective conductivity tensor associated with our granular material model, the goal of this chapter was to include the effect of imperfect contacts on the problem. We began by experimentally exploring the change in the resistance of two half-cylinders in contact due to the apparent contact area between them, modified by increasing the load on the system. We designed the experiments to be as close as possible to the theory outlined by Hertz and Holm in order to compare the results to predicted behaviour. Despite our best efforts, our experiments disagree with the theoretical expectation. Similar disagreement is also observed in the literature [103], therefore we concluded that the experiments exhibited much more physical complexity than was captured in the Hertz-Holm predictions. A key result from this analysis was the further affirmation that the resistance due to particle contacts constitutes a significant proportion of the bulk resistance of a collection of particles. The literature suggests that the resistance at a contact is attributed to more than just constriction resistance, thus we sought to include the contribution of imperfect contacts in our homogenisation model.

To allow for an imperfect contact, we introduced the concept of a thin, resistive oxide layer at the particle contact, hence increasing the resistance to electric current conducting through. We modelled this mathematically by considering the electric current flux to be proportional to a jump in the electric potential at the contact interfaces, hence we modified the contact boundary conditions in our model. We emphasised that this small change to the governing equations resulted in a substantial change to the numerical methods necessary to solve the homogenisation cell problem. We then explained the homogenisation methodology due to a 2D example with this new boundary condition.

We began our numerical analysis by introducing the finite element scheme known as the discontinuous Galerkin method to solve the new cell problem, in particular we

considered the symmetric interior penalty Galerkin method. We derived the corresponding variational form and solved the non-dimensional steady current conduction model via both homogenisation and directly. By calculating the L^2-error between the two solutions, we demonstrated that the homogenised solution is a good approximation to the direct solution and is much more computationally efficient to obtain.

Finally, we solved the homogenisation cell problem for a variety of contact conductance parameters λ_c to study its effect on the effective conductivity tensor, thereby verifying the significance of thin, resistive layers. We noted an approximately linear relationship between σ_{eff} and λ_c. We further recalled the $O(1/\log\epsilon)$ dependence of the effective conductivity on contact size ϵ discussed in Chapter 5. The combination of these effects indicates a prominent influence of particle contact properties on the effective conductivity of the bulk, granular material.

We have considered the electrical problem in isolation, however, such thin, resistive layers will likely influence the thermal problem due to localised Ohmic heating at the contacts. We extend the techniques discussed in this chapter to the coupled electrothermal model in Appendix B.

Chapter 7

Conclusion

Determining the effective properties of granular material is important for many industrial applications, in particular, metallurgical furnaces. By considering the heat treatment of carbon in a calciner furnace, we outlined the critical processes contributing to the successful graphitisation of granular anthracite due to Ohmic heating caused by large alternating currents, thus highlighting the necessity of mathematical models to understand the interdependent mechanisms. In particular, we emphasised the dependence of the calcination process on electrical and thermal transfer in granular material, indicating the difficulties associated with scale disparities, contact resistance and radiative transfer. Using systematic homogenisation theory, we applied the method of multiple scales to study the electrothermal behaviour of a periodic array of idealised particles to deduce the effective electrical and thermal conductivities. We demonstrated that our multiple scales model accurately approximates the true solution to the problem and justified the computational benefit, concluding that sufficient accuracy can be achieved in a numerically feasible and efficient way. In this chapter, we summarise the key findings of our work and outline the industrial benefit before finally mentioning some extensions that would improve the model by allowing for more physical details to be included.

7.1 Summary of key results

Electrical and thermal conduction through a granular material is very complicated due to the dependence on the microstructure, that is, electric current and heat must conduct through tiny, imperfect contacts between particles and radiative transfer occurs within gas-filled voids. In fact, the bulk electrical resistivity of the granular material, in other words the total resistivity due to the particles, the voids and any other participating material within the calciner, is primarily determined by the contact resistance

between particles. We defined contact resistance to consist of constriction resistance incurred by current having to conduct through very small areas and oxide-layer resistance that is a consequence of imperfect contacts. Furthermore, the high gradients in electric potential lead to large heating in regions close to the contacts and for the resulting temperatures typical within a calciner, the effect of radiation is a dominating thermal transfer effect. There are millions of such contacts and voids among the anthracite particles within a calciner, therefore mathematically and numerically accounting for these microscopic effects directly is highly infeasible. This has been attempted using Discrete Element Methods (DEM), however the microscopic particle contacts require an extremely fine mesh to resolve the behaviour, therefore allowing for millions of contacts requiring such refinement renders the numerical techniques intractable.

Homogenisation of steady electrical and thermal conduction

In Chapter 3, we exploited the vast discrepancy between the scale of the furnace and the scale of the particles to apply the method of multiple scales to the electrical conduction throughout an idealised, periodic array of regular particles. We outlined the mathematical derivation of the homogenised model and the effective electrical conductivity, noting that the geometrical complexities associated with the microstructure were captured in this effective parameter. The effective conductivity tensor contains an integral over the unit cell which we defined to be a single particle and depends on the solution to the microscopic cell problem, derived through the homogenisation process. The beauty of this multiple scales model is that we reduced a complicated problem with intricate microstructure to a representative microscopic cell problem, needed to be solved only once, and a macroscopic conduction problem to be solved in a homogeneous domain. We solved the model in `FEniCS` [6] and demonstrated the approximation accuracy and numerical benefit by comparing the homogenised solution with one obtained by directly solving the problem for a two-dimensional domain, considering the particles to be truncated circles. This simple framework was chosen so that the direct solution could be solved on a single workstation within a reasonable length of time. By decreasing the size of such particles, we exhibited the decrease in approximation error between the two solutions and noticed that the computational cost of the direct solution quickly became infeasible, without even reaching realistic numbers of particles. Given this deterioration in the direct solution for a two-dimensional problem, we can expect even more limited performance of a three-dimensional solution, which is really the situation of interest. We concluded

that the homogenised solution accuracy paired with its numerical accessibility deems it a satisfactory model to approximate electric current conduction through a granular material.

We then built upon our model by including the effect of Ohmic heating, namely, we coupled the electric current conduction with steady heat conduction with a source term due to Ohmic heating. We further enforced the dependency of the electrical and thermal conductivities on temperature, noting that the electrical conductivity of anthracite increases sharply and considerably at some critical temperature value. The derivation of the homogenised model closely followed the electrical-only problem and we again derived effective parameters, namely the effective electrical and thermal conductivities along with an effective Ohmic heating term. We demonstrated the numerical advantage of the homogenised model, verifying with the same simple two-dimensional example that the coupled problem can be accurately approximated by the multiple scales model which is numerically accessible. We noted that for a special case of external boundary conditions imposed on the macroscopic model, we can simplify the problem from a coupled system of two partial differential equations for the electric potential and the temperature to a single ordinary differential equation and Laplace's equation. We required that the boundary conditions for the electric potential and the temperature both satisfy Dirichlet conditions along the same boundary portion and both satisfy Neumann conditions elsewhere. Following the framework in [48] we considered the temperature as a function of the potential, namely $T = f(\phi)$ and hence obtained an ODE for f from which T can be defined following the deduction of ϕ from Poisson's equation for steady current conduction. We verified that the homogenised solutions could be modelled in the same way, namely $T_0 = f(\phi_0)$, therefore concluding that for this special case, one need only solve the electric conduction model by homogenisation and can obtain the temperature profile from the ODE. We similarly validated this method by demonstrating the agreement between the solution with the direct solution and illustrated the preferable computational cost.

Homogenisation of the radiative operator

In Chapter 4 we extended our model to account for the effects of radiation, motivated by the fact that heat transfer by radiation in the gas-filled voids between particles is significant for the temperatures typical within a calciner. We introduced the non-linear, non-local, integral boundary condition associated with this phenomenon. The form of this condition makes it complicated to include in mathematical models, particularly within homogenisation models as it is not immediately obvious how to

consider an integral in the multiple scales framework. Chapman and McBurnie [19] demonstrate that a naïve approach will lead to incorrect solutions, in particular, one must carefully account for macroscale variation when dealing with the integral due to its non-locality. The multiple scales analysis conducted in the previous chapters can be extended to include this intricacy. We outlined the derivation of an appropriate homogenised model for a solid, conductive matrix perforated with spherical gas-filled voids. The geometry was chosen for analytical ease, namely the radiative boundary condition is easily defined for a spherical surface, however the analysis is valid for more complicated, irregular void structures. One must be able to describe the surface orientation in the form of a view-factor, but the mathematical homogenisation technique is identical. As with our previous models, we obtained a homogenised model that depends on an effective thermal conductivity tensor which is a function of the solution to the cell problem defined within a representative microscopic volume. The effective conductivity comprised two terms: the effective conduction term which is identical to that obtained for the non-radiative model and the effective radiation term which contains the non-local radiative operator defined on a microscopic void. The radiative term also contains T_0, the homogenised temperature, therefore the homogenised model for this problem is non-linear and hence more computationally expensive to solve. Through numerical exploration we illustrated that, even for high temperatures, radiation does not dominate over conduction because the solid material is the rate-limiting factor, thus the effective-conductivity saturated at high temperatures. We demonstrated that the homogenised solution agrees with the solution obtained by direct calculation and verified the computational benefit of our model. We then outlined the coupled electrothermal model with radiative effects, stating the homogenised model and the effective parameters.

Analytical analysis of constriction resistance

In Chapter 5 we explored the effect of small contacts on electric current conduction, motivated by the dependence of the bulk electrical resistivity on the contact resistance, namely, we studied the component of contact resistance termed constriction resistance. We began by considering a simple, two-dimensional example where we approximated a particle as an infinite strip of uniform conductivity with two contact interfaces of width ϵ symmetrically aligned on each boundary, where ϵ was much smaller than the width of the strip. Enforcing Dirichlet boundary conditions at these contacts and homogeneous Neumann conditions elsewhere, we claimed that the geometry was representative of two-dimensional current conduction in through the top

contact and out the bottom contact, where the remaining boundaries represent the interface between conducting particle and insulating gas. Due to the analytical ease associated with infinite, two-dimensional domains and complex analysis, we obtained an explicit solution for the complex potential, of which the electric potential is the real part. From our analysis we deduced that the total electric current through the contact behaves like $O(1/\log\epsilon)$, therefore we concluded that there are high potential gradients close to the contacts compared to those far from the contacts. This agreed with our expectations into the importance of constriction resistance on steady current conduction.

We then demonstrated the efficacy of the method of matched asymptotics by obtaining the same relationship for the two-dimensional electric current conduction, hence prompting us to study a three-dimensional example using these techniques. We considered our particle as a unit cube, modelling the contacts as circles of diameter $\epsilon \ll 1$ centred on the top and bottom faces where the potential satisfied Dirichlet conditions and enforcing homogeneous Neumann conditions upon the remaining boundary surfaces. We deduced in the three-dimensional case that the total current through the contact behaves like $O(\epsilon)$ which is in agreement with the foundational work of Holm [46]. From this analysis we outlined that the homogenisation cell problem could be solved by matched asymptotics, demonstrating that the behaviour of the cell solution follows that deduced in our analytical analysis. The evident dependence of the cell problem solution on small particle contacts allowed us to speculate that including realistic particle geometries is less important than correctly accounting for the size and nature of particle contacts, therefore we can simplify the cell geometry and focus on accurate descriptions of the particle contacts.

Including oxide layer resistance in homogenisation model

Finally, in Chapter 6 we included the effect of imperfect contacts on electric current conduction by considering oxide-layer resistance at the interface between particles. This involved a thin, resistive layer between particles and hence the derivation of a jump in the electric potential from one particle to another. This effect was modelled such that the electric flux at the contacts was proportional to the jump and the constant of proportionality was termed the contact conductance, defined to be a function of both the conductivity and width of the resistive layer. We then conducted a multiple scales analysis on the steady current conduction model similar to that outlined in Chapter 3, however the original continuity condition imposed on contact interfaces

was replaced with the jump condition. We obtained a homogenised macroscopic model with effective parameters dependent on a microscopic cell problem.

Although a seemingly minor change to the mathematical model, this addition of a jump condition brought with it significant numerical complexities. Namely, the finite element methods used in the previous chapters were no longer appropriate, therefore we considered discontinuous elements and implemented the Symmetric Interior Penalty Galerkin method to account for discontinuities in the solution. This required a more careful deduction of the variational form which was now defined on every element and summed over the total number of elements. In particular, it was necessary to include stabilisation and penalisation terms to ensure symmetry and positive-definiteness of the variational form. Furthermore, to solve the periodic cell problem using discontinuous elements required careful definition of the mesh, as periodicity and discontinuities are difficult to combine. We verified our homogenised solution against the direct solution as with the other homogenisation models, noting similar approximation accuracy and computational efficiency.

7.2 Guidelines for the industrial partner

The initial motivation for this project stemmed from the research goals of NORCE under the project Electrical Conditions and their Process Interactions in High Temperature Metallurgical Reactors (ElMet) in collaboration with the Norwegian University of Science and Technology (NTNU), industrial companies Elkem and Eramet and the University of Santiago de Compostela.

The models discussed in this thesis provide a numerically accessible way to obtain approximate solutions to describe electric current conduction and the consequential Ohmic heating of granular material within a furnace and have been used to gain preliminary intuition into the inner mechanisms of the calcination process. The homogenisation model requires a variety of input parameters. Firstly the operating parameters such as furnace dimensions, voltage drop and external boundary conditions and secondly the material properties such as particle size, expected contact size, contact conductance and finally, the electrical and thermal conductivity functions. With careful consideration into the material properties, one can modify the operating parameters, in particular the applied voltage to study the effect on the temperature profile within the furnace. The maximum temperature of each anthracite particle is responsible for the degree of graphitisation of the material. The homogeni-

sation model will allow quantitative study of the process and provide estimations of the properties of the final product.

The material properties of the anthracite require more careful study, namely, one must deduce representative particle and contact sizes and propose an estimation for the contact conductance. However, such approximations can likely be obtained through experimental analysis on a small collection of anthracite particles. In Section 7.3, we discuss how one might include a distribution of particle and contact sizes throughout the furnace. The model is highly dependent on the temperature-dependent electrical and thermal conductivity functions. In Chapter 3, we proposed possibilities for such functions based upon the work of Celzard and Clendenin [17, 23], noting that the electrical conductivity increases in a sigmoid fashion whilst thermal conductivity is linear with temperature. Note that in our numerical examples, we proposed values for the lower and upper bounds α, β for the electrical conductivity along with a critical temperature T_c at which the sharp change takes place, using κ to determine the slope of this increase. On the other hand, we approximated the thermal conductivity as constant ξ due to its negligible change compared to the electrical conductivity. The accuracy of the model can be improved by considering realistic conductivity functions, or at the very least, appropriate estimations of $\alpha, \beta, \kappa, T_c, \xi$.

Having derived the homogenised coupled electrothermal conduction model in Chapter 3, we then considered the effects of radiation and oxide-layer resistance in isolation. This was primarily to avoid repetition of previously discussed results and focus on each of the critical phenomena individually. It is possible to obtain a single model that incorporates all of these effects, however this requires careful definition of the geometry, in particular the unit cell. Most prominently, the radiation problem requires the definition of a view-factor associated with the radiative surfaces, namely, we must be able to define a function that describes the orientation of the surface to capture where the radiation will propagate when emitted from a point on the surface. This is particularly complicated in three dimensions because, in principal, the voids could constitute a single, continuous gas-filled medium. For example, in the case of a periodic array of truncated spheres, the void space between particles is a continuous domain, therefore cannot be defined as a collection of closed volumes. Defining the view-factor for such a domain is extremely complicated and would likely require simplifications and assumptions on how far radiation can propagate in order to be accounted for in the model. Consequently, the definition of an appropriate cell problem is difficult as the void cannot be entirely captured within a single representative cell. Therefore, to include both radiation and small contacts in a three-dimensional

problem, one must carefully define the problem geometry. However, despite these geometrical complications, the mathematical homogenisation technique is identical and a complete model can be obtained by combining the various homogenisation models discussed in this thesis. We discuss the influence of contact resistance on Ohmic heating in Appendix B.

7.3 Possible extensions

The homogenisation models discussed throughout this thesis assume a periodic microstructure, which we generally considered to be a single, truncated circular/spherical particle, except for the radiation problem in Chapter 4. Of course the particles within a calciner furnace are not periodically distributed and are certainly not spherical, therefore it is reasonable to consider more realistic cell structures. There are techniques discussed within the literature for considering non-periodicity of the microstructure. The authors in [81] discuss near-periodic media, in particular homogenising the electrical activity of cardiac tissue. Using a curvilinear coordinate transform, the authors map the near-periodic microscale to a periodic domain. Macroscopic behaviour of a poroelastic medium with surface growth of the solid pores is described in [77], where the authors consider homogenisation by multiple scales to obtain an effective model on the macroscale where time-dependent growth is encapsulated in the coefficients of the model. These models both require the cell problem to be solved at every point in the macroscale, which thereby reduces the computational efficiency. The work presented in [13, 27], however, outlines how the method of multiple scales can be applied to non-uniform and non-periodic structures, provided the microstructure is locally periodic. They apply this idea to transport of solute in a porous medium and in particular allow the dimension of the pores to vary slowly on the macroscale.

We can extend the ideas of [13, 27] to include particle variation within our homogenisation model. Given the dominance of resistance due to the contacts between particles when deriving the effective conductivities, one mechanism would be to consider slowly varying contact sizes throughout the macrostructure. This could be directly correlated to the mechanical stresses within the furnace, allowing for an estimation of an important aspect of granular materials that has thus far been neglected, namely the mechanical interactions between particles. We understand that the size of the contacts between particles is dependent on the forces between them [15, 32, 39, 44, 46], however we have not accounted for such dependence in our model so far.

By obtaining an estimation for the stress profile of the granular material within the furnace, one could deduce approximations for the expected area of contact between particles subject to such stress, thereby obtaining a macroscopically spatially-varying function $\epsilon(\mathbf{x})$ to represent the contact sizes throughout the furnace. This slowly varying function will hence be a parameter in the microscopic cell problem, thereby the effective conductivity functions will depend on the macroscale according to $\epsilon(\mathbf{x})$.

Further extensions to the mechanical problem could be the study of granular flow. In our model we included a stationary material, however we mentioned in Chapter 2 that the particles move through the furnace which will cause the orientation of particles and contacts with neighbouring particles to change throughout the homogenisation process. This will affect the electric current conduction and Ohmic heating. Granular flow theory associated with hopper drainage is one of the simplest examples because it requires gravity only and a number of continuum models have been proposed [68, 69, 79]. Discrete or DEM methods have been extensively applied to granular flow [65, 107, 108], however such models are extremely computationally expensive. Another discrete approach is the "spot model" [12, 86] which is a microscopic mechanism for particle rearrangement in granular flow. The method considers the movement of particles in local groups, requiring that they must move cooperatively. The spot model can accurately reproduce DEM simulations of granular drainage at a much lower computational cost. Granular flow is an extremely complicated problem in itself, therefore coupling it with the homogenisation models explained in this thesis is an arduous endeavour.

A less involved mechanism to extend the room for detail in our model is the adaptation of the periodic cell problem to allow us to consider more complicated or realistic particle distributions. This approach retains the periodicity associated with our homogenisation models, yet allows for a range of particle sizes to be considered. We note again that defining the cell problem is complicated by the radiation problem, particularly for three-dimensional structures. However, assuming that appropriate measures can be taken to ensure the encapsulation of gas-filled voids within the unit cell, or merely neglecting radiative effects altogether, our homogenisation models are valid for more general particle geometries. For example, instead of considering a single particle in the unit cell, thereby assuming that all the particles within the furnace are uniform in size and alignment, one could model the cell as a collection of particles, the size distribution of which could be chosen to represent the distribution expected within the furnace. Therefore we could include variations in the particle size, contact

size, number of contacts, size of void fraction, among other features to study their effect on the effective conductivity.

This is mostly a numerical exercise, as it involves more complicated definition of the cell geometry and intricate meshing of the unit cell domain. For example, the more particles per unit cell, the more contacts per cell and hence the finer the mesh must be in these regions. This will increase the computational expense, however the efficiency of solving such a problem by homogenisation will undoubtedly still be preferable to direct solutions or DEM.

Appendix A

Defining the electrical and thermal conductivity functions

In Section 3.1, we proposed functions to describe the electrical and thermal conductivity of anthracite. In this appendix, we discuss how such functions influence the electric potential and temperature profile when used as inputs to the coupled electrothermal model (3.66)–(3.70).

Recall the general non-dimensional electrical conductivity function outlined in Chapter 3,

$$\sigma(T) = \frac{\alpha}{\beta} \exp\left(\frac{\log(\beta/\alpha)}{1 + \exp\left(-\kappa(\zeta T + T_{\min} - T_c)\right)}\right). \tag{A.1}$$

where α and β are the minimum and maximum conductivity values respectively, $T_{\min}$ is the minimum temperature, T_c is the critical temperature at which we observe a sharp change in conductivity, κ controls the slope of the increase and ζ is the dimensional parameter given by

$$\zeta = \frac{\beta(\phi^T - \phi^B)^2}{\xi}, \tag{A.2}$$

for voltages ϕ^T and ϕ^B and ξ is a characteristic size of thermal conductivity. Given a voltage drop $\Delta\phi = \phi^T - \phi^B$ across the furnace along with a minimum temperature $T_{\min}$ and critical temperature T_c, we wish to study the influence of the conductivity parameters α, β, κ and ξ on the electric potential and temperature profile. In a similar study, Fowler et al. [35] explored the same electrothermal conduction model in the context of thermistors, considering an electrical conductivity function that decreases rapidly with temperature. The authors conduct an asymptotic analysis to determine dimensionless parameters that can be used to understand what conditions are necessary for a thermistor to reach the critical "switching temperature".

In Section 3.5, we explained that for a special case, namely when the Dirichlet and Neumann boundary portions for the temperature and electric potential are the same, we can write $T = f(\phi)$ and hence we derived an ODE (3.139)–(3.140) for f. For simple conductivity functions, we can obtain an analytical solution to this ODE, thus we can study the influence of conductivity parameters on the temperature profile as a function of the electric potential.

To conduct an analytical analysis, we approximate the electrical conductivity function (A.1) using a piecewise linear function, namely

$$\sigma(T) = \begin{cases} \alpha/\beta, & T \leq T_\alpha, \\ \frac{1-\alpha/\beta}{T_\beta - T_\alpha}(T - T_\alpha) + \alpha/\beta, & T_\alpha \leq T \leq T_\beta, \\ 1, & T \geq T_\beta, \end{cases} \tag{A.3}$$

for some T_α and T_β that we choose. The actual and approximate conductivity functions for parameters

$$\begin{aligned} &\alpha = 1\,\mathrm{Sm}^{-1}, \quad \beta = 120\,\mathrm{Sm}^{-1}, \quad \kappa = 1.6 \times 10^{-2}\,(^\circ\mathrm{C})^{-1}, \quad \xi = 0.7\,\mathrm{Wm}^{-1}\mathrm{K}^{-1}, \\ &\phi^T = 56\,\mathrm{V}, \quad \phi^B = 0\,\mathrm{V}, \quad T_{\min} = 37\,^\circ\mathrm{C}, \quad T_c = T_\alpha = 700\,^\circ\mathrm{C}, \quad T_\beta = 950\,^\circ\mathrm{C}, \end{aligned} \tag{A.4}$$

are plotted in Figure A.1.

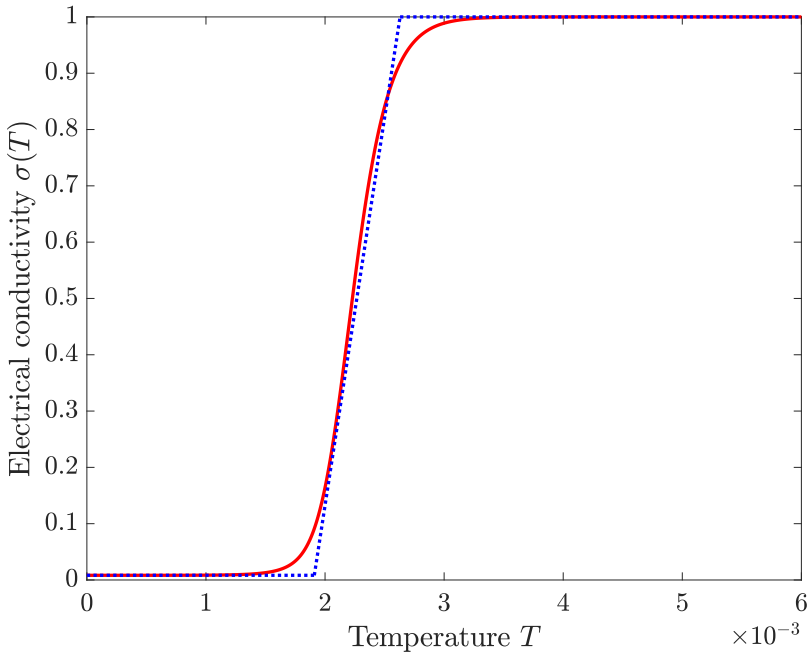


Figure A.1: Electrical conductivity function (solid red line) approximated by a piecewise linear function (dotted blue line) given by (A.3) for parameters (A.4).

We recall the ODE (3.139)–(3.140) of Section 3.5 to describe the temperature in terms of the electrical potential for constant non-dimensional thermal conductivity $k = 1$

$$\frac{\mathrm{d}}{\mathrm{d}\phi}\left(\frac{1}{\sigma(T)}\frac{\mathrm{d}f}{\mathrm{d}\phi}\right) = -1, \tag{A.5}$$

and general electrical conductivity $\sigma(T)$. We define general symmetric boundary conditions

$$f(\phi_0) = f(\phi_1) = T_0, \tag{A.6}$$

for ϕ_0, ϕ_1 and T_0 uniform, non-dimensional values of the potential and temperature respectively. Following the methods outlined in Section 3.5, the solution of (A.5)–(A.6) can be written as

$$\int_{T_0}^{f(\phi)} \frac{1}{\sigma(t)}\mathrm{d}t = -\frac{1}{2}\phi^2 + \frac{\phi_0+\phi_1}{2}\phi - \frac{\phi_0\phi_1}{2}. \tag{A.7}$$

Given this, we can write

$$\frac{1}{\sigma}\frac{\mathrm{d}f}{\mathrm{d}\phi} = -\phi + \frac{\phi_0+\phi_1}{2}, \tag{A.8}$$

thus the function $f(\phi)$ has exactly one maximum at $\phi = (\phi_0 + \phi_1)/2$. We see this is true for the example in Section 3.5 where the maximum occurs at $\phi = 0.5$.

When considering (A.5)–(A.6) for the electrical conductivity given by (A.3), we can define three problems within the three regions, each satisfying (A.5) but with differing boundary conditions. We will analyse each region with the appropriate boundary conditions separately.

Region A: $\sigma = \alpha/\beta$

We consider the problem (A.5) for $\sigma = \alpha/\beta$ and define the boundary conditions

$$f(0) = f(1) = 0. \tag{A.9}$$

The solution is given by

$$f(\phi) = \frac{\alpha}{2\beta}\phi(1-\phi). \tag{A.10}$$

We are only interested in this solution when $T \leq T_\alpha$, therefore we introduce ϕ_α such that $f(\phi_\alpha) = T_\alpha$; thus,

$$\phi_\alpha = \frac{1}{2} - \frac{1}{2}\sqrt{1 - \frac{8\beta}{\alpha}T_\alpha}. \tag{A.11}$$

This tells us that for a transition from Region A to Region B to occur, namely, for the temperature to reach T_α so that the electrical conductivity begins to increase, we require

$$T_\alpha < \frac{\alpha}{8\beta}. \tag{A.12}$$

If this condition is not satisfied then the maximum temperature $T_{\max}$ will occur in Region A at $\phi_\alpha = 0.5$ and will be defined as the right-hand side of (A.12).

Assuming this is not the case and in fact (A.12) is satisfied, we progress to study the behaviour in Region B.

Region B: $\sigma(T) = aT + b$

We consider the problem (A.5) for linear conductivity $\sigma(T) = aT + b$ where

$$a = \frac{1 - \alpha/\beta}{T_\beta - T_\alpha}, \qquad b = \alpha/\beta - aT_\alpha, \tag{A.13}$$

and define the boundary conditions

$$f(\phi_\alpha) = f(1 - \phi_\alpha) = T_\alpha. \tag{A.14}$$

In this case, the solution is

$$f(\phi) = \frac{(T_\beta - T_\alpha)}{\beta/\alpha - 1}\left[\exp\left(\frac{1 - \alpha/\beta}{2(T_\beta - T_\alpha)}\left[\phi(1-\phi) - \phi_\alpha(1-\phi_\alpha)\right]\right) - 1\right] + T_\alpha. \tag{A.15}$$

We are only interested in this solution when $T_\alpha \leq T \leq T_\beta$, therefore we introduce ϕ_β such that $f(\phi_\beta) = T_\beta$, thus we obtain the expression

$$\phi_\beta = \frac{1}{2} - \frac{1}{2}\sqrt{1 - 4\left(\frac{2(T_\beta - T_\alpha)}{1 - \alpha/\beta}\log(\beta/\alpha) + \phi_\alpha(1-\phi_\alpha)\right)}. \tag{A.16}$$

Thus, for a transition from Region B to Region C to occur, namely for the temperature to reach T_β so that the electrical conductivity levels off at its maximum value, we require

$$T_\beta < T_\alpha + \frac{1 - \alpha/\beta}{2\log(\beta/\alpha)}\left(\frac{1}{4} + \phi_\alpha(\phi_\alpha - 1)\right). \tag{A.17}$$

Similarly to the analysis in Region A, if this condition is not satisfied, then the maximum temperature $T_{\max}$ would be reached in Region B at $\phi_\beta = 0.5$ and defined as the right-hand side of (A.17).

We again assume that condition (A.17) is satisfied and proceed to Region C.

Region C: $\sigma = 1$

We consider the problem (A.5) for $\sigma = 1$, and define the boundary conditions

$$f(\phi_\beta) = f(1 - \phi_\beta) = T_\beta. \tag{A.18}$$

The solution is given by

$$f(\phi) = \frac{1}{2}\phi(1 - \phi) - \frac{1}{2}\phi_\beta(1 - \phi_\beta) + T_\beta. \tag{A.19}$$

Thus, the maximum temperature $T_{\max}$ will occur in Region C at $\phi = 0.5$ and is given by

$$T_{\max} = \frac{1}{8} + \frac{1}{2}\phi_\beta(\phi_\beta - 1) + T_\beta. \tag{A.20}$$

Thus, we expect $T = f(\phi)$ for a piecewise electrical conductivity (A.3) to resemble Figure A.2, where there are three clear regions corresponding to the piecewise linear components of f can be seen.

Discussion

From the analysis outlined above, we can choose parameters for the electric and thermal conductivities in our homogenisation analysis outlined in this thesis to ensure that the temperature distribution is such that the change in electrical conductivity is recognised. If conditions (A.12) and (A.17) are not met then the temperature profile exhibits very different behaviour, as discussed in Section 3.4.

We include the solution to the ODE (A.5)–(A.6) for the electrical conductivity given by (A.1) with parameters (A.4) in Figure A.3 and notice that the shape is very similar to that predicted by the piecewise linear analysis above, namely we notice the three regions corresponding to the respective regions in the electrical conductivity function.

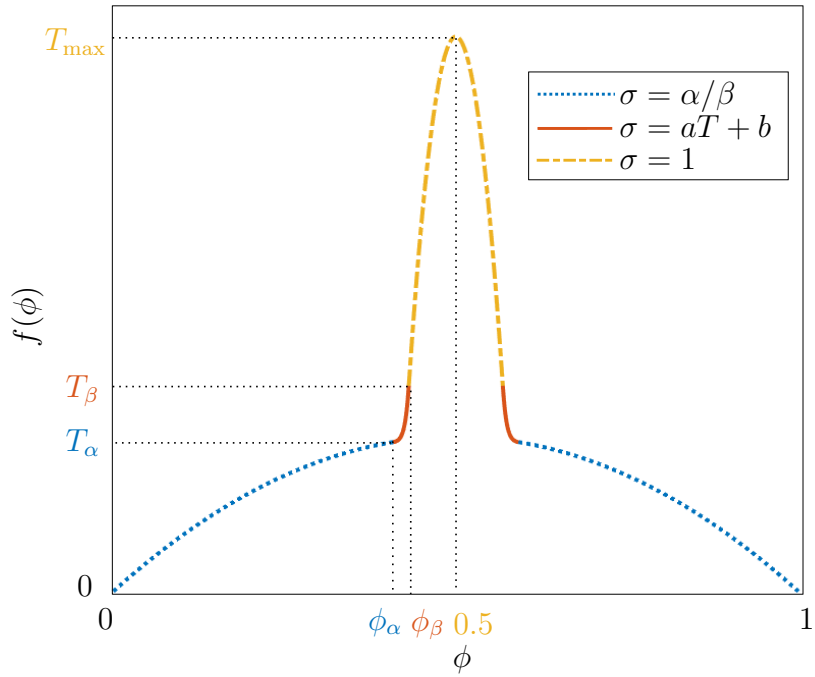


Figure A.2: Expected shape of the solution of the ODE (A.5)–(A.6) for the piecewise linear conductivity function (A.3) given that conditions (A.12) and (A.17) are satisfied.

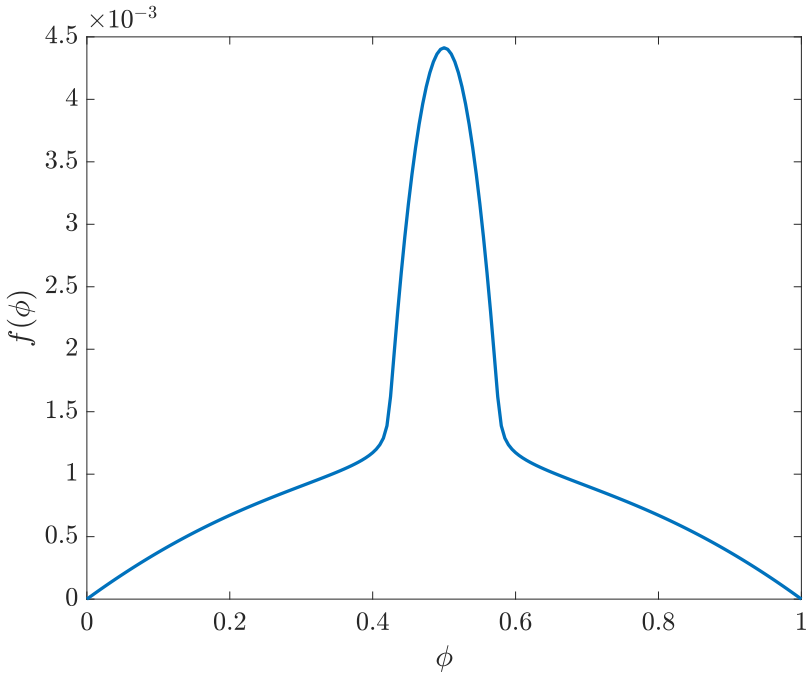


Figure A.3: Solution of the ODE (A.5)–(A.6) for the electrical conductivity given by (A.1) with parameters (A.4).

Appendix B

Homogenisation of the coupled problem with contact resistance

In Chapter 6, we included the effect of electrical contact resistance due to a thin, resistive layer between particles on electric current flow, however, we did not couple this to the thermal problem. In this appendix, we outline the effect of thin, electrically and thermally resistive layers on the Ohmic heating of a granular material.

B.1 Derivation of the boundary condition

As we did in Chapter 6, we consider a particle contact of size $\epsilon\delta L$ where the surfaces are separated by a very thin layer. We allow this layer to be of width $\nu \ll \epsilon\delta L$ and denote the thermal and electrical conductivity k_ν and σ_ν respectively. The layer is located between two particles of thermal and electrical conductivity k and σ respectively. The layer is extremely thin with respect to its other dimensions, therefore we consider one-dimensional current conduction with Ohmic heating in this region. We denote the boundaries between the particles and the layer Γ^- and Γ^+, as in Figure B.1. From continuity of temperature and heat flux at each boundary $\Gamma^\pm$, we arrive at two conditions:

$$[k\nabla T \cdot \mathbf{n}^-]_-^+ = -\sigma_c[\phi]^2, \tag{B.1}$$

$$k\nabla T \cdot \mathbf{n}^-|_{\Gamma^-} = k_c[T]_-^+ + \frac{\sigma_c}{2}[\phi]^2, \tag{B.2}$$

where we introduce the contact thermal and electrical conductances $k_c = k_\nu/\nu$ and $\sigma_c = \sigma_\nu/\nu$ respectively. Note that $[T]_-^+$ denotes the jump in temperature across the layer from Γ^- to Γ^+. Since the jump in ϕ is squared, the direction of the jump is irrelevant, namely $([\phi]_-^+)^2 = ([\phi]_+^-)^2 = [\phi]^2$. We also denote by $\mathbf{n}^-$ the outwards unit

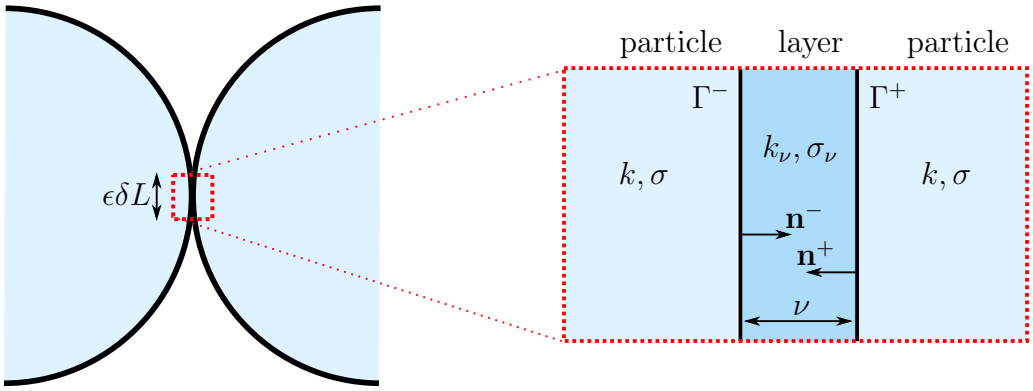


Figure B.1: Schematic of a thin layer of thermal conductivity k_ν and width $\nu \ll \epsilon\delta L$ between two particles of conductivity k.

normal to Γ^- and similarly $\mathbf{n}^+$ for Γ^+. By expanding the left-hand side of (B.1) and substituting in (B.2), we obtain

$$k\nabla T \cdot \mathbf{n}^-|_{\Gamma^+} = k_c[T]^+_- - \frac{\sigma_c}{2}[\phi]^2, \tag{B.3}$$

$$k\nabla T \cdot \mathbf{n}^+|_{\Gamma^+} = k_c[T]^-_+ + \frac{\sigma_c}{2}[\phi]^2, \tag{B.4}$$

which we can simply write as

$$k\nabla T \cdot \mathbf{n} = k_c[T] + \frac{\sigma_c}{2}[\phi]^2, \tag{B.5}$$

at each contact, where $\mathbf{n}$ is the unit normal in the direction of the jump in temperature $[T]$.

This boundary condition encapsulates the discontinuities in the temperature and the heat flux across the particle contacts. It is important to note that from now on, when we deal with such contacts, we must be careful to consider the temperature and heat flux on each side. We will use $\pm$ notation to represent which side of the contact we are considering.

B.2 Homogenisation

We again consider steady current conduction with Ohmic heating throughout the same domain as in Chapters 3 and 6, namely $\tilde{\Omega}$ of size L composed of solid particles $\tilde{\Omega}^S$ of electrical conductivity $\tilde{\sigma}(\tilde{T})$ and thermal conductivity $\tilde{k}(\tilde{T})$ and gas-filled voids as depicted in Figure 6.7. Note that we use the tilde-notation to indicate dimensional parameters. Neglecting radiation for the purpose of this appendix, we consider insulating boundaries between the solid and voids $\tilde{\Gamma}_{W,i}$ for both heat and

current, whereas we enforce the jump conditions for at the particle contacts $\tilde{\Gamma}_{C,j}$. The problem is thereby

$$\left.\begin{aligned}\tilde{\nabla}\cdot(\tilde{\sigma}(\tilde{T})\tilde{\nabla}\tilde{\phi}(\tilde{T}))=0,\\ \tilde{\nabla}\cdot(\tilde{k}(\tilde{T})\tilde{\nabla}\tilde{T}(\tilde{\mathbf{x}}))+\tilde{\sigma}(\tilde{T})\tilde{\nabla}\tilde{\phi}(\tilde{\mathbf{x}})^{\top}\tilde{\nabla}\tilde{\phi}(\tilde{\mathbf{x}})=0,\end{aligned}\right\} \quad \tilde{\mathbf{x}}\in\tilde{\Omega}^{S}, \tag{B.6}$$

$$\left.\begin{aligned}\tilde{\sigma}(\tilde{T})\tilde{\nabla}\tilde{\phi}(\tilde{T})\cdot\mathbf{n}=\sigma_c[\tilde{\phi}(\tilde{\mathbf{x}})],\\ \tilde{k}(\tilde{T})\tilde{\nabla}\tilde{T}(\tilde{\mathbf{x}})\cdot\mathbf{n}=k_c[\tilde{T}(\tilde{\mathbf{x}})]+\tfrac{\sigma_c}{2}[\tilde{\phi}(\tilde{\mathbf{x}})]^2,\end{aligned}\right\} \quad \tilde{\mathbf{x}}\in\tilde{\Gamma}_{C,j}\,\forall j, \tag{B.7}$$

$$\left.\begin{aligned}\tilde{\nabla}\tilde{\phi}(\tilde{\mathbf{x}})\cdot\mathbf{n}=0,\\ \tilde{\nabla}\tilde{T}(\tilde{\mathbf{x}})\cdot\mathbf{n}=0,\end{aligned}\right\} \quad \tilde{\mathbf{x}}\in\tilde{\Gamma}_{W,i}\,\forall i\cup\partial\tilde{\Omega}_N, \tag{B.8}$$

$$\left.\begin{aligned}\tilde{\phi}(\tilde{\mathbf{x}})=\phi_D(\tilde{\mathbf{x}}),\\ \tilde{T}(\tilde{\mathbf{x}})=T_D(\tilde{\mathbf{x}}),\end{aligned}\right\} \quad \tilde{\mathbf{x}}\in\partial\tilde{\Omega}_D, \tag{B.9}$$

where $\mathbf{n}$ is the outwards normal to the surface and $[\tilde{\phi}]$ and $[\tilde{T}]$ denote the jump in the potential and temperature respectively across the surface in the direction $\mathbf{n}$. We again prescribe $\phi_D(\tilde{\mathbf{x}})$ and $T_D(\tilde{\mathbf{x}})$ on $\partial\tilde{\Omega}_D=\partial\tilde{\Omega}_D^T\cup\partial\tilde{\Omega}_D^B$ as

$$\phi_D(\tilde{\mathbf{x}})=\begin{cases}\phi^T, & \tilde{\mathbf{x}}\in\partial\tilde{\Omega}_D^T,\\ \phi^B, & \tilde{\mathbf{x}}\in\partial\tilde{\Omega}_D^B,\end{cases}\qquad T_D(\tilde{\mathbf{x}})=T_{\min},\quad \tilde{\mathbf{x}}\in\partial\tilde{\Omega}_D. \tag{B.10}$$

Dimensionless equations

We scale our variables in the same way as in Chapters 3 and 6, namely,

$$\tilde{\mathbf{x}}=L\mathbf{x},\qquad \tilde{\phi}=(\phi^T-\phi^B)\phi+\phi^B,\qquad \tilde{T}=\zeta T+T_{\min}. \tag{B.11}$$

For the purposes of this appendix we will allow the thermal and electrical conductivities k and σ to be constant. From (B.6), we define

$$\zeta=\frac{\sigma(\phi^T-\phi^B)^2}{k}, \tag{B.12}$$

and the contact boundary conditions (B.7) become

$$\nabla\phi(\mathbf{x})\cdot\mathbf{n}=\frac{\sigma_c L}{\sigma}[\phi(\mathbf{x})], \tag{B.13}$$

$$\nabla T(\mathbf{x})\cdot\mathbf{n}=\frac{k_c L}{k}[T(\mathbf{x})]+\frac{\sigma_c L}{2\sigma}[\phi(\mathbf{x})]^2, \tag{B.14}$$

We are interested in the behaviour on the lengthscale of a particle. We rescale the spatial variable to account for this,

$$\mathbf{x}=\delta\mathbf{y}, \tag{B.15}$$

therefore (B.13)–(B.14) becomes

$$\nabla_{\mathbf{y}}\phi \cdot \mathbf{n} = \frac{\sigma_c \delta L}{\sigma}[\phi], \tag{B.16}$$

$$\nabla_{\mathbf{y}} T \cdot \mathbf{n} = \frac{k_c \delta L}{k}[T] + \frac{\sigma_c \delta L}{2\sigma}[\phi]^2. \tag{B.17}$$

We recall from Chapter 6 that we study the case when

$$\lambda_c = \frac{\sigma_c \delta L}{\sigma} = O(1), \tag{B.18}$$

in order to consider a balance between the material electrical conductivity and contact electrical conductance. Similarly, we consider

$$\eta_c = \frac{k_c \delta L}{k} = O(1), \tag{B.19}$$

to analyse the problem when the material thermal conductivity, thermal contact conductance and Ohmic heating at the particle contacts are of the same order of magnitude on the lengthscale of a particle.

We therefore write the dimensionless problem,

$$\left.\begin{aligned} \nabla^2\phi(\mathbf{x}) &= 0, \\ \nabla^2 T(\mathbf{x}) + \nabla\phi(\mathbf{x})^\top \nabla\phi(\mathbf{x}) &= 0, \end{aligned}\right\} \quad \mathbf{x} \in \Omega^S, \tag{B.20}$$

$$\left.\begin{aligned} \nabla\phi(\mathbf{x}) \cdot \mathbf{n} &= \tfrac{\lambda_c}{\delta}[\phi(\mathbf{x})], \\ \nabla T(\mathbf{x}) \cdot \mathbf{n} &= \tfrac{1}{\delta}\left(\eta_c[T(\mathbf{x})] + \tfrac{\lambda_c}{2}[\phi(\mathbf{x})]^2\right), \end{aligned}\right\} \quad \mathbf{x} \in \Gamma_{C,j}\,\forall j, \tag{B.21}$$

$$\left.\begin{aligned} \nabla\phi(\mathbf{x}) \cdot \mathbf{n} &= 0, \\ \nabla T(\mathbf{x}) \cdot \mathbf{n} &= 0, \end{aligned}\right\} \quad \mathbf{x} \in \partial\Omega_N \cup \Gamma_{W,i}\,\forall i, \tag{B.22}$$

$$\left.\begin{aligned} \phi(\mathbf{x}) &= 1, \\ T(\mathbf{x}) &= 0, \end{aligned}\right\} \quad \mathbf{x} \in \partial\Omega_D^T, \tag{B.23}$$

$$\left.\begin{aligned} \phi(\mathbf{x}) &= 0, \\ T(\mathbf{x}) &= 0, \end{aligned}\right\} \quad \mathbf{x} \in \partial\Omega_D^B. \tag{B.24}$$

B.2.1 Homogenisation of jump condition

We follow the same homogenisation procedure as in Chapter 6, in particular, the homogenisation of the electrical problem is identical and that of the thermal problem is similar. Therefore we will state the relevant results for the electrical problem and only include detail into the new thermal boundary condition at particle contacts.

Leading-order problem

$$\nabla_{\mathbf{y}}^2 T_0 + \nabla_{\mathbf{y}} \phi_0^T \nabla_{\mathbf{y}} \phi_0 = 0, \qquad \mathbf{y} \in \omega^S, \tag{B.25}$$

$$\nabla_{\mathbf{y}} T_0 \cdot \mathbf{n} = \eta_c [T_0] + \frac{\lambda_c}{2} [\phi_0]^2, \qquad \mathbf{y} \in \gamma_c, \tag{B.26}$$

$$\nabla_{\mathbf{y}} T_0 \cdot \mathbf{n} = 0, \qquad \mathbf{y} \in \gamma_w. \tag{B.27}$$

From the electrical problem, $\nabla_{\mathbf{y}} \phi_0 = 0$ and $[\phi_0] = 0$, thus following the same analysis as the electrical problem, we similarly deduce

$$\nabla_{\mathbf{y}} T_0 = 0, \qquad [T_0] = 0, \qquad \Rightarrow T_0 = T_0(\mathbf{x}). \tag{B.28}$$

First-order problem

$$\nabla_{\mathbf{y}}^2 T_1 = 0, \qquad \mathbf{y} \in \omega^S, \tag{B.29}$$

$$(\nabla_{\mathbf{y}} T_1 + \nabla_{\mathbf{x}} T_0) \cdot \mathbf{n} = \eta_c [T_1], \qquad \mathbf{y} \in \gamma_c, \tag{B.30}$$

$$(\nabla_{\mathbf{y}} T_1 + \nabla_{\mathbf{x}} T_0) \cdot \mathbf{n} = 0, \qquad \mathbf{y} \in \gamma_w. \tag{B.31}$$

As before, we introduce vector functions $\mathbf{\Psi}(\mathbf{y})$ and $\mathbf{\Phi}(\mathbf{y})$ and write

$$T_1(\mathbf{x}, \mathbf{y}) = \mathbf{\Psi}(\mathbf{y}) \cdot \nabla_{\mathbf{x}} T_0(\mathbf{x}) + \hat{T}_1(\mathbf{x}), \qquad \phi_1(\mathbf{x}, \mathbf{y}) = \mathbf{\Phi}(\mathbf{y}) \cdot \nabla_{\mathbf{x}} \phi_0(\mathbf{x}) + \hat{\phi}_1(\mathbf{x}), \tag{B.32}$$

thus we deduce the cell problems

$$\nabla_{\mathbf{y}}^2 \mathbf{\Psi} = 0, \qquad \mathbf{y} \in \omega^S, \tag{B.33}$$

$$(\mathbf{I} + \nabla_{\mathbf{y}} \mathbf{\Psi}) \cdot \mathbf{n} = \eta_c [\mathbf{\Psi}], \qquad \mathbf{y} \in \gamma_c, \tag{B.34}$$

$$(\mathbf{I} + \nabla_{\mathbf{y}} \mathbf{\Psi}) \cdot \mathbf{n} = 0, \qquad \mathbf{y} \in \gamma_w, \tag{B.35}$$

$$\nabla_{\mathbf{y}}^2 \mathbf{\Phi} = 0, \qquad \mathbf{y} \in \omega^S, \tag{B.36}$$

$$(\mathbf{I} + \nabla_{\mathbf{y}} \mathbf{\Phi}) \cdot \mathbf{n} = \lambda_c [\mathbf{\Phi}], \qquad \mathbf{y} \in \gamma_c, \tag{B.37}$$

$$(\mathbf{I} + \nabla_{\mathbf{y}} \mathbf{\Phi}) \cdot \mathbf{n} = 0, \qquad \mathbf{y} \in \gamma_w. \tag{B.38}$$

First-order problem

$$\begin{aligned} &\nabla_{\mathbf{y}} \cdot (\nabla_{\mathbf{y}} T_2 + \nabla_{\mathbf{x}} T_1) + \nabla_{\mathbf{x}} \cdot (\nabla_{\mathbf{y}} T_1 + \nabla_{\mathbf{x}} T_0) \\ &\quad + (\nabla_{\mathbf{x}} \phi_0 + \nabla_{\mathbf{y}} \phi_1)^\top (\nabla_{\mathbf{x}} \phi_0 + \nabla_{\mathbf{y}} \phi_1) = 0, \qquad \mathbf{y} \in \omega^S, \end{aligned} \tag{B.39}$$

$$(\nabla_{\mathbf{y}} T_2 + \nabla_{\mathbf{x}} T_1) \cdot \mathbf{n} = \eta_c [T_2] + \frac{\lambda_c}{2} [\phi_1]^2, \qquad \mathbf{y} \in \gamma_c, \tag{B.40}$$

$$(\nabla_{\mathbf{y}} T_2 + \nabla_{\mathbf{x}} T_1) \cdot \mathbf{n} = 0, \qquad \mathbf{y} \in \gamma_w. \tag{B.41}$$

We integrate (B.39) over ω^S and apply the boundary conditions. Let us consider the first term in (B.39) separately.

$$\int_{\omega^S} \nabla_{\mathbf{y}} \cdot (\nabla_{\mathbf{y}} T_2 + \nabla_{\mathbf{x}} T_1)\,\mathrm{d}\mathbf{y} = \int_{\partial\omega^S} (\nabla_{\mathbf{y}} T_2 + \nabla_{\mathbf{x}} T_1) \cdot \mathbf{n}\,\mathrm{d}S, \tag{B.42}$$

$$= \frac{1}{2}\int_{\gamma_c} \left((\nabla_{\mathbf{y}} T_2^+ + \nabla_{\mathbf{x}} T_1^+) \cdot \mathbf{n}^+ + (\nabla_{\mathbf{y}} T_2^- + \nabla_{\mathbf{x}} T_1^-) \cdot \mathbf{n}^-\right) \mathrm{d}S, \tag{B.43}$$

$$= \frac{1}{2}\int_{\gamma_c} \left(\eta_c [T_2]_+^- + \frac{\lambda_c}{2}[\phi_1]^2 + \eta_c [T_2]_-^+ + \frac{\lambda_c}{2}[\phi_1]^2\right) \mathrm{d}S. \tag{B.44}$$

where the $\pm$ superscripts denote the temperature and flux values on each side of the particle contact. Similarly to our analysis in Chapter 6, we must be careful to not double-count the contributions of the particle contacts. We note that because γ_c lies on the boundary of the periodic cell, the outer side of the contact boundary on one side of the cell is equivalent to the inner side of the contact boundary on the opposite side of the cell, as in Figure 6.8. This is why we divide (B.43) by 2. Therefore we conclude that

$$\int_{\omega^S} \nabla_{\mathbf{y}} (\nabla_{\mathbf{y}} T_2 + \nabla_{\mathbf{x}} T_1)\,\mathrm{d}\mathbf{y} = \frac{\lambda_c}{2}\int_{\gamma_c} [\phi_1]^2\,\mathrm{d}S. \tag{B.45}$$

Recalling the expressions for T_1 and ϕ_1 in terms of $\boldsymbol{\Psi}$ and $\boldsymbol{\Phi}$ given by (B.32), we write the integral of (B.39) over ω^S as

$$\nabla_{\mathbf{x}} \cdot \left(\left\{\int_{\omega^S} (\mathrm{I} + \nabla_{\mathbf{y}} \boldsymbol{\Psi})\,\mathrm{d}\mathbf{y}\right\} \nabla_{\mathbf{x}} T_0\right) + \nabla_{\mathbf{x}} \phi_0^\top \left(\int_{\omega^S} (\mathbf{I} + \nabla_{\mathbf{y}} \boldsymbol{\Phi})^\top (\mathbf{I} + \nabla_{\mathbf{y}} \boldsymbol{\Phi}) \mathrm{d}\mathbf{y} + \frac{\lambda_c}{2}\int_{\gamma_c} [\boldsymbol{\Phi}]^2 \mathrm{d}S\right) \nabla_{\mathbf{x}} \phi_0 = 0, \tag{B.46}$$

where, in index notation,

$$(\nabla_{\mathbf{y}} \boldsymbol{\Phi})_{ij} = \partial_i \Phi_j, \qquad \left([\boldsymbol{\Phi}]^2\right)_{i,j} = [\Phi_i][\Phi_j]. \tag{B.47}$$

We can simplify the second term on the left-hand side of (B.46). In particular, consider

$$\int_{\omega^S} (\mathbf{I} + \nabla_{\mathbf{y}} \boldsymbol{\Phi})^\top (\mathbf{I} + \nabla_{\mathbf{y}} \boldsymbol{\Phi})\,\mathrm{d}\mathbf{y} = \int_{\omega^S} (\mathbf{I} + \nabla_{\mathbf{y}} \boldsymbol{\Phi}) \mathrm{d}\mathbf{y} + \int_{\omega^S} \nabla_{\mathbf{y}} \boldsymbol{\Phi}^\top \mathrm{d}\mathbf{y} + \int_{\omega^S} \nabla_{\mathbf{y}} \boldsymbol{\Phi}^\top \nabla_{\mathbf{y}} \boldsymbol{\Phi} \mathrm{d}\mathbf{y}. \tag{B.48}$$

Following from the same analysis as in Chapter 3, we consider the third term on the right-hand side of (B.48), namely

$$\left(\int_{\omega^S} \nabla_{\mathbf{y}} \mathbf{\Phi}^\top \nabla_{\mathbf{y}} \mathbf{\Phi} \mathrm{d}\mathbf{y}\right)_{ij} = \int_{\omega^S} (\partial_k \Phi_i)(\partial_k \Phi_j)\,\mathrm{d}\mathbf{y}, \tag{B.49}$$

$$= \int_{\omega^S} \partial_k(\Phi_i \partial_k \Phi_j) - \Phi_i \partial_k \partial_k \Phi_j\,\mathrm{d}\mathbf{y}, \tag{B.50}$$

$$= \int_{\partial\omega} \Phi_i \partial_k \Phi_j n_k\,\mathrm{d}S - \int_{\omega^S} \Phi_i \partial_k \partial_k \Phi_j\,\mathrm{d}\mathbf{y}. \tag{B.51}$$

Recall the cell problem for $\mathbf{\Phi}$ (B.36)–(B.38) in Einstein summation convention,

$$\partial_k \partial_k \Phi_j = 0, \qquad \text{in } \omega^S, \tag{B.52}$$

$$\partial_k \Phi_j n_k + n_j = 0, \qquad \text{on } \gamma_w, \tag{B.53}$$

$$\partial_k \Phi_j n_k + n_j = \lambda_c[\Phi_j], \qquad \text{on } \gamma_c. \tag{B.54}$$

Therefore, the volume integral in (B.51) disappears due to (B.52) and we split the boundary integral into γ_c and γ_w, keeping in mind the discontinuities across γ_c,

$$\begin{aligned}\int_{\partial\omega} \Phi_i \partial_k \Phi_j n_k\,\mathrm{d}S = &-\int_{\gamma_w} \Phi_i n_j\,\mathrm{d}S \\ &+ \frac{1}{2}\int_{\gamma_c} \left(\Phi_i^+ \left(\lambda_c[\Phi_j]_+^- - n_j^-\right) + \Phi_i^- \left(\lambda_c[\Phi_j]_-^+ - n_j^+\right)\right)\mathrm{d}S,\end{aligned} \tag{B.55}$$

$$= -\int_{\partial\omega} \Phi_i n_j\,\mathrm{d}S - \int_{\gamma_c} \Phi_i n_j\,\mathrm{d}S + \frac{\lambda_c}{2}\int_{\gamma_c} (\Phi_i^+ - \Phi_i^-)[\Phi_j]_+^- \mathrm{d}S, \tag{B.56}$$

$$= -\int_{\omega^S} \partial_j \Phi_i\,\mathrm{d}\mathbf{y} - \frac{\lambda_c}{2}\int_{\gamma_c} [\Phi_i][\Phi_j]\mathrm{d}S, \tag{B.57}$$

$$= -\left(\int_{\omega^S} \nabla_{\mathbf{y}} \mathbf{\Phi}^\top \mathrm{d}\mathbf{y}\right)_{ij} - \left(\frac{\lambda_c}{2}\int_{\gamma_c} [\mathbf{\Phi}]^2\,\mathrm{d}S\right)_{ij}. \tag{B.58}$$

Therefore, (B.48) can be written

$$\int_{\omega^S} \left(\mathbf{I} + \nabla_{\mathbf{y}} \mathbf{\Phi}\right)^\top \left(\mathbf{I} + \nabla_{\mathbf{y}} \mathbf{\Phi}\right) \mathrm{d}\mathbf{y} = \int_{\omega^S} (\mathbf{I} + \nabla_{\mathbf{y}} \mathbf{\Phi})\mathbf{d}\mathbf{y} - \frac{\lambda_c}{2}\int_{\gamma_c} [\mathbf{\Phi}]^2 \mathrm{d}S, \tag{B.59}$$

and the homogenised equation (B.46) becomes

$$\nabla_{\mathbf{x}} \cdot \left(\left\{\int_{\omega^S} (\mathrm{I} + \nabla_{\mathbf{y}} \mathbf{\Psi})\,\mathrm{d}\mathbf{y}\right\} \nabla_{\mathbf{x}} T_0\right) + \nabla_{\mathbf{x}} \phi_0^\top \left(\int_{\omega^S} (\mathbf{I} + \nabla_{\mathbf{y}} \mathbf{\Phi})\mathrm{d}\mathbf{y}\right) \nabla_{\mathbf{x}} \phi_0 = 0, \tag{B.60}$$

which we write as

$$\nabla_{\mathbf{x}} \cdot (\boldsymbol{k}_{\text{eff}} \nabla_{\mathbf{x}} T_0) + q_{\text{eff}} = 0, \tag{B.61}$$

where the effective thermal conductivity $\boldsymbol{k}_{\text{eff}}$, effective electrical conductivity $\boldsymbol{\sigma}_{\text{eff}}$ and effective Ohmic heating q_{eff} are given by

$$\boldsymbol{k}_{\text{eff}} = \int_{\omega^S} (\mathbf{I} + \nabla_{\mathbf{y}} \boldsymbol{\Psi}) \mathbf{dy}, \tag{B.62}$$

$$\boldsymbol{\sigma}_{\text{eff}} = \int_{\omega^S} (\mathbf{I} + \nabla_{\mathbf{y}} \boldsymbol{\Phi}) \mathbf{dy}, \tag{B.63}$$

$$q_{\text{eff}} = \nabla_{\mathbf{x}} \phi_0 \cdot \boldsymbol{\sigma}_{\text{eff}} \nabla_{\mathbf{x}} \phi_0. \tag{B.64}$$

Bibliography

[1] H. T. Aichlmayr and F. Kulacki. "The effective thermal conductivity of saturated porous media". In: *Advances in Heat Transfer* 39 (2006), pp. 377–460.

[2] G. Allaire and M. Amar. "Boundary layer tails in periodic homogenization". In: *ESAIM: Control, Optimisation and Calculus of Variations* 4 (1999), pp. 209–243.

[3] G. Allaire and K. El Ganaoui. "Homogenization of a conductive and radiative heat transfer problem". In: *Multiscale Modeling & Simulation* 7.3 (2009), pp. 1148–1170.

[4] G. Allaire and Z. Habibi. "Homogenization of a conductive, convective, and radiative heat transfer problem in a heterogeneous domain". In: *SIAM Journal on Mathematical Analysis* 45.3 (2013), pp. 1136–1178.

[5] G. Allaire and Z. Habibi. "Second order corrector in the homogenization of a conductive-radiative heat transfer problem". In: *Discrete and Continuous Dynamical Systems-Series B* 18.1 (2013), pp. 1–36.

[6] M. S. Alnæs, J. Blechta, J. Hake, A. Johansson, B. Kehlet, A. Logg, C. Richardson, J. Ring, M. E. Rognes, and G. N. Wells. "The FEniCS project version 1.5". In: *Archive of Numerical Software* 3.100 (2015), pp. 9–23.

[7] D. N. Arnold. "An interior penalty finite element method with discontinuous elements". In: *SIAM Journal on Numerical Analysis* 19.4 (1982), pp. 742–760.

[8] D. N. Arnold, F. Brezzi, B. Cockburn, and L. D. Marini. "Unified analysis of discontinuous Galerkin methods for elliptic problems". In: *SIAM Journal on Numerical Analysis* 39.5 (2002), pp. 1749–1779.

[9] I. Babuška. "The finite element method with penalty". In: *Mathematics of Computation* 27.122 (1973), pp. 221–228.

[10] I. Babuška and M. Zlámal. "Nonconforming elements in the finite element method with penalty". In: *SIAM Journal on Numerical Analysis* 10.5 (1973), pp. 863–875.

[11] G. K. Batchelor and R. O'Brien. "Thermal or electrical conduction through a granular material". In: *Proceedings of the Royal Society of London. A. Mathematical and Physical Sciences* 355.1682 (1977), pp. 313–333.

[12] M. Z. Bazant. "The spot model for random-packing dynamics". In: *Mechanics of Materials* 38.8-10 (2006), pp. 717–731.

[13] M. Bruna and S. J. Chapman. “Diffusion in spatially varying porous media”. In: *SIAM Journal on Applied Mathematics* 75.4 (2015), pp. 1648–1674.

[14] C. Budd, S. Chapman, J. King, A. Lacey, D. Larson, M. Peletier, C. Please, D. Riley, A. Wheeler, and G. Wood. “Temperature variations and control of a Calciner”. In: (1995).

[15] A. Bush, R. Gibson, and T. Thomas. “The elastic contact of a rough surface”. In: *Wear* 35.1 (1975), pp. 87–111.

[16] G. F. Carrier, M. Krook, and C. E. Pearson. *Functions of a complex variable: theory and technique*. Vol. 49. SIAM, 2005.

[17] A. Celzard, J. Marêché, F. Payot, D. Bégin, and G. Furdin. “Electrical conductivity of anthracites as a function of heat treatment temperature”. In: *Carbon* 38.8 (2000), pp. 1207–1215.

[18] S. Chandrasekhar. *Radiative transfer*. Courier Corporation, 2013.

[19] S. Chapman and S. McBurnie. “Integral constraints in multiple-scales problems”. In: *European Journal of Applied Mathematics* 26.5 (2015), pp. 595–614.

[20] S. Chapman, R. Shipley, and R. Jawad. “Multiscale modeling of fluid transport in tumors”. In: *Bulletin of mathematical biology* 70.8 (2008), p. 2334.

[21] C. R. Chester. *Techniques in partial differential equations*. McGraw-Hill, 1971.

[22] G. Cimatti. “Remark on existence and uniqueness for the thermistor problem under mixed boundary conditions”. In: *Quarterly of Applied Mathematics* 47.1 (1989), pp. 117–121.

[23] J. Clendenin, K. Barclay, H. Donald, G. Gillmore, and C. Wright. “Thermal and electrical properties of anthracite and bituminous coals”. In: *Transactions of the Seventh Annual Anthracite Conference of Lehigh University*. 1949.

[24] J. Clouet. “The Rosseland approximation for radiative transfer problems in heterogeneous media”. In: *Journal of Quantitative Spectroscopy and Radiative Transfer* 58.1 (1997), pp. 33–43.

[25] B. Cockburn, G. E. Karniadakis, and C. W. Shu. *Discontinuous Galerkin methods: theory, computation and applications*. Vol. 11. Springer Science and Business Media, 2012.

[26] R. Crane and R. Vachon. “A prediction of the bounds on the effective thermal conductivity of granular materials”. In: *International Journal of Heat and Mass Transfer* 20.7 (1977), pp. 711–723.

[27] M. P. Dalwadi, I. M. Griffiths, and M. Bruna. “Understanding how porosity gradients can make a better filter using homogenization theory”. In: *Proceedings of the Royal Society A: Mathematical, Physical and Engineering Sciences* 471.2182 (2015), p. 20150464.

[28] M. Dhainaut. “Simulation of the electric field in a submerged arc furnace”. In: *Proceedings of the Tenth International Ferroalloy Congress*. 2004, pp. 605–613.

[29] H. Dijs and D. Smith. "Factors affecting the resistivity and reactivity of carbonaceous reducing agents for the electric smelting industry". In: *Journal of the South African Institute of Mining and Metallurgy* 80.8 (1980), pp. 289–296.

[30] H. Dindi, X. H. Bai, and W. B. Krantz. "Thermal and electrical property measurements for coal". In: *Fuel* 68.2 (1989), pp. 185–192.

[31] J. Douglas and T. Dupont. "Interior penalty procedures for elliptic and parabolic Galerkin methods". In: *Computing Methods in Applied Sciences*. Springer, 1976, pp. 207–216.

[32] P. A. Eidem. "Electrical resistivity of coke beds". PhD thesis. Norges Teknisk-Naturvitenskapelige Universitet, Fakultet for Naturvitenskap og Teknologi, Institutt for Materialteknologi, 2008.

[33] Y. Epshteyn and B. Rivière. "Estimation of penalty parameters for symmetric interior penalty Galerkin methods". In: *Journal of Computational and Applied Mathematics* 206.2 (2007), pp. 843–872.

[34] A. Espinola, P. M. Miguel, M. R. Salles, and A. R. Pinto. "Electrical properties of carbons – resistance of powder materials". In: *Carbon* 24.3 (1986), pp. 337–341.

[35] A. Fowler, I. Frigaard, and S. Howison. "Temperature surges in current-limiting circuit devices". In: *SIAM Journal on Applied Mathematics* 52.4 (1992), pp. 998–1011.

[36] J. Francl and W. Kingery. "Thermal conductivity: IX, experimental investigation of effect of porosity on thermal conductivity". In: *Journal of the American Ceramic Society* 37.2 (1954), pp. 99–107.

[37] M. Gasik. *Handbook of ferroalloys: theory and technology*. Butterworth-Heinemann, 2013.

[38] J. Greenwood and J. P. Williamson. "Contact of nominally flat surfaces". In: *Proceedings of the Royal Society of London. Series A. Mathematical and Physical Sciences* 295.1442 (1966), pp. 300–319.

[39] J. A. Greenwood. "Constriction resistance and the real area of contact". In: *British Journal of Applied Physics* 17.12 (1966), p. 1621.

[40] A. Gusarov. "Model of radiative heat transfer in heterogeneous multiphase media". In: *Physical Review B* 81.6 (2010), p. 064202.

[41] G. A. Hackett, J. W. Zondlo, and R. Svensson. "Evaluation of carbon materials for use in a direct carbon fuel cell". In: *Journal of Power Sources* 168.1 (2007), pp. 111–118.

[42] K. Halden, A. De Alwis, and P. Fryer. "Changes in the electrical conductivity of foods during Ohmic heating". In: *International Journal of Food Science & Technology* 25.1 (1990), pp. 9–25.

[43] S. A. Halvorsen. Private communication. 2016.

[44] H. Hertz, D. E. Jones, and G. A. Schott. *Miscellaneous papers*. Macmillan and Company, 1896.

[45] E. Hinch. *Perturbation methods*. Cambridge University Press, 1991.

[46] R. Holm. *Electric contacts: theory and application*. Springer Science & Business Media, 2013.

[47] J. R. Howell, M. P. Menguc, and R. Siegel. *Thermal radiation heat transfer*. CRC press, 2015.

[48] S. Howison. "A note on the thermistor problem in two space dimensions". In: *Quarterly of Applied Mathematics* 47.3 (1989), pp. 509–512.

[49] S. Howison. *Practical applied mathematics: modelling, analysis, approximation*. 38. Cambridge University Press, 2005.

[50] S. Howison, J. Rodrigues, and M. Shillor. "Stationary solutions to the thermistor problem". In: *Journal of Mathematical Analysis and Applications* 174.2 (1993), pp. 573–588.

[51] C. Hsu, P. Cheng, and K. Wong. "Modified Zehner-Schlunder models for stagnant thermal conductivity of porous media". In: *International Journal of Heat and Mass Transfer* 37.17 (1994), pp. 2751–2759.

[52] R. L. Jackson and J. L. Streator. "A multi-scale model for contact between rough surfaces". In: *Wear* 261.11-12 (2006), pp. 1337–1347.

[53] E. Jones, T. Oliphant, P. Peterson, et al. *SciPy: Open source scientific tools for Python*. 2001.

[54] M. Kaviany. *Principles of heat transfer in porous media*. Springer Science and Business Media, 2012.

[55] K. B. Kiradjiev, S. A. Halvorsen, R. A. Van Gorder, and S. D. Howison. "Maxwell-type models for the effective thermal conductivity of a porous material with radiative transfer in the voids". In: *International Journal of Thermal Sciences* 145 (2019), p. 106009.

[56] L. Kogut and K. Komvopoulos. "Electrical contact resistance theory for conductive rough surfaces separated by a thin insulating film". In: *Journal of Applied Physics* 95.2 (2004), pp. 576–585.

[57] A. Lacey. "Thermal runaway in a non-local problem modelling Ohmic heating: Part I: Model derivation and some special cases". In: *European journal of applied Mathematics* 6.2 (1995), pp. 127–144.

[58] A. Lacey, D. Tzanetis, and P. Vlamos. "Behaviour of a non-local reactive convective problem modelling Ohmic heating of foods". In: *The Quarterly Journal of Mechanics and Applied Mathematics* 52.4 (1999), pp. 623–644.

[59] J. Lions. *Some methods in the mathematical analysis of systems and their control*. Beijing, Science Press, 1981.

[60] A. Luikov, A. Shashkov, L. Vasiliev, and Y. E. Fraiman. "Thermal conductivity of porous systems". In: *International Journal of Heat and Mass Transfer* 11.2 (1968), pp. 117–140.

[61] Q. Ma and J. Cui. "Second-order two-scale analysis method for the heat conductive problem with radiation boundary condition in periodical porous domain". In: *Communications in Computational Physics* 14.4 (2013), pp. 1027–1057.

[62] O. A. Marina, L. R. Pederson, M. C. Williams, G. W. Coffey, K. D. Meinhardt, C. D. Nguyen, and E. C. Thomsen. "Electrode performance in reversible solid oxide fuel cells". In: *Journal of the Electrochemical Society* 154.5 (2007), B452–B459.

[63] J. C. Maxwell. *A treatise on electricity and magnetism*. Vol. 1. Oxford: Clarendon Press, 1873.

[64] S. E. McBurnie. "Sound propagation through bubbly liquids". PhD thesis. Oxford University, 2010.

[65] H. Mio, M. Kadowaki, S. Matsuzaki, and K. Kunitomo. "Development of particle flow simulator in charging process of blast furnace by discrete element method". In: *Minerals Engineering* 33 (2012), pp. 27–33.

[66] M. F. Modest. *Radiative heat transfer*. Academic Press, 2013.

[67] S. Moskow and M. Vogelius. "First-order corrections to the homogenised eigenvalues of a periodic composite medium. A convergence proof'. In: *Proceedings of the Royal Society of Edinburgh Section A: Mathematics* 127.6 (1997), pp. 1263–1299.

[68] W. Mullins. "Critique and comparison of two stochastic theories of gravity-induced particle flow". In: *Powder Technology* 23.1 (1979), pp. 115–119.

[69] R. Nedderman and U. Tüzün. "A kinematic model for the flow of granular materials". In: *Powder Technology* 22.2 (1979), pp. 243–253.

[70] B. Nijboer and F. De Wette. "On the calculation of lattice sums". In: *Physica* 23.1-5 (1957), pp. 309–321.

[71] J. R. Ockendon, S. Howison, A. Lacey, and A. Movchan. *Applied partial differential equations*. Oxford University Press on Demand, 2003.

[72] S. E. Olsen, S. Olsen, M. Tangstad, and T. Lindstad. *Production of manganese ferroalloys*. Tapir Academic Press, 2007.

[73] T. Orzechowski, M. Rosen, H. Kornblum, J. Porter, L. Suter, A. Thiessen, and R. Wallace. "The Rosseland mean opacity of a composite material at high temperatures". In: *AIP Conference Proceedings*. Vol. 381. 1. American Institute of Physics. 1996, pp. 287–294.

[74] E. S. Palencia. *Non-homogeneous media and vibration theory*. Springer-Verlag, 1980.

[75] E. Pasternak and H. B. Mühlhaus. "Generalised homogenisation procedures for granular materials". In: *Mathematics and Mechanics of Granular Materials*. Springer, 2005, pp. 199–229.

[76] G. Pavliotis and A. Stuart. *Multiscale methods: averaging and homogenization*. Springer Science and Business Media, 2008.

[77] R. Penta, D. Ambrosi, and R. Shipley. "Effective governing equations for poroelastic growing media". In: *Quarterly Journal of Mechanics and Applied Mathematics* 67.1 (2014), pp. 69–91.

[78] R. Powell and F. Schofield. "The thermal and electrical conductivities of carbon and graphite to high temperatures". In: *Proceedings of the Physical Society* 51.1 (1939), p. 153.

[79] J. R. Prakash and K. K. Rao. "Steady compressible flow of cohesionless granular materials through a wedge-shaped bunker". In: *Journal of fluid mechanics* 225 (1991), pp. 21–80.

[80] F. Rathgeber, D. A. Ham, L. Mitchell, M. Lange, F. Luporini, A. T. McRae, G.-T. Bercea, G. R. Markall, and P. H. Kelly. "Firedrake: automating the finite element method by composing abstractions". In: *ACM Transactions on Mathematical Software (TOMS)* 43.3 (2017), p. 24.

[81] G. Richardson and S. J. Chapman. "Derivation of the bidomain equations for a beating heart with a general microstructure". In: *SIAM Journal on Applied Mathematics* 71.3 (2011), pp. 657–675.

[82] B. Rivière. *Discontinuous Galerkin methods for solving elliptic and parabolic equations: theory and implementation*. SIAM, 2008.

[83] B. Rivière, M. F. Wheeler, and V. Girault. "Improved energy estimates for interior penalty, constrained and discontinuous Galerkin methods for elliptic problems. Part I". In: *Computational Geosciences* 3.3-4 (1999), pp. 337–360.

[84] S. Rosseland. *Theoretical astrophysics; atomic theory and the analysis of stellar atmospheres and envelopes*. Clarendon Press, Oxford, 1936.

[85] H. Russell. "Principles of heat flow in porous insulators". In: *Journal of the American Ceramic Society* 18.1-12 (1935), pp. 1–5.

[86] C. H. Rycroft. "Multiscale modeling in granular flow". PhD thesis. Massachusetts Institute of Technology, Department of Mathematics, 2007.

[87] J. F. Schatz and G. Simmons. "Thermal conductivity of Earth materials at high temperatures". In: *Journal of Geophysical Research* 77.35 (1972), pp. 6966–6983.

[88] R. Sengupta, M. Bhattacharya, S. Bandyopadhyay, and A. K. Bhowmick. "A review on the mechanical and electrical properties of graphite and modified graphite reinforced polymer composites". In: *Progress in Polymer Science* 36.5 (2011), pp. 638–670.

[89] P. G. Slade. *Electrical contacts: principles and applications*. CRC press, 2017.

[90] B. M. Sloman, C. P. Please, R. A. Van Gorder, A. M. Valderhaug, R. G. Birkeland, and H. Wegge. "A heat and mass transfer model of a silicon pilot furnace". In: *Metallurgical and Materials Transactions B* 48.5 (2017), pp. 2664–2676.

[91] M. Sørlie and H. Gran. "Cathode collector bar-to-carbon contact resistance". In: *Light Metals 1992* (1992), pp. 779–787.

[92] M. Sørlie, H. Gran, and H. A. Øye. "Property changes of cathode lining materials during cell operation". In: *Essential Readings in Light Metals*. Springer, 2016, pp. 936–945.

[93] M. Sparta. *Computed tomography scans of carbon materials*. NORCE internal report. 2019.

[94] M. Spinnler, E. R. Winter, and R. Viskanta. "Studies on high-temperature multilayer thermal insulations". In: *International Journal of Heat and Mass Transfer* 47.6-7 (2004), pp. 1305–1312.

[95] R. Stirling. "Ohmic heating-a new process for the food industry". In: *Power Engineering Journal* 1.6 (1987), pp. 365–371.

[96] C. Tien. "Thermal radiation in packed and fluidized beds". In: *Journal of Heat transfer* 110.4b (1988), pp. 1230–1242.

[97] T. Tiihonen. "Stefan–Boltzmann radiation on non-convex surfaces". In: *Mathematical Methods in the Applied Sciences* 20.1 (1997), pp. 47–57.

[98] E. Tsotsas and H. Martin. "Thermal conductivity of packed beds: a review". In: *Chemical Engineering and Processing: Process Intensification* 22.1 (1987), pp. 19–37.

[99] N. Wakao and K. Kato. "Effective thermal conductivity of packed beds". In: *Journal of Chemical Engineering of Japan* 2.1 (1969), pp. 24–33.

[100] R. R. Walton. "Furnaces, Electric, Resistance Furnaces". In: *Kirk-Othmer Encyclopedia of Chemical Technology* (2000).

[101] M. F. Wheeler. "An elliptic collocation-finite element method with interior penalties". In: *SIAM Journal on Numerical Analysis* 15.1 (1978), pp. 152–161.

[102] P. Zehner and E. Schlunder. "Thermal conductivity of granular material at moderate temperatures". In: *Chemie Ingenieur Technik* 42.14 (1970), pp. 933–941.

[103] Y. Zeroukhi, E. Napieralska-Juszczak, G. Vega, K. Komeza, F. Morganti, and S. Wiak. "Dependence of the contact resistance on the design of stranded conductors". In: *Sensors* 14.8 (2014), pp. 13925–13942.

[104] C. Zhao, T. Lu, H. Hodson, and J. Jackson. "The temperature dependence of effective thermal conductivity of open-celled steel alloy foams". In: *Materials Science and Engineering: A* 367.1-2 (2004), pp. 123–131.

[105] J. Zhou, A. Yu, and Y. Zhang. "A boundary element method for evaluation of the effective thermal conductivity of packed beds". In: *Journal of Heat Transfer* 129.3 (2007), pp. 363–371.

[106] Q. Zhou, H. Zhang, and Y. Zheng. "A homogenization technique for heat transfer in periodic granular materials". In: *Advanced Powder Technology* 23.1 (2012), pp. 104–114.

[107] Z. Zhou, H. Zhu, A. Yu, B. Wright, D. Pinson, and P. Zulli. "Discrete particle simulation of solid flow in a model blast furnace". In: *ISIJ International* 45.12 (2005), pp. 1828–1837.

[108] Z. Zhou, H. Zhu, A. Yu, B. Wright, and P. Zulli. "Discrete particle simulation of gas–solid flow in a blast furnace". In: *Computers and Chemical Engineering* 32.8 (2008), pp. 1760–1772.

[109] I. Zucker. "Functional equations for poly-dimensional zeta functions and the evaluation of Madelung constants". In: *Journal of Physics A: Mathematical and General* 9.4 (1976), p. 499.

[110] I. Zucker. "Madelung constants and lattice sums for invariant cubic lattice complexes and certain tetragonal structures". In: *Journal of Physics A: Mathematical and General* 8.11 (1975), p. 1734.

[111] D. Zumbrunnen, R. Viskanta, and F. Incropera. "Heat transfer through granular beds at high temperature". In: *Wärme-und Stoffübertragung* 18.4 (1984), pp. 221–226.